Experimental Investigation of the Auto-Ignition Characteristics of Oxygenated Reference Fuel Compounds

by

Stephen Michael Walton

A dissertation submitted in partial fulfillment
of the requirements for the degree of
Doctor of Philosophy
(Mechanical Engineering)
in The University of Michigan
2008

Doctoral Committee:
        Professor Margaret S. Wooldridge, Chair
        Professor Arvind Atreya
        Professor Elaine S. Oran
        Professor Johannes W. Schwank

to my family

for a lifetime of support and encouragement

Acknowledgments

I would first like to thank Professor Margaret Wooldridge for her support and guidance over the past several years of my graduate studies. Her concern, encouragement, and insight throughout the many research and life challenges I faced, including my battle with Hodgkin's Disease, made this a very rewarding experience.

I would also like to thank my additional dissertation committee members, Professor Arvind Atreya, Professor Elaine Oran, and Professor Johannes Schwank for the generous contribution of their time and oversight.

I also appreciate the support of Department of Energy through the University HCCI Consortium for their financial contributions, as well as many travel awards from Rackham, the Combustion Institute, and the American Society of Mechanical Engineers.

I also have been rewarded with many new colleagues, including those who greeted me when I arrived; Xin He, Brad Zigler, Smitesh Bakrania, Michael Donovan, Travis Palmer, Tiffany Miller, and Melissa Chernovsky, and those who will see me graduate; James Wiswall, Carlos Perez, Dimitris Assanis, Paul Teini, and Darshan Karwat, among others I am sure to have left out. Your personal encouragement, recommendations, assistance, and friendships have been vital to this journey.

There are many other people who have assisted in the development of the hardware for the experimental facility. I would like to acknowledge the help from John Mears, Kent Pruss, and in particular Steve Emanuel, who always was ready for a new adventure in the machine shop.

Table of Contents

List of Tables

List of Figures

xv

List of Appendices

Appendix

Abstract

The increased use of biofuels presents an opportunity to improve combustion performance while simultaneously reducing greenhouse gases and pollutant emissions. Realization of this potential, however, requires a more complete understanding of the fundamental reaction chemistry at conditions relevant to advanced combustion systems, i.e., moderate temperatures and elevated pressures. This work focused on improving the fundamental understanding of the auto-ignition chemistry of oxygenated reference fuel compounds. A systematic study of the effects of ester structure on ignition chemistry was performed using the University of Michigan Rapid Compression Facility. The ignition properties of the ester compounds were investigated over a broad range of pressures (P=5-20 atm) and temperatures (T=850-1150 K) which are directly relevant to advanced combustion engine strategies.

As part of this work, new and improved diagnostics were developed to enhance the characterization of the ester ignition properties. Specifically, a color high-speed digital imaging system was developed and used to identify ignition regimes. Additionally, the RCF gas-sampling system was re-designed to allow sampling of intermediate species at higher pressures.

Ignition delay time measurements for five esters were determined using the RCF. The esters were selected to systematically consider the chemical structure of the compounds. Five C_5 esters were studied. Three were saturated: methyl butanoate, butyl methanoate, and ethyl propanoate; and two were unsaturated: methyl crotonate and methyl trans-3-hexenoate. Correlations for the ignition delay time measurements

were developed for each of the esters. The unsaturated esters were found to be more reactive than their saturated counterparts, with the largest unsaturated ester, methyl trans-3-hexenoate having the highest reactivity. The two isomers of the saturated esters, butyl methanoate and ethyl propanoate, were more reactive than the isomer methyl butanoate. The results are explained if we assume that butyl methanoate and ethyl propanoate form intermediate ring structures which decompose more rapidly than esters such as methyl butanoate, which do not form ring structures.

Modeling studies of the reaction chemistry were conducted for methyl butanoate and ethyl propanoate, for which detailed mechanisms were available in the literature. The new experimental data indicated that literature rate coefficients for some of the methyl butanoate/HO_2 reactions were too fast. Modifying the values for the rate coefficients, within the theoretical uncertainties for the reactions, led to excellent agreement between the model predictions and the experimental data for the ignition delay time data from both the UM RCF and shock tube studies conducted at higher temperatures. Comparison of the modeling results with the intermediates measured during methyl butanoate ignition indicated that pathways leading to the formation of small hydrocarbons (specifically methane, ethane, ethane, propane, propene, and 1-butene) are relatively well represented in the reaction mechanism, with levels of agreement within several hundred ppm. The experimental data for oxygenate species were in good qualitative agreement with model calculations when those species are present in large concentrations (e.g. methyl acrylate, methyl-3-butenoate, and methyl crotonate).

An initial investigation of possible synergies between ester and hydrocarbon chemistry was also conducted as part of this work. Blends of the unsaturated ester methyl trans-3-hexenoate were found to suppress the negative temperature coefficient behavior of the hydrocarbon reference fuel n-heptane.

The results of this work provide archival benchmark data for improved understand-

ing of the dominant reaction pathways and species controlling the auto-ignition of oxygenated reference fuel compounds. These data also provide a path for continued development of chemical kinetic models to optimize practical combustion systems.

Chapter 1

Introduction

Biomass fuel systems show promise as alternatives to existing fossil fuel technology, and they can be applied to many existing combustion systems. Biofuels are especially relevant to transportation systems where energy density and refueling time are important. Biofueled combustion systems have the potential to reduce greenhouse gas emissions throughout the fuel life cycle, while offsetting fossil fuel consumption. As the depletion of fossil energy resources and the impacts of global warming become more urgent, many existing combustion technologies will be revised to operate using biomass fuels.

Biofuels are derived from recently living organic material, which has obtained the majority of its stored energy from the sun. The plants chosen for biofuel production generally varies by geography, with countries focusing on fast growing native plants. For example, the United States has focused development on soybeans for biodiesel, corn for ethanol, and more recently switchgrass for ethanol. Europe has focused on different feedstocks: rapeseed for biodiesel, with wheat and sugarbeet for ethanol. Brazil is currently utilizing sugar cane for ethanol, while India uses jatropha for biodiesel, and Southeast asia uses palm oil for biodiesel. In some cases efforts are on a more localized scale, for example Spain is focusing on the use of sunflower to produce biodiesel. The process of deriving the end fuel from each of the feedstocks differs, and,

in the case of biodiesels, the end fuel derived from each of the feedstocks differs as well. The generation of the final fuel is a result of transesterification of the triacyl glycerides that comprise vegetable oils from various plants. This process requires the use of alcohol, typically methanol or ethanol, with a catalyst to yield esters with glycerol as a primary byproduct. As a result of this process, biodiesel fuels consist of saturated and unsaturated methyl and ethyl esters, and these esters generally contain 12 or more carbon atoms (1), as shown in Fig. 1.1. This figure shows the reactivity of the different esters, as cetane number, and also shows number of carbon atoms and double bonds present in fuels derived from many different feedstocks. For example, methyl oleate (C18:1) contains 18 carbon atoms, and has one double bond.

TABLE 2. List of Biodiesel Fuels Tested in This Study (LFFAG = low free fatty acid grease, HFFAG = high free fatty acid grease)

fuels tested	cetane no.	density, g/cm^3	iodine no.	water/sediment, vol %	glycerol free/bound, wt %	acid no.	oxygen, wt %
	ASTM D613	ASTM D4052	ASTM D1510	ASTM D2709	Christina Planc	ASTM D664	ASTM D5291
methyl soy	47.2	0.8877[a]	133[b]	0[a]	0.001/0.797[a]	0.32[a]	11.16
edible methyl tallow	62.9	0.8708[a]	64[b]	0.05[a]	0/0.102[a]	0.32[a]	11.74
inedible methyl tallow	61.7	0.8767[a]	64[b]	0[a]	0/0.159[a]	0.44[a]	11.08
methyl canola	55.0	0.8811[a]	97[b]	0[a]	0.001/0.196[a]	0.13[a]	11.04
methyl lard	63.6	0.8762[a]		0.6[a]	0/0.160[a]	0.76[a]	11.82
methyl LFFAG	57.8	0.8789[a]		0[a]	0/0.256[a]	0.41[a]	11.10
methyl HFFAG (Bio3000)	52.9[a]	0.8767[a]		0.21[a]	0.010/0.064[a]	0.36	11.28
methyl laurate (C12:0)	61.2	0.8730	0.3	0	0/0.003	0.06	14.68
methyl palmitate (C16:0)	74.3[b]	0.8674	0.5	0	0/0.011	0.16	11.98
methyl stearate (C18:0)	86.9[b]	0.8684	0.5	0.005	0/0.035	1.9	11.84
ethyl stearate (C18:0)	76.8[b]	0.8636	1	0	0/0.024	0.01	10.84
methyl oleate (C18:1)	56.0	0.8796	90	0	0/0.022	0.13	11.44
methyl linoleate (C18:2)	41.7	0.8943	151	0	0.001/0.126	0.41	11.76
ethyl linoleate (C18:2)	44.4	0.8869	140	0	0/0.089	0.81	11.05
methyl linolenate (C18:3)	45.9	0.8941	165	0	0/0.089	0.23	11.25
ethyl linseed	43.4	0.8942	157	0	0/0.041	2.9	11.19
methyl soy (soyagold)	52.3	0.8836	121	0	0.007/0.223	0.15	11.44
methyl hydrogenated soy		0.8688	6	0	0.001/0.099	4.66	11.10
ethyl soy	47.3	0.8817	122	0	0.003/0.031	3.02	11.55
ethyl hydrogenated soy		0.8643	6	0	0/0.097	3.94	6.52
1:2 M-sterate:M-linseed			66	0	0/0.032	1.62	

[a] From Kinast (7). [b] From Graboski and McCormick (1).

Figure 1.1   Table from McCormick *et al.* (1) describing the actual composition of biodiesel from various feedstocks

Although the most recent interest in biofuels is related to concerns about pollution and global warming, the use of biofuels has been demonstrated many times in modern history. For example, Rudolph Diesel originally designed the diesel engine to run on peanut oil, which he successfully demonstrated in 1892. A few years later, in 1908, the original Ford Model T engine, utilizing the Otto cycle, was designed to run on ethanol. Despite these successes, the infrastructure supporting these developments

changed when fossil fuels were discovered to be widely available. Fossil fuels were adopted quickly because they were much cheaper than the biofuels they were replacing. When fossil fuel was unavailable, resourceful countries redeveloped the infrastructure to utilize biofuels. For example, Germany blended alcohol fermented from potatoes into gasoline during World War II, and Britian blended grain alcohol during the same period.

Now, as fossil fuel is becoming more scarce, countries are investing resources in the large-scale commercialization of biofuels. Brazil began widely developing its ethanol program based on sugar cane in the 1980's, so that now over 30% of its mobile power generation comes from this source. In many other countries, including the United States, blended biofuels are already being blended into fossil fuels at compositions up to 20% biofuel. In addition, many new vehicles are being produced that operate on much higher blending ratios, generally up to 85% biofuel.

The addition of biofuel to fossil fuel has many effects, including changes in cetane or octane number, and changes in emissions. Several experimental and modeling studies have shown that the addition of oxygenated compounds in general, and biodiesel specifically, to diesel fuel reduces the particulate emissions of combustion. In contrast to the decrease in particulate emissions, NO_x levels increase in engine studies as the biodiesel fraction of the fuel was increased. Additional emissions concerns that affect biofuels include increases in several non-regulated air toxics, including ozone precursors. In order to realize the potential of biomass fuels in displacing traditional petroleum derived fuels with minimal unwanted emissions, characterization of the biofuel combustion properties, including detailed understanding of the oxidation kinetics, is vital.

The present work focuses on the oxidation kinetics of reference biofuel compounds. For this study, a reference fuel is a compound that is similar in structure to more complex real fuels, and is chosen as a simplified model of the ignition behavior. A
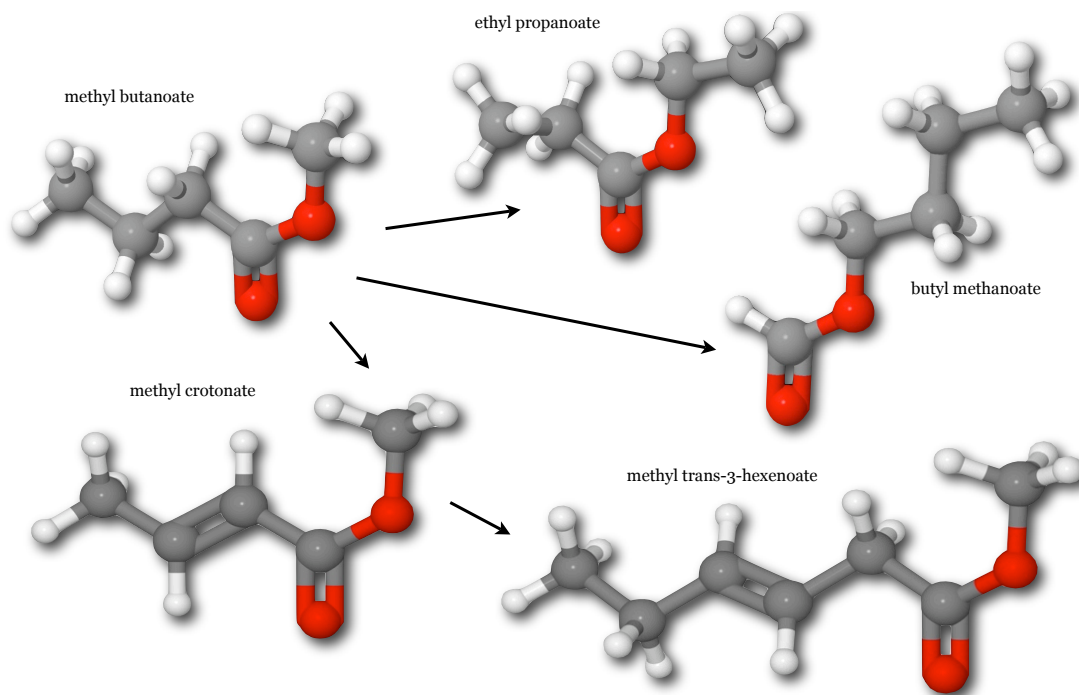
Figure 1.2 Structure of the different esters studies in this work. The first experiments investigated the ignition properties of methyl butanoate. The structure of the following esters was systematically changed to investigate the differences in ignition properties according to alkyl chain lengths, and levels of saturation.

systematic investigation of the effects of chemical structure on key reaction properties was conducted. Figure 1.2 shows the structure of the various esters investigated in this work using the University of Michigan Rapid Compression Facility. The first study considers the reactivity of the C_5 ester reference fuel, methyl butanoate. This study is followed by comparison with the ignition properties of two additional fully saturated C_5 ester isomers, butyl methanoate and ethyl propanoate. The comparison with ethyl propanoate includes a modeling study that starts with and subsequently refines a detailed reaction mechanism. A more detailed analysis of methyl butanoate ignition utilized intermediate species sampling and identification, and compared the results with modeling using a detailed reaction mechanism.

Two additional esters were investigated to expand the range of ester structures considered in this work. Methyl crotonate, an unsaturated C_5 ester and a critical intermediate in the ignition of methyl butanoate, was studied to investigate the effects

4

of degree of saturation on the reactivity of the C_5 esters. A larger unsaturated methyl ester, methyl trans-3-hexenoate, was also investigated as it may be large enough to demonstrate negative temperature coefficient (NTC) behavior not observed during the ignition of the C_5 esters. Finally, the ignition of blends of methyl trans-3-hexenoate with n-heptane representing a biodiesel/petroleum diesel blend were studied to investigate the effects of combined ester and hydrocarbon chemical kinetics that can be expected from the blending of biodiesel fuels.

Chapter 2

Scientific Background

2.1 Biofuels in Engine Studies

One combustion technology that shows immediate promise in its ability to make efficient use of biofuels is the compression ignition diesel engine. The high efficiency of the diesel engine is attractive, but there are drawbacks. For example, there can be relatively high levels of particulate and NO_x emissions relative to other combustion strategies, such as the spark ignition engine. The potential to reduce these emissions while maintaining high efficiency in a carbon neutral fuel cycle is driving the development of new combustion strategies that utilize a biodiesel infrastructure.

Much progress has been made demonstrating the operation of compression ignition engines using biodiesel and other biofuel blends. There have been many studies of biofuel combustion in widely varying research engines. These studies typically compare the combustion properties of different biofuels or additives to a reference fossil fuel case. Common diagnostics are cylinder pressure time histories and measurements of engine out emissions.

Several experimental and modeling studies have shown that addition of oxygenated compounds in general, and biofuels specifically, to diesel fuel reduces the particulate emission of combustion (2; 3; 4; 5; 6; 7; 8; 9). The modeling study of Westbrook *et*

al. (10) proposed that the fuel-bound oxygen in biomass suppresses the formation of soot by lowering the overall fuel/oxygen equivalence ratio (ϕ), and the oxygen present in the fuel molecule reduces the number of steps required for complete oxidation of the fuel. In addition, it has been shown that oxygenates have varying levels of soot reduction capability. This has been demonstrated in an engine imaging study by Mueller *et al.* (11) and through exhaust emissions measurements by Gonzales *et al.* (12). These results imply that molecular structure has a noticeable effect on the engine out particulate emissions.

In contrast to the decrease in particulate emissions, NO_x levels have been reported to increase in engine studies as the biodiesel fraction of the fuel was increased (1; 7; 9). This may be attributed to a different mechanism than the traditional PM/NO_x tradeoff (1), and may be a unique chemical effect, as it is not entirely explained by differences in the density or heat content of the biodiesel fuels (1). In some engine studies, in which the adiabatic flame temperature is significantly lower due to oxygen addition lowering the global equivalence ratio, expected reductions in NO_x have been observed (Miyamoto *et al.* (13)).

Additional emissions concerns regarding biofuel use include increases in several non-regulated air toxics. Ozone precursors, such as carbonyls, acetaldehyde, propionaldehyde and acetone have been found to increase in biodiesel combustion relative to traditional petroleum diesel combustion (14; 15). Increases in these emissions have the potential for detrimental impact on local and regional air quality and environmental health, and emissions of these precursors are likely to be regulated in the near future.

In addition to emissions issues, the use of neat biofuels, or the addition of biofuels to fossil fuels, affects the combustion phasing and ignition timing of the mixture. Methyl tert-butyl ether (MTBE) was previously added to gasoline to increase the octane number of the fuel. Similarly, dimethyl ether (DME) has been added to diesel fuel to increase the cetane number. These fuel modifications allow more efficient use

of fuel in engines that have been optimized for certain operating conditions.

In order to fully realize the potential of biomass fuels for use in traditional diesel and new innovative engine applications, detailed understanding of the combustion kinetics is vital. McCormick *et al.* (1) investigated the emissions levels from varying biodiesel feedstocks in a heavy duty engine. Recognizing that biodiesel fuel typically consists of saturated and unsaturated methyl and ethyl esters generally containing 12 or more carbon atoms, they focused on the effects of chain length and saturation. They observed several structural effects on emissions: decreasing the level of saturation increased NO_x emissions, but did not affect particulate emissions; and for saturated esters, increasing the carbon chain length reduced NO_x emissions, but did not affect particulate emissions.

These observations are similar to the conclusions of many other studies demonstrating that oxygenated fuels behave differently than traditional fossil fuels, and have the ability to reduce certain harmful emissions. The studies also demonstrate that the structure of the fuel, and composition, can have a large impact on the oxidation kinetics and emissions when these fuels are used in practical devices. Thorough understanding of the combustion characteristics, including detailed knowledge of reaction kinetics, is necessary to develop practical devices capable of effectively utilizing biofuels.

2.2 Technical Approach Studying Ester Kinetics

Typical biodiesel fuels consist of relatively large methyl and ethyl esters. However these large oxygenated hydrocarbons are challenging to study experimentally, computationally, and theoretically. By developing an understanding of smaller chain esters, we hope to create an effective means to extrapolate our understanding to larger esters. In addition, quantitative knowledge of how these smaller esters react is necessary for large ester chemistry as the smaller esters are often key intermediates.

Although much is known about hydrocarbon chemistry, much less is known about oxygenated hydrocarbons. There are very few experimental data available in the literature focusing on the elementary reaction chemistry of esters. Fisher *et al.* (16) identified methyl butanoate, a small saturated methyl ester, as a surrogate compound capable of representing certain aspects of larger ester oxidation. Fisher *et al.* (16) developed a detailed reaction mechanism based on the results of previous fuel pyrolysis studies in constant volume isothermal reactors for P=0.13-0.54 atm, T=520-740 K, and ϕ=0.65-3.25 (17; 18). Fisher *et al.* (16) proposed that methyl butanoate is large enough to allow fast RO_2 isomerization reactions that control fuel autoignition under the low temperature and moderate pressure conditions found in diesel engines.

To further explore methyl butanoate oxidation at fuel oxidation conditions, Gaïl *et al.* (19) utilized data from a jet-stirred reactor at P=1 atm, T=800-1350 K, ϕ=1.13, from a variable pressure flow reactor at P=12.5 atm, T=500-900 K, ϕ=0.35-1.5, and from an opposed flow diffusion flame at P=1 atm, T=1218 K. Gaïl *et al.* (19) also compared their experimental results against a slightly modified version of the reaction mechanism of Fisher *et al.*(16) and noted some disagreement between the model and the mechanism at the lower temperatures studied. They also observed very little low temperature chemistry, suggesting that methyl butanoate has different autoignition characteristics than real biodiesel fuels such as soy methyl ester (19). They further suggested that mono-unsaturated or di-unsaturated methyl esters of longer chains might be more appropriate as a model biodiesel fuel, and that the role of the C=C bond should be further investigated.

Sarathy *et al.* (20) used the same experimental facilities as Gaïl *et al.* (19) and built this previous study on the engine study of McCormick *et al.* (1). They investigated the effects of saturation on the level of soot precursors formed from two C_5 ester isomers; methyl butanoate, and methyl crotonate. The unsaturated isomer (methyl crotonate) produced higher amounts of soot precursors, (e.g. acetylene and benzene) than the

saturated isomer (methyl butanoate), yet demonstrated similar overall reactivity (20).

Metcalfe *et al.* (21) recently studied the high temperature oxidation of two saturated and unbranched $C_5H_{10}O_2$ ester isomers, methyl butanoate and ethyl propanoate, in a shock tube at P=1 and 4 atm, T=1100-1670 K, and ϕ=0.25-1.5. They observed much faster ignition for ethyl propanoate when compared to methyl butanoate, especially at low temperatures. They also compared their results with a modified reaction mechanism based on the mechanism of Fisher *et al.* (16). The modeling results of Metcalfe *et al.* (21) had good agreement with the experimental ignition delay time data for both methyl butanoate and ethyl propanoate over the range of conditions studied, and captured the faster ignition delay times of ethyl propanoate. This was attributed to the higher reactivity of the fuel decomposition products of ethyl propanoate, which decomposes via a six-centered mechanism yielding the highly reactive "intermediate fuels," ethylene and propanoic acid (22).

Schwartz *et al.* (22) examined five saturated $C_5H_{10}O_2$ ester isomers: methyl butanoate, methyl isobutyrate, ethyl propanoate, propyl ethanoate, and isopropyl ethanoate. They studied the ester fuel decomposition in an ester-doped methane diffusion flame. They observed that six-centered dissociation is a lower activation energy decomposition pathway for molecules capable of forming an intermediate ring, while the remaining esters will directly undergo unimolecular fission or H-abstraction. During the six-centered dissociation, the molecule first forms a unique intermediate ring complex, which then undergoes unimolecular fission, forming a carboxylic acid and an alkene, which are much more reactive than the products of the other decomposition pathways.

2.3 Objectives of Current Work

The fundamental hypothesis of this dissertation study is that the effects of functional group structure affect the combustion, ignition and pollutant emission chemistry of oxygenated hydrocarbons and that quantitative investigation of the structural effects will allow the development of rules for how classes of compounds react. Such rules would enable the quantitative understanding of the dominant species and reactions controlling the ignition of bio-fuel compounds, guiding the development of practical fuels and optimization of advanced combustion systems.

The primary objective of the current work is to test the hypothesis, and expand our understanding of the fundamental ignition chemistry of representative ester compounds at high pressures and low temperatures. The following sections present the outcomes of the experimental methods via several ignition studies. We have examined the reactivity of methyl butanoate, butyl methanoate, ethyl propanoate, methyl crotonate, and methyl trans-3-hexenoate in terms of the ignition delay time in the University of Michigan Rapid Compression Facility (UM RCF) at conditions applicable to low temperature combustion systems and diesel engine operation. We compare the results to previous studies of $C_5H_{10}O_2$ ignition by Metcalfe *et al.* (21), and discuss the results in terms of the reaction pathways presented by Schwartz *et al.* (22).

The ability to achieve homogenous reaction conditions in the UM RCF also enables the application of a high speed gas sampling system that can be used in conjunction with the high-speed imaging system in UM RCF experiments. The new gas sampling system is capable of studying higher pressure conditions than previously capable, greater than 10 atm, as well as increasing the temporal and concentration resolution of intermediate species. The high-speed gas sampling system provides the ability to generate experimental concentration-time histories for intermediate species during the ignition event, with simultaneous pressure and high-speed imaging data. These diagnostics are used to investigate the effects of fuel structure, such as branching and

saturation, on fuel decomposition pathways, reactivity, and pollution emissions. The results of this study enable quantitative understanding of the dominant species and reactions controlling the ignition of bio-fuel compounds, guiding the development of practical fuels and optimization of advanced combustion systems.

Chapter 3

Experimental Approach

3.1 University of Michigan Rapid Compression Facility (UM RCF)

The UM RCF can be used to investigate the auto-ignition characteristics of fuel/oxidizer mixtures over a large range of pressures and temperatures. The UM RCF is a single shot free piston device, in which the sabot (free piston) is driven directly by compressed air. During a UM RCF experiment, a large high-speed globe valve is opened, allowing compressed air to rapidly accelerate the sabot. As the sabot travels down the length of the driven section, the test gas mixture is compressed ahead of the nosecone. The travel of the sabot is arrested by an interference fit between the nosecone and the extension section. The test conditions are defined by the composition of the test gas mixture, the initial pressure of the mixture, and the chosen compression ratio determined by the specific UM RCF configuration. The compression ratios can be varied between $\sim$10-40, which can result in test conditions spanning pressures from $\sim$1-60 atm and temperatures from $\sim$800-2000 K. The auto-ignition of the test gas mixture is then recorded using a combination of several different diagnostics. These diagnostics can include pressure measurements, temperature measurements, light emission, high-speed imaging, and intermediate species or radical concentration measurements.

The UM RCF consists of five major components: the driver section, the driven section, the test manifold (consisting of the convergent section, the extension section, the instrumented test section, and the end wall), the sabot (free piston), and the hydraulic control-valve assembly used to initiate and experiment. A detailed rendering of the UM RCF, highlighting each of its components is shown in Fig. 3.1. The driver section is a long steel cylinder (5.64 m long, 154 mm i.d.) that is filled with pressurized air. The driver section is separated from the driven section (2.74 m long, 101.2 mm i.d.) via a large fast-acting hydraulic globe valve assembly (Fisher Controls) and a scored sheet of plastic (0.05 mm, Mylar®). The driven section is a long stainless steel tube with a honed and chromed interior surface which allows the U-rings on the sabot to seal against the inner diameter, separating the test gas mixture from the compressed air driver gas. The downstream end of the driven section is connected to the test manifold. The sabot has a replaceable nosecone which is made of ultra-high molecular weight polyethylene. The body of the sabot is solid (Delrin®) and contains a copper counterweight to balance the nosecone. Custom u-ring seals (virgin Teflon®with stainless steel radial springs) eliminate gas blow-by past the sabot. The sabot is specifically designed to capture the rolled up vortex from the wall as the nosecone seats in the extension section. This prevents the vortex from entering the test manifold and introducing turbulence into the test volume.

A schematic of the test manifold and imaging system is shown in Fig. 3.2. The stainless steel convergent section bridges the 101.2 mm bore of the driven section to the 50.8 mm bore of the remainder of the test manifold components. The total length of the extension section is variable by design (through combinations of subcomponents, including a transparent side view imaging section) to yield different compression ratios. The test section has a length of 50.6 mm, and is equipped with two optical ports for line of sight laser access, a pressure transducer port, and two additional instrumentation ports. For the current study, the test section was instrumented with
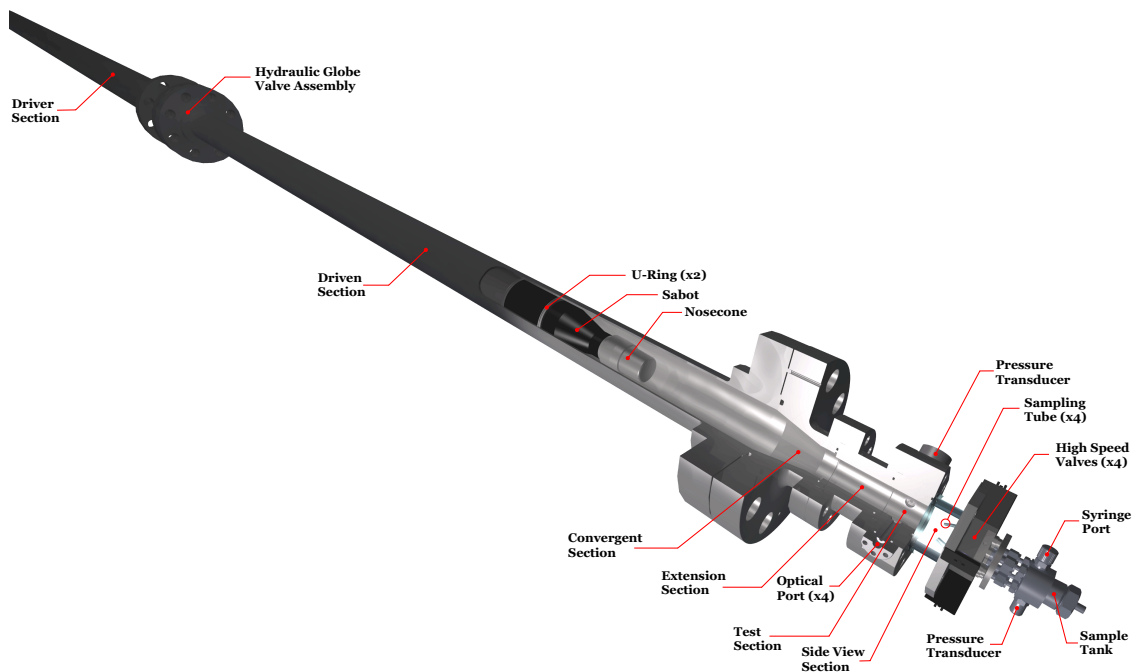
Figure 3.1 Detailed rendering of the UM RCF, highlighting the major components. In this view the UM RCF is configured for high-speed gas sampling and side view imaging.

a piezoelectric transducer (Kistler 6041AX4) and charge amplifier (Kistler 5010B) for pressure measurements. Several end walls are available to seal the test manifold. The transparent end walls seal the test manifold and allow end view optical access to the entire test volume as shown in Fig. 3.2. The sampling end wall is fitted with high speed valves and sampling tubes to allow high speed gas sampling of the test mixture for subsequent gas chromatographical analysis. Detailed descriptions of the diagnostics and operating procedures are in the sections that follow.

3.1.1 UM RCF preparation details

Prior to each experiment the driven section and test manifold of UM RCF must be disassembled and cleaned to ensure that there are no impurities that could affect the ignition chemistry of the mixture. (Note, particles are sometimes produced in the UM RCF as a result of abrasion between the u-rings on the sabot and the wall of
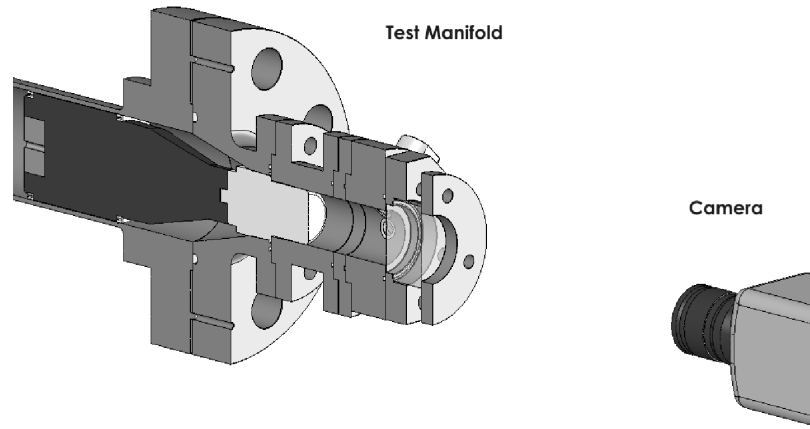
(a) Isometric cross-section view
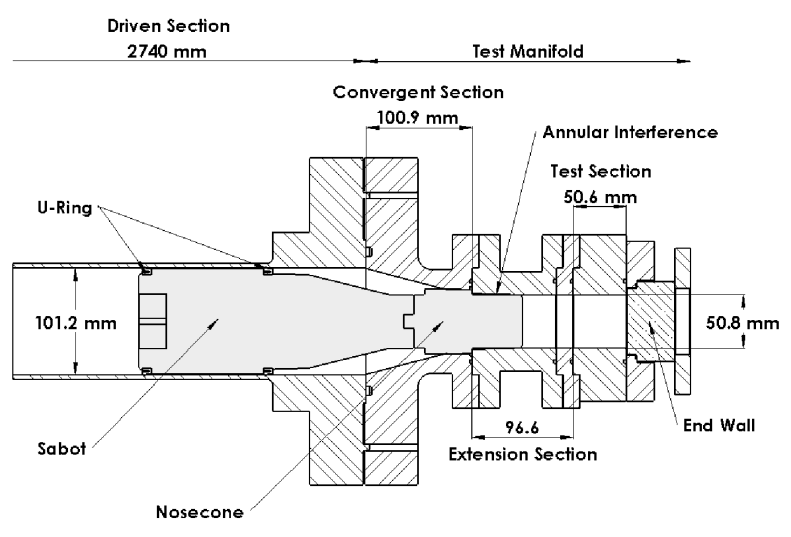
(b) Cross-section view

Figure 3.2 Experimental schematic of the test section of the UM RCF, demonstrating the camera perspective for end view high-speed imaging. The sabot nose cone is shown in the final seated position.

the driven section.) Once the UM RCF is disassembled, all of the interior surfaces and o-ring seals are thoroughly cleaned with methanol (99.9%, Fisher Scientific) and lint free synthetic wipes (Prowipe, Berkshire Engineering). The barrel of the driven section is cleaned with a large bundle of wipes that are fastened to flexible teflon tubing and wetted with methanol. This large "pipe cleaner" is then pulled through the barrel three times or more to ensure that there are no particles or other residues

16

remaining.

The sabot is also thoroughly cleaned, and the teflon u-rings and the ultra-high-molecular-weight polyethylene (UHMW-PE) nosecone are inspected and replaced if necessary. Prior to inspection, the nosecone is pressed out of the extension section using a pneumatic press when the test manifold is disassembled. The nosecone is replaced if any large ridges or dents are present on the leading annular surface (See Appendix A). The u-rings are replaced if the sabot can easily be extracted from the barrel by hand, or if the u-rings spin easily on the sabot, indicating that they may no longer seal with the barrel of the driven section. The sabot is then inserted into the upstream end of the driven section and all of the o-rings are lightly greased with vacuum grease and replaced. The plastic sheet is then scored (Appendix A) with a rotary cutter, and placed between the hydraulic globe valve and driven section and then clamped in place by those sections as they are fastened together.

The test manifold is then reassembled after the required compression ratio is determined through consideration of the nosecone geometry, test gas composition, and effective pressure and temperature conditions required. Table A.1 in Appendix A, shows some common combinations of subcomponents and the resulting compression ratios. The components are then assembled, first with the convergent section to bridge the diameter of the driven section to the test manifold. The large through bolts are carefully tightened, taking care to keep the faces of the large flanges parallel. The stainless steel extension section subcomponents are then attached, and together must have enough axial length to ensure that the nosecone will not enter into the polycarbonate side view imaging section, the polycarbonate thermocouple section, or the instrumented test section, whichever is adjacent. The remaining components, including the instrumented test section, the thermocouple section, and the side view imaging section, are then attached in the order chosen for the given experiment. Finally, either an imaging or sampling end wall is attached and the smaller through

bolts of the test manifold are tightened together.

Once the UM RCF is reassembled, the pressure transducers must be reconnected, and their respective amplifiers turned on. The quick-connect at the center of the driven section, connecting it to the mixture preparation manifold must also be reconnected. The UM RCF must then be pumped to very low pressures using the diffusion vacuum pump connected to the mixture preparation manifold. Once this process is begun, the valve isolating the small vacuum pump from the globe valve, must be alternatively open and closed until the pressure in the UM RCF is below 50 torr. This vacuum pump and procedure is necessary to prevent a large pressure gradient across the plastic sheet to ensure that the sheet is not broken prior to the experiment. When all the rigid and flexible seals are working properly, the UM RCF takes $\sim 2-4$ hours to evacuate to $\sim$0.10 torr. Depending on the desired accuracy, ultimate pressures ranging from 0.05 to 1.0 torr in the UM RCF are required prior to an experiment.

At this point, an experiment is ready to be conducted, and all of the required diagnostics must be properly configured and connected to the data acquisition system. When this is completed, the UM RCF is isolated from the manifold vacuum pump and a previously prepared test gas mixture is charged into the driven section. The valve isolating the driven section from the manifold is then closed, and the UM RCF is armed. Immediately before the experiment, the valve isolating the globe valve from the vacuum pump is closed. The arming process is covered in more detail in the data acquisition section.

3.1.2 Mixture preparation details

Test gas mixtures are specifically tailored to work with the targeted compression ratio of the chosen test manifold configuration. The specific heat of the mixture is changed by adjusting the amount of different inert diluents among nitrogen, argon, and carbon dioxide. Altering the diluent composition, when used in conjunction with varying

compression ratios, produces a broad range of possible test temperatures. The test pressure is varied by changing the charge pressure. Mixtures are prepared prior to evacuating the UM RCF. In order to reduce the mixture uncertainty, each of the constituents must be of very high purity. Prior to making a mixture the mixing tank is pumped down with the diffusion vacuum pump to a pressure of 0.05 torr. The tank is then vented to the room, and pumped down to the same pressure again. This process is repeated twice and may take around 1 hour. This process is used to ensure the small amount of gas remaining in the mixing tank is air (O_2 + 3.76N_2). The gas cylinder lines must then be purged into the exhaust system for around 30 seconds each to ensure that any room air that leaked into the lines is no longer present. Many of the fuels used also are in liquid form at STP. To utilize these fuels, they are the first component charged into the mixing tank. The mixture must be selected to ensure that the required partial pressure of the fuel is below the partial pressure of the fuel at room temperature. Again, to remove any room air in the fuel flask, the flask is purged under vacuum for ~30 seconds. At this point, the mixture preparation manifold is twice purged and vented with room air similar to the mixing tank so that we may assume that the trace contents are air.

The initial pressure in the mixing tank is then recorded using the low pressure transducer (Varian CDG Gauge, 0-100 torr) on the manifold. The fuel is then charged into the mixing tank, and the final pressure is recorded. The fuel mole fraction has the largest impact on the mixture behavior so is charged first using the higher accuracy of the low pressure transducer. The final partial pressure readings are recorded on the experiment information form (Appendix A) from both the low pressure transducer and the high pressure transducer (Varian CDG Gauge, 0-1000 torr) in order to shift the scale of the high pressure transducer accordingly. Oxygen, the component that has the second highest impact on the mixture behavior is charged next, and the total mixture pressure is recorded. This process is then continued until the mixture is

complete. The mixing tank is then isolated from the manifold, and then evacuated along with the remainder of the UM RCF.

3.1.3 High-speed imaging details

Two imaging end walls, quartz or polycarbonate, can be used to provide optical access to the test manifold. The quartz end wall (with a diameter of 78 mm and a thickness of 45.25 mm) has a double layer anti-reflective coating on both faces. The coating is optimized for transmission of visible wavelengths and the window has excellent reflection- and glare-reduction properties. The polycarbonate (Lexan®) end walls are polished (140×140 mm square with a thickness of 12.5 mm) and have no coatings. Peak transmission for the polycarbonate end walls occurs at visible wavelengths. When the polycarbonate windows were used, the windows were replaced regularly (every 5-10 experiments) in order to maintain high image quality.

The side view imaging section is also made of polycarbonate, and has similar optical properties to that of the polycarbonate end wall. This section the thinnest wall possible, while maintaining the inner diameter of the test manifold and allowing for proper sealing of the test manifold components. The thin wall (82 mm o.d., 50.8 mm i.d.) minimizes the the distortion of the captured images caused by the lens effect of the continuously curved surface.

The large size of the quartz and polycarbonate end walls allows the entire test volume to be imaged using a high-speed color digital video camera (Vision Research, Phantom V7.1, 800×600 pixel SR-CMOS 48 bit color array, capable of 160 kHz at reduced spatial resolution). The camera array records RGB signals using spectral filters. The red channel uses a high pass filter with approximately 95% transmission above 615 nm. The green channel uses a band pass filter with approximately 82% peak transmission at 530 nm. The blue channel uses a band pass filter with approximately 86% peak transmission at 460 nm. The actual spectral response curves for the camera

sensor are in Appendix A. A fast 50 mm lens (f/0.95 Navitar TV Lens) and a 10 mm c-mount extension tube were used with the camera to optimize the capture of available light emission. No additional spectral filtering is currently used.

For end view imaging the camera is mounted on a translating cart which rests on the same rails as the UM RCF. Using the interface software (Phantom 607xp) combined with a slow frame rate, the camera is then axially aligned with the test manifold ∼40 cm from end wall, and the camera is focused on a plane inside the test section, 2 cm from the end wall. For side view imaging, the camera is mounted on a vertical optical rail on the optical table adjacent to the test manifold. The camera is again placed ∼40 cm from the outer diameter of the side view imaging section, and is aligned so there is a clear view between the threaded rods that provide the clamping force that holds the test manifold together. The side view imaging data are used along with the high speed gas sampling system for these experiments. It is important to assemble the clear side view imaging section adjacent to the gas sampling end wall in order to image the volume nearest the sampling tubes during the experiment. To maximize the capture of the emission from the test section and limit the depth of field, the wide aperture lens is used in the fully open position. The camera frame rate and spatial resolution are set at this time, and the image properties are set to their default values. The camera sensor is then calibrated using a black reference (where the camera lens was covered) and the zero signal level of each pixel in the CMOS array is assigned.

The high-speed digital camera is used to acquire continuous full-frame color video sequences of visible emission from the ignition experiments at speeds from 10,000 to 60,000 frames per second (fps). The frame rate has an inverse relation to the total spatial resolution. For these studies 26,000 fps is the typical frame rate, and the maximum allowable spatial resolution of 256×256 pixels is used. These settings result in each frame corresponding to approximately 38 μsec (the maximum allowable exposure

time at this frame rate), and each pixel in the CMOS array imaging focused light from a volume with a height×width×depth of approximately 198μm$\times198\mu$m$\times2$ mm. In addition to these camera settings, the post trigger setting must be determined. When armed, the camera continuously acquires images, and overwrites the oldest images. The value selected for the post trigger determines how much of the cameras allocated memory will be devoted to recording new images after the trigger event. For these experiments, the post trigger value is generally set so that the same number of frames will be recorded both before and after the trigger.

The camera was triggered by a circuit designed to output a pulse to the trigger input of the camera. The signal to the triggering circuit (Appendix A) was supplied by a photo-detector (Hamamatsu S1787-12) located on the driven section of the RCF. Emission from a laser diode (TIM-201-3, 3 mW, 650 nm) was directed onto the active element of the photo-detector such that the laser emission was orthogonal to the path of the sabot. When the sabot passed the laser diode, the change in signal from the photo-detector triggered the pulse generator (Stanford Research Systems DG535), which then triggered the camera. Using this arrangement, images were acquired throughout the compression and ignition processes.

Once the images are acquired, the OK option is selected in the camera control software and then the start and end save points are determined to capture both the end of compression and the end of ignition. This also determines how large the saved file will be. The image properties (e.g. gamma, contrast, etc.) are then adjusted to help view the images if necessary. However, the image properties must be reset to their default setting prior to saving the file because the saving process overwrites the default image settings.

3.1.4 High-speed gas sampling

The high-speed gas sampling system is detailed further in section 6, but its functionality and design considerations are briefly described here. The high-speed gas sampling system consists of a specially designed stainless steel end wall for the test manifold. The sample tank is instrumented with a high speed pressure transducer (Kistler 4045A2) and amplifier (Kistler 4618A0) to monitor the sampling system performance. The sample tank also has a syringe port to extract the sample and transfer it to the gas chromatographs.

The end wall of the sampling system has four integrated fast acting solenoid driven poppet valves (Festo MHE3) that are plumbed together through a manifold and a sampling tank (Fig. 3.3). The end wall and valve assembly was designed to reduce compositional uncertainty, by reducing the dead volume through shortening the length from the end of the sample tube to the valve. This is shown schematically in Appendix A, where the valve body in the new configuration is pressed directly against the end wall, avoiding the valve body adapter and an additional fitting.
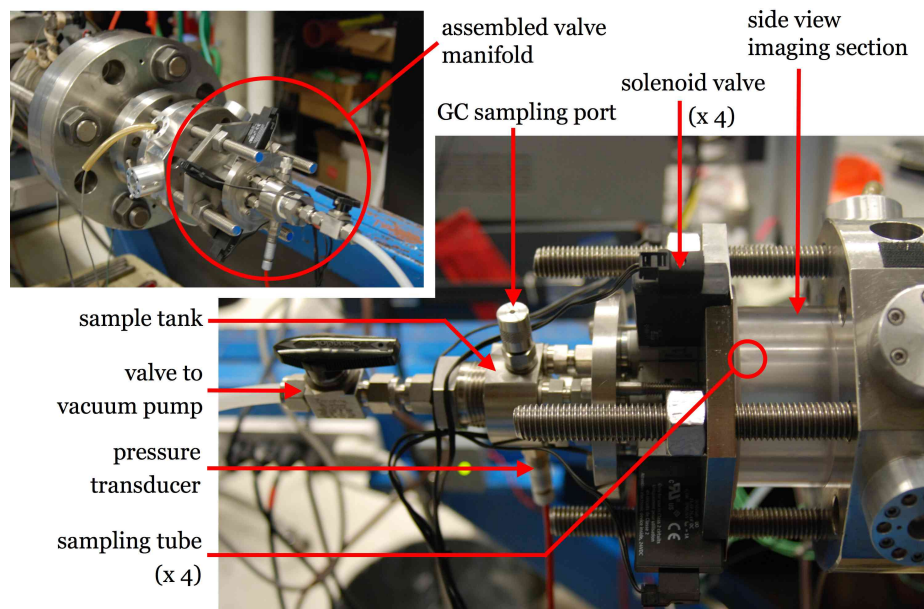
Figure 3.3 Photographs of the high-speed gas sampling manifold, demonstrating the proximity of the side view imaging section.

Further reduction in compositional uncertainty can be achieved by increasing the total sample mass. This is accomplished by increasing the size of the valves. In this case, the orifice of each valve is approximated by a 3 mm diameter circle, and also by increasing the number of valves to four. Additional reduction in compositional uncertainty can be achieved by increasing the post sample pressure above the ambient to ensure that any leak that is present will be out of the sampling tank, and leaking will not dilute the sample. For this reason the test volume is vented immediately after an experiment, to prevent high pressure post combustion gases from leaking across the poppet valves into the sample tank.

Uncertainties in sampling time can also been reduced by shortening the sampling time. This is achieved by keeping the valves in the partially open and fully open position for a shorter amount of time. To accomplish this, the valves must be modified and driven at a much higher rate. This requires specific modifications to the return spring, and its preload, as well as designing a circuit to drive the solenoid at high power to overcome the increased spring power. In addition to lowering the sampling time, these modifications allow the valves to be operated at much higher pressures than the unmodified valves, up to at least 10 atmospheres. The specifics of these modifications are presented in Appendix A. The operational procedure is discussed in Sec. 6, along with characterization of the system.

3.1.5 Data acquisition

Data acquisition is performed using the National Instruments Labview 8.2 software combined with an NI cDAQ-9172 USB chassis. The specific data acquisition modules used are: the NI cRIO-9215 for analog data acquistion at 60 kHz, and the NI 9401 for digital triggering purposes. A Labview interface (Appendix A) has been developed in order to acquire the analog data and ensure its synchronization with the high speed digital imaging and the gas sampling system.

Once the Labview interface is running, the analog data signals and triggering functions are checked. This check includes the test section pressure signal, the diode laser trigger signal from the driven section, the sampling system pressure signal, and the TTL signal from the pulse generator used to trigger/synchronize the sampling system and the high speed camera. Once the program is running, it continuously displays the real-time values for these data signals. Acquisition begins when the MAN button on the pulse generator used to initiate the experiment (HP 8112A) is depressed. The radio button labeled 'Start Trigger' will light green, and the ambient temperature is recorded via a thermocouple. The sequence that stops the acquisition begins when the pulse delay generator triggering the camera and sampling system (SRS DG535) gives its output pulse. The radio button labeled 'Stop Trigger' will light green. The pulse delay generator is configured to trigger the stop sequence at the same instant the camera is triggered and the valves are first opened. This functionality is checked by turning off the laser diode power on the driven section trigger, in order to begin the pulse sequence of the pulse delay generator. The triggers are employed to minimize the size of the data file, and allow for more automated data acquisition and analysis. After the data are acquired, an interactive plot of the last 250 ms of the data file, which contains the most relevant information is displayed.

To finish the set up of the UM RCF prior to an experiment, several steps must be taken. First, the pulse generator (HP 8112A) and servo controller (Shore Western SC-3000C) used to operate the hydraulic globe valve (Fisher Controls) must be checked to confirm that all of the values are correct (Appendix A). Next, the emergency power shut off switch to the hydraulic pump is cycled to ensure its power system is ready. Next, the amplifier for the pressure transducer on the test section (Kistler 5010B) must be checked to confirm its multiplier values are correct (Appendix A), and allowed at least 15 minutes to become thermally stable.

After the driving electronics have been checked and all of the additional diagnostics

are ready, the UM RCF is ready for an experiment, and the driver section is ready to be charged with high pressure air. The driver section is charged to a pressure according to the targeted compression ratio, the initial charge pressure, and the condition of the u-rings and nosecone. Some guidelines for driver pressure are found in Appendix A. The next step is to charge a mixture into the driven section. In order to do this, the vacuum pump on the mixture preparation manifold must be isolated, and the initial pressure is recorded using the high and low pressure Varian transducers. The mixture is then charged into the driven section using the metering valve isolating the mixture storage tank, and the final charge pressure is recorded using both high and low pressure Varian capacitance diaphragm gauges. The valve isolating the UM RCF from the driven section is then closed.

The next step is arming the UM RCF, and specifically the hydraulic globe valve. The first step is to pull on the power switch to the servo controller, which activates the pump for the hydraulic globe valve. The servo is controller is then armed by depressing the large green HIGH button. At this point the UM RCF is armed. Next the valve isolating the dead volume between the globe valve and the plastic sheet from the small vacuum pump must be closed. Additionally, the valve on the gas sampling tank must be closed, if applicable, and the gas sampling power supply must be armed. Once these steps are completed, the UM RCF is fired, and acquisition is begun by depressing the MAN button on the pulse generator. This should release the sabot, thus completing the compression and ignition process, and trigger the diagnostics and stop sequence.

Immediately following the experiment, the power to the servo controller should be pushed OFF, and the driver section and the driven section should be vented to release pressure. At this time the additional steps required to save the imaging data and continue the GC analysis are taken. Following these additional diagnostic steps, the saved analog data is analyzed using the Matlab files in Appendix B to determine

the final experimental parameters and conditions, including the pressure, temperature, and ignition delay time.

3.2 University of Michigan Rapid Compression Facility Studies

Many devices are suited to studying the oxidation kinetics of fuels, including stirred reactors, flow reactors, shock tubes, and rapid compression machines. The University of Michigan Rapid Compression Facility (UM RCF) has the capability of targeting the high-pressure, and moderate-temperature conditions directly applicable to advanced combustion strategies. The UM RCF has been thoroughly characterized through extensive studies of reacting mixtures, for which several diagnostics have been developed. Some of these studies and diagnostics are highlighted in the sections that follow.

3.2.1 General UM RCF Characterization

Extensive characterization of the pressure and temperature time-histories found in the UM RCF are presented in Donovan (23), He (24), and Donovan *et al.* (25). Many rapid compression experiments of inert gas mixtures were performed to develop an understanding of the pressure and temperature behavior in the UM RCF. The pressure was shown to increase very rapidly during the last 20 ms of the compression process, and it was determined that the ratio of final/initial pressure in the test section should be used as an appropriate effective compression ratio. This enables a definition of compression ratio that is unaffected by any gas blow-by past the seals on the sabot. This definition for compression ratio is also unaffected by the inability to accurately define a geometric compression ratio as a result of the annular shoulder region integral to the UM RCF design. (Recall the shoulder region prevents vortical fluid from entering the test volume.)

The temperature distribution in the UM RCF test volume was also investigated using fine wire thermocouples. The thermocouple measurements show that the actual temperature of the core region differs from the predicted temperature (using the definition of the effective compression ratio) by 1-14% depending on the mixture conditions. Using these pressure and temperature measurements, it was shown that for a large "core region" present in the test volume, most relevant to combustion studies, the compression process in in the UM RCF can be accurately modeled as isentropic. The thermocouple measurements in the test manifold also demonstrated uniform temperatures were valid for at least 70% of the diameter. High speed imaging data indicate the percentage of the volume that may be considered part of the core region may be much higher, around 90%. The large size of the core region, and the unique design of the sabot, allow test conditions to be sustained in the core region for up to 50 ms, generally affording much longer test times than provided by other facilities capable of targeting high pressures and intermediate temperatures.

3.2.2 UM RCF High-Speed Imaging

The high-speed digital imaging diagnostic was developed for UM RCF studies to investigate ignition phenomena of combusting mixtures. During UM RCF ignition studies of iso-octane mixtures (26; 27), the presence of reaction fronts prior to volumetric ignition was observed at certain conditions through simultaneous imaging and pressure data, while volumetric ignition with no spatially-resolved features occurred at other conditions. Figures 3.4 and 3.5 are two examples of imaging sequences acquired during ignition that highlight the differences in the two ignition regimes.

A study utilizing this diagnostic was previously published in *Combustion and Flame* by Walton *et al.* (28), where a thorough discussion of the results for iso/octane/air mixtures can be found. This paper is attached in Appendix C. The presence of non-uniform ignition can have significant impacts on the many of the diagnostics
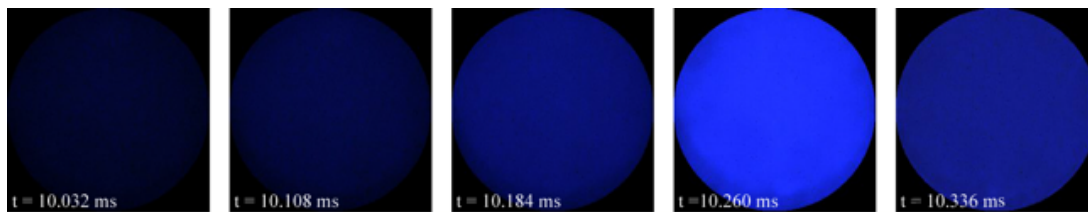
Figure 3.4 Imaging sequence demonstrating volumetric ignition where $\phi = 0.30$, $T_{eff} = 1020$ K, $P_{eff} = 9.0$ atm, inert/$O_2 = 5.00$, $\tau_{ign} = 10.3$ ms, 26,000 fps (color adjusted for clarity). Note not all frames in the imaging sequence are presented. From Walton *et al.* (28).
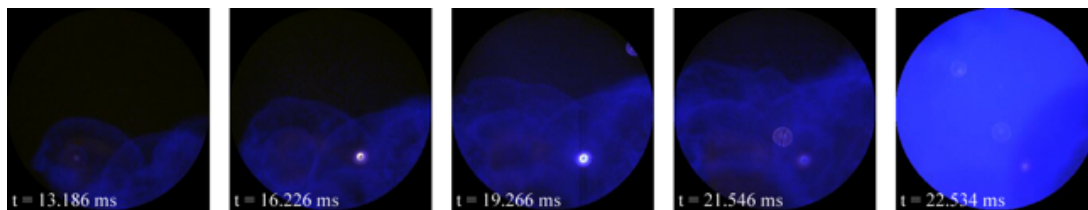
Figure 3.5 Imaging sequence demonstrating the presence of reaction fronts prior to volumetric ignition and $\phi = 0.20$, $T_{eff} = 917$ K, $P_{eff} = 10.8$ atm, inert/$O_2 = 1.38$, $\tau_{ign} = 22.5$ ms, 26,000 fps (color adjusted for clarity). Note not all frames in the imaging sequence are presented. From Walton *et al.* (28).

used in the UM RCF, and question the validity of many homogeneous models. It is important to ensure that test conditions result in homogeneous ignition near the diagnostic tools if line of sight laser absorption or intermediate speciation via gas samping is going to be utilized.

Similar behavior has been observed in many other UM RCF studies, including reacting mixtures of methanol, methyl butanate, butyl methanoate, and syngas. The syngas system has also previously received close attention in the UM RCF, and is discussed in the publication in the *Proceedings of International Combustion Institute* by Walton *et al.* (29). This paper is also attached in Appendix D.

3.2.3   UM RCF Intermediates of Speciation

The development of a high speed gas sampling system for intermediate speciation during iso-octane auto-ignition has been demonstrated and is thoroughly discussed in He *et al.* (30). Direct measurements of intermediate species concentrations are critical to understanding fuel decomposition and oxidation pathways that dominate reactivity and pollution formation. The previous intermediate speciation studies quantified 30 hydrocarbon and oxygenate species. Two conditions were studied, P=5.2 atm, T=1000 K, ϕ=0.4, and P=4.8 atm, T=975 K, and ϕ=1.2. The results were compared with model prediction from the iso-octane model of Curran *et al.* (31), and were generally in good agreement.

For the high speed sampling studies, the test gas mixture was sampled in 2 ms discrete intervals. The sampling intervals started after the end of compression, continued through the ignition delay time, to the point of ignition as shown in Figure 3.6.
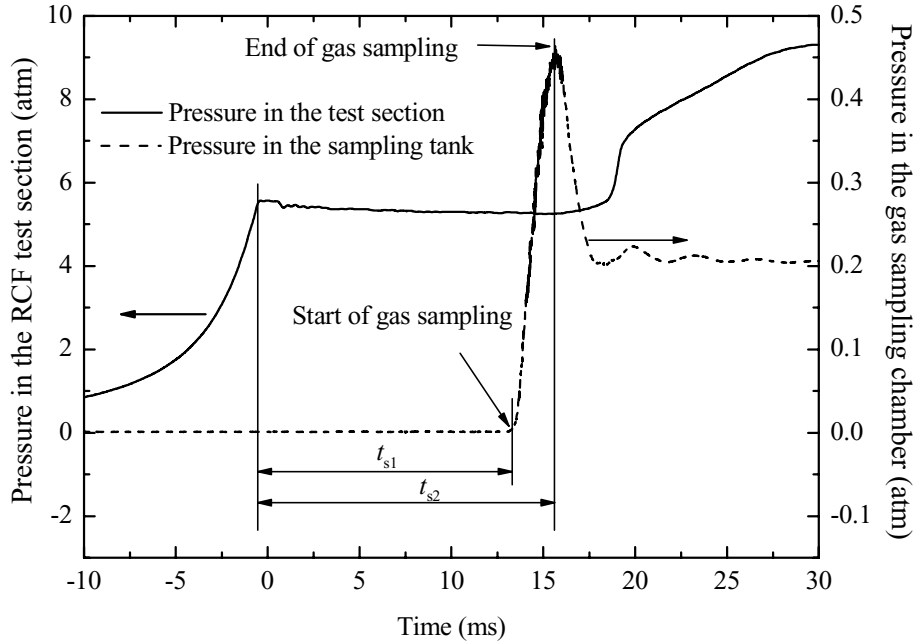
Figure 3.6   Typical pressure time histories in the test section and sample chamber during an ignition experiment for conditions of $P_{eff} = 5.34$ atm, $T_{eff} = 1002$ K, $\phi = 0.4$, and (N_2 + Ar)/O_2 = 5. From He *et al.* (30).

A fraction of each sample was injected into each of four gas chromatographs. These

four GC's have 5 detectors each optimized to determine concentrations of different types of compounds in the sampled gas, including stable species, oxygenates, C_1-C_5 hydrocarbons, C_5-C_{10} hydrocarbons, and hydrogen. An example chromatogram from the GC optimized to identify oxygenates is shown in Fig. 3.7, where many peaks, include acetaldehyde (CH_3CHO) are clearly identified.
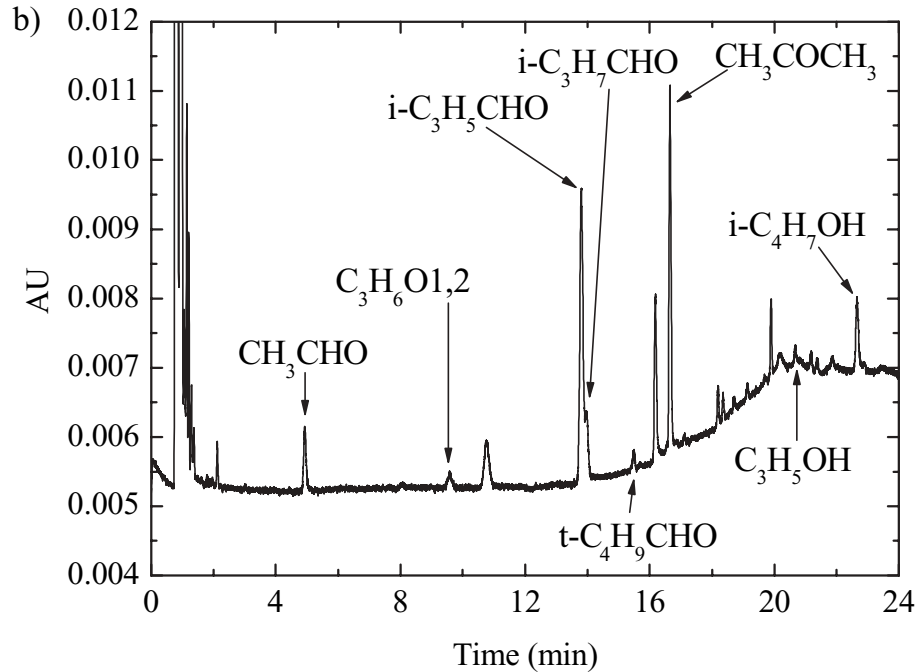
Figure 3.7 Typical chromatogram data for oxygenates. Experimental conditions are those of Figure 3.6: $P_{eff} = 5.34$ atm, $T_{eff} = 1002$ K, $\phi = 0.4$, and (N_2 + Ar)/O_2 = 5. From He *et al.* (30).

Using this species and concentration identification method, the species concentration time-histories can be mapped over the entire duration of the ignition delay time. The sampling times are scaled according to the total (ideally identical) ignition delay time for each sampling experiment to compare sampling times from different experiments. Using the actual species concentrations, and the normalized sampling time, figures are generated for each individual compound similar to Fig. 3.8 for acetaldehyde.

Using these methods, important species and reactions can be determined for specific mixture properties and compositions. These data can also be compared to existing

v)
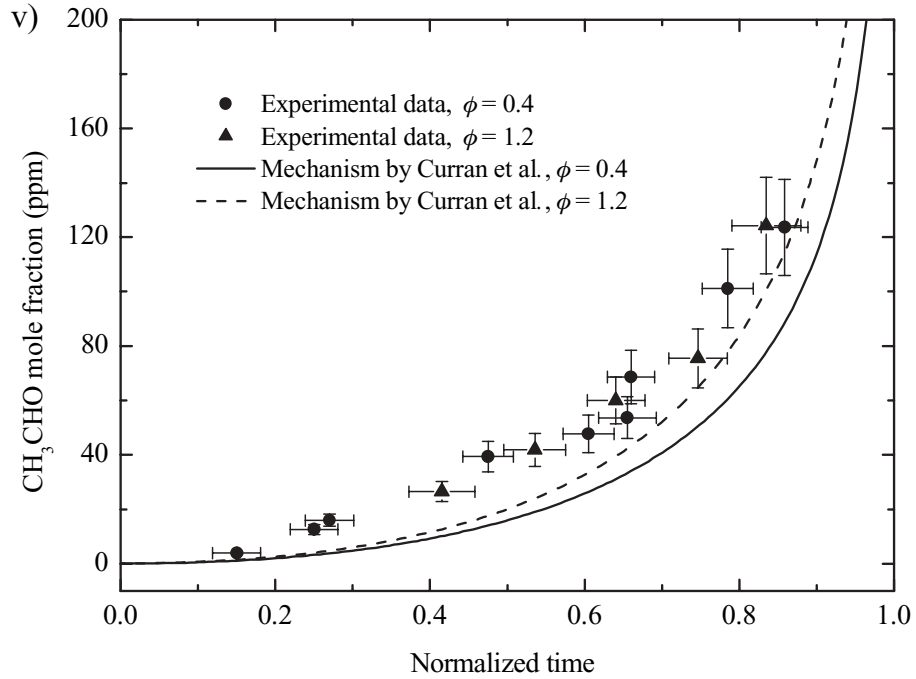
Figure 3.8 Experimental and modeling results for CH_3CHO intermediate gas species during isooctane ignition for the target conditions of $P_{eff} = 5.2$ atm, $T_{eff} = 1000$ K, $\phi = 0.4$, and $P_{eff} = 4.8$ atm, $T_{eff} = 975$ K, $\phi = 1.2$. From He *et al.* (30).

reaction mechanisms or used for the development of practical devices and models. The work for this study includes the development of an improved gas sampling system which is described in detail in Chapter 6.

Chapter 4

Ignition Behavior of C$_5$ Esters with Varying Alkyl Chain Lengths: Methyl Butanoate and Butyl Methanoate

The following section presents the results of recent recent studies of C$_5$ ester auto-ignition in the UM RCF. The results presented here include pressure time-histories and the results of high speed imaging. The discussion includes comparison to previous work in terms of dominant reaction pathways. This work is part of the *Proceedings of the ASME International Mechanical Engineering Congress and Exposition*, held in November 2007 (32).

4.1   Introduction

The objective of the current work was to further expand our understanding of the fundamental ignition chemistry of C$_5$ esters at high pressures and low temperatures. This paper presents the results of an experimental investigation of two isomers of the C$_5$H$_{10}$O$_2$ ester: methyl butanoate and butyl methanoate. We have examined the reactivity in terms of the ignition delay time of these isomers in the University of Michigan Rapid Compression Facility (UM RCF), at conditions applicable to low

temperature combustion systems and diesel engine operation. We compare the results to previous studies of $C_5H_{10}O_2$ ignition by Metcalfe *et al.*(21), and discuss the results in terms of the reaction pathways presented by Schwartz *et al.*(22).

4.2 Typical Methyl Butanoate Ignition: Pressure Results

Mixtures and conditions for study were selected to compare the ignition properties of two $C_5H_{10}O_2$ isomers, and also be relevant to low temperature engine combustion strategies. Specifically, the temperature ranged from T=869-1109 K, the pressure from P=4.7-19.6 atm, and the equivalence ratio from ϕ=0.30-1.21.

Typical pressure and pressure derivative data for $C_5H_{10}O_2$ ignition experiments are shown in Figs. 4.1 and 4.2. The initial pressure rise in each experiment is due to compression of the test gas mixture ahead of the sabot. At the end of compression, the pressure reaches the first maximum. This time is set as t = 0 sec and is labeled P_{max} in the figures. The pressure then decreases slightly due to cooling losses to the test volume walls. After a delay period, the mixture auto-ignites resulting in a rapid increase in pressure for all cases.

The effective test conditions were determined using the pressure time-history from each experiment. The effective pressure (P_{eff}) was defined as the time-integrated average pressure from the maximum pressure (P_{max}) at the end of compression to the point of maximum rate of pressure rise (dP/dt_{max}), or

$$P_{eff} = \frac{1}{(t_{dP/dt_{max}} - t_{P_{max}})} \int_{t_{P_{max}}}^{t_{dP/dt_{max}}} P \cdot dt \,. \tag{4.1}$$

The effective temperature for each experiment was determined, as in previous UM RCF studies (25; 26; 27; 28; 29), using the effective pressure and by numerical integration
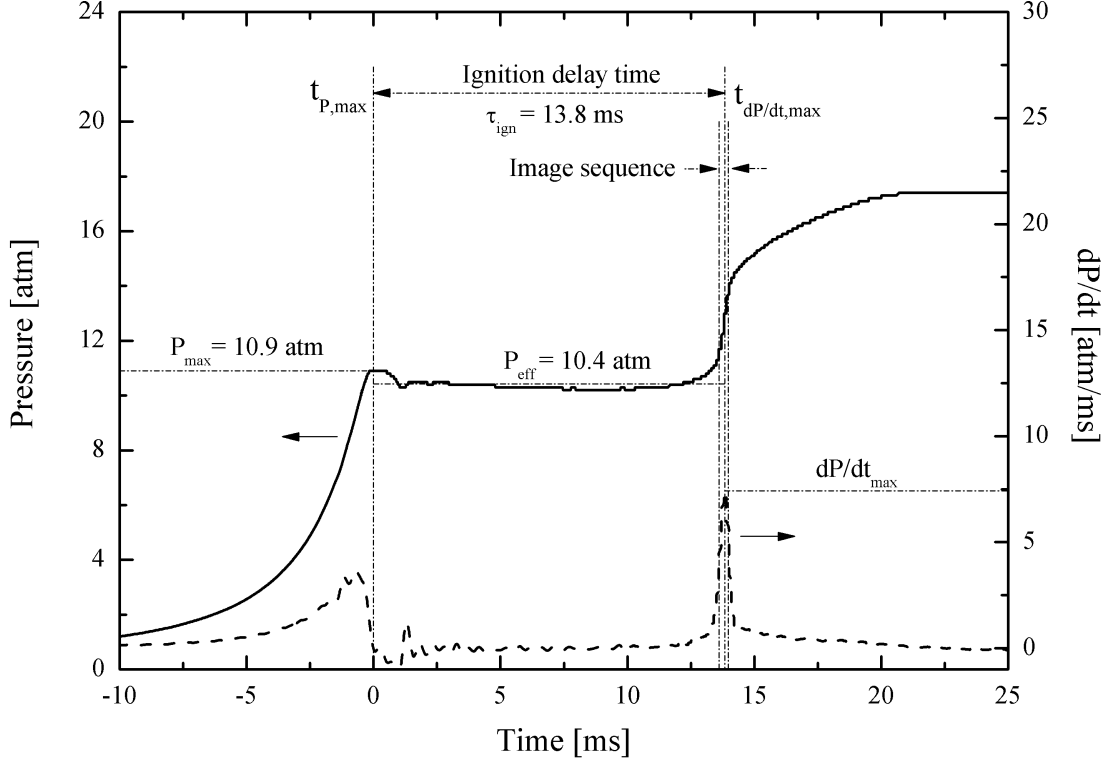
Figure 4.1 Typical pressure (——) and pressure derivative (- - -) time-histories for methyl butanoate ignition experiments where volumetric ignition is observed, experimental conditions of: P_{eff}=10.4 atm, T_{eff}=1005 K, ϕ=0.30, Inert/O_2=3.76.

of the isentropic relation

$$\int_{T_o}^{T_{eff}} \frac{\gamma}{\gamma - 1}\, d\, ln(T) = ln\left(\frac{P_{eff}}{P_o}\right), \qquad (4.2)$$

where P_o is the initial charge pressure, T_o is the initial temperature (typically 298 K), and γ is the temperature-dependent ratio of the specific heats of the unreacted test gas mixture, which is determined using the NASA thermodynamic data base (33) and from the thermodynamic data for methyl butanoate from Fisher *et al.* (16). The temperature dependent specific heat of butyl methanoate was assumed to be the same as that of methyl butanoate.

For each experiment, the ignition delay time (τ_{ign}) was determined using the pressure time-history, and defined as the time between P_{max} and dP/dt_{max}. This
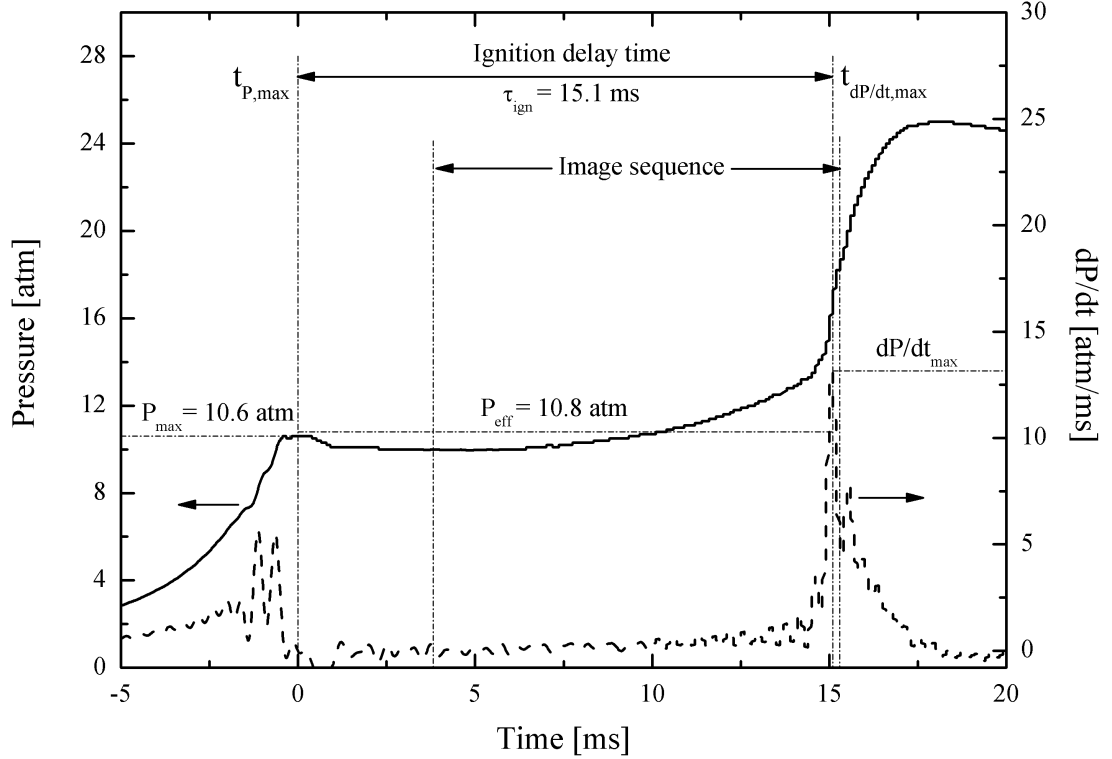
Figure 4.2 Typical pressure (——) and pressure derivative (- - -) time-histories for methyl butanoate ignition experiments where reaction fronts are observed prior to volumetric ignition, experimental conditions of: P_{eff}=10.8 atm, T_{eff}=963 K, ϕ=0.60, Inert/O_2=3.76.

definition for τ_{ign} is illustrated in Figs. 4.1 and 4.2, and was developed in previous UM RCF ignition studies, where it was determined to be very robust when different ignition regimes were present (28; 29).

4.3 Typical Methyl Butanoate Ignition: Imaging Results

As with previous autoignition studies in the UM RCF (28), high speed imaging was acquired for each ignition experiment, and can be used to quantitatively evaluate the homogeneity of ignition. The results for this study demonstrate the presence of two ignition regimes. Conditions exist where only volumetric ignition occurred (Fig. 4.1), and also where reaction fronts preceded volumetric ignition (Fig. 4.2). The presence

of two ignition regimes has been discussed in detail in studies of iso-octane ignition (28).

Imaging sequences corresponding to the pressure time-histories of Figs. 4.1 and 4.2, are shown in Figs. 4.3 and 4.4. It is evident from the imaging sequences that when volumetric ignition is observed, the mixture ignites very uniformly, with little spatially resolved structure. This is seen visually as a slow increase in blue emission, with the peak in blue emission associated with the maximum of the pressure derivative. The pressure also remains relatively constant during the ignition delay for cases of volumetric ignition. Other mixtures, particularly those with higher fuel concentrations, exhibit visible emission as reaction fronts early during the ignition delay time as shown in Fig. 4.4. Reaction fronts are associated with the moderate pressure rise observed prior to the maximum dP/dt (see Fig. 4.2). The peak in the pressure derivative is again associated with the maximum intensity of the blue emission, and is denoted as the time of ignition.

| t = 13.716 ms | t = 13.754 ms | t = 13.792 ms | t = 13.830 ms | t = 13.868 ms |
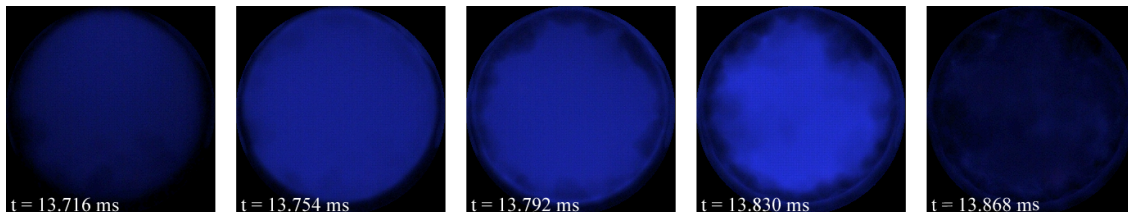
Figure 4.3 Imaging sequence corresponding to the data and time interval of Fig. 4.1, and conditions of: P_{eff}=10.4 atm, T_{eff}=1005 K, ϕ=0.30, Inert/O$_2$=3.76, τ_{ign}=13.8 ms, 26,000 fps (color adjusted for clarity). The time interval spanned for these frames is shown in Fig. 4.1.

4.4 Summary of Methyl Butanoate Ignition Data

A summary of the methyl butanoate ignition data, including the measured ignition delay time and test conditions for each experiment, is presented in Table 4.1. In the table, the equivalence ratio (ϕ) is defined as the actual carbon (C) to oxygen (O) ratio
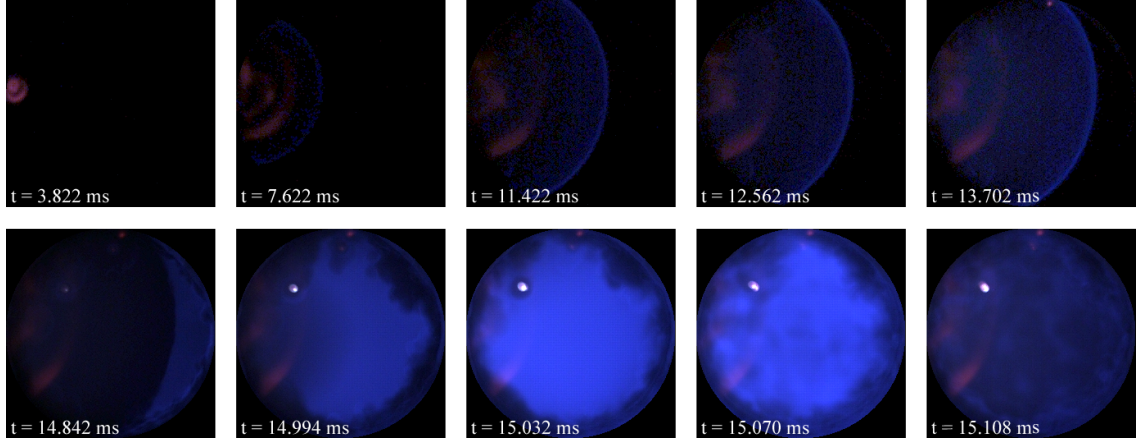
Figure 4.4 Imaging sequence corresponding to the data and time interval of Fig. 4.2, and conditions of: P_{eff}=10.8 atm, T_{eff}=963 K, ϕ=0.60, Inert/O$_2$=3.76, τ_{ign}=15.1 ms, 26,000 fps (color adjusted for clarity). Note not all frames in the imaging sequence are presented. The time interval spanned for these frames is shown in Fig. 4.2.

in the test mixture divided by the stoichiometric carbon to oxygen ratio, assuming complete combustion (only CO_2 and H_2O product species) for the ester fuel. The inert gas to O_2 molar ratio is also provided in Table 4.1, as an indication of the dilution of the mixture. The inert gases used included nitrogen, argon, and carbon dioxide. The mixture components are provided on a mole fraction basis (e.g. χ_{O_2} is the mole fraction of oxygen in the mixture on a percent basis).

Regression analysis can be used to identify trends in the τ_{ign} data for each of the isomers considered in this work and to isolate the effects of parameters of interest, e.g. temperature, pressure, ϕ, χ_{O_2}. Regression analysis was conducted on the complete τ_{ign} data of Table 4.1 for methyl butanoate. Multiple forms of the expression were considered, yielding similar qualities of fit. For consistency, and to maintain the ability to expand the data set in the future, the same form as was used in previous UM RCF ignition studies (26; 27; 28; 29) is used here:

$$\tau_{ign_{mb}} = 3.2 \times 10^{-3} \times P^{-1.21} \phi^{-0.77} \chi_{O_2}^{-1.62} \times \tag{4.3}$$

$$exp(30300/R_{[cal/mol/K]} T),$$

38

Table 4.1 Summary of experimental conditions and results for methyl butanoate ignition. The mixture composition is provided on a mole basis. The equivalence ratio is based on C to O molar ratios.

ϕ	Inert /O_2	Test gas composition[a]				P_{eff} [atm]	T_{eff} [K]	τ_{ign} [ms]
		χ_{mb} [%]	χ_{O_2} [%]	χ_{N_2} [%]	χ_{Ar} [%]			
0.39	4.94	1.01	16.66	64.54	17.79	10.2	1001	16.5
1.21	5.00	3.00	16.18	25.10	55.73	11.1	1019	5.3[b]
0.40	3.76	1.27	20.75	74.71	3.26	9.8	938	33.4
0.40	3.76	1.27	20.75	74.71	3.26	9.6	935	36.6
0.40	3.76	1.27	20.76	62.31	15.66	9.9	992	14.9
0.40	3.76	1.27	20.73	51.68	26.31	10.3	1053	6.3
0.40	3.76	1.27	20.75	42.32	35.66	10.5	1109	2.7
0.38	3.76	1.20	20.75	62.40	15.64	5.4	1015	21.9
0.39	3.75	1.24	20.77	62.54	15.44	4.9	989	36.6
0.39	3.76	1.26	20.74	62.42	15.58	5.4	1014	17.9
0.40	3.76	1.28	20.74	74.69	3.29	10.4	953	24.0
0.40	3.76	1.27	20.74	74.69	3.29	11.1	969	17.4
0.60	3.76	1.90	20.61	62.26	15.24	10.9	968	12.5[b]
0.60	3.76	1.90	20.61	62.22	15.27	10.8	963	15.1[b]
0.30	3.76	0.95	20.81	68.71	9.53	10.2	998	15.9
0.30	3.76	0.95	20.81	68.72	9.52	10.4	1005	13.8
0.30	3.77	0.96	20.74	68.54	9.56	14.7	991	11.4
0.30	3.77	0.96	20.75	68.57	9.56	14.5	988	11.6
0.30	3.76	0.96	20.80	68.60	9.54	18.6	978	9.8
0.30	3.75	0.96	20.81	68.59	9.55	19.6	991	7.7
0.30	3.76	0.96	20.79	68.65	9.60	5.0	994	46.9
0.30	3.76	0.96	20.79	68.65	9.60	4.7	979	48.6
0.30	3.76	0.95	20.82	61.06	17.16	7.9	1046	10.2
0.30	3.76	0.95	20.82	61.07	17.15	7.9	1047	11.2
0.30	3.76	0.95	20.81	52.52	25.73	8.1	1094	4.7
0.30	3.76	0.96	20.81	52.36	25.87	8.1	1098	4.6

[a]Balance CO_2
[b]Conditions where reaction fronts were observed

with an R^2 value of 0.97. This regression is shown in Fig. 4.11.

The recommended uncertainty in the ignition delay time measurements is based on the uncertainty of the measured variables used in the regression and the corresponding effects of the uncertainties on the predicted ignition delay time. The sensitivity of

the measured parameters was defined using the appropriate partial derivatives of the regression expression. The total uncertainty was then evaluated using the square-root of the sum of the squares for each contribution. The uncertainty for the methyl butanoate τ_{ign} is $\pm 16\%$, and is primarily due to the uncertainty in the pressure measurement using the pressure transducers, and the chosen definition for the effective pressure. The uncertainty is shown by the representative error bars in Fig. 4.11.

Summaries of the effects of temperature, pressure, equivalence ratio, and oxygen mole fraction on τ_{ign} are shown in Figs 4.5 - 4.8, respectively, where the data have been normalized as necessary using Eq. (4.3). Equation (4.3) is provided in each of the figures for reference as the solid line. Also shown in Figs. 4.5 - 4.8 are prediction for τ_{ign} based on the chemical kinetic mechansim of Fisher *et al.* (16), using the homogeneous reactor model from the CHEMKIN 4.1 suite (34), with the effective conditions and unreacted mixture composition as initial conditions to the model. As is shown in the figures, the mechanism predicts ignition to occur 2-3 times faster than was observed in the UM RCF studies. Further discussion of the modeling results can be found in Chapter 5.

4.5 Comparison of Methyl Butanoate and Butyl Methanoate Ignition Results

Ignition studies of two small esters were performed using a rapid compression facility (RCF). The esters (methyl butanoate and butyl methanoate) were chosen to have matching molecular weights, and C:H:O ratios, while varying the lengths of the constituent alkyl chains. The effect of functional group size on ignition delay time was investigated using pressure time-histories and high-speed digital imaging. The mixtures studied covered a range of conditions relevant to oxygenated fuels and fuel additives, including bio-derived fuels. Low-temperature and moderate-pressure
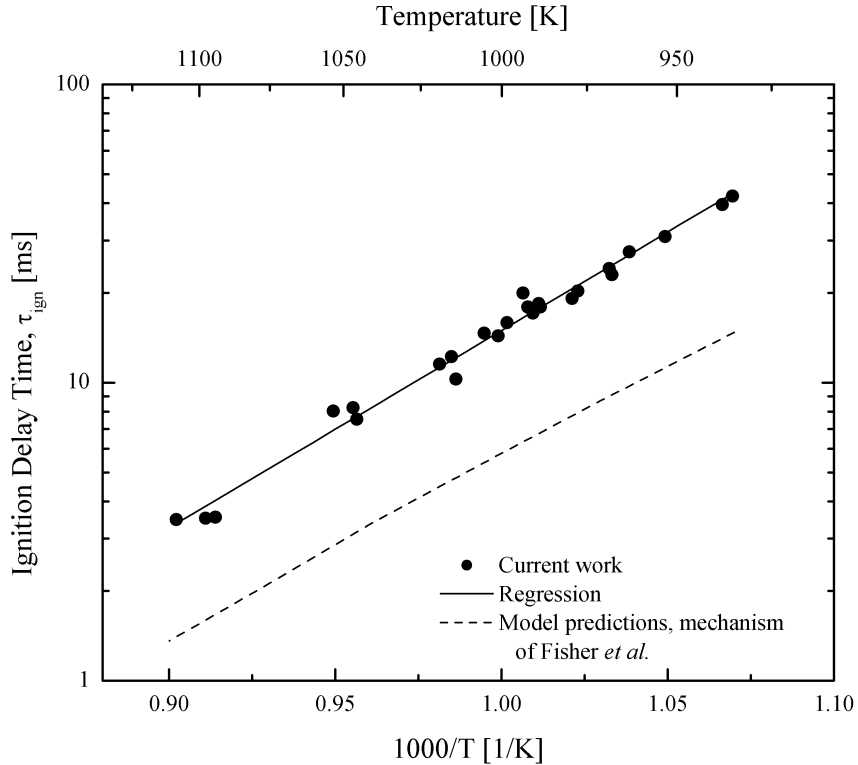
Figure 4.5 Summary of reaction front and homogeneous ignition data for methyl butanoate ignition delay time as a function of temperature. The experimental data have been normalized to $P = 10$ atm, $\phi = 0.3$, and $O_2 = 21\%$ using Eq. (4.3). Equation (4.3), and the results of model predictions for τ_{ign} based on the reaction mechanism of Fisher *et al.* (16) are provided for comparison.

conditions were selected for study due to their relevance to advanced low-temperature combustion strategies, and internal combustion engine conditions. The results are discussed in terms of the reaction pathways affecting the ignition properties.

4.5.1 Typical Butyl Methanoate Ignition Results

Figures 4.9 and 4.10 present pressure and corresponding imaging sequence data for a typical butyl methanoate experiment. The general features of the pressure data are the same as observed for the volumetric ignition conditions of methyl butanoate. Only volumetric ignition of the butyl methanoate mixtures was observed for the lean
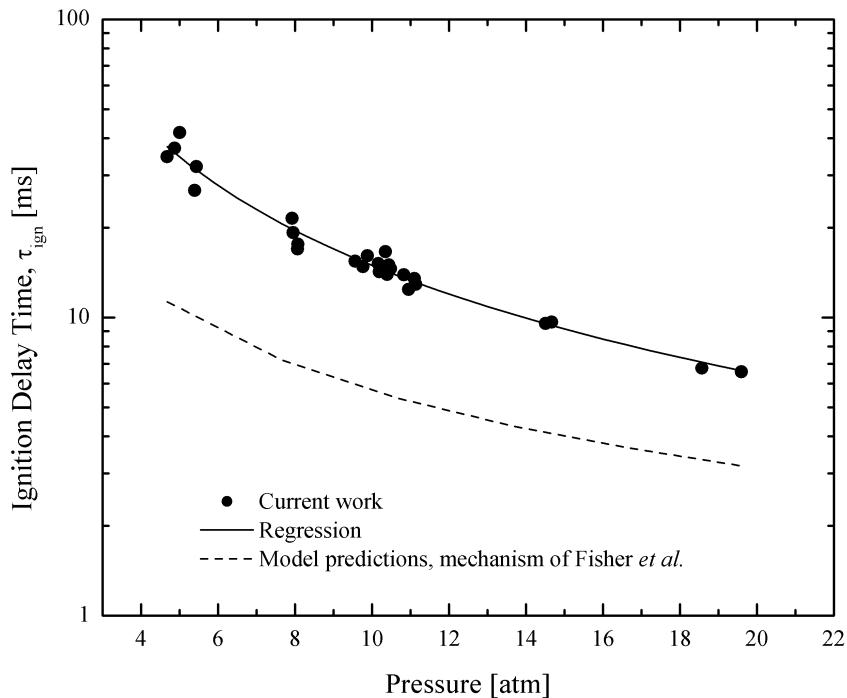
Figure 4.6 Summary of reaction front and homogeneous ignition data for methyl bu-tanoate ignition delay time as a function of temperature. The experimental data have been normalized to $T = 1000$ K, $\phi = 0.3$, and $O_2 = 21\%$ using Eq. (4.3). Equation (4.3), and the results of model predictions for τ_{ign} based on the reaction mechanism of Fisher *et al.* (16) are provided for comparison.

conditions studied here. Table 4.2 presents a summary of the butyl methanoate results.

4.6 Summary of Butyl Methanoate Ignition Data

Figure 4.11 provides a summary of the results for ignition delay time for the two esters studied in this work compared with previous studies of $C_5H_{10}O_2$ ignition. It can be seen in the figure that the ignition delay time results from the previous shock tube study of Metcalfe *et al.* (21) were taken at higher temperatures (T=1100-1670 K). The data from (21) were also at different pressures (P = 1 and 4 atm), and spanned equivalence ratios from ϕ=0.25-1.5. In addition to the ignition delay time
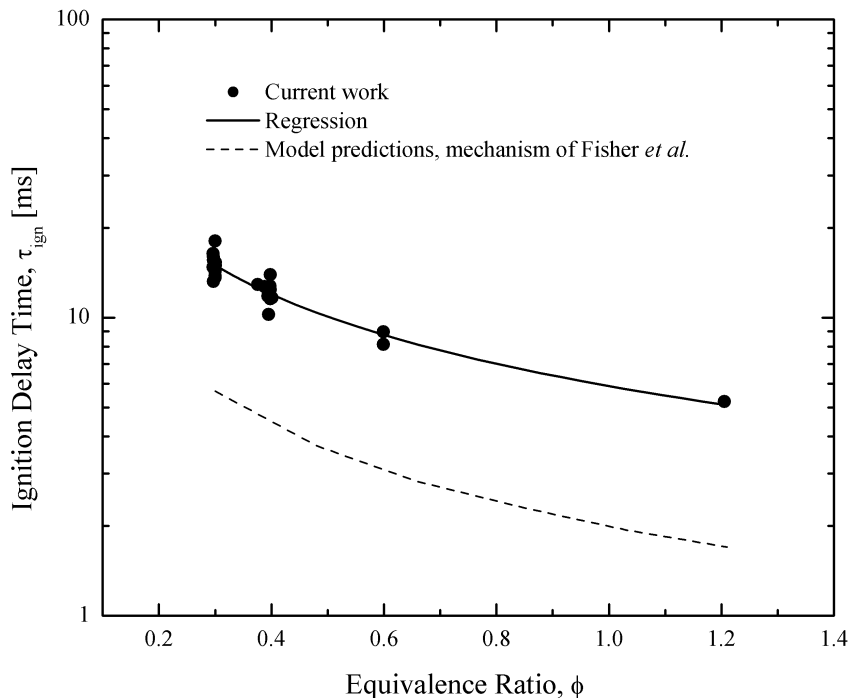
Figure 4.7 Summary of reaction front and homogeneous ignition data for methyl butanoate ignition delay time as a function of temperature. The experimental data have been normalized to $T = 1000$ K, $P = 10$ atm, and $O_2 = 21\%$ using Eq. (4.3). Equation (4.3), and the results of model predictions for τ_{ign} based on the reaction mechanism of Fisher *et al.* (16) are provided for comparison.

data, Metcalfe *et al.* (21) also refined the mechanism of Fisher *et al.* (16) to obtain better agreement at the higher temperature conditions they investigated. The results of their model predictions are shown as the dashed lines passing through their ignition data in Fig. 4.11.

Regression analysis was also used to identify trends in the τ_{ign} data of Table 4.2 for butyl methanoate. Because the data were obtained at nominally fixed dilution, equivalence ratio, and pressure, an Arrhenius form to the expression was used:

$$\tau_{ign_{bm}} = 5.8 \times 10^{-7} \times exp(31700/R_{[cal/mol/K]} T) . \tag{4.4}$$
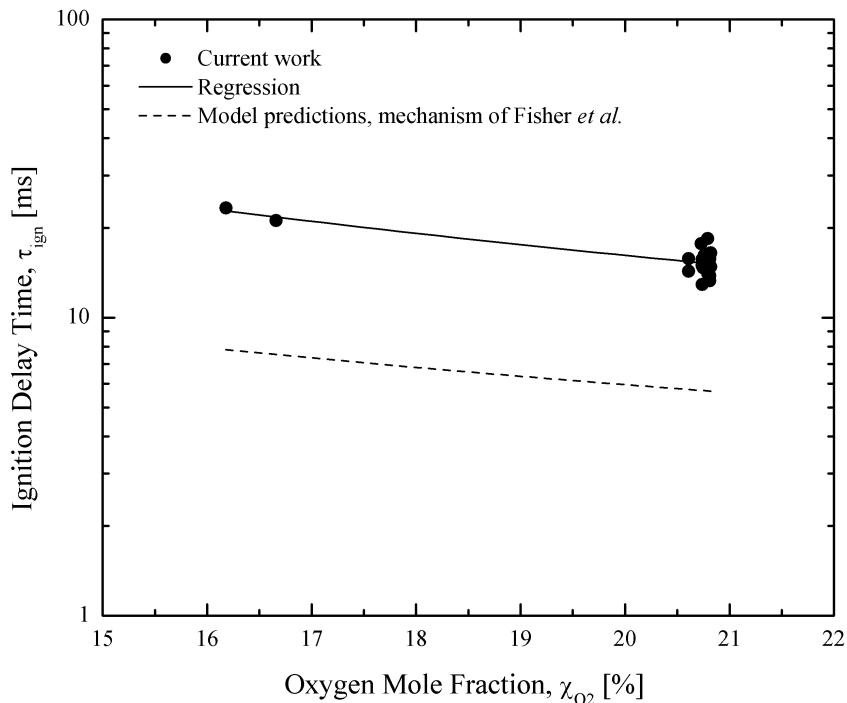
Figure 4.8 Summary of reaction front and homogeneous ignition data for methyl butanoate ignition delay time as a function of temperature. The experimental data have been normalized to $T = 1000$ K, $P = 10$ atm, and $\phi = 0.3$ using Eq. (4.3). Equation (4.3), and the results of model predictions for τ_{ign} based on the reaction mechanism of Fisher *et al.* (16) are provided for comparison.

with an R^2 value of 0.98. This regression is also shown in Fig. 4.11. The recommended uncertainty for the butyl methanoate ignition data is $\pm 17\%$, and is also predominantly due to the uncertainty in the measured pressure.

4.7 Discussion of Methyl Butanoate and Butyl Methanoate Igntion

As seen in Fig. 4.11, the activation energy of methyl butanoate changes between the high-temperature data of Metcalfe *et al.* (21) and the low-temperature data of this study. The activation energy is much larger for the high temperature data set than
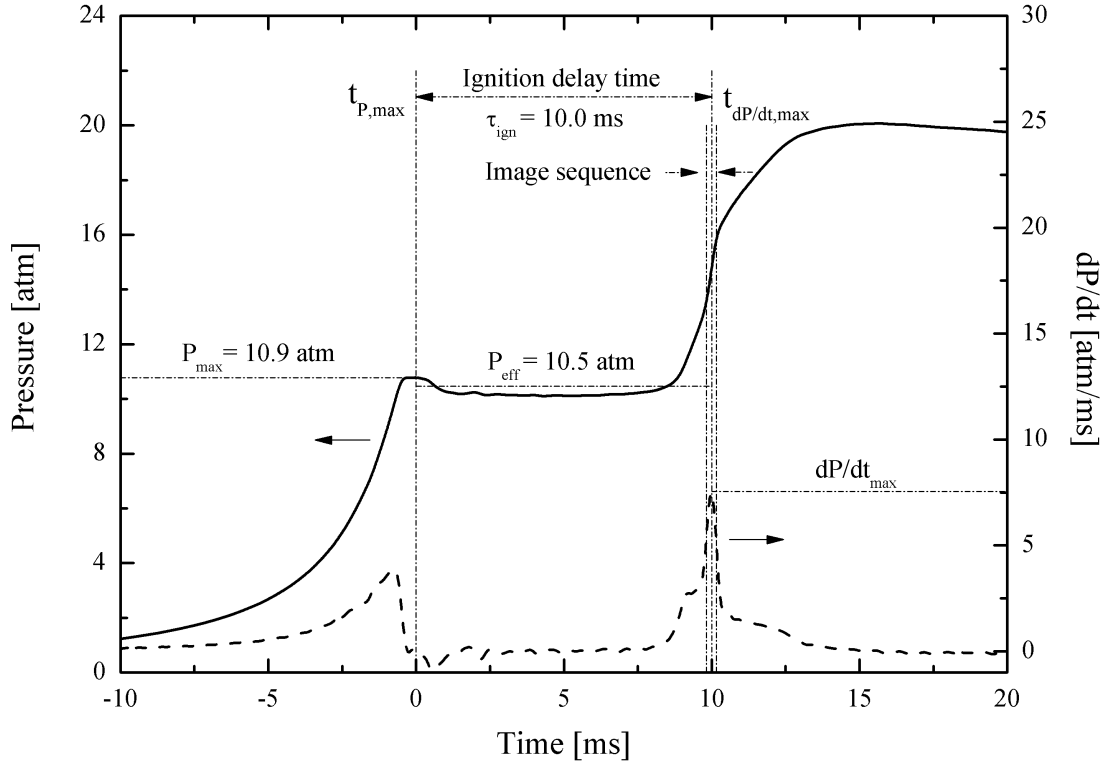
Figure 4.9 Typical pressure (——) and pressure derivative (- - -) time-histories for butyl methanoate ignition experiments where volumetric ignition is observed, experimental conditions of: P_{eff}=10.5 atm, T_{eff}=960 K, ϕ=0.40, Inert/O_2=3.76.
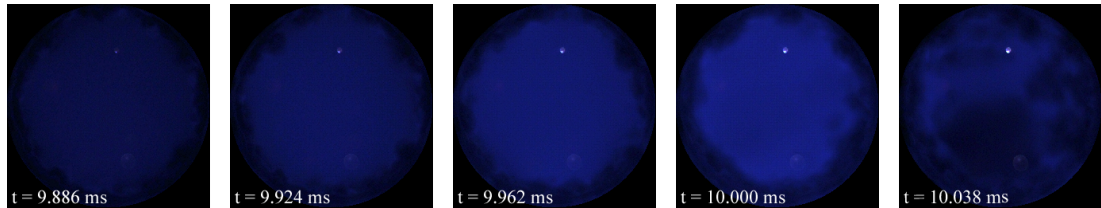
Figure 4.10 Imaging sequence corresponding to the data and time interval of Fig. 4.9, and conditions of: P_{eff}=10.5 atm, T_{eff}=960 K, ϕ=0.40, Inert/O_2=3.76, τ_{ign}=10.0 ms, 26,000 fps (color adjusted for clarity). The time interval spanned for these frames is shown in Fig. 4.9.

for the lower temperature data. Additional functional dependencies of parameters other than temperature have not yet been investigated for butyl-methanoate.

When looking at the temperature dependence, both the high temperature data of Metcalfe *et al.* (21) and the lower temperature data of the current work show similar trends when comparing the ignition delay times of the $C_5H_{10}O_2$ isomers. Metcalfe *et*

Table 4.2 Summary of experimental conditions and results for butyl methanoate ignition. The mixture composition is provided on a mole basis. The equivalence ratio is based on C to O molar ratios.

ϕ	Inert /O_2	Test gas composition[a]				P_{eff} [atm]	T_{eff} [K]	τ_{ign} [ms]
		χ_{bm} [%]	χ_{O_2} [%]	χ_{N_2} [%]	χ_{Ar} [%]			
0.40	3.76	1.27	20.75	62.36	15.62	10.9	1022	3.2
0.40	3.76	1.27	20.75	62.35	15.63	10.6	1014	4.1
0.40	3.76	1.27	20.74	71.25	0.00	10.3	905	29.1
0.40	3.76	1.28	20.73	71.25	0.00	10.4	908	29.9
0.40	3.75	1.27	20.77	60.70	0.00	11.0	869	45.6
0.40	3.76	1.27	20.76	77.28	0.69	10.5	960	10.0
0.40	3.76	1.27	20.76	77.28	0.69	10.3	957	11.4

[a]Balance CO_2

al. (21) has shown that ethyl propanoate ignites faster than methyl butanoate over the temperature range shown in Fig. 4.11, at both $P = 1$ and 4 atm. The current study shows that butyl methanoate also ignites faster than methyl butanoate.

The faster ignition of the butyl methanoate compared to methyl butanoate observed in this study may be explained by differences in reaction sequences proposed by Schwartz *et al.* (22). Schwartz *et al.* (22) suggested that the slow decomposition rate of methyl butanoate relative to some other $C_5H_{10}O_2$ isomers investigated in their study was due to the primary decomposition path favored by methyl butanoate; specifically, a reaction sequence dominated by bimolecular H-atom abstraction reactions. Other C_5 esters investigated by Schwartz *et al.* (22) which exhibited faster decomposition rates were proposed to follow faster unimolecular six-centered dissociation decomposition pathways.

Six-centered dissociation is considered the primary decomposition pathway for esters capable of forming the necessary intermediate ring, such as ethyl propanoate and butyl methanoate. To form the intermediate complex the ester must have at least two carbons in the alcohol group. A ring can then form comprised of the carbonyl group,
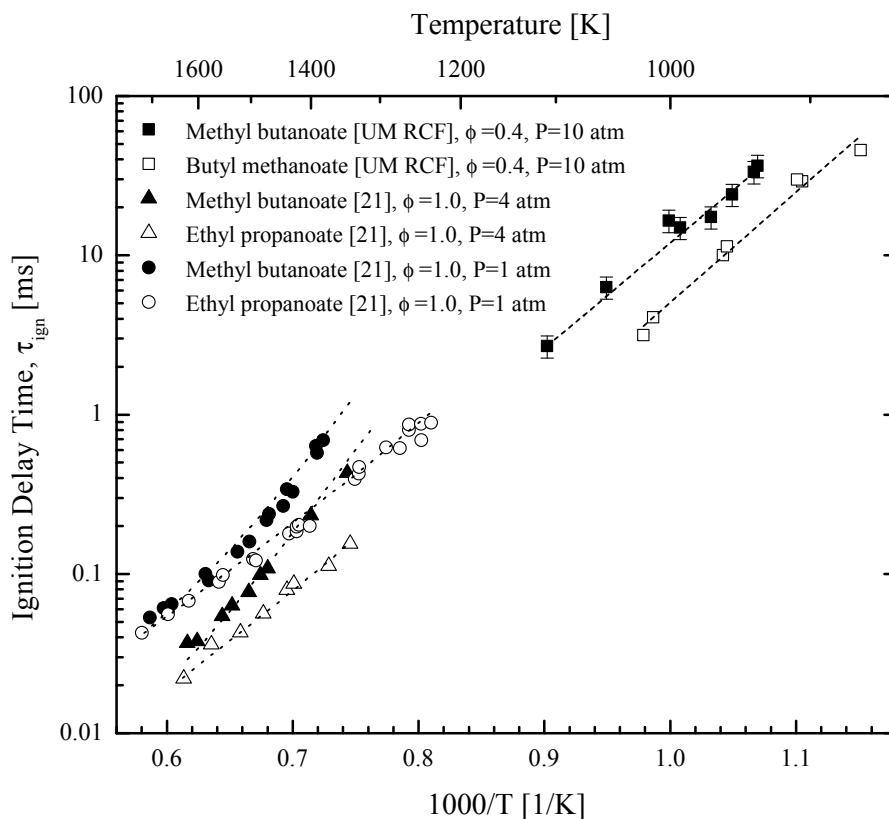
Figure 4.11 Comparison of current ($P_{eff} \cong 10$ atm data) and previous ignition delay time studies for $C_5H_{10}O_2$ isomers. The lines through the UM RCF data are Eqs. (4.3) and (4.4). The other data are results of the shock tube experiments from the study of Metcalfe *et al.* (21), and the lines are their associated model predictions.

the single bonded O atom, the next two adjacent C atoms in the alcohol group, and a single H atom bonded to the second C atom. This intermediate ring forms as shown in Fig. 4.12 for ethyl propanoate, and as shown in Fig. 4.13 for butyl methanoate. The ring decomposes resulting in two highly reactive products: a carboxylic acid and an alkene, leading to much faster ignition than observed by esters that do not form the intermediate ring.

Metcalfe *et al.* (21) considered the possible formation of an intermediate ring during methyl butanoate decomposition as shown in Fig. 4.14. They added this reaction
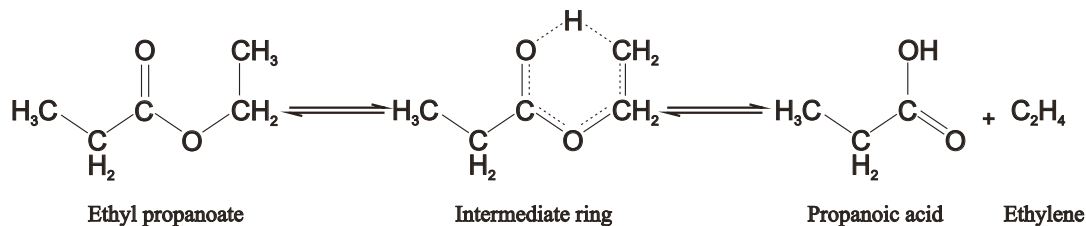
Figure 4.12 Six-centered unimolecular decomposition for ethyl propanoate producing propanoic acid and ethylene. Adapted from Metcalfe *et al.* (21).
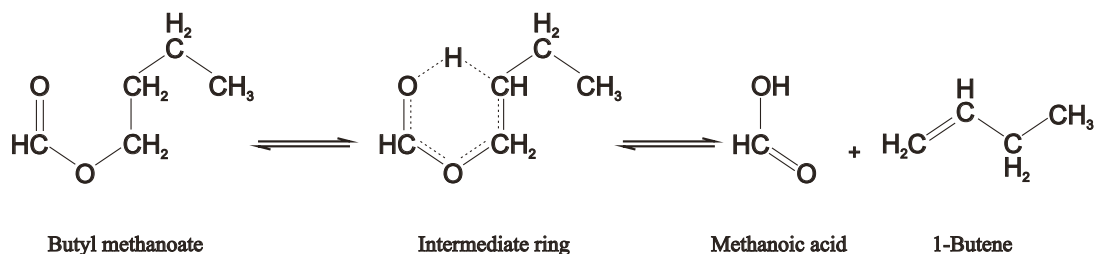
Figure 4.13 Six-centered unimolecular decomposition for butyl methanoate producing methanoic acid and 1-butene.

step to their modified reaction mechanism, and modeled the ring as forming from the carbonyl group, and the C atoms in the alkyl chain of the acid group. However, they found that this pathway contributes very little ($<1\%$) to the methyl butanoate decomposition for the conditions they studied.

The UM RCF results support the trends observed in the studies by Schwartz *et al.* (22) and Metcalfe *et al.* (21). The faster ignition delay times determined for butyl methanoate compared to methyl butanoate indicates the butyl methanoate also favors the more rapid reaction sequence of unimolecular decomposition at the conditions of the current study. Additional experimental measurements of the key intermediates can help quantify the relative contributions of the decomposition reactions and clarify the overall reaction sequence.
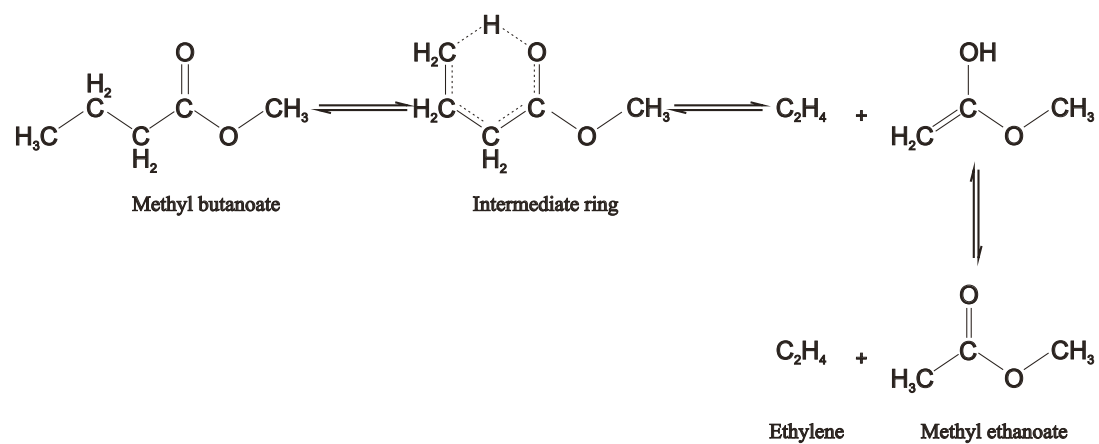
Figure 4.14 Six-centered unimolecular decomposition for methyl butanoate producing methyl ethanoate and ethylene. Adapted from Metcalfe *et al.* (21).

Chapter 5

Ignition Behavior and Modeling of C$_5$ Esters with Varying Alkyl Chain Lengths: Methyl Butanoate and Ethyl Propanoate

The work presented in this chapter has been accepted to be published in the *Proceedings of the 32nd International Symposium on Combustion*, held in August 2008.

5.1 Introduction

Ignition studies of two C$_5$ esters were performed using a rapid compression facility. Methyl butanoate and ethyl propanoate were chosen to have matching molecular weights and C:H:O ratios while varying the length of the constituent alkyl chains. The effect of functional group size on ignition delay time was investigated using pressure time-histories and high-speed digital imaging. Low-temperature, moderate-pressure conditions were selected for study due to the relevance to low-temperature combustion strategies and internal combustion engine conditions. The experiments covered a range of conditions: T=935-1117 K, P=4.7-19.6 atm, and ϕ=0.3-0.4. The experimental data are compared to previous high-temperature studies and chemical modeling. A new mechanism for methyl butanoate and ethyl propanoate ignition is presented. The

modeling and experimental data are in very good agreement for methyl butanaote and yield good agreement for ethyl propanoate.

5.2 Experimental Data

Mixtures and conditions for study were selected to compare the ignition properties of the two $C_5H_{10}O_2$ isomers: methyl butanoate and ethyl propanoate. Specifically, the temperature varied from T=935-1117 K, the pressure varied from P=4.7-19.6 atm, and lean conditions were studied (ϕ=0.3-0.4). The dilution of the fuel and O_2 mixtures was kept constant throughout this study with (total inert gases)/$O_2 \cong 3.76$. The inert gases were varied (Ar, N_2, or CO_2) to assist in controlling the end of compression pressure and temperature.

Typical pressure and pressure derivative data for $C_5H_{10}O_2$ ignition experiments are shown in Fig. 5.1. The initial pressure rise is due to compression of the test gas mixture ahead of the sabot. At the end of compression, the pressure reaches the first maximum. This time is set as t = 0 sec and is labeled P_{max} in the figure. The pressure then decreases slightly due to cooling losses to the test volume walls. After a delay period, the mixture auto-ignites resulting in a rapid increase in pressure for all cases. As demonstrated in Fig. 5.1, none of the experimental data presented in this study exhibited two-stage ignition behavior.

The effective test conditions are again determined using the previously described method using the pressure time-history from each experiment. For each experiment, the ignition delay time (τ_{ign}) was determined using the pressure time-history, and is defined as the time between P_{max} and dP/dt_{max}. This definition for τ_{ign} is illustrated again in Fig. 5.1,

High-speed imaging was also acquired for each ignition experiment. The imaging was used to ensure the homogeneity of the ignition conditions in the test volume for
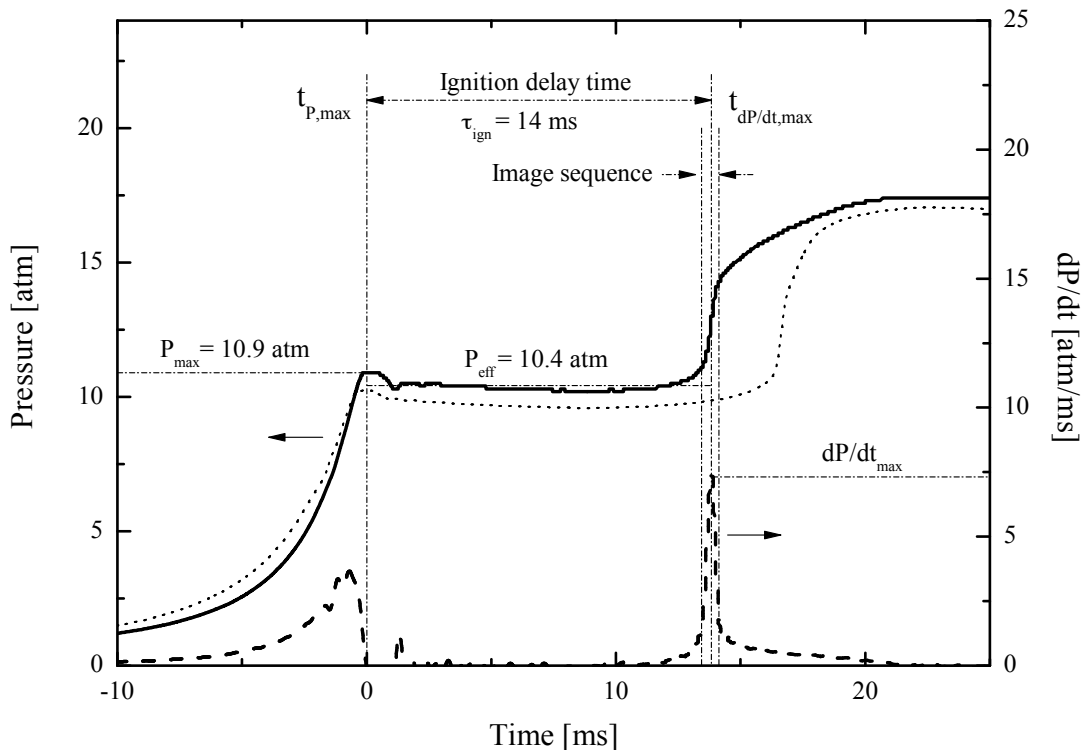
Figure 5.1 Typical pressure (——) and pressure derivative (- - -) time-histories for methyl butanoate ignition experiments with experimental conditions; P_{eff}=10.4 atm, T_{eff}=1005 K, ϕ=0.30, Inert/O_2=3.76, τ_{ign}=14 ms. Also included in this figure are typical pressure time-history data for ethyl propanoate; ($\cdot \cdot \cdot$, P_{eff}=9.8 atm, T_{eff}=995 K, ϕ=0.30, Inert/O_2=3.76, τ_{ign}=17 ms).

each experiment. An imaging sequence corresponding to the pressure time-history for methyl butanoate ignition is shown in Fig. 5.2. As seen in Fig. 5.2, the mixture ignites uniformly with little spatially resolved structure. The peak in the blue emission corresponds to the maximum in the pressure derivative. Note the pressure remains approximately constant during the ignition delay. Similar ignition behavior was observed for the ethyl propanoate experiments. A typical pressure time-history for ethyl propanoate is included in Fig. 5.1. The general features of the pressure data are similar for both esters. The imaging data (not included here for ethyl propanoate) demonstrate uniform volumetric ignition. An uncertainty analysis was completed using the same method described in He *et al.* (26) and Walton *et al.* (28). The

average uncertainty for the τ_{ign} measurements for this study is $\pm16\%$ for both methyl butanoate and ethyl propanoate, and is primarily due to the uncertainty in the pressure measurement.

t = 13.716 ms   t = 13.754 ms   t = 13.792 ms   t = 13.830 ms   t = 13.868 ms
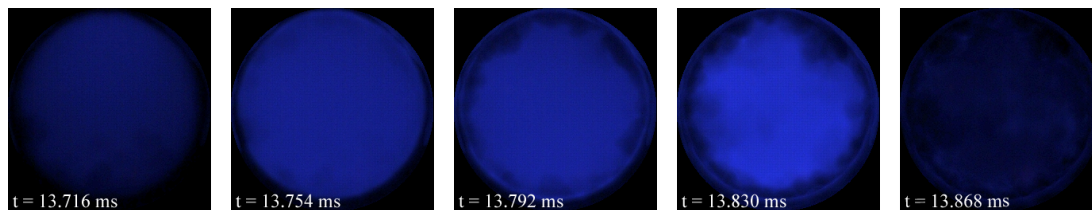
Figure 5.2   Imaging sequence corresponding to the methyl butanoate data and time interval presented in Fig. 5.1 (26,000 fps, color adjusted for clarity).

A summary of the methyl butanoate ignition data, including the measured ignition delay time and test conditions for each experiment, is presented in Table 5.1. Table 5.2 presents a summary of the ethyl propanoate results. Figure 5.3 provides a summary of the results for τ_{ign} for both esters studied in this work for P$\cong$10 atm. The data are compared with previous high-temperature studies of $C_5H_{10}O_2$ ester ignition. The data from Metcalfe *et al.* (21) were obtained at lower pressures (P = 1 and 4 atm), and over the temperature range T=1100-1670 K, with ϕ=1.0. Metcalfe *et al.* (21) refined the mechanism for methyl butanoate oxidation of Fisher *et al.* (16) to include ethyl propanoate and to obtain better agreement at the conditions they investigated. The results of their model predictions are shown in Fig. 5.3. As seen in Fig. 5.3 for methyl butanoate, the low temperature results from the present experiments show a smaller effective activation energy than the high temperature results of Metcalfe *et al.* (21). In addition, the low temperature ethyl propanoate ignition data indicate a higher effective activation energy than the low temperature data for methyl butanoate. Insight into these differences can be gained through detailed kinetic modeling, which can also be used to reconcile the apparently different high and low temperature trends.

Overall, the experimental results show that ethyl propanoate ignites more rapidly than methyl butanoate under the same experimental conditions. This is consistent
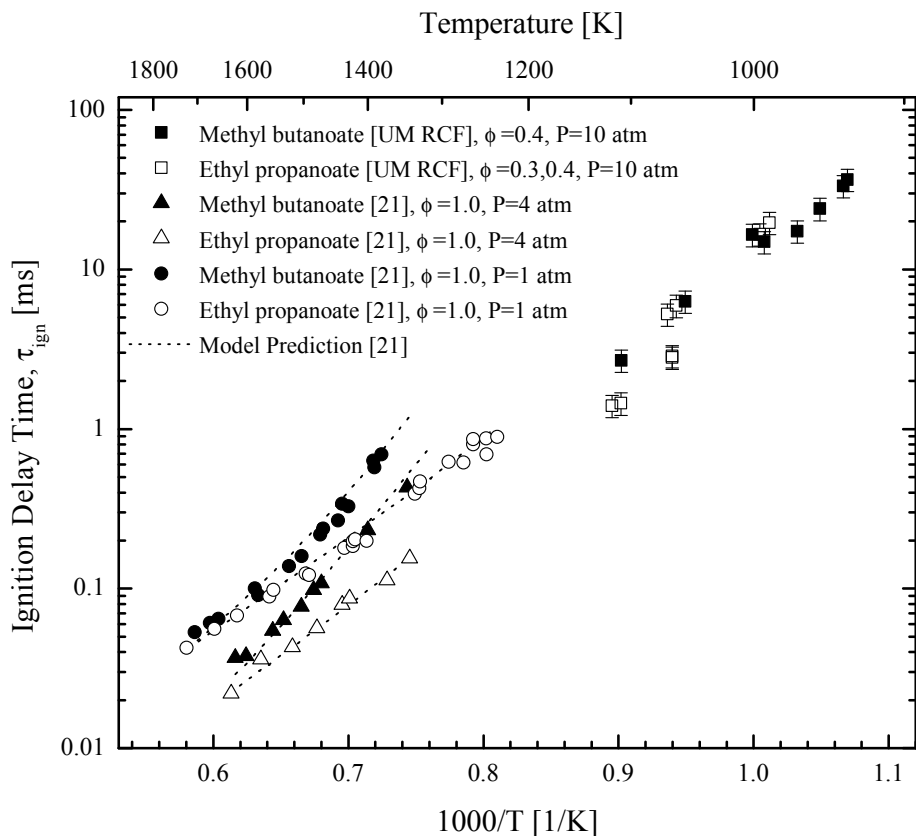
Figure 5.3 Comparison of current ($P_{eff} \cong 10$ atm data) and previous ignition delay time studies for $C_5H_{10}O_2$ isomers. The high temperature data are from Metcalfe *et al.* (21), and the dotted lines $(\cdot \cdot \cdot)$ are their associated model predictions. The error bars represent the uncertainty in the UM RCF data.

with analyses by Schwartz *et al.* (22) and Metcalfe *et al.* (21), who showed that the two isomers react via quite different reaction pathways. Methyl butanoate reacts primarily through bimolecular reactions in which radical species abstract H atoms from methyl butanoate; the resulting radical species from methyl butanoate then decompose and produce additional radical species to continue the process. In contrast, ethyl propanoate reacts via a much different pathway, with a particularly low energy barrier that is not available to methyl butanoate. This pathway involves the formation of a six-membered transition state that transfers an H atom from the ethyl group

Table 5.1 Summary of experimental conditions and results, and modeling results for methyl butanoate ignition. All mixture composition data are provided on a mole basis. The equivalence ratio (ϕ) is based on the C to O molar ratios of the actual and stoichiometric conditions. The inert gas to O_2 molar ratio $\cong 3.76$ for all experiments. Model predictions for ignition delay times were made using the modified methyl butanoate/ethyl propanoate reaction mechanism and are listed as τ_{pred}.

| ϕ | Test gas composition[a] | | | | P_{eff} [atm] | T_{eff} [K] | τ_{ign} [ms] | τ_{pred} [ms] |
	χ_{mb} [%]	χ_{O_2} [%]	χ_{N_2} [%]	χ_{Ar} [%]				
0.40	1.27	20.8	74.7	3.3	9.8	938	33	30
0.40	1.27	20.8	74.7	3.3	9.6	935	37	32
0.40	1.27	20.8	62.3	15.7	9.9	992	15	13
0.40	1.27	20.7	51.7	26.3	10.3	1053	6.3	6.8
0.40	1.27	20.8	42.3	35.7	10.5	1109	2.7	4.2
0.38	1.20	20.8	62.4	15.6	5.4	1015	22	21
0.39	1.24	20.8	62.5	15.4	4.9	989	37	30
0.39	1.26	20.7	62.4	15.6	5.4	1014	18	20
0.40	1.28	20.7	74.7	3.3	10.4	953	24	22
0.40	1.27	20.7	74.7	3.3	11.1	969	17	17
0.30	0.95	20.8	68.7	9.5	10.2	998	16	15
0.30	0.95	20.8	68.7	9.5	10.4	1005	14	14
0.30	0.96	20.7	68.5	9.6	14.7	991	11	12
0.30	0.96	20.8	68.6	9.6	14.5	988	12	13
0.30	0.96	20.8	68.6	9.5	18.6	978	9.8	11
0.30	0.96	20.8	68.6	9.6	19.6	991	7.7	9.1
0.30	0.96	20.8	68.7	9.6	5.0	994	47	33
0.30	0.96	20.8	68.7	9.6	4.7	979	49	43
0.30	0.95	20.8	61.1	17.2	7.9	1046	10	12
0.30	0.95	20.8	61.1	17.2	7.9	1047	11	12
0.30	0.95	20.8	52.5	25.7	8.1	1094	4.7	7.2
0.30	0.96	20.8	52.4	25.9	8.1	1098	4.6	6.9

[a]Balance CO_2

in ethyl propanoate to the C=O group within the molecule. This transition state then decomposes rapidly to produce ethene and propanoic acid, both of which are much more reactive than methyl butanoate. This reaction pathway is not possible for methyl butanoate, since its methyl group enables only a five-membered transition state that has a much higher activation energy barrier for H atom transfer. The same six-membered transition state, producing ethene and a carboxylic acid, is important

in oxidation of ethyl formate and ethyl acetate (35), and the same rate expression is used in the present ethyl propanoate reaction mechanism (21).

Table 5.2 Summary of experimental conditions and results, and modeling results for ethyl propanoate ignition. All mixture composition data are provided on a mole basis. The equivalence ratio (ϕ) is based on the C to O molar ratios of the actual and stoichiometric conditions. The inert gas to O_2 molar ratio $\cong 3.76$ for all experiments. Model predictions for ignition delay times were made using the modified methyl butanoate/ethyl propanoate reaction mechanism and are listed as τ_{pred}.

ϕ	Test gas composition[a]				P_{eff} [atm]	T_{eff} [K]	τ_{ign} [ms]	τ_{pred} [ms]
	χ_{ep} [%]	χ_{O_2} [%]	χ_{N_2} [%]	χ_{Ar} [%]				
0.40	1.27	20.7	51.6	26.4	10.6	1064	2.9	3.3
0.40	1.27	20.7	51.6	26.4	10.6	1064	2.8	3.3
0.30	0.96	20.8	68.7	9.5	9.6	988	20	14
0.30	0.96	20.8	68.7	9.5	9.8	995	17	12
0.30	0.96	20.8	58.1	20.2	10.5	1061	5.9	4.0
0.30	0.96	20.8	58.0	20.2	10.8	1068	5.2	3.6
0.30	0.96	20.8	48.7	29.5	10.7	1117	1.4	1.7
0.30	0.96	20.8	48.7	29.5	10.4	1109	1.5	2.0

[a]Balance CO_2

Metcalfe *et al.* (21) considered the possible formation of an intermediate ring during methyl butanoate decomposition. They added this reaction step to their modified reaction mechanism, and modeled the ring as forming from the carbonyl group, and the C atoms in the alkyl chain of the acid group. However, they found that this pathway contributes very little (<1%) to the methyl butanoate decomposition for the conditions they studied.

The UM RCF results are consistent with the trends observed in the high-temperature studies by Schwartz *et al.* (22) and Metcalfe *et al.* (21). As such, we propose that ethyl propanoate favors the more rapid reaction sequence of uni-molecular decomposition at these low-temperature conditions as well. Additional experimental measurements of the key intermediates can help quantify the relative contributions of the decomposition reactions and clarify the overall reaction sequence.

5.3 Kinetic Modeling

Metcalfe *et al.* (21) recently added an ethyl propanoate submechanism to the methyl butanoate mechanism of Fisher *et al.* (16) and included a few revised reaction rates (including H atom abstraction from methyl butanoate and formaldehyde production) from Gaïl *et al.* (19). In the current work, the reaction mechanism from Metcalfe *et al.* (21) was modified slightly to improve the agreement between the computed and experimental results. For the conditions of this experimental study, H atom abstraction from the C_5 ester by HO_2 accelerates ignition by forming H_2O_2, which then decomposes into two OH radicals. H abstraction from the C_5 ester by H atoms decreases the overall rate of ignition because these reactions compete with the principal chain branching reaction between H and O_2, producing O and OH radicals. Since the computed results were uniformly more reactive than the experiments, the A-coefficients for the two most sensitive reactions between methyl butanoate and H were increased by a factor of two (mb+h=h2+mb4j, mb+h=h2+mbmj), and the remaining mb + H reactions were changed to the generalized Arrhenius form to span the temperature range of both the UM RCF data and the Metcalfe *et al.* (21) shock tube data. Additionally, the A-coefficients for all of the reactions between methyl butanoate and HO_2 were decreased by a factor of 0.77, and the A-coefficients for all of the forward reactions between ethyl propanoate and HO_2 were decreased by a factor of 0.65. The specific reactions and the modified rate coefficient expressions are summarized in Table 5.3. Note these small changes are within the uncertainty bounds for each of the reaction rate expressions.

All of the simulations of the UM RCF experiments assumed that combustion takes place homogeneously at constant volume, with negligible heat loss during the ignition delay period. No reaction was considered during the compression stroke, which is appropriate unless the ignition delay becomes very short compared with the last few milliseconds of the compression stroke. Ignition was defined computationally as the

Table 5.3 Summary of reactions[a] modified in this work for the methyl butanoate/ethyl propanoate reaction mechanism. The remainder of the mechanism was unchanged from Metcalfe *et al.* (21). The rate coefficients are listed in the generalized Arrhenius form $k = AT^n exp(-E_a/RT)$[b]

Reaction	A	n	E_a
mb + ho2 = h2o2 + mb4j	1.900×10^{12}	0.0	20440
mb + ho2 = h2o2 + mb3j	1.300×10^{12}	0.0	17690
mb + ho2 = h2o2 + mb2j	1.300×10^{12}	0.0	17690
mb + ho2 = h2o2 + mbmj	1.900×10^{12}	0.0	20440
mb + h = h2 + mb4j	1.880×10^{5}	2.75	6280
mb + h = h2 + mb3j	1.300×10^{6}	2.4	4471
mb + h = h2 + mb2j	1.300×10^{6}	2.4	4471
mb + h = h2 + mbmj	1.880×10^{5}	2.75	6280
ep + ho2 = h2o2 + ep3j	8.300×10^{3}	2.55	16490
ep + ho2 = h2o2 + ep2j	1.500×10^{12}	0.0	14400
ep + ho2 = h2o2 + epej	2.500×10^{3}	2.55	10530
ep + ho2 = h2o2 + epmj	8.300×10^{3}	2.55	16490

[a]Notation from Metcalfe *et al.* (21)
[b]Units are mole, cm, sec., cal., and K

maximum rate of temperature rise of the reacting mixture.

Computed results from the modified mechanism for methyl butanoate ignition are shown as the solid and dashed lines in Fig. 5.4, calculated for $\phi = 0.4$ and 0.3, respectively, and at 10 atm pressure. The UM RCF results for both $\phi = 0.3$ and 0.4 are shown as symbols. The experimental results include the ϕ=0.3 and 0.4 cases for pressures between 7.9 and 14.7 atm. Model predictions for the experimental conditions that extend beyond P=10 atm are shown in Table 5.1. The overall agreement between the computed and experimental results is excellent at both low and high temperatures. The computed curve extends to high temperatures, showing a perceptible increase in the overall slope or effective activation energy. Computed results for methyl butanoate ignition at $\phi = 1$ and 4 atm are shown as the dotted curve, indicating the predicted change in ignition delay that should be expected for the difference due to the larger equivalence ratio and lower pressure between the two experimental studies.
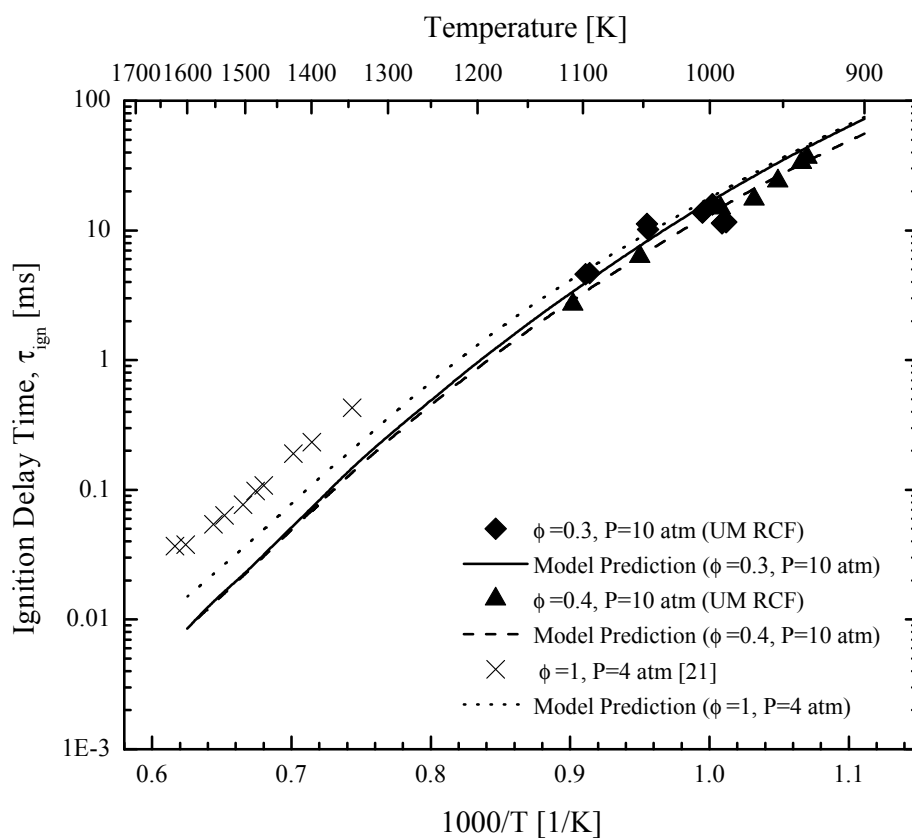
Figure 5.4 Comparison of model predictions with current and previous experimental data for methyl butanoate ignition. The solid (——) line is the model prediction for the ϕ=0.3, low temperature conditions of this study. The dashed (- - -) line is the model prediction for the ϕ=0.4, low temperature conditions of this study. The dotted ($\cdot \cdot \cdot$) line is the model prediction for the high temperature, stoichiometric conditions of Metcalfe *et al.* (21).

Computed results for ethyl propanoate are shown as the solid and dashed lines in Fig. 5.5, calculated for $\phi = 0.4$ and 0.3, respectively, and at 10 atm pressure. The UM RCF results for both $\phi = 0.3$ and 0.4 are also shown. The two curves show the expected changes in ignition delay time as the equivalence ratio is changed from 0.4 to 0.3 at fixed pressure. Some of the experimental results agree very well with the modeling results, while others are slower than the calculated values by a factor of about 2. The Metcalfe *et al.* (21) high-temperature shock tube results are shown

in Fig. 5.5, describing experiments at $\phi = 0.25$ and 0.5, both at 4 atm pressure. Modeling results for the Metcalfe *et al.* mixtures at $\phi = 0.5$ are shown as the dotted curve in Fig. 5.5.
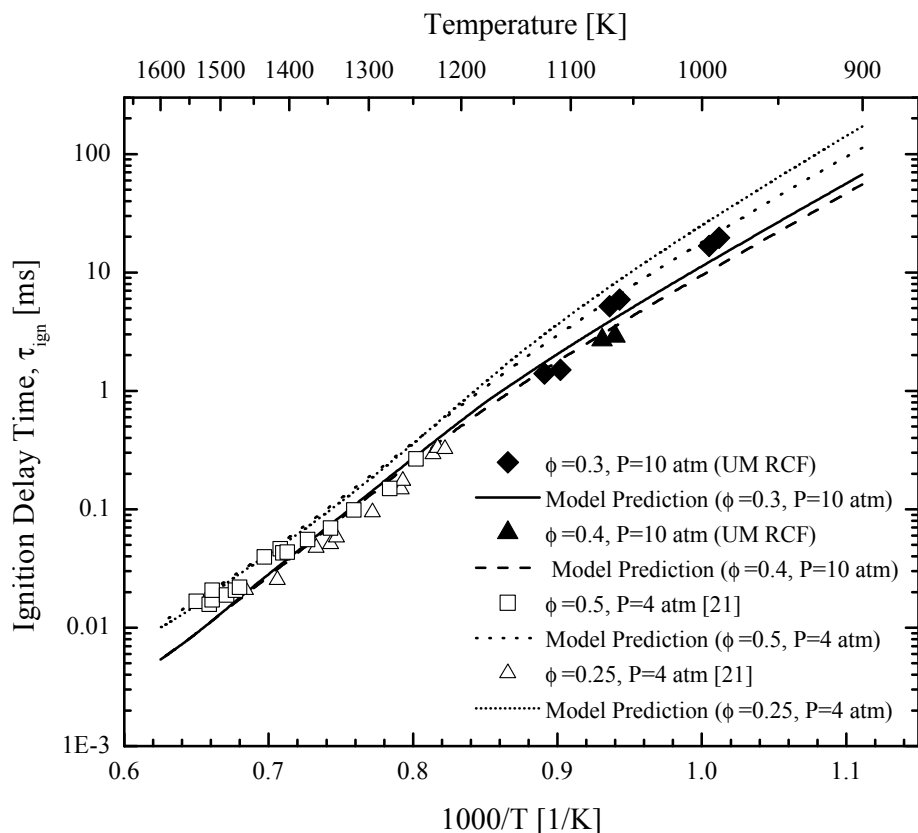
Figure 5.5 Comparison of model predictions with current and previous experimental data for ethyl propanoate ignition. The solid (——) line is the model prediction for the $\phi=0.3$, low temperature conditions of this study. The dashed (- - -) line is the model prediction for the $\phi=0.4$, low temperature conditions of this study. The dotted ($\cdot \cdot \cdot$) line is the model prediction for the $\phi=0.5$, high temperature conditions of Metcalfe *et al.* (21). The short dotted ($\cdots$) line is the model prediction for the $\phi=0.25$, high temperature conditions of Metcalfe *et al.* (21).

The results for methyl butanoate and ethyl propanoate both show the same curvature in the computed ignition delay curves between 1100 K and 1200 K, producing a somewhat lower effective activation energy at lower temperatures. The modeling calculations show that this effect is due to the emergence of H atom abstraction

reactions from these fuels by HO_2 and CH_3O_2 radicals as temperature decreases, which produce H_2O_2 and CH_3O_2H respectively. At these temperatures, these products rapidly decompose to yield OH + OH and CH_3O + OH, providing chain branching and a more rapid ignition. However, none of the reaction temperatures are low enough to determine whether or not alkylperoxy radical isomerization reaction and a negative temperature coefficient (NTC) region should be expected for these fuels. Based on the length of the hydrocarbon chains in both molecules, such NTC behavior is quite unlikely, in agreement with comments by Gaïl *et al.* (19). The computations agree with the experimental results that methyl butanoate is slower to ignite than the other fuels and that part of the difference is related to the fact that the six-centered molecular elimination reaction of methyl butanoate is slower and leads to less reactive intermediate species than the corresponding reactions in ethyl propanoate.

We have used the kinetic modeling results to connect the high temperature ignition results of Metcalfe *et al.* (21) and the present intermediate temperature ignition experiments into a single, internally consistent family of ignition results, which assists in the extraction of analytical results from the experiments. For example, use of the experimental RCF results alone for ethyl propanoate would suggest an effective activation energy of 45.6 kcal/mol, although the slope of the curve in Fig. 5.5 shows that this value should be closer to 31 kcal/mol. Alternatively, extrapolation of the high-temperature activation energy for methyl butanoate to low temperatures would lead to a significant error.

5.4   Summary and Conclusions

This work presents the first rapid compression facility data on low temperature ignition of methyl butanoate and ethyl propanoate. The UM RCF data indicate a lower activation energy for methyl butanoate over the temperature range (T=935-1109

K) considered here, when compared to the higher temperature ignition data in the existing literature. Ethyl propanoate exhibited faster ignition delay times compared to methyl butanoate for the ϕ=0.3-0.4 conditions studied. The results support the supposition that methyl butanoate consumption is dominated by relatively slow bi-molecular H-atom abstraction reactions, whereas ethyl propanoate consumption is dominated by faster unimolecular decomposition. Ester molecular structure is not only important for identifying and quantifying ignition properties; Schwartz *et al.* (22) have suggested that the formation of an intermediate ring structure can lead to the formation of aromatics and soot through the formation of highly reactive alkenes, such as propene and the subsequent formation of propargyl radicals. The majority of biodiesels are comprised primarily of methyl and ethyl esters. The actual chemical composition is a function of plant feedstock as well as processing method, fuel age, etc. Understanding the differences in decomposition pathways for esters of different structure is necessary to develop predictive rules for how different biodiesels will react. The present work is part of a longer-term effort to understand the chemistry and combustion properties of biofuels in general. This study presents ignition behavior of key reference compounds that exhibit features we expect will remain important for real biofuels. Further studies of ester intermediates can help clarify and quantify these important reaction sequences.

Chapter 6

Detailed Investigation of Methyl Butanoate Ignition: High Speed Intermediate Gas Sampling

Ignition studies that yield quantitative data on the intermediate species provide new and more rigorous benchmarks to determine the reaction pathways important during the combustion of esters. This chapter presents the method utilized and the results of the high speed gas sampling of intermediate species during the auto-ignition of methyl butanoate. Methyl butanoate was originally chosen as an oxygenated reference fuel for several reasons. Methyl butanoate has an ester structure that is common to real biodiesels derived from plant oils. This structure is an essential building block of the larger real fuels, therefore thorough understanding of the oxidation chemistry of this simpler structure will provide insight into the actual pathways of larger esters. This has been recognized by several research efforts, and an oxidation model has been proposed (16). Modifications to this model have been discussed in Chapter 5. The previous methyl butanoate ignition studies and the revised model have been used to design these experiments to maximize the impact of this study, ensuring the validity of the necessary experimental assumptions in the UM RCF.

6.1 Sampling Method Overview

After a general understanding of the ignition behavior of C_5 esters was gained, ethyl butanoate was chosen for sampling experiments due to the characteristic chemical structure methyl butanoate represents. Detailed chemical kinetic mechanisms were also available for comparison (16; 21). Detailed understanding of the reaction pathways of methyl butanoate and the intermediates species will improve our understanding of the reaction pathways that are important during combustion of this key compound. Such improved knowledge will help develop more robust representations of the methyl butanoate chemistry and with developing mechanisms of biofuels and other esters.

High speed gas sampling of stable intermediate species was the diagnostic method chosen for this study. This diagnostic tool allows for the qualitative and quantitative determination of intermediate species concentration time-histories during each UM RCF experiment. The determination of these intermediate species concentrations gives insight into possible reaction pathways active during intermediate pressure and temperature conditions. The species time-histories can also enable refinement of reaction rates for improved quantitative agreement of the chemical kinetic model with experimental data.

For the experiments, a new high speed intermediate gas sampling system was developed. The system allows higher pressure experiments (up to ≈ 10 atm), which is valuable for understanding pressure effects. Mixture conditions were chosen to provide conditions optimized for gas sampling. The key features include ignition delay times long enough for many discrete sampling events in roughly 2 millisecond increments, uniform ignition (confirmed through high speed imaging), low initial fuel concentration ($\chi_{fuel} = 0.97\%$), low water concentrations during the sampling times to minimize condensation ($\chi_{h2o} \approx 10,000$ ppm at 95% of the ignition delay time), and lastly good experimental repeatability (less than 0.24% standard deviation in P_{max} at the end of compression). According to these criteria, a lean mixture with a

level of dilution comparable to air was selected. Many experiments were conducted to evaluate the repeatability of the chosen mixture in combination with the necessary UM RCF components (short extension section, stainless steel thermocouple section, side view imaging window, and short nosecone). The target mixture and experimental conditions were: ϕ=0.30, P_{eff}=10.2 atm, T_{eff}=985 K, Inert/O_2=3.76.

Typical pressure and pressure derivative data for the methyl butanoate sampling experiments experiments are shown in Fig. 6.1. The initial pressure rise in each experiment is due to compression of the test gas mixture ahead of the sabot. At the end of compression, the pressure reaches the first maximum. This time is set as t = 0 sec and is labeled P_{max} in the figures. The pressure then decreases slightly due to cooling losses to the test volume walls. After a delay period, the mixture auto-ignites resulting in a rapid increase in pressure for all cases. Unlike the previous UM RCF ignition studies of methyl butanoate; a sample of the core gas is extracted to a vacuum chamber using the high speed gas sampling system during the ignition delay period. After each experiment the sample from the sampling tank was extracted using a sealed and locking gas chromatography syringe. The sample was then analyzed using the five gas chromatography methods described below. The gas sampling system is described in detail in Section 6. The pressure time-history of the sampling tank is also shown in Fig. 6.1.

Side view images corresponding to the experiment of Fig. 6.1 are shown in Fig. 6.2. The side view imaging window allows optical access not previously available during sampling experiments. The images confirm homogeneous ignition inside the test volume for each of the sampling experiments conducted. Note the location of the sampling tubes in the right side of the images in Fig. 6.2. The sampling tubes extend into the homogeneously reacting "core" region. This allows direct comparison of the sampling experiments to the homogeneous CHEMKIN reactor model predictions described below.
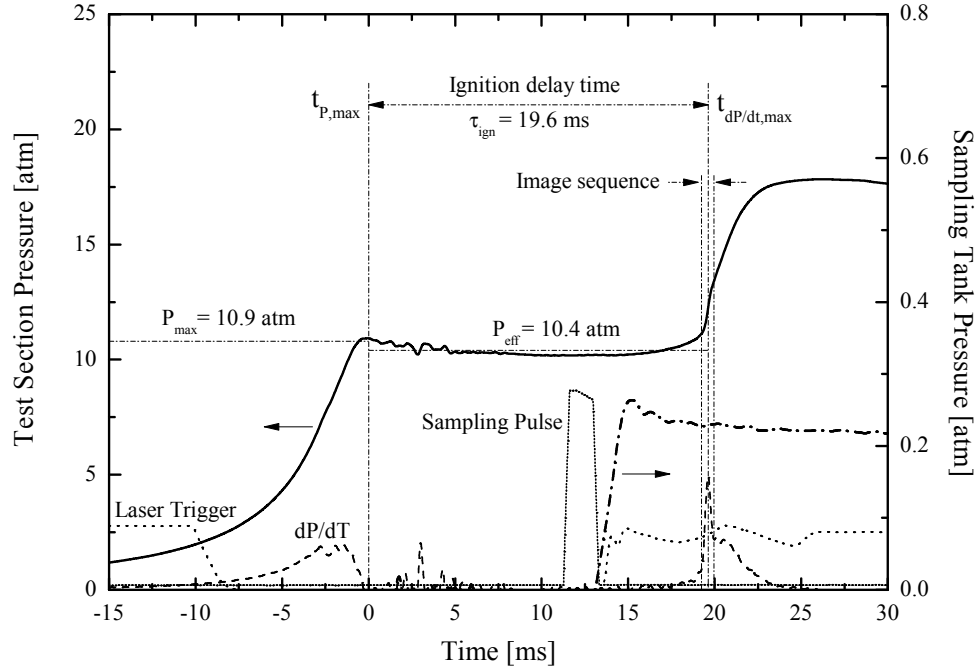
Figure 6.1 Typical test section pressure (——), test section pressure derivative (- - -), and sampling tank pressure (– · –) time-histories for methyl butanoate ignition experiments conducted using the gas sampling system. Also shown in this figure are the sabot/laser trigger signal, and the sampling/camera trigger from the pulse generator. Experimental conditions were: P_{eff}=10.4 atm, T_{eff}=985 K, ϕ=0.30, Inert/O_2=3.76.
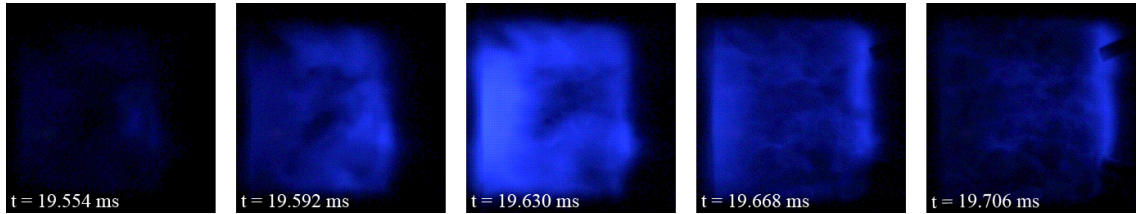
Figure 6.2 Imaging sequence corresponding to the data and time interval of Fig. 6.1, and conditions of P_{eff}=10.4 atm, T_{eff}=985 K, ϕ=0.30, Inert/O_2=3.76, τ_{ign}=19.6 ms, 26,000 fps (color adjusted for clarity). The time interval spanned for these frames is shown in Fig. 6.1.

The effective test conditions were determined using the pressure time-history from each experiment. The effective pressure (P_{eff}) was defined as the time-integrated average pressure from the maximum pressure (P_{max}) at the end of compression to the

point of maximum rate of pressure rise (dP/dt_{max}), or

$$P_{eff} = \frac{1}{(t_{dP/dt_{max}} - t_{P_{max}})} \int_{t_{P_{max}}}^{t_{dP/dt_{max}}} P \cdot dt \,. \tag{6.1}$$

The effective temperature for each experiment was determined, as in previous UM RCF studies (25; 26; 27; 28; 29), using the effective pressure and by numerical integration of the isentropic relation

$$\int_{T_o}^{T_{eff}} \frac{\gamma}{\gamma - 1} \, d \ln(T) = \ln\left(\frac{P_{eff}}{P_o}\right), \tag{6.2}$$

where P_o is the initial charge pressure, T_o is the initial temperature (typically 298 K), and γ is the temperature-dependent ratio of the specific heats of the unreacted test gas mixture, which is determined using the NASA thermodynamic data base (33) and from the thermodynamic data for methyl butanoate from Fisher *et al.* (16).

For each experiment, the ignition delay time (τ_{ign}) was determined using the pressure time-history, and defined as the time between P_{max} and dP/dt_{max}. This definition for τ_{ign} is illustrated in Fig. 6.1, and was developed in previous UM RCF ignition studies, where it was determined to be very robust when different ignition regimes were present (28; 29). For comparison with the sampling results, the time domain for all data are normalized by the ignition delay time. Where t=0 is defined as the end of compression (P_{max}), and t=1 is defined as the time of ignition, which remains the time where the maximum of dP/dt_{max} occurs.

6.2 High-Speed Gas Sampling System

The high speed gas sampling system was custom designed to work specifically with the UM RCF and the experimental diagnostics already present on the RCF. The gas sampling system was designed to utilize as many commercially available parts, while

meeting the many design constraints. The sampling system was targeted to operate at effective pressures up to 10 atm, while minimizing the sampling concentration uncertainties (due to dead volume and leak rates in the sampling valves) and the sampling time uncertainties (due to the response times of the sampling valves).

The first components chosen for integration into the new high speed gas sampling system were the valves. Festo MHE3 valves were chosen primarily because of their fast stock response time (3 ms) given a large (3 mm) nominal orifice. The Festo valves used are small linear solenoid driven poppet valves designed to be normally closed. The valves use rubber o-rings to seal against steel faces. An exploded photograph of the valve is found in Fig. A.8 of App. A. The factory response time is reported as the time it takes for the downstream pressure to go from 10% to 90% of the total downstream pressure delta. The Festo MHE3 valves are advertised with a maximum operating pressure of 4 atm, and are designed to have a 100% duty cycle at 24 volts and 1 amp. The primary constraint on the duty factor is thermal management of the heat from the solenoid.

For the sampling system to operate at the targeted pressure condition of 10 atm, several modifications had to be made to the Festo solenoid valves. First, in order to complete the closing of the valve against the higher pressure flow from the UM RCF test section into the sampling chamber, a stronger return spring had to be exchanged for the factory original spring. Several springs were tested with various amounts of preload. Eventually, the strongest readily available spring that could fit inside the armature was chosen (Century Spring part no. II-96). This spring was also preloaded as much as possible while still allowing the full travel of the armature using three size 000 brass washers. The stronger force of the return spring was also chosen to increase the closing response time of the valve. During this rebuild process, and periodically thereafter, all of the rubber o-rings and faces were cleaned and lubricated with silicone vacuum grease. This is necessary to ensure that the seals will be adequate under the

vacuum conditions present in the UM RCF.

After reassembly the Festo valves require much more force to actuate. This is a result of the much stronger return spring used to close the valve and the additional friction due to the vacuum grease. To overcome this force the solenoid valves need to be driven with much more power than their duty cycle rating. The primary limitation of the solenoids, the thermal management of the coil, should not be an issue because the valves are fired at most (during testing) in 30 second intervals. The secondary limitation is the arcing of the the solenoid coils as a result of an excessive driving potential. The limit was found to be around 75 volts to ensure a few hundred operations of the solenoid. The solenoids can draw significantly more than 1 amp at this voltage, therefore a new fast switching power supply was necessary to power the cluster of 4 valves that is used in the sampling system.

To satisfy the requirements of high power and high speed, a new power supply was developed to work with the existing triggering capabilities. A group of three 1000 μF capacitors was charged using an external high voltage power supply, and discharged using two parallel high power MOSFETs (NTE3207), as shown in Fig. A.10 of App. A. The MOSFETs were triggered using an output from the pulse generator (Stanford Research Systems DG535) shown in Fig. A.6 of App. A.

Once the valves were selected a new end wall was developed to integrate 4 valves into the UM RCF with minimum sampling dead volume. The valves can be attached using the threaded, or push-lock connections available on the valve body adapters for connecting them to stock tubing. If this method is used, the valves stand off distance from the sampling end wall is approximately 10 mm as shown in Fig. A.7(a) of App. A. This end wall attachment method results in a large dead volume in the sampling tube, end wall, fitting, and valve body adapter. If the valve body adapter is removed, and a new end wall is custom machined to seal against the valve body itself, the dead volume can be reduced to just the volume in the sampling tube and the end wall, as

shown in Fig. A.7(b). However, this attachment method requires careful alignment of additional components to create a seal between the end wall and the o-ring present in the valve body. A photograph showing the completed sampling manifold, including sample tank, pressure transducer, GC septum, and quarter turn vacuum isolation valve is shown in Fig. 3.3.

The procedure used for high pressure gas sampling system in the UM RCF is as follows. Prior to conducting an experiment, the pressure transducer amplifier is connected and powered. The sampling tank is then evacuated along with the remainder of the UM RCF. The number of valves to be used (one to four), the sampling duration, and the sampling delay need to be determined prior to the experiment. The sampling delay time is the time between the triggering of the pulse generator (Stanford Research Systems DG535) by the sabot breaking the laser diode beam, and the triggering of the sampling valves. This delay time is changed in order to sample at a different time during each experiment. A post trigger delay time was also programmed into the pulse delay generator to keep it occupied for around 90 seconds after the initial trigger input. This prevents any subsequent triggering of the sampling valves as the sabot oscillates in the driven section a few times after the nosecone is seated.

Once the gas sampling parameters are determined, the system is ready to be charged and armed. The power supply system is charged using a high voltage, low current power supply (Kepco APH2000M). It takes ~45 seconds to initially charge the capacitor bank which consists of three 1000 μF electrolytic capacitors. The capacitors are charged to ~75 volts, and upon triggering are discharged through two parallel high power MOSFETS (NTE2307). A schematic of the custom power supply circuit is shown in Appendix A. After the capacitors are charged, the system is armed by switching the toggle switch to the ON position, this allows the signal from the pulse generator to reach the MOSFETS, which in turn discharges the capacitors through the solenoid coils in the high speed poppet valves. The system is armed immediately

before the experiment is conducted, after the system has been charged, after the pulse generator is ready, and after the laser diode trigger on the driven section is ready. This prevents accidental triggering (an occasional result of electrical noise).

After arming the sampling system, the experiment can be conducted. Immediately prior to running the experiment, the sampling tank must be isolated from the vacuum pump. This is done at the same time the other valves are closed when arming the UM RCF. Immediately after the experiment, the capacitor power supply is switched OFF, and the test manifold is vented to prevent any small leak across the high speed poppet valves from contaminating the sample. After this is done, the sample may be drawn into the syringe (Vici, Pressure-Lok, 5 mL) through the syringe port, to be taken to the gas chromatographs for analysis.

Several experiments were conducted to characterize the behavior of the high-speed gas sampling system. The first tests were to examine the response time of the modified valves, to determine how long the pulse width should be. The pulse width needs to be long enough to completely energize the solenoid to open the valves, but short enough to avoid excess sample from being drawn from the test section which would quench the test volume. It was found that a minimum pulse width of 1.7 ms from the pulse generator was necessary to reliably activate the sampling valves. This results in sample gas being extracted from the test section over a duration of $\sim$1.3-1.4 ms. The definition of the sampling duration is shown in Fig. 6.3. First, two reference values were determined based on the sampling tank pressure time-history. One reference value is determined from the early portion of the sampling tank pressure prior to sampling (P=0 atm, t=-15 to 14 ms in Fig. 6.3), and another reference value is determined from the sampling tank pressure after sampling (post sampling chamber pressure, t=14 to 25 ms in Fig. 6.3). These lines are fit in order to eliminate complications from mechanical noise resulting from the seating of the nosecone in the convergent section of the UM RCF. Another line is fit to the pressure rise that occurs during
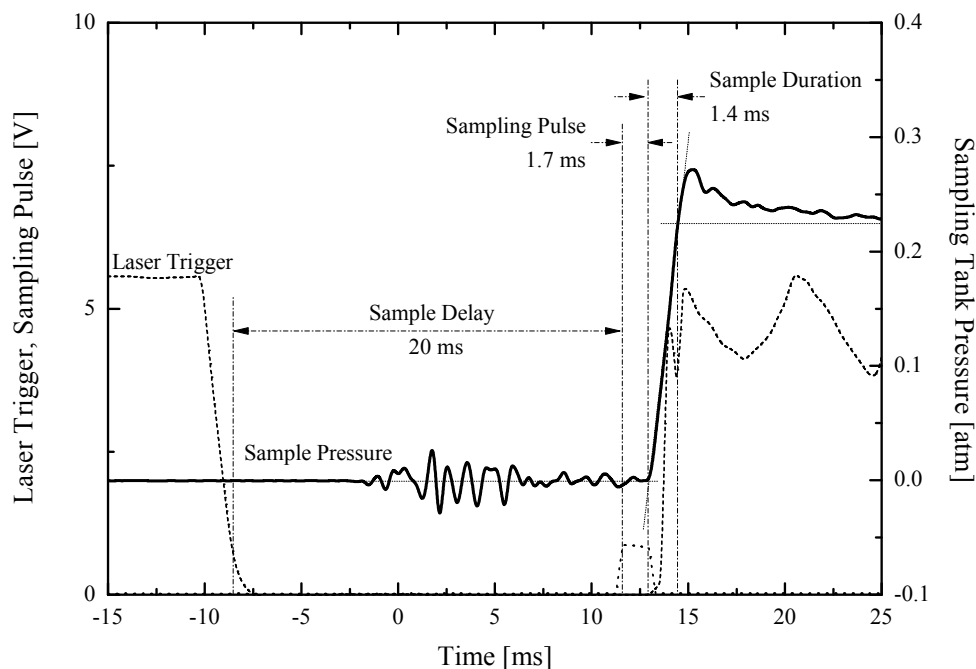
Figure 6.3 Typical sampling tank pressure time-history (——) for methyl butanoate ignition experiments. This example corresponds to the data of Figs. 6.1 and 6.2, with experimental conditions of P_{eff}=10.4 atm, T_{eff}=985 K, ϕ=0.30, Inert/O_2=3.76. This figure highlights the trigger timing used for the gas sampling experiments. The laser trigger decreases to 0 when the sabot blocks the laser, which triggers the pulse generator. The pulse generator has a programmable sample delay time (20 ms in this example), followed by a TTL pulse of 1.7 ms to the valve power supply, resulting in a sampling duration of approximately 1.4 ms.

gas sampling. The time where the fit to pressure rise intersects the average baseline pressure is defined as the sample start time, $t_{s,1}$. The time where the pressure rise fit intersects the average post-sample chamber pressure is defined as the sample end time, $t_{s,2}$. The total sampling time is defined as the average of these two times:

$$t_s = \frac{t_{s,1} + t_{s,2}}{2}. \tag{6.3}$$

During the characterization process, it was found that only one valve was necessary to obtain enough sample to have high signal to noise values on the gas chromatograms.

Using one valve results in a sample pressure of approximately 1/4 atmosphere after the sampling event duration of ∼1.3 ms. Using only one valve reduces the uncertainty from the dead volume of the extra sampling tubes, while maintaining a pressure gradient between the sample tank and ambient which is sufficiently small to minimize dilution of the sample by room air.

6.3   Gas Chromatography

6.3.1   Calibration Species Selection

Chemical modeling was used to initially identify species that could be present during methyl butanoate ignition experiments. The model predictions were used to direct calibration of the gas chromatographs. The first step was to generate plots of species time-histories that were binned according to their maximum concentration during the ignition delay time. This was accomplished through a semi-automated method: first exporting all species time-histories from CHEMKIN, and then filtering and plotting them using a custom MATLAB script, found in App. B.

The species were binned into 6 groups, those with concentrations above 2000 ppm, between 1000 to 2000 ppm, 100 to 1000 ppm, 10 to 100 ppm, 1 to 10 ppm, and lastly, between 1 ppb and 1 ppm. These binned species time-histories are shown in Figs. 6.4 - 6.9. This first step in organizing species allowed identification of species of higher concentrations, which tend to be easier to identify using gas chromatography. Starting in descending order of concentration, stable species that could be detected using the selected gas chromatography were identified. This list was compared with species available from chemical suppliers which could be handled without the use of a fume hood. These species were further narrowed by their significance in the overall reaction mechanism. The mechanism is too large to perform a sensitivity analysis using desktop computers; thus species important in the formation of pollutant emissions, or those

that are suspected to be part of competing reaction pathways or in pathways of high levels of uncertainty were prioritized. The final list of species to be investigated using the gas chromatographs, with some additional properties and safety information is shown in Tables 6.1 - 6.3.
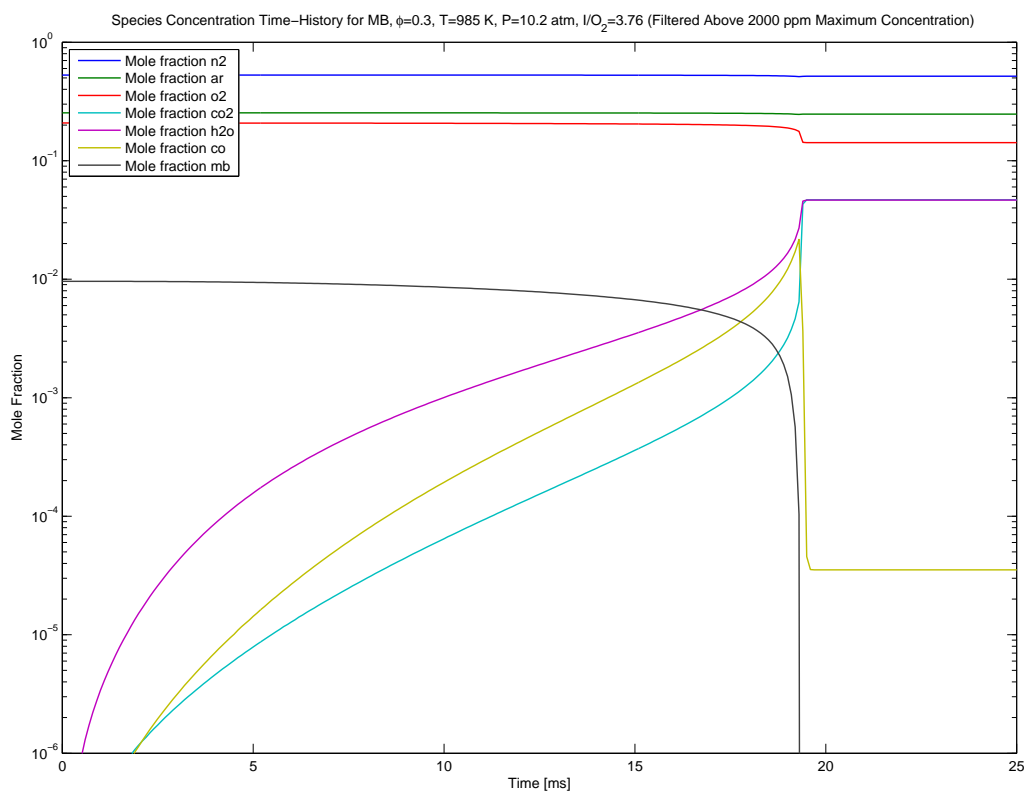
Figure 6.4 Model predictions for concentration time-histories of reactants, products, and intermediate species during the ignition of methyl butanoate at conditions of ϕ=0.30, P_{eff}=10.2 atm, T_{eff}=985 K, Inert/O_2=3.76. This figure contains species binned above a maximum concentration 2000 ppm.

Species Concentration Time–History for MB, ϕ=0.3, T=985 K, P=10.2 atm, I/O$_2$=3.76 (Filtered Between 1000 ppm and 2000 ppm Maximum Concentration)
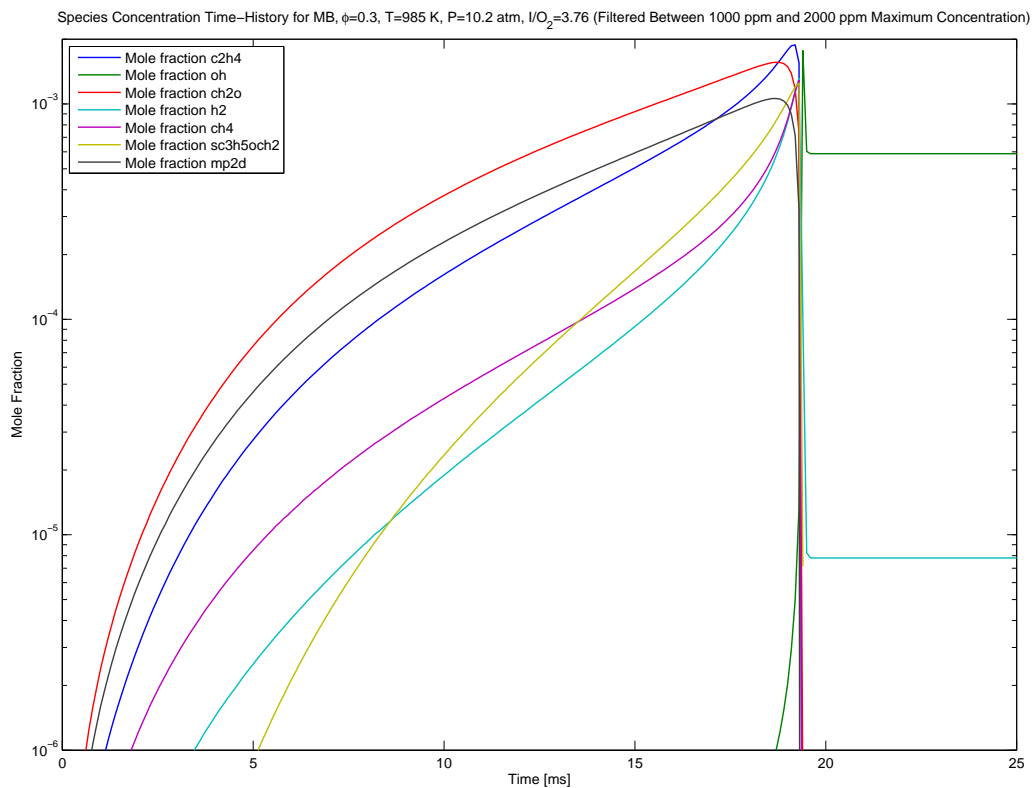
Figure 6.5 Model predictions for concentration time-histories of intermediate species during the ignition of methyl butanoate at conditions of ϕ=0.30, P_{eff}=10.2 atm, T_{eff}=985 K, Inert/O$_2$=3.76. This figure contains species binned between maximum concentrations of 1000 and 2000 ppm.
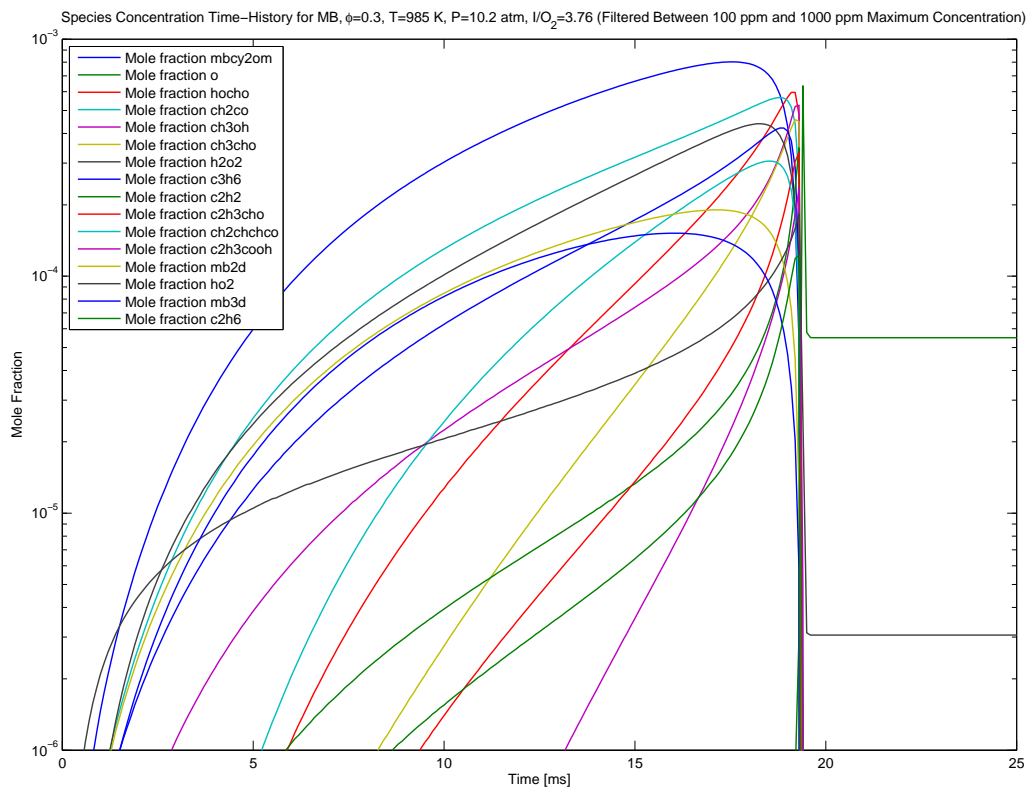
Figure 6.6 Model predictions for concentration time-histories of intermediate species during the ignition of methyl butanoate at conditions of ϕ=0.30, P_{eff}=10.2 atm, T_{eff}=985 K, Inert/O_2=3.76. This figure contains species binned between maximum concentrations of 100 and 1000 ppm.
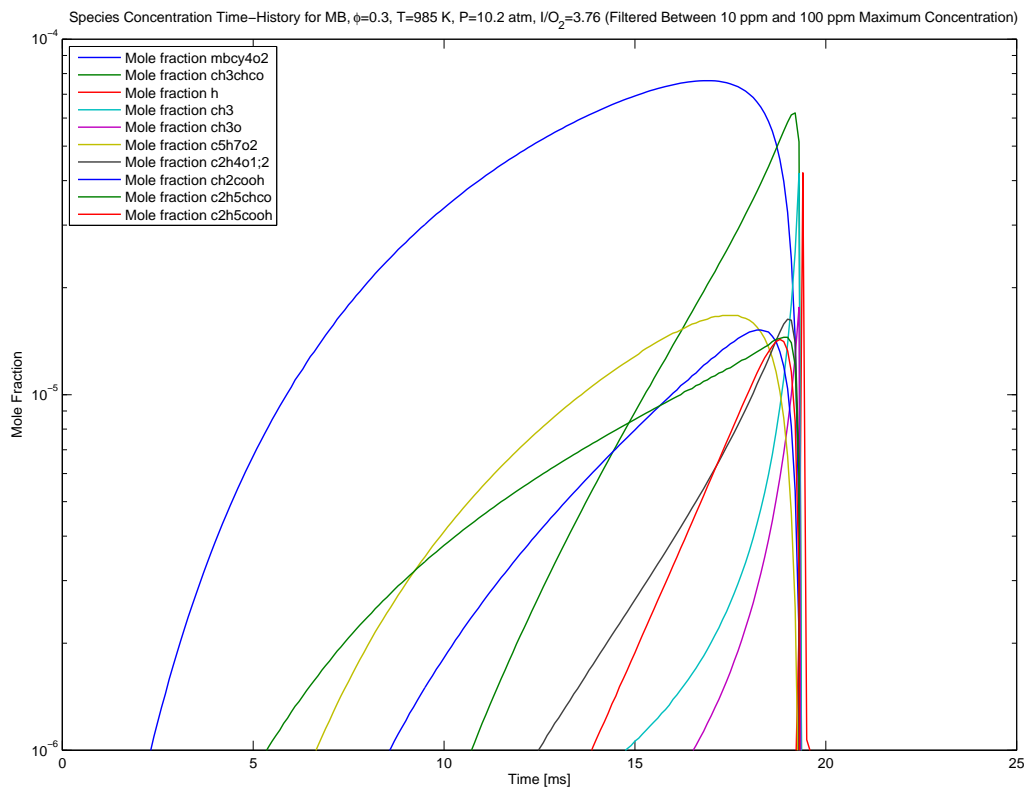
Figure 6.7 Model predictions for concentration time-histories of intermediate species during the ignition of methyl butanoate at conditions of $\phi=0.30$, $P_{eff}=10.2$ atm, $T_{eff}=985$ K, Inert/O_2=3.76. This figure contains species binned between maximum concentrations of 10 and 100 ppm.

Species Concentration Time–History for MB, φ=0.3, T=985 K, P=10.2 atm, I/O₂=3.76 (Filtered Between 1 ppm and 10 ppm Maximum Concentration)
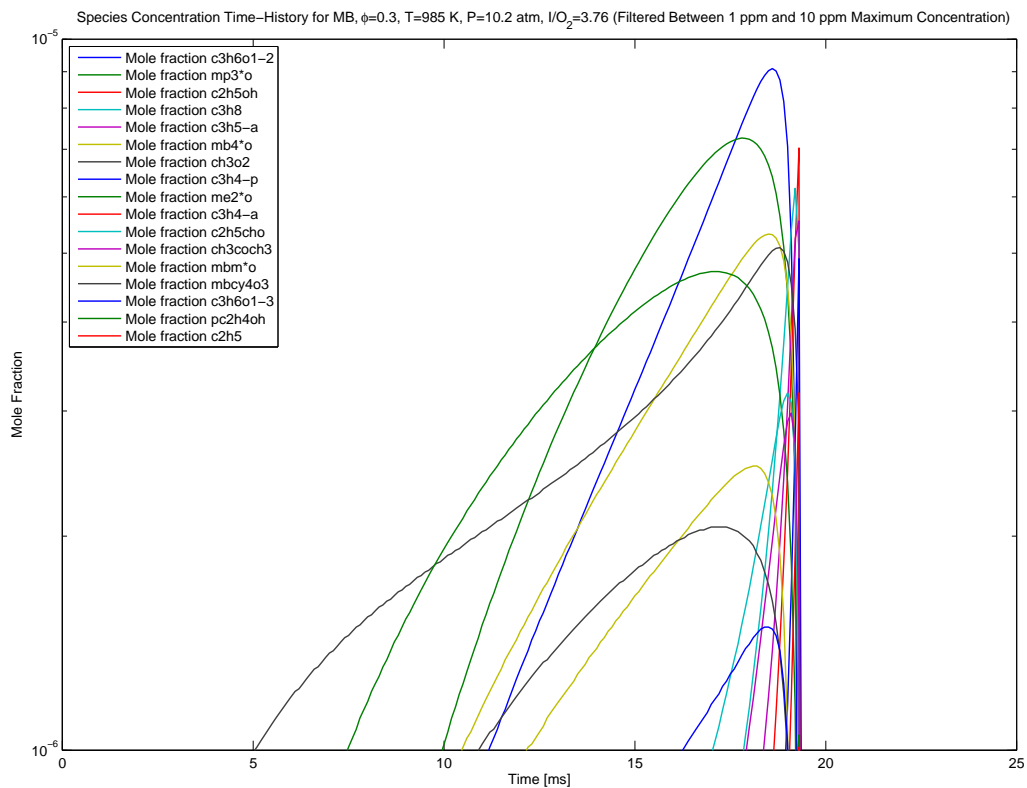
Figure 6.8 Model predictions for concentration time-histories of intermediate species during the ignition of methyl butanoate at conditions of ϕ=0.30, P_{eff}=10.2 atm, T_{eff}=985 K, Inert/O_2=3.76. This figure contains species binned between maximum concentrations of 1 and 10 ppm.
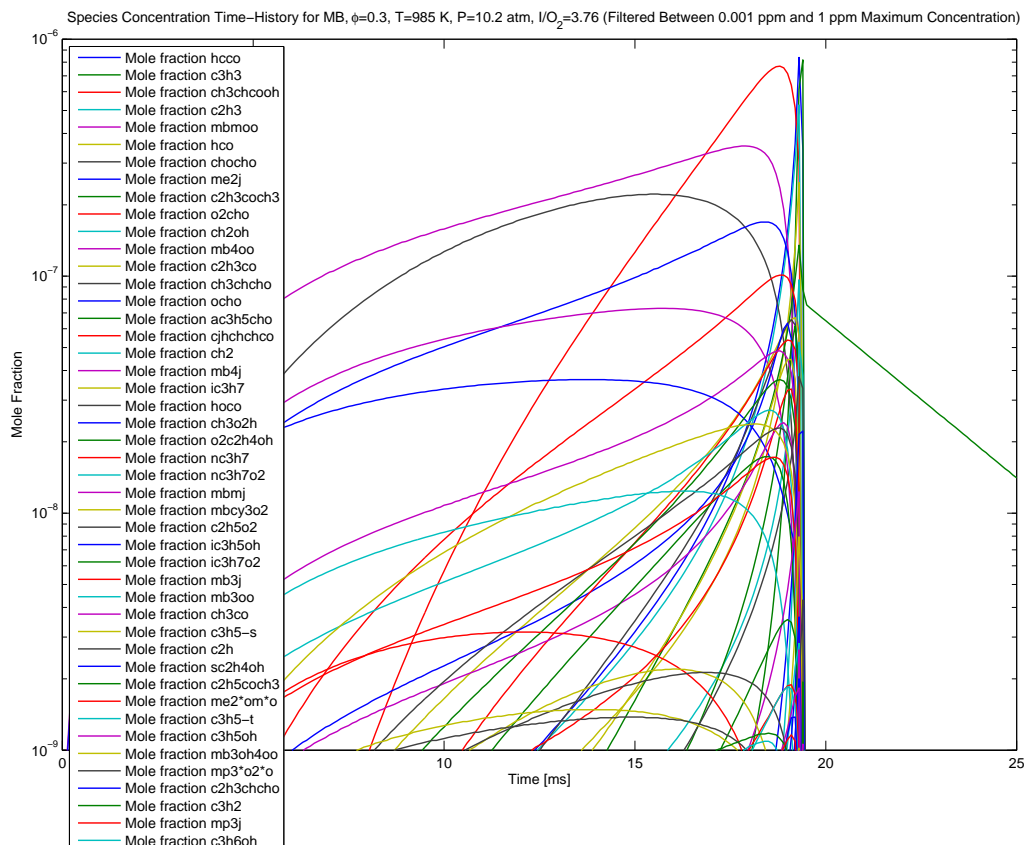
Figure 6.9 Model predictions for concentration time-histories of intermediate species during the ignition of methyl butanoate at conditions of ϕ=0.30, P_{eff}=10.2 atm, T_{eff}=985 K, Inert/O_2=3.76. This figure contains species binned between maximum concentrations of 1 ppb and 1 ppm.

Table 6.1 Summary of compounds (all from Sigma-Aldrich) used for calibration of the gas chromatographs.

Mechanism Notation	CAS Number	Sigma-Aldrich Name	Purity [%]	Primary Contaminants	Bottle Size	Hazard Codes[a]
mb	623-42-7	Methyl butyrate	99.8	-	5 mL	F, Xn
mb2d	623-43-8	Methyl crotonate	98	Methyl iso-crotonate	500 mL	F, Xi
mb3d	3724-55-8	Methyl 3-butenoate	95	-	1 g	F
mp2d	96-33-3	Methyl acrylate	99.5	-	5 mL	F, Xn
c2h5cooh	79-09-4	Propionic acid	99.8	-	250 mL	C
ch2o	50-00-0	Formaldehyde solution	37% wt.	H_2O, 10-15% methanol	25 mL	T
hocho	64-18-6	Formic acid	98	CH_2O, acetic acid	50 mL	C
ch3cho	75-07-0	Acetaldehyde	99.5	Free acids	100 mL	F+, Xn
c2h3cho	107-02-8	Acrolein	99	-	10 mL	F, T+, N
ch3oh	67-56-1	Methanol	99.9	-	10 mL	F, T
c2h3cooh	79-10-7	Acrylic acid	99	Water	250 mL	C, N

[a]F=Highly flammable, F+= Extremely flammable, T=Toxic, T+=Very toxic C=Corrosive, Xn=Harmful, Xi=Irritant, N=Harmful to environment

Table 6.2 Summary of species and concentrations in the hydrocarbon gas mixture used for calibration of the gas chromatographs.

Mechanism Notation	CAS Number	Name	Concentration [ppm]
c2h6	74-84-0	Ethane	0.501 %
c2h4	74-85-1	Ethylene, Ethene	1.001 %
c3h8	74-98-6	Propane	510
c3h6	115-07-1	Propylene, Propene	499
c3h4-p	74-99-7	Methyl acetylene, Propyne	1482
c3h4-a	463-49-0	Allene, 1,2-Propadiene	495
-	106-97-8	n-Butane	498
1-c4h8	106-98-9	1-Butene	491
-	107-00-6	Ethyl Acetylene	483
xc4h6	106-99-0	1,3-Butadiene	496
xc5h10	109-67-1	1-Pentene	497
-	109-66-0	n-Pentane	497
-	7440-59-7	Helium	Balance

6.3.2   Gas Chromatography Methods

The gas chromatography methods were tailored to minimize the uncertainties in the species measurements and maximize the number of species that could be accurately measured using the ovens, detectors, and columns available. The entire gas chromatography system consists of four Perkin Elmer ovens, each with manual flow control, and with automatic pneumatic valve actuation for all but one oven. The carrier gases are

Table 6.3 Summary of concentrations in the $CO/CH_4/CO_2$ gas mixture used for calibration of the gas chromatographs.

Mechanism Notation	CAS Number	Name	Concentration [%]
co	630-08-0	Carbon monoxide	0.1910 %
ch4	74-82-8	Methane	0.1940 %
co2	124-38-9	Carbon dioxide	1.956 %
n2	7727-37-9	Nitrogen	Balance

pre-purified and filtered helium or argon. The carrier gases are filtered to remove water vapor, oxygen, and hydrocarbons. Two types of detectors are available for detection of the intermediate species, thermal conductivity detectors and flame ionization detectors. The thermal conductivity detector (TCD) is a non-destructive detector used here for the quantification of stable gases such as Ar, N_2, O_2, and CO_2. The flame ionization detector (FID) is used for the quantification of the intermediate organic species. The detector temperatures are always at least 50° C above the column temperature to prevent condensation of intermediates within the detector.

The first oven contains a TCD detector and two separate capillary columns for the analysis of permanent gases. The columns utilize helium as the carrier gas, and the first column (Varian Porobond Q FS) is used as a filter for the second column (Varian CP Molsieve FA FS), to ensure that polar species are not allowed to enter the second column (which would damage the second column). The non-polar species travel through the first column faster, allowing a valve event between the elution of the non-polar and polar species. The non-polar species pass into the second column before the valve is switched. The second column then separates the stable gases, such as Ar, O_2, N_2, and CH_4, while the polar compounds, like CO_2 elute directly from the first column to the TCD detector. This method utilizes a constant temperature analysis time, followed by a brief increase in temperature to clean the column for the next sample. A summary of the hardware configurations for the gas chromatography is found Table 6.4. A summary of the analysis methods, including oven temperatures,

carrier gas flowrates, and programmed events can be found in Table 6.5. Diagrams of the sampling valve configurations can be found in He (24).

The second oven contains an FID detector with one capillary column (Varian CP PLOT LowOx FS) using helium as the carrier gas for the analysis of oxygenates. This column has a relatively unstable stationary phase. To avoid erroneous peaks resulting from the elution of the stationary phase, a particulate filter (Varian CP 4017) was placed downstream of the capillary column directly before the FID detector. This oven uses a ramped temperature program to optimize peak separation with reasonable elution times. The column is then cleaned with a short high temperature pulse.

The third oven contains an FID detector and one capillary column (Varian CP Al_2O_3/Na_2SO_4 FS) using helium as the carrier gas for the analysis of light hydrocarbons. This oven also follows a ramped temperature program followed by a high temperature pulse to clean the column.

The fourth oven contains one FID detector and one TCD detector. The FID detector is connected to a single capillary column (Restek RTX-1 FS) and uses helium as the carrier gas for the analysis of oxygenates and large hydrocarbons. The TCD detector is also connected to a single column (Restek Shin-Carbon ST) and uses argon as the carrier gas for the analysis of other stable species, such as H_2, O_2, and N_2. The oven uses a constant temperature analysis method, followed by a high temperature pulse to clean the columns.

Table 6.4 Summary of the GC equipment and the maximum column temperatures.

Oven	Column	Col. Dimensions	T_{max}	$T_{16hrs.}$
GC1-	Varian CP Molsieve 5A FS	25m x 0.53mm i.d.	350°C	350°C
P.E. Autosystem GC	Varian Porobond Q FS	25m x 0.53mm i.d.	320°C	250°C
GC2-	Varian CP PLOT LowOx FS	10m x 0.53mm i.d.	350°C	300°C
P.E. Autosystem GC				
GC3-	Varian CP Al_2O_3/Na_2SO_4 FS	50m x 0.53mm i.d.	200°C	200°C
P.E. Autosystem GC				
GC4-	Restek RTX-1 FS (A)	60m x 0.32mm i.d.	320°C	150°C
P.E. Clarus 500GC	Restek Shin-Carbon ST (B)	5m x 0.75mm i.d.	330°C	150°C

Table 6.5 Summary of the GC analysis programs. All programs contain 54 minutes of analysis, followed by 6 minutes of increasing temperature to purge the column. GC's with TCD's have isothermal analysis programs. The valves are all started in the sampling position (ON). The flowrates for the FID flames are 45 ml/min H_2 and 450 ml/min air.

Detector (Method 5)	Temperature Program, 1hr	Events	Carrier Gas/ Setting	Detector/ Temp.	Range/ Atten.
GC1	30°C (55 min) → 10°C/min → 100°C	0.01 GSV1 OFF 1.83 GSV1 ON	Helium 26.0 cm/sec	TCD 150°C	3 4
GC2	80°C (10 min) → 10°C/min → 150°C (33 min) → 10°C/min → 310°C	0.03 GSV1 OFF	Helium 34.0 cm/sec	FID 150°C	1 1
GC3	40°C (10 min) → 10°C/min → 140°C (34 min) → 10°C/min → 200°C	0.03 GSV1 OFF	Helium 36.0 cm/sec	FID 150°C	1 1
GC4A	40°C (54 min) → 10°C/min → 100°C	0.01 GSV3 ON 0.10 GSV1 ON	Helium 20.0 cm/sec	FID 150°C	1 1
GC4B	40°C (54 min) → 10°C/min → 100°C	0.01 GSV3 ON 0.10 GSV1 ON	Argon 15.0 ml/min	TCD 200°C	+40 mA 1

The columns must be conditioned periodically to maximize the quality of the chromatograms. The conditioning process heats the columns above their analysis temperatures to remove water and heavy components trapped in the columns that otherwise decrease the separation and detectability of compounds of interest. Each column has specific temperature limits depending on the type of condensed phases present in the column. A summary of these temperature limits, and the oven in which the column is located are found in Table 6.4. Two conditioning programs were found to result in the best system performance. Both programs are summarized in Table 6.6. The standby programs are 8 hour programs that are run overnight to prepare the columns for the analysis the following day. The longer 18 hour programs are used when there is ample time between experiments, such as over the weekends. This longer conditioning program is an additional precaution against column poisoning as a result of water or other contaminants.

6.3.3 Species Calibration

After the initial targeted intermediate species of interest were identified, and after the gas chromatography methods were determined, the gas chromatographs needed to be calibrated. Without a mass spectrometer in conjunction with the analysis, each pure component needs to be calibrated individually, with few exceptions. To do this, pure intermediate species diluted by the carrier gas in known concentrations were introduced into the gas chromatographs to determine the retention times and detector response. The calibration mixtures were prepared using the mixture manifold on the UM RCF.

For both calibration and analysis, the output chromatograms from the four ovens were recorded using a custom LabVIEW interface. For this purpose several LabVIEW interfaces were written. The primary code was written to record the chromatograms (millivolts vs. seconds) from the detector ouput. Another code was written to preview

Table 6.6 Summary of the GC preparation programs. Both sets of preparation programs are run with the 10-port valves in the sampling position. The detector heaters are turned on for the conditioning program and for the standby programs with the same range and attenuation values that are used for analysis. Note that the GC's return to the start of program temperature when the cycle is completed. Also note that the standby programs start and end at the start of program temperatures used for analysis.

Oven	Conditioning (Method 3, 18hr)	Standby (Method 4, 8hr)
GC1	30°C (18 min) → 5°C/min → 320°C (30min) → -5°C/min → 250°C (16hr)	30°C (2min) → 5°C/min → 250°C (2.5hr) → -5°C/min → 30°C (4hr)
GC2	40°C (18 min) → 5°C/min → 350°C (30min) → -5°C/min → 300°C (16hr)	80°C (24 min) → 5°C/min → 300°C (2hr) → -5°C/min → 40°C (4hr)
GC3	40°C (28 min) → 5°C/min → 200°C (17hr)	40°C (26 min) → 5°C/min → 200°C (2.5hr) → -5°C/min → 40°C (4hr)
GC4	40°C (30 min) → 5°C/min → 320°C (3hr) → -5°C/min → 150°C (13hr)	40°C (16 min) → 5°C/min → 150°C (3hr) → -5°C/min → 40°C (4hr)

the detector output, and another was written to view the previously recorded output.

To allow for automatic analysis of the chromatograms, the LabVIEW code has to be synchronized with the gas chromatograph methods. To achieve this, the hardware triggers on each of the GC ovens and the National Instruments Data Acquisition card (PXI 4472) were wired together and attached to a momentary pushbutton switch. When the switched is depressed, the circuit is shorted, and the ovens and data acquisition code begins to run. In order for the data to be easily compatible with Microsoft Excel based software, the chromatograms have to contain less than 32,000 data points.

To meet this requirement given the method duration, and to meet the ≈18 points required per peak for good peak fit, the chosen recording rate was 8 Hz. A screenshot of the LabVIEW user interface and the block diagram is found in Appendices B.3 and B.4.

Once the chromatograms have been acquired, they are imported in the chromatogram analysis software, Clarity®(Data Apex). Clarity is a powerful peak integration software package that can be purchased separately from any gas chromatograph hardware. After the chromatograms from known concentration calibration mixtures are imported into Clarity®, retention times and detector response are saved in calibration files. The chromatograms from the UM RCF sampling experiments are then compared to the calibration files to determine the species and concentrations in unknown mixtures.

6.3.4 Typical Speciation Results for Methyl Butanoate Ignition

Figures 6.10-6.14 are example chromatograms from analysis of actual UM RCF sampling experiments acquired using the gas chromatograph methods. Certain peaks are identified for reference.

The chromatogram from GC 1 shown in Fig. 6.10 show large baseline shifts as a result of flowrate changes occuring during valve actuation. The steady state flowrate of the two sampling valve positions are different and make quantification of species in this column difficult. However, the identification of carbon monoxide and carbon dioxide is possible. Carbon dioxide elutes through the detector after approximately 2.2 minutes, but was not detected during any of the sampling experiments. Additional development of the programming for GC 1 may yield quantitative data for CO; however, no results are included for GC 1 in this study.

Figure 6.11 shows an example chromatogram from GC 2 for the analysis of oxy-

genated species. It can be seen from this chromatogram that light hydrocarbons elute quickly from this column and do not interfere with the oxygenated species. This column demonstrates good peak shapes for the species of interest, but does not separate the species well for good quantification. Many methods were attempted to allow quantitative measurements, however, the convolution of the peaks limited this chromatograph to species identification and qualitative data. An additional complication for the oxygenates is the lack of pure reference compounds for calibration. The effects of impurities in the reference compounds were exacerbated by non-linear FID response.

Figure 6.12 shows an example chromatogram from GC 3 for the analysis of light hydrocarbon species. The selected column and oven method provided excellent peak separation for identification and quantification.

Figure 6.13 shows an example chromatogram from GC 4a, using the FID detector for the analysis of oxygenated species. This column demonstrated high sensitivity to oxygenated species, but was found to have poor repeatability. The method did not yield quantitative results, despite many attempts at different calibration methods. Figure 6.14 shows an example chromatogram from GC 4b, using the TCD detector, and argon carrier gas for the detection of hydrogen. Additional development of the programming for GC 4b may yield quantitative data for H_2; however, no results are included for GC 4 in this study.
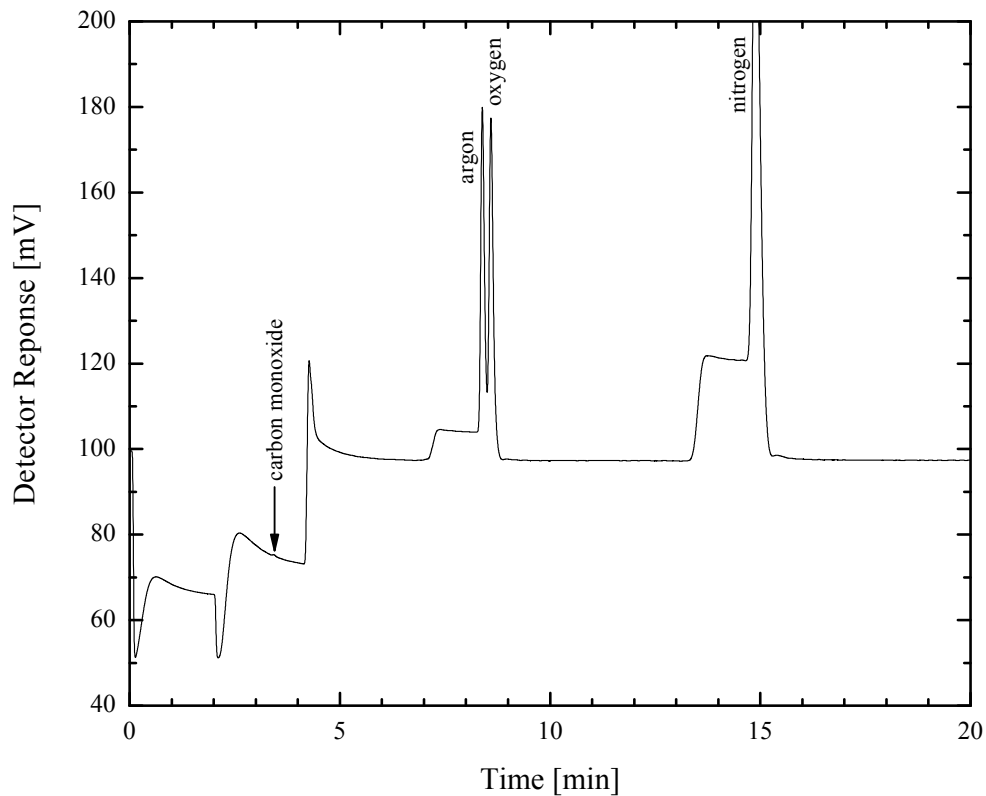
Figure 6.10 Typical gas chromatogram spectrum from GC 1 (using a TCD detector) for the analysis of permanent gases during methyl butanoate ignition for targeted RCF conditions of ϕ=0.30, P_{eff}=10.2 atm, T_{eff}=985 K, inert/O_2=3.76, and for a sampling time of $t_{s,norm}$=0.79. Certain peaks are identified for reference.
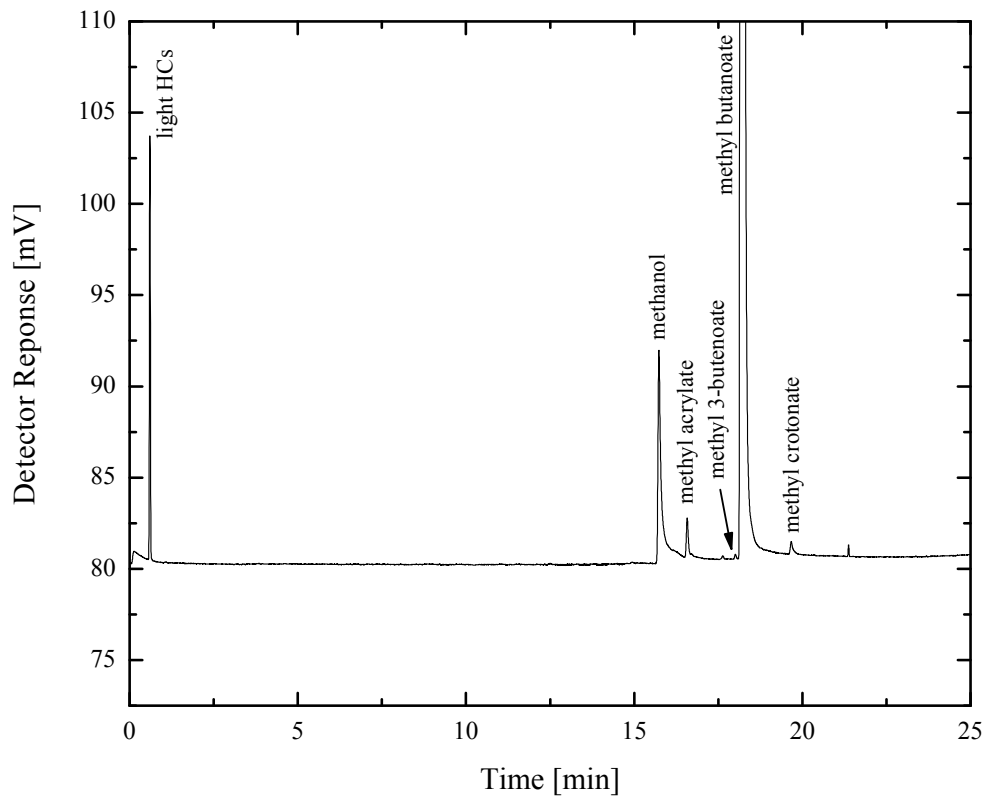
Figure 6.11 Typical gas chromatogram spectrum from GC 2 (using a FID detector) for the analysis of oxygenated species present during methyl butanoate ignition for targeted RCF conditions of ϕ=0.30, P_{eff}=10.2 atm, T_{eff}=985 K, inert/O_2=3.76, and for a sampling time of $t_{s,norm}$=0.36. Certain peaks are identified for reference.
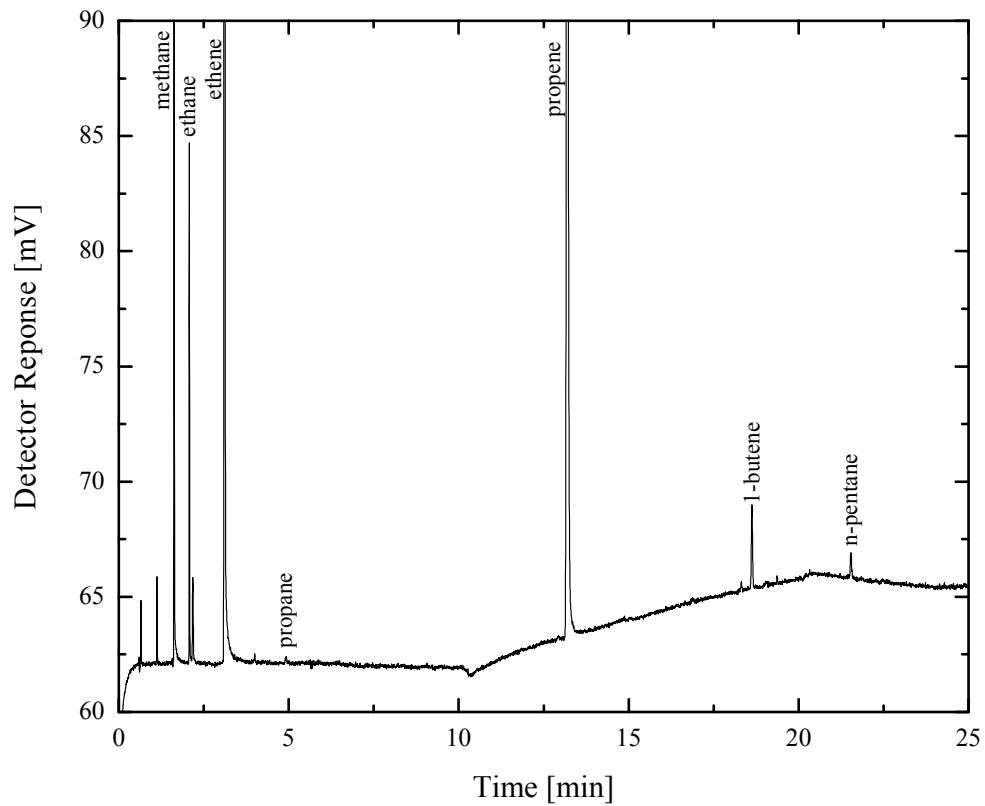
Figure 6.12 Typical gas chromatogram spectrum from GC 3 (using a FID detector) for the analysis of light hydrocarbons present during methyl butanoate ignition for targeted RCF conditions of ϕ=0.30, P_{eff}=10.2 atm, T_{eff}=985 K, inert/O_2=3.76, and for a sampling time of $t_{s,norm}$=0.92. Certain peaks are identified for reference.
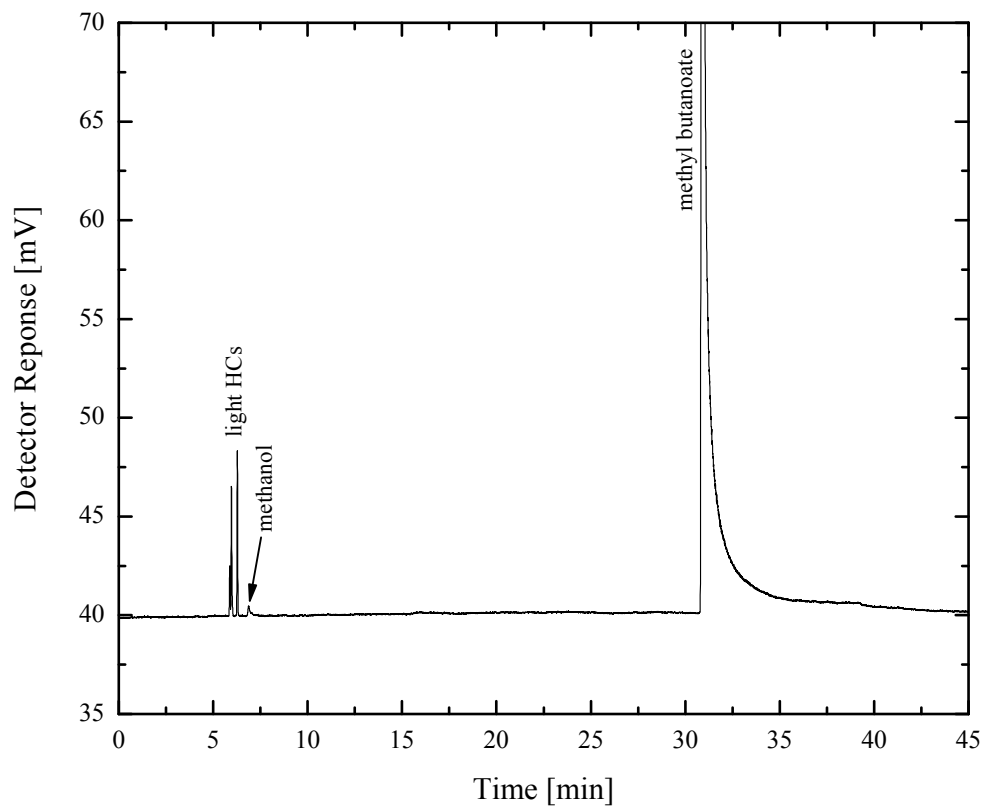
Figure 6.13 Typical gas chromatogram spectrum from GC 4a (using a FID detector) for the analysis of oxygenated species present during methyl butanoate ignition for targeted RCF conditions of ϕ=0.30, P_{eff}=10.2 atm, T_{eff}=985 K, inert/O_2=3.76, and for a sampling time of $t_{s,norm}$=0.36. Certain peaks are identified for reference.
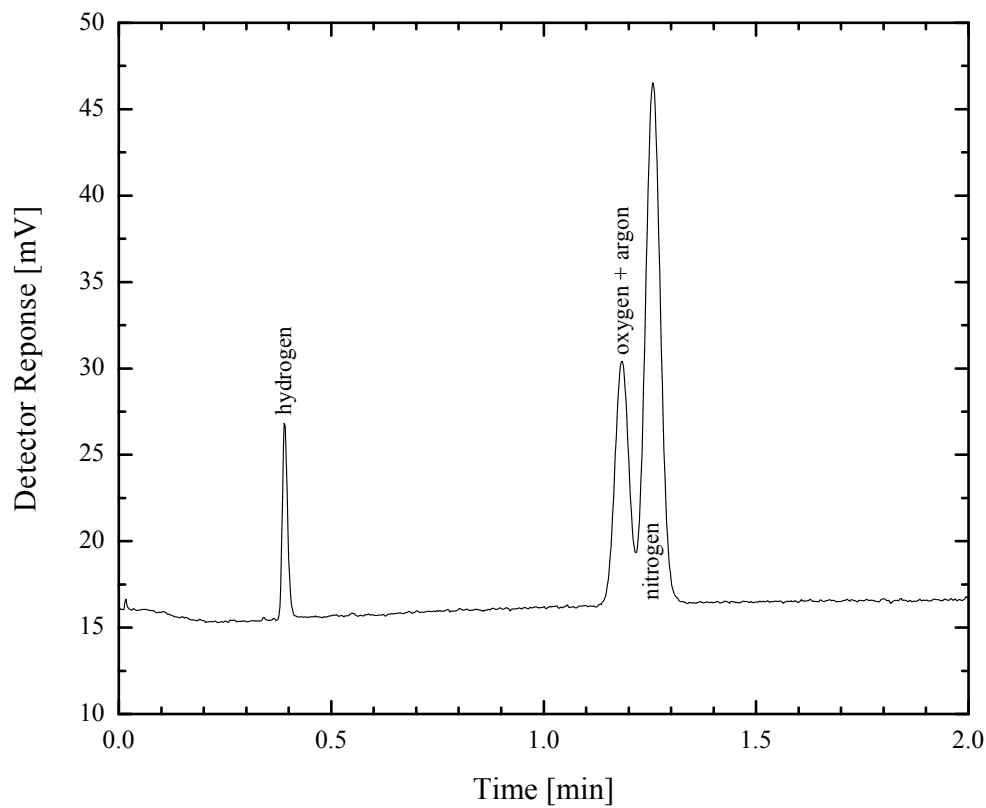
Figure 6.14 Typical gas chromatogram spectrum from GC 4b (using a TCD detector) for the analysis of permanent gases during methyl butanoate ignition for targeted RCF conditions of ϕ=0.30, P_{eff}=10.2 atm, T_{eff}=985 K, inert/O_2=3.76, and for a sampling time of $t_{s,norm}$=0.79. Certain peaks are identified for reference.

6.4 Methyl Butanoate Sampling Results

6.4.1 Summary of Methyl Butanoate Sampling Experiments

A summary of the methyl butanoate sampling experiments, including the measured ignition delay time, the sampling time, and test conditions for each experiment, is presented in Table 6.7. In the table, the equivalence ratio (ϕ) is defined as the actual carbon to oxygen ratio in the test mixture divided by the stoichiometric carbon to oxygen ratio. The inert gas to O_2 molar ratio is also provided in Table 6.7, as an indication of the dilution of the mixture. The inert gases used included nitrogen, argon, and carbon dioxide. The mixture components are provided on a mole fraction basis (e.g. χ_{O_2} is the mole fraction of oxygen in the mixture on a percent basis).
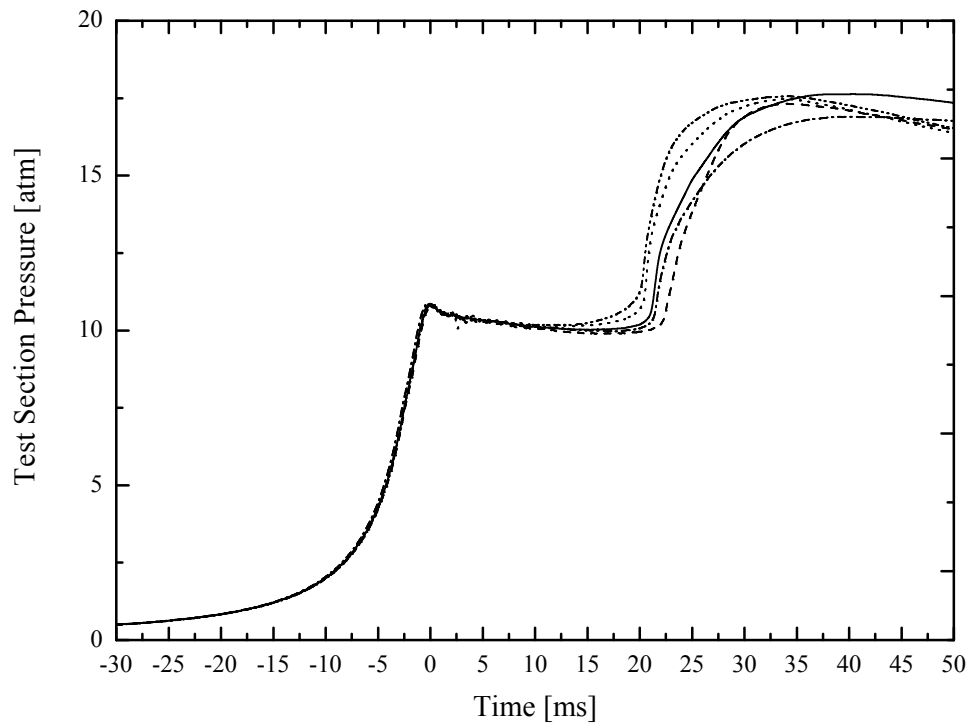
Figure 6.15 Non-normalized experimental pressure time-histories, demonstrating the repeatability of the sampling experiments.

Figure 6.15 shows five non-normalized pressure time-histories for five of the sampling experiments. This figure demonstrates the level of repeatability of the sampling experiments. Note the nearly identical, smooth compression processes. Also note that the end of compression pressure for the sample experiments have a standard deviation of 0.24%. The slight decrease in pressure due to heat losses to the test manifold walls, prior to the sampling event are also extremely consistent. The primary cause of the variation in the pressure time-history and the ignition delay time for the experiments is the difference in the sampling time and the sampling interval. During the sampling intervals slightly different amounts of reacting gas are removed from the test volume in each experiment. Additionally, the sampling event slightly cools the test gas mixture due to expansion, leading to a 5% standard deviation in ignition delay time. To minimize the impact of these differences on the speciation results, the time domain is normalized by the actual ignition delay time for each experiment. Figure 6.16 includes the pressure time histories for the same 5 sampling events, after they have been normalized by the ignition delay time for each experiment. The normalized time scale is used for comparison between each experiment, and against the model predictions, as described earlier.

Table 6.7 Summary of experimental conditions and results for methyl butanoate ignition high-speed gas sampling experiments presented in Figs. 6.17-6.22. The targeted mixture condition is ϕ=0.3 and the inert/O$_2$=3.76. The mixture composition is provided on a mole basis. The definitions of the sampling times and the ignition time are provided in the supporting text.

ϕ	Inert /O$_2$	Test gas composition^a				P_{eff} [atm]	T_{eff} [K]	$t_{s,1}$ [ms]	$t_{s,2}$ [ms]	t_s [ms]	τ_{ign} [ms]	$t_{s,norm}$ [ms]
		χ_{mb} [%]	χ_{O_2} [%]	χ_{N_2} [%]	χ_{Ar} [%]							
-0.3	3.76	0.96	20.79	52.89	25.25	10.2	984	19.11	20.48	19.80	21.53	0.92
-0.3	3.76	0.96	20.79	52.89	25.25	10.0	977	11.03	12.55	11.79	24.18	0.49
-0.3	3.76	0.96	20.79	52.89	25.25	10.3	984	1.18	2.48	1.83	21.66	0.08
-0.3	3.76	0.96	20.79	52.89	25.25	10.4	988	15.26	16.63	15.94	20.11	0.79
-0.3	3.76	0.96	20.79	52.89	25.25	10.2	979	7.31	8.80	8.06	22.65	0.36
-0.3	3.76	0.96	20.79	52.89	25.25	10.4	985	13.02	14.46	13.74	19.63	0.70
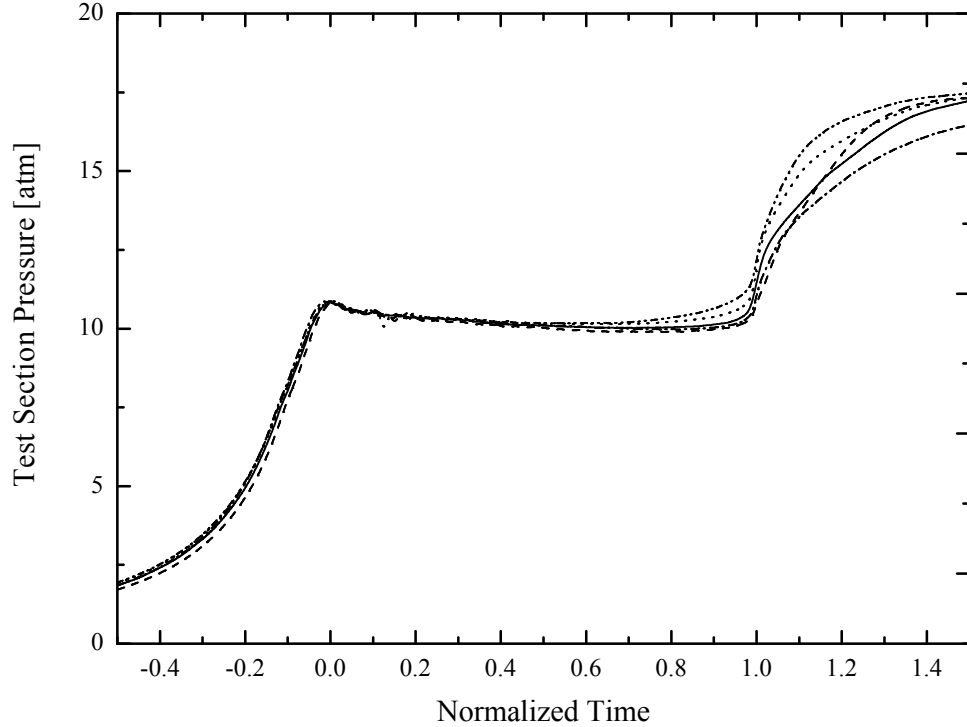
Figure 6.16 Normalized experimental test volume pressure time-histories.

6.4.2 Intermediate Species Time-Histories

For every experiment, the intermediate species of interest are quantified using the previously outlined methods. Collectively the data are the experimental concentration time-histories for each species during ignition. As noted earlier, the slight variations in the experimental conditions result in slightly different ignition delay times. Hence, a normalized sampling time is defined as the actual sampling time divided by the specific ignition delay time:

$$t_{s,norm} = \frac{t_s}{\tau_{ign}}. \tag{6.4}$$

Using the normalized sampling time, the composite data yield a concentration time history for each of the species measured, as shown in Fig. 6.17 for methane. Quantitative hydrocarbon intermediate species time-histories from GC 3 will be presented here. GC 2 and GC 4a target oxygenated species, however, due to peak overlap, and column saturation, only qualitative discussion of sample chromatograms is presented here. GC1 and GC4b target permanent gases, and example chromatograms were included earlier for reference.

Figures 6.17-6.22 show the concentration time-histories for each intermediate compound quantified using the sampling methods. The experimental data are compared to the concentration time-history predictions from the mechanism presented in Chapter 5. In addition, each of these figures includes a time normalized experimental pressure time-history for reference.

6.4.3   Species Mole Fraction Uncertainties

There are several contributions to the uncertainties that are shown as error bars in Figs. 6.17-6.22. Many of the experimental uncertainties apply to all of the species, such as dilution resulting from the dead volume in the sampling section. Other uncertainties, such as the purity of the calibration compounds, affect each species individually. These uncertainties are discussed below.

The horizontal error bars in Figs. 6.17-6.22 are uncertainties in the sampling time. The uncertainty in sampling time is primarily a result of the sampling duration. The sampling interval is the entire time the valves are open to extract sample from the test volume. During the ignition delay time, the species mole fractions are continually changing, therefore the mole fraction in the sampling tank is time averaged over this sampling interval. To determine the uncertainty shown in the figures, the sampling interval is multiplied by the standard deviation of the ignition delay times prior to normalization, which is approximately 5% of the normalized time.
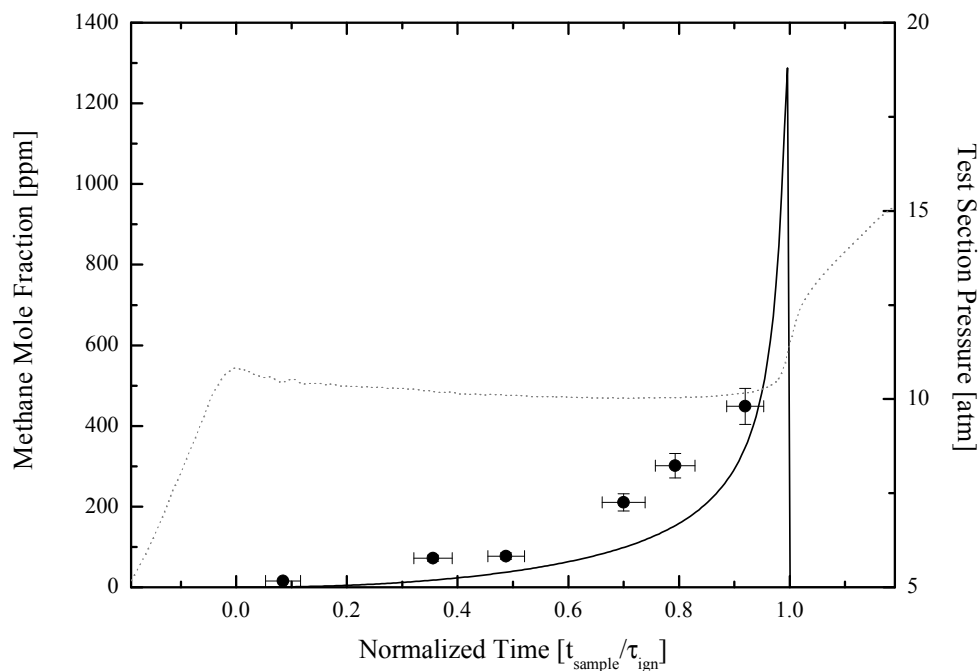
Figure 6.17 Experimental and modeling results for the methane time-history for target conditions of ϕ=0.30, P_{eff}=10.2, T_{eff}=985 K, Inert/O_2=3.76. The symbols are the experimentally determined species mole fractions for each discrete sampling event. The error bars are the experimental uncertainties discussed in Sec. 6. The CHEMKIN model prediction is shown as the solid line (——). An experimental pressure time-history for the sampling condition is also shown for reference as the gray dashed line (- - -). The time domain has been normalized from t=0 (end of compression) to t=1 (time of ignition). See text for details.

The vertical error bars are the uncertainty in the species mole fraction. The first contribution to the uncertainty is from the dead volume in the gas sampling system. Physically, the dead volume is the internal diameter of the sampling tube and the small portion of the body of the sampling valve upstream of the sealing face. The dead volume is comprised mostly of a stainless tube with a diameter of approximately 1 mm and a volume of 0.22 mL. When the sampling valve opens the unreacted gases in the dead volume are first drawn into the 20 mL sampling tank, followed by the reacting "core" gases. Therefore, the core gas sample is diluted by the dead volume.
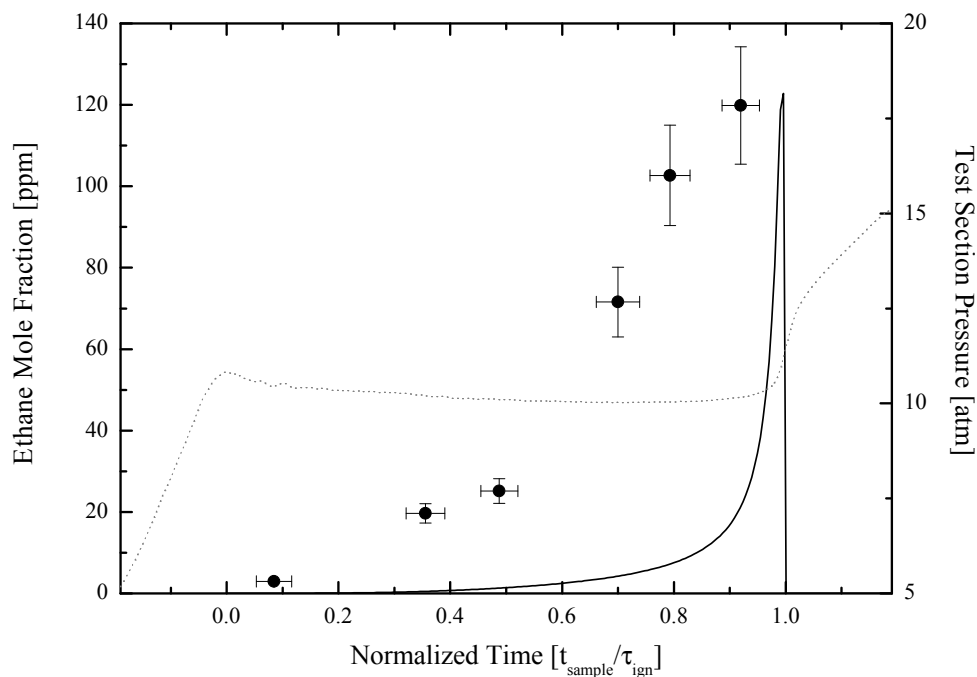
Figure 6.18 Experimental and modeling results for the ethane time-history for target conditions of ϕ=0.30, P_{eff}=10.2, T_{eff}=985 K, Inert/O_2=3.76. The symbols are the experimentally determined species mole fractions for each discrete sampling event. The error bars are the experimental uncertainties discussed in Sec. 6. The CHEMKIN model prediction is shown as the solid line (——). An experimental pressure time-history for the sampling condition is also shown for reference as the gray dashed line (- - -). The time domain has been normalized from t=0 (end of compression) to t=1 (time of ignition). See text for details.

The gas in the dead volume is estimated to be at a temperature of approximately 450 K with an uncertainty of ±50 K. The gases in the dead volume are considered too cold to react and are assumed to have the same composition as the charge mixture. During the sampling event the gases are quickly quenched as they expand into the vacuum of the sampling tank. Using the ideal gas law $PV = n\overline{R}T$, the amount of gas in the dead volume and the amount of gas in the sampling tank after sample collection can be determined. It is found that approximately 36% ±5% of the sample is comprised of gases from the dead volume. The uncertainty of ±5% is due to the estimate of the
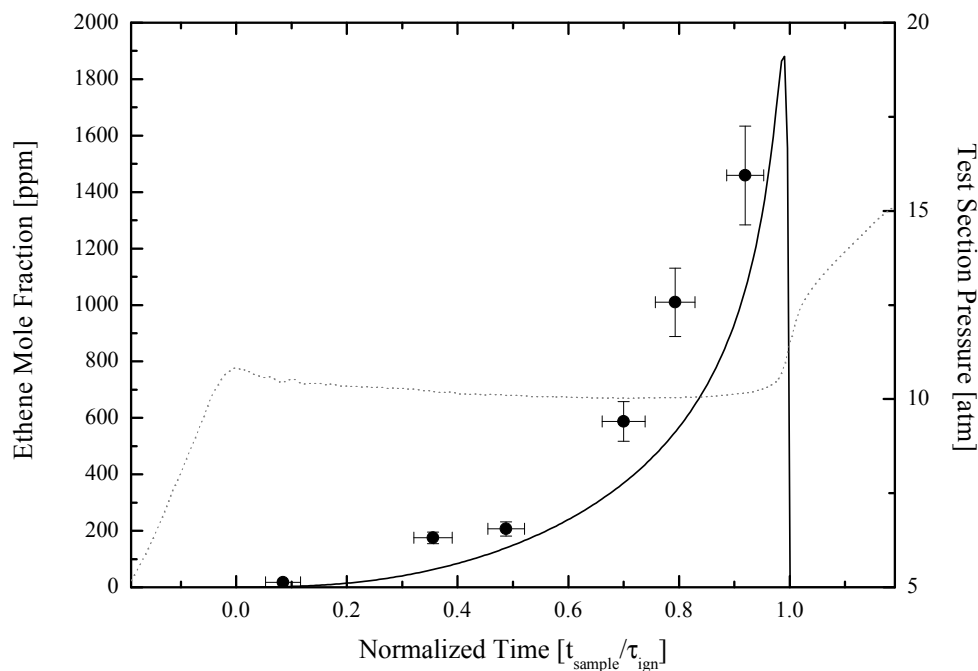
Figure 6.19 Experimental and modeling results for the ethene time-history for target conditions of ϕ=0.30, P_{eff}=10.2, T_{eff}=985 K, Inert/O_2=3.76. The symbols are the experimentally determined species mole fractions for each discrete sampling event. The error bars are the experimental uncertainties discussed in Sec. 6. The CHEMKIN model prediction is shown as the solid line (——). An experimental pressure time-history for the sampling condition is also shown for reference as the gray dashed line (- - -). The time domain has been normalized from t=0 (end of compression) to t=1 (time of ignition). See text for details.

dead volume temperature, and translates directly to a $\pm 5\%$ uncertainty contribution to the intermediate species mole fractions.

The second contribution to the species concentration uncertainty is from the calibration of the gas chromatographs and from the preparation of the calibration gas mixtures. The calibration of the hydrocarbons in GC 3 results in an average standard deviation of 12%. These uncertainties must be combined with the purity of the actual calibration sample, and are combined using a sum of the squares method to yield an average uncertainty of 13% for hydrocarbons. The actual uncertainty in each species
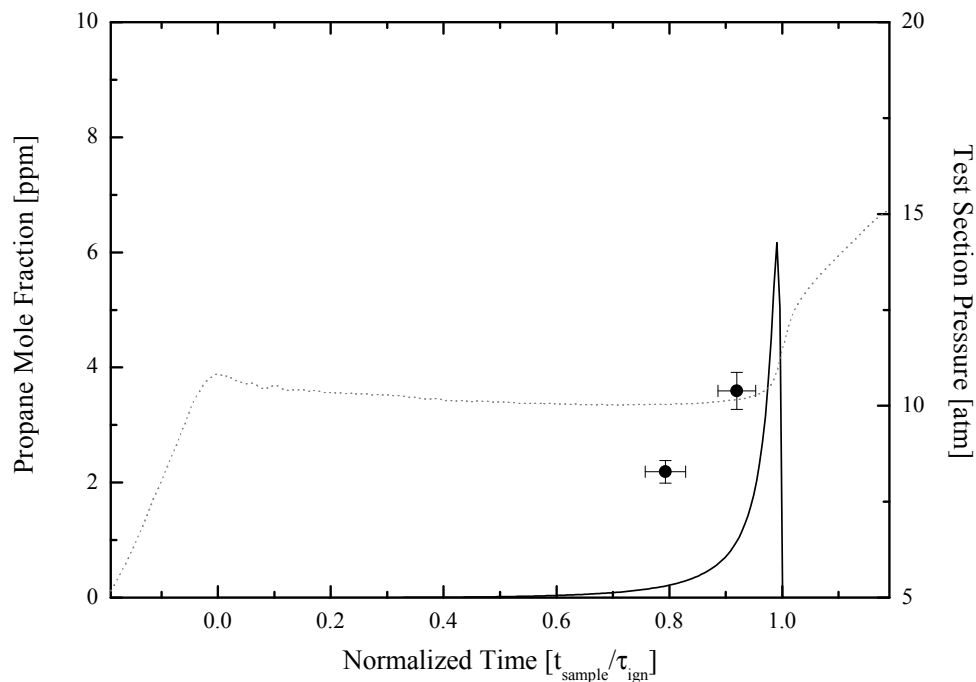
Figure 6.20 Experimental and modeling results for the propane time-history for target conditions of ϕ=0.30, P_{eff}=10.2, T_{eff}=985 K, Inert/O_2=3.76. The symbols are the experimentally determined species mole fractions for each discrete sampling event. The error bars are the experimental uncertainties discussed in Sec. 6. The CHEMKIN model prediction is shown as the solid line (——). An experimental pressure time-history for the sampling condition is also shown for reference as the gray dashed line (- - -). The time domain has been normalized from t=0 (end of compression) to t=1 (time of ignition). See text for details.

mole fraction is shown as the vertical error bars in Figs. 6.17-6.22.

6.5   Discussion of Methyl Butanoate Sampling Results

The results of the high-speed gas sampling experiments provide rigorous quantitative benchmarks for improving the understanding of the reaction pathways unique to the combustion of oxygenated hydrocarbon compounds. For this study, the model
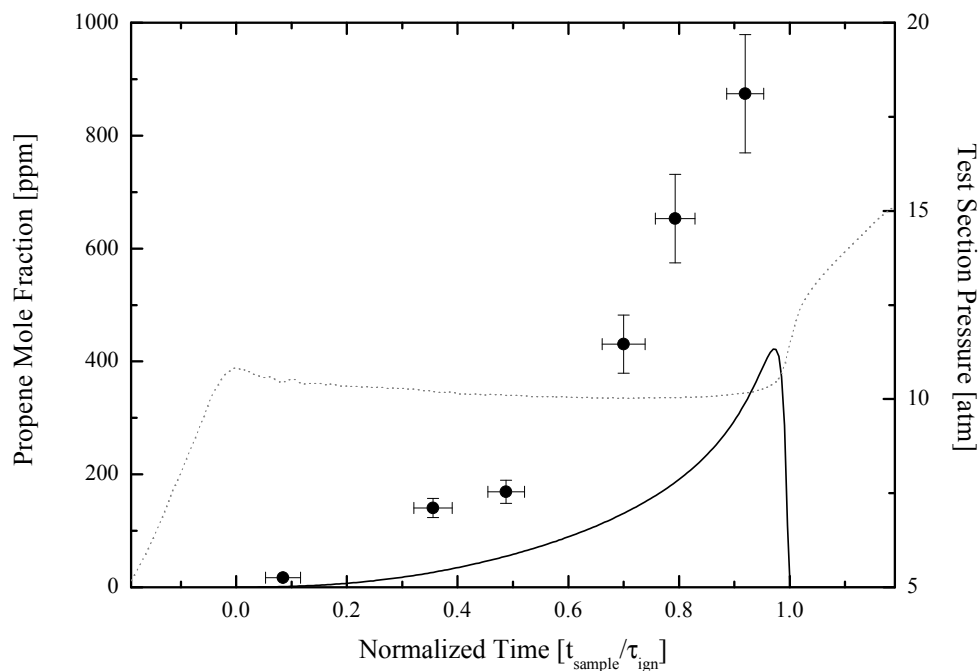
Figure 6.21 Experimental and modeling results for the propene time-history for target conditions of ϕ=0.30, P_{eff}=10.2, T_{eff}=985 K, Inert/O_2=3.76. The symbols are the experimentally determined species mole fractions for each discrete sampling event. The error bars are the experimental uncertainties discussed in Sec. 6. The CHEMKIN model prediction is shown as the solid line (——). An experimental pressure time-history for the sampling condition is also shown for reference as the gray dashed line (- - -). The time domain has been normalized from t=0 (end of compression) to t=1 (time of ignition). See text for details.

predictions were generated using the CHEMKIN package and the reaction mechanism presented in Chapter 5. The model predicts an ignition delay time of 19.4 ms for the targeted sampling condition of ϕ=0.30, P_{eff}=10.2 atm, T_{eff}=985 K, Inert/O_2=3.76. This is in very good agreement with the average ignition delay time of 21.6 ms for the experiments presented here; however, more accurate data on the species concentrations are necessary for improved understanding of the actual chemical pathways. For example, a factor of two discrepancy is seen in the prediction of methyl crotonate ignition delay time using the same model (see Fig. 7.3 of Chapter 7), and methyl
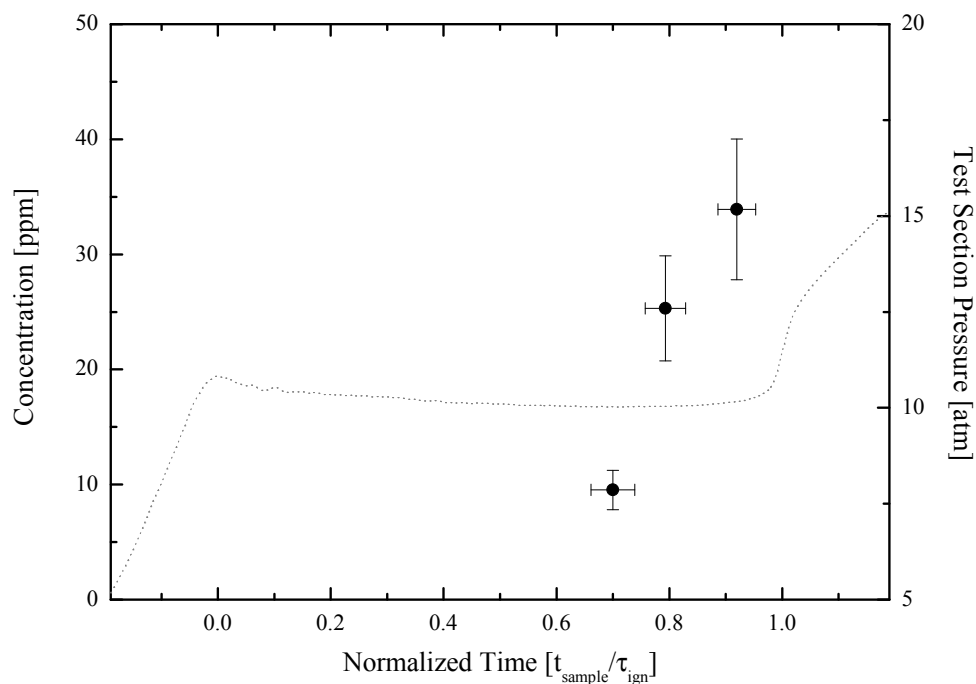
Figure 6.22 Experimental and modeling results for the 1-butene time-history for target conditions of ϕ=0.30, P_{eff}=10.2, T_{eff}=985 K, Inert/O_2=3.76. The symbols are the experimentally determined species mole fractions for each discrete sampling event. The error bars are the experimental uncertainties discussed in Sec. 6. The CHEMKIN model prediction is shown as the solid line (——). An experimental pressure time-history for the sampling condition is also shown for reference as the gray dashed line (- - -). The time domain has been normalized from t=0 (end of compression) to t=1 (time of ignition). See text for details.

crotonate is a key intermediate in the oxidation of methyl butanoate.

Figures 6.17-6.22 present the model predictions for the intermediate species measured in this methyl butanoate ignition study.

Figure 6.17 shows that the model has good agreement with the experimental results for methane mole fraction, within 100 ppm throughout the ignition period. A similar level of quantitative agreement is seen for the ethene concentration time-history of Fig. 6.19. The experimentally determined mole fractions for ethane (Fig. 6.18), propane (Fig. 6.20), and propene (Fig. 6.21) were all found to be several times higher than the
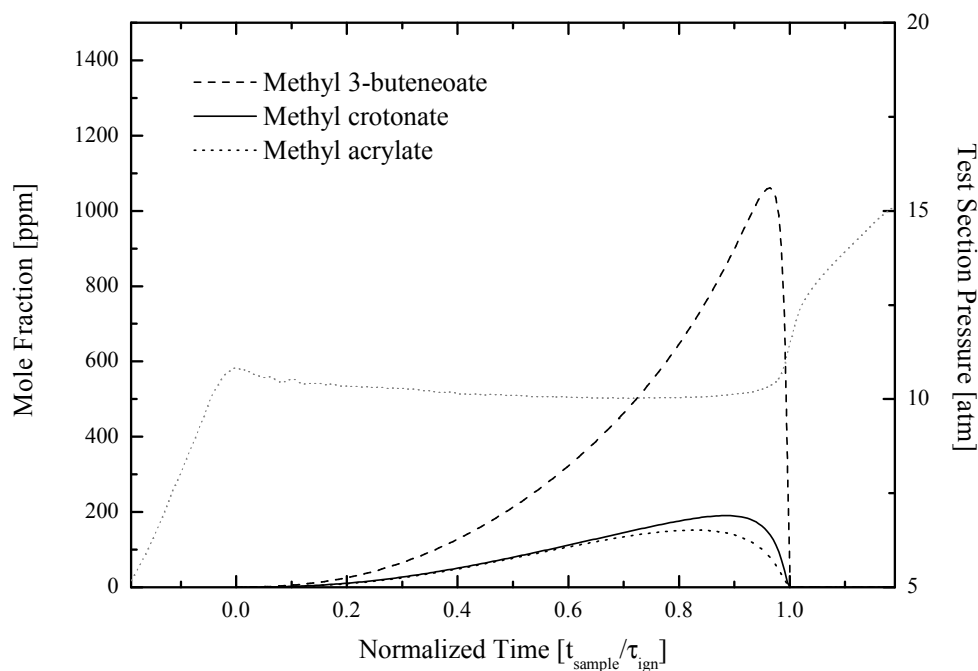
Figure 6.23 Modeling results for methyl 3-butenoate, methyl crotonate, and methyl acrylate time-histories for target conditions of ϕ=0.30, P_{eff}=10.2, T_{eff}=985 K, Inert/O_2=3.76. An experimental pressure time-history for the sampling condition is also shown for reference as the gray dashed line (- - -). The time domain has been normalized from t=0 (end of compression) to t=1 (time of ignition). See text for details.

model predictions. 1-Butene was found to have mole fractions on the order of tens of ppm, whereas the model predicts this species in sub ppm levels as shown in Fig. 6.22. These small alkenes lead to the formation of aromatics and thus soot. These are important species to accurately predict and to can further our insight into the affects on soot chemistry that can occur through the use of biofuels.

Several oxygenated species were identified to be present during the oxidation of the methyl butanoate at the condition investigated here. The poor selectivity of the method in GC 2 and the saturation of GC 4 prevented absolute quantification of these species; however, a qualitative comparison can be made. Methyl acrylate, methyl-3-butenoate, and methyl crotonate were all found in significant concentrations

as shown in Fig. 6.11. These species are involved in the major decomposition pathways predicted by the model and are predicted to occur in high concentrations. The model predictions for these species are show in Fig. 6.23.

The columns chosen for the gas chromatography analysis presented in this study were defined by previous studies using the UM RCF. The oven methods were altered for improved identification of oxygenated species, however future studies of intermediate speciation of similar reference compounds would benefit from the selection of more selective columns and detectors. For example, the FID response to methanol is orders of magnitude greater than that for the ester compounds and complicated the quantification of the ester species.

Chapter 7

Ignition Behavior of Esters with Varying Levels of Saturation: Methyl Butanoate, Methyl Crotonate, and Methyl trans-3 Hexenoate

7.1   Introduction

In addition to experiments focusing on the effects of isomer structure, investigation of unsaturated esters is necessary to understand the effects of varying saturation on the auto-ignition properties. Real biodiesels tend to be long chain esters with varying levels of saturation, consequently the results of these studies are important to develop an understanding of the ignition properties of biodiesels. The first necessary comparison is between an unsaturated C_5 ester, methyl crotonate and the saturated C_5 esters already investigated. Methyl crotoante has been investigated previously in a jet stirred reactor by Sarathy *et al.* (20). This ester has the same alkyl chain lengths as those of methyl butanoate, but methyl crotonate includes a single double bond.

After methyl crotonate, the next compound chosen for investigation was methyl trans-3-hexenoate. This compound was chosen in order to determine the difference

in reactivity between two unsaturated esters of different size. The effects of size are expected to be clearly evident in the relative reactivity of the esters. There is also interest in the NTC properties of this ester, as methyl butanoate, and methyl crotonate are not large enough to exhibit the NTC behavior characteristic of diesel type fuels. These are the first experimental ignition studies of methyl trans-3-hexenoate, and are vital to the understanding of larger ester chemistry, and the development of chemical kinetic models.

7.2 Typical Methyl Crotonate Ignition: Pressure Results

Mixtures and conditions for study were selected to compare directly to the ignition results of the prior studies of methyl butanoate, butyl methanoate, and ethyl propanoate. Specifically, the temperature ranged from T=951-1066 K, the pressure was nominally constant at P=10.5 atm, and the equivalence ratio was fixed at ϕ=0.30.

Typical pressure and pressure derivative data for methyl crotonate ignition experiments are shown in Fig. 7.1. The initial pressure rise in each experiment is due to compression of the test gas mixture ahead of the sabot. At the end of compression, the pressure reaches the first maximum. This time is set as t = 0 sec and is labeled P_{max} in the figures. The pressure then decreases slightly due to cooling losses to the test volume walls. After a delay period, the mixture auto-ignites resulting in a rapid increase in pressure for all cases.

The effective test conditions were determined using the pressure time-history from each experiment. The effective pressure (P_{eff}) was defined using the same definition as earlier studies, as the time-integrated average pressure from the maximum pressure (P_{max}) at the end of compression to the point of maximum rate of pressure rise
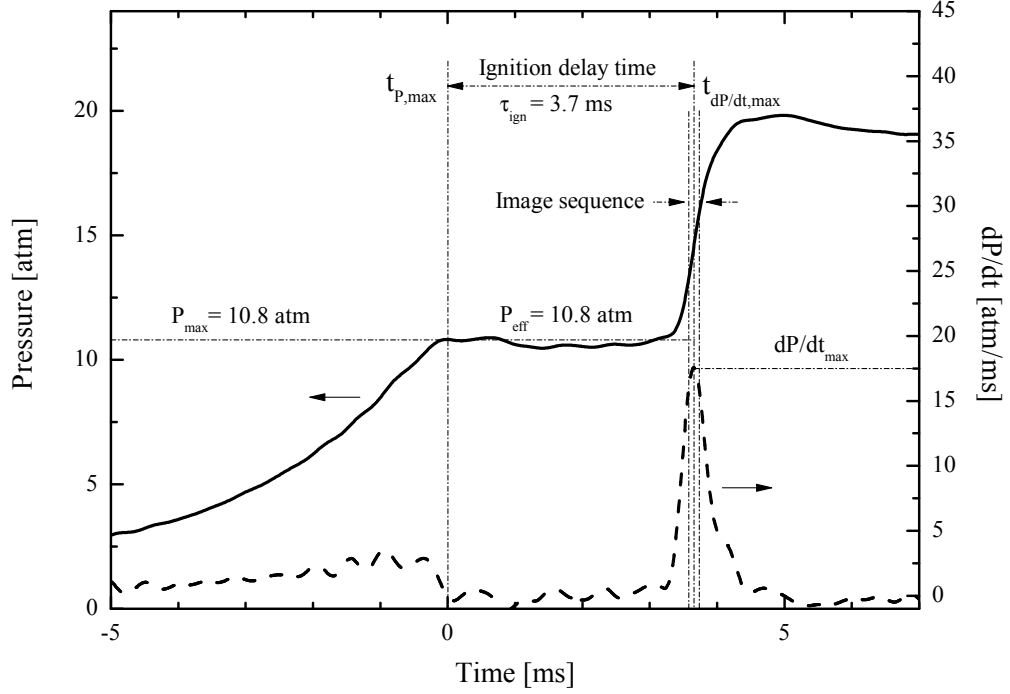
Figure 7.1 Typical pressure (——) and pressure derivative (- - -) time-histories for methyl crotonate ignition experiments where volumetric ignition is observed, experimental conditions of: P_{eff}=10.8 atm, T_{eff}=1066 K, ϕ=0.30, Inert/O_2=3.76.

(dP/dt_{max}), or

$$P_{eff} = \frac{1}{(t_{dP/dt_{max}} - t_{P_{max}})} \int_{t_{P_{max}}}^{t_{dP/dt_{max}}} P \cdot dt \,. \tag{7.1}$$

The effective temperature for each experiment was determined, as in previous UM RCF studies (25; 26; 27; 28; 29), using the effective pressure and by numerical integration of the isentropic relation

$$\int_{T_o}^{T_{eff}} \frac{\gamma}{\gamma - 1} \, d\,ln(T) = ln\left(\frac{P_{eff}}{P_o}\right) \,, \tag{7.2}$$

where P_o is the initial charge pressure, T_o is the initial temperature (typically 298 K),

and γ is the temperature-dependent ratio of the specific heats of the unreacted test gas mixture, which is determined using the NASA thermodynamic data base (33) and from the thermodynamic data for methyl crotonate from Fisher *et al.* (16). The temperature dependent specific heat data of methyl trans-3-hexenoate was taken from Dayma *et al.* (36), who have developed a mechanism for the saturated C_7 ester, methyl hexanoate.

For each experiment, the ignition delay time (τ_{ign}) was determined using the pressure time-history, and defined as the time between P_{max} and dP/dt_{max}. This definition for τ_{ign} is illustrated in Fig. 7.1, and was developed in previous UM RCF ignition studies, where it was determined to be very robust when different ignition regimes were present (28; 29).

7.3 Typical Methyl Crotonate Ignition: Imaging Results

As with previous autoignition studies in the UM RCF (28), high speed imaging was acquired for each ignition experiment, and can be used to quantitatively evaluate the homogeneity of ignition. Only homogeneous, volumetric ignition was observed for the conditions studied. The imaging sequence corresponding to the pressure time-history of Fig. 7.1 is shown in Fig. 7.2. It is evident from the images that the mixture ignites very uniformly, with little spatially resolved structure. Ignition is seen visually as a increase in blue emission, with the peak in blue emission associated with the maximum of the pressure derivative.
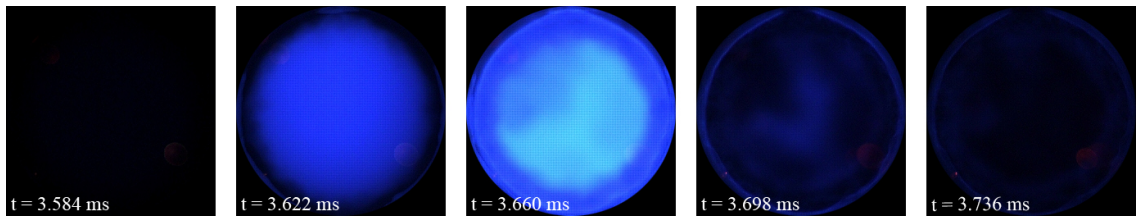
Figure 7.2 Imaging sequence corresponding to the data and time interval of Fig. 7.1, and conditions of P_{eff}=10.8 atm, T_{eff}=1066 K, ϕ=0.30, Inert/O_2=3.76, τ_{ign}=3.7 ms, 26,000 fps (no color adjustment). The time interval spanned for these frames is shown in Fig. 7.1.

7.4 Summary of Methyl Crotonate Ignition Data

A summary of the methyl crotonate ignition data, including the measured ignition delay time and test conditions for each experiment, is presented in Table 7.1. In the table, the equivalence ratio (ϕ) is defined as the actual carbon to oxygen ratio in the test mixture divided by the stoichiometric carbon to oxygen ratio. The inert gas to O_2 molar ratio is also provided in Table 7.1, as an indication of the dilution of the mixture. The inert gases used included nitrogen, and argon. The mixture components are provided on a mole fraction basis (e.g. χ_{O_2} is the mole fraction of oxygen in the

mixture on a percent basis).

Table 7.1 Summary of experimental conditions and results for methyl crotonate ignition. The mixture composition is provided on a mole basis. The equivalence ratio is based on C to O molar ratios.

ϕ	**Inert** $/O_2$	**Test gas composition**[a]				P_{eff} [atm]	T_{eff} [K]	τ_{ign} [ms]
		χ_{mc} [%]	χ_{O_2} [%]	χ_{N_2} [%]	χ_{Ar} [%]			
0.30	3.76	1.04	20.79	73.25	4.92	10.2	951	24.5
0.30	3.76	1.04	20.79	73.25	4.92	10.3	952	23.9
0.30	3.76	1.04	20.81	67.07	11.09	10.2	977	15.6
0.30	3.76	1.04	20.81	67.06	11.09	10.3	979	14.8
0.30	3.75	1.04	20.82	61.40	16.75	10.4	1005	10.1
0.30	3.75	1.04	20.82	61.35	16.79	10.5	1008	9.3
0.30	3.76	1.04	20.80	56.06	22.10	10.7	1037	5.6
0.30	3.76	1.04	20.80	56.07	22.09	10.7	1038	5.7
0.30	3.76	1.04	20.79	51.19	26.98	10.3	1054	4.4
0.30	3.76	1.04	20.79	51.20	26.97	10.8	1066	3.7

The ignition data from Table 7.1 are shown in Fig. 7.3. Regression analysis can be used to identify trends or differences in the τ_{ign} data for each of the unsaturated esters considered in this work. Regression analysis was conducted on the complete τ_{ign} data of Table 7.1 for methyl crotonate. Because the data were obtained at nominally fixed dilution, equivalence ratio, and pressure, an Arrhenius form to the expression was used. The resulting expression:

$$\tau_{ign_{mc}} = 5.6 \times 10^{-7} \times \ exp(33200/R_{[cal/mol/K]}\,T)\,, \tag{7.3}$$

has an R^2 value of 0.99. The regression is shown in Fig. 7.3.

The recommended uncertainty in the ignition delay time measurements is based on the uncertainty of the measured variables used in the regression and the corresponding effects of the uncertainties on the predicted ignition delay time. The sensitivity of the measured parameters was defined using the appropriate partial derivatives of the

regression expression. The total uncertainty was then evaluated using the square-root of the sum of the squares for each contribution. The uncertainty for the methyl crotonate τ_{ign} is $\pm 16.5\%$, and is primarily due to the uncertainty in the pressure measurement. The uncertainty is shown by the representative error bars in Fig. 7.3.
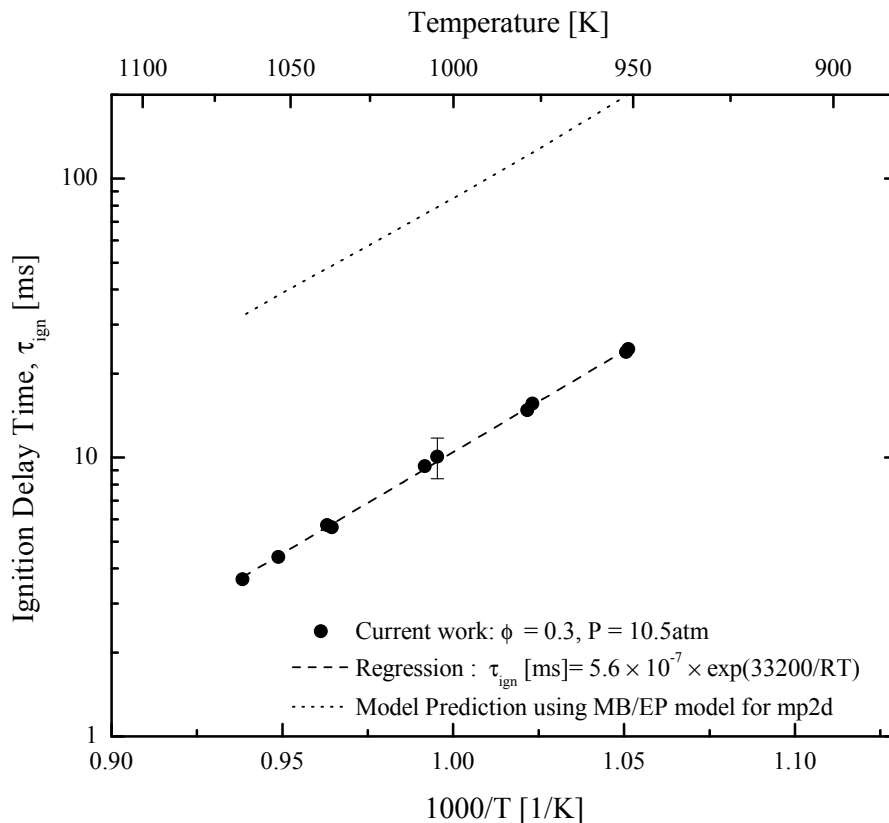
Figure 7.3 Summary of homogeneous ignition data for methyl crotonate ignition delay time as a function of temperature. The experimental data are nominally at $P = 10.5$ atm, $\phi = 0.3$, and $O_2 = 21\%$. The regression, Eq. (7.3), is provided for comparison.

Figure 7.3 also includes model predictions for methyl crotonate ignition using the modified mechanism for methyl butanoate and ethyl propanoate discussed in Chapter 5. The notation used in the model for methyl crotonate is 'mp2d'. Methyl crotonate is an intermediate that is formed from one of several possible pathways included for methyl butanoate oxidation in the model. As can be seen in Fig. 7.3, the model

accurately predicts the activation energy for methyl crotonate ignition, but predicts ignition delay times an order of magnitude longer than those observed experimentally in the UM RCF. The existing model was not optimized for the ignition of methyl crotonate. Most of the possible pathways for radical abstraction from this compound are not included in the model, as methyl crotonate was only one of several possible pathways for methyl butanoate oxidation. The new data for methyl crotonate ignition are invaluable benchmarks for inclusion of additional intermediate reaction pathways into the existing methyl butanoate/ethyl propanoate oxidation model, and for the refinement of existing reaction rates.

7.5 Typical Methyl trans-3-Hexenoate Ignition Results

Figures 7.4 and 7.5 present pressure and corresponding imaging sequence data for a typical methyl trans-3-hexenoate experiment. Methyl trans-3-hexenoate is an unsaturated C_7 ester chosen as a direct comparison against the unsaturated C_5 ester, methyl crotonate, to study the effects of size on the ignition properties of unsaturated esters. The general features of the experimental pressure data are the same as observed for the volumetric ignition conditions of methyl crotonate. No reaction fronts were observed for the methyl trans-3-hexenoate mixtures at the conditions studied here. Table 7.2 presents a summary of the methyl trans-3-hexenoate results.

7.6 Summary of Methyl trans-3-Hexenoate Ignition Data

A summary of the methyl trans-3-hexenoate ignition data, including the measured ignition delay time and test conditions for each experiment, is presented in Table 7.2. In the table, the equivalence ratio (ϕ) is defined as the actual carbon to oxygen ratio

112
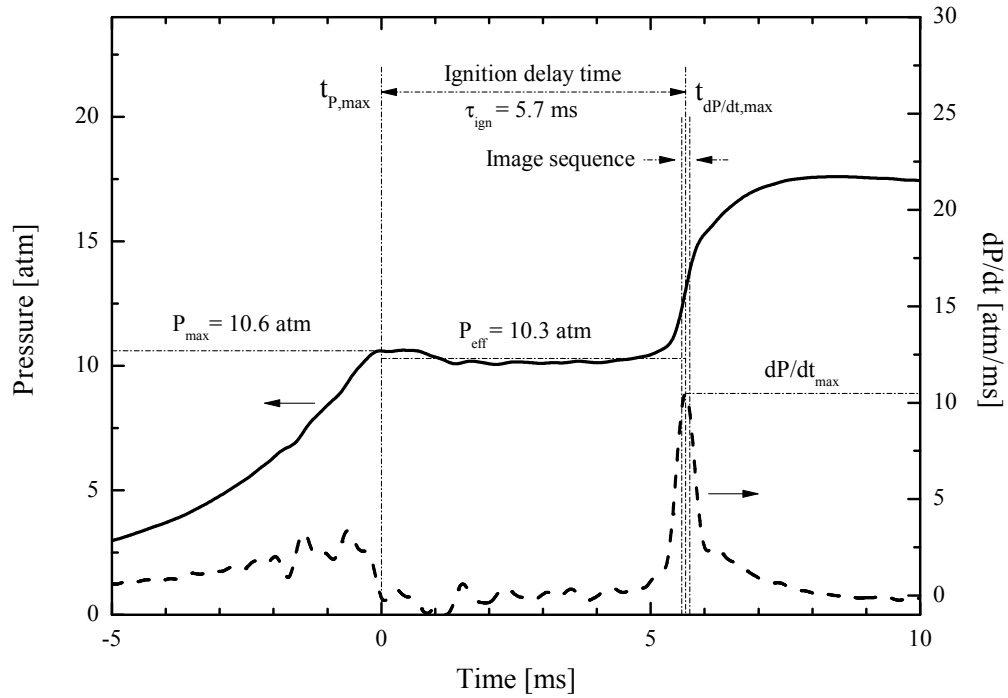
Figure 7.4 Typical pressure (——) and pressure derivative (- - -) time-histories for methyl trans-3-hexenoate ignition experiments where volumetric ignition is observed, experimental conditions of P_{eff}=10.3 atm, T_{eff}=1009 K, ϕ=0.30, Inert/O$_2$=3.76.
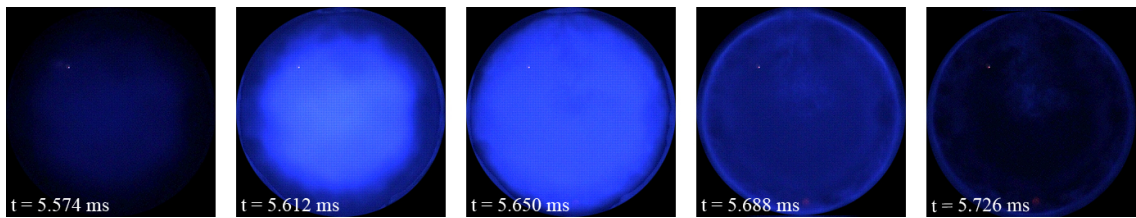
Figure 7.5 Imaging sequence corresponding to the data and time interval of Fig. 7.4, and conditions of: P_{eff}=10.3 atm, T_{eff}=1009 K, ϕ=0.30, Inert/O$_2$=3.76, τ_{ign}=5.7 ms, 26,000 fps (color adjusted for clarity). The time interval spanned for these frames is shown in Fig. 7.4.

in the test mixture divided by the stoichiometric carbon to oxygen ratio. The inert gas to O$_2$ molar ratio is also provided in Table 7.2, as an indication of the dilution of the mixture. The inert gases used included nitrogen, and argon. The mixture components are provided on a mole fraction basis (e.g. χ_{O_2} is the mole fraction of oxygen in the

mixture on a percent basis).

Table 7.2 Summary of experimental conditions and results for methyl trans-3-hexenoate ignition. The mixture composition is provided on a mole basis. The equivalence ratio is based on C to O molar ratios.

ϕ	**Inert** $/\mathbf{O_2}$	**Test gas composition**[a]				P_{eff} [atm]	T_{eff} [K]	τ_{ign} [ms]
		χ_{m3h} [%]	χ_{O_2} [%]	χ_{N_2} [%]	χ_{Ar} [%]			
0.30	3.76	0.69	20.87	70.46	-	10.3	899	33.2
0.27	3.75	0.64	20.89	70.55	-	10.4	906	29.6
0.30	3.76	0.69	20.87	75.44	-	10.4	928	18.4
0.30	3.76	0.69	20.87	75.44	-	10.5	931	17.8
0.30	3.75	0.69	20.93	76.19	2.19	10.7	961	10.6
0.29	3.76	0.67	20.86	70.16	8.31	10.6	985	8.3
0.30	3.75	0.69	20.89	64.42	14.01	10.3	1006	5.8
0.30	3.75	0.69	20.89	64.41	14.01	10.3	1009	5.7
0.30	3.76	0.69	20.87	59.40	19.04	10.7	1041	3.3
0.30	3.76	0.69	20.87	59.41	19.03	10.8	1044	3.3

[a]Balance CO_2

The ignition data from Table 7.2 are shown in Fig. 7.6. Regression analysis was used to identify trends in the τ_{ign} data of Table 7.2 for methyl trans-3-hexenoate. Because the data were obtained at nominally fixed dilution, equivalence ratio, and pressure, an Arrhenius form to the expression was used, yielding:

$$\tau_{ign_{m3h}} = 2.5 \times 10^{-6} \times \, exp(29300/R_{[cal/mol/K]}\, T)\,. \tag{7.4}$$

with an R^2 value of 0.99. The regression is shown in Fig. 7.6. The recommended uncertainty for the methyl trans-3-hexenoate ignition data is $\pm 15.5\%$, and is predominantly due to the uncertainty in the measured pressure. The high R^2 values are a testament to the repeatability of the experiments in the UM RCF when homogeneous conditions are being investigated, and to the ability to accurately achieve the targeted experimental conditions.
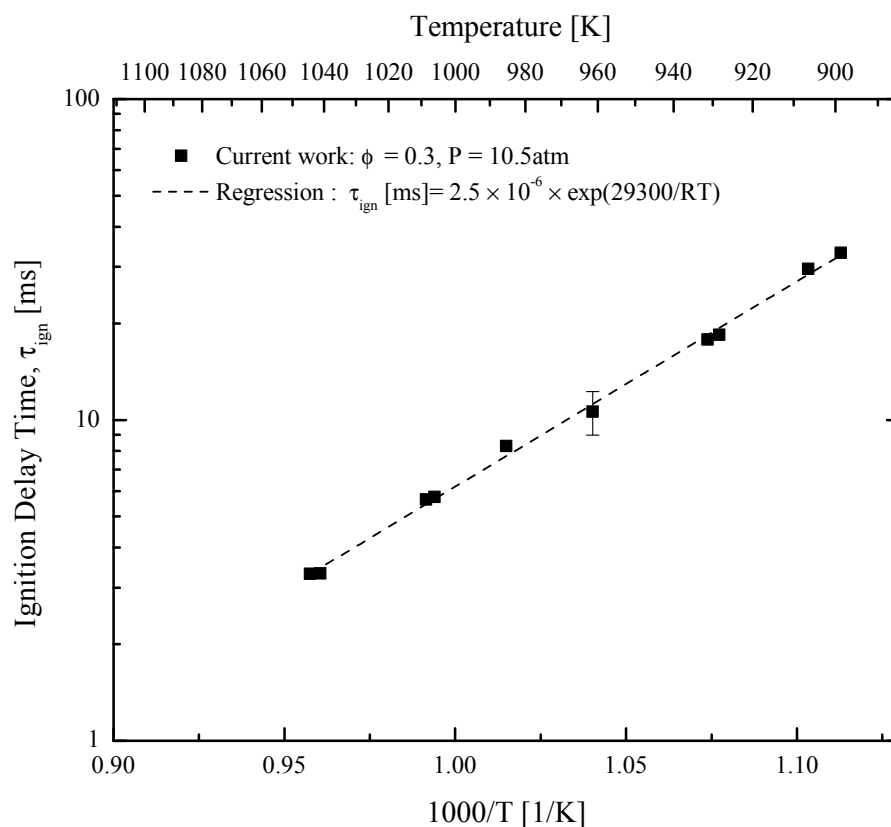
Figure 7.6 Summary of homogeneous ignition data for methyl trans-3-hexenoate ignition delay time as a function of temperature. The experimental data are nominally at $P = 10.5$ atm, $\phi = 0.3$, and $O_2 = 21\%$. The regression, Eq. (7.4) is provided for comparison.

7.7 Discussion of Unsaturated Ester Igntion

The reactivity of the two unsaturated esters can be compared on an Arrhenius plot as shown in Fig. 7.7. Both esters have similar activation energies. The figure shows the increased reactivity of the larger of the two unsaturated esters, methyl trans-3-hexenoate, over the range of temperatures studied here. However, if the results are extrapolated to higher temperatures, the small difference in activation energy would lead to more similar reactivity at higher temperature.

Methyl trans-3-hexenoate exhibits ignition delay times that are approximately 50%
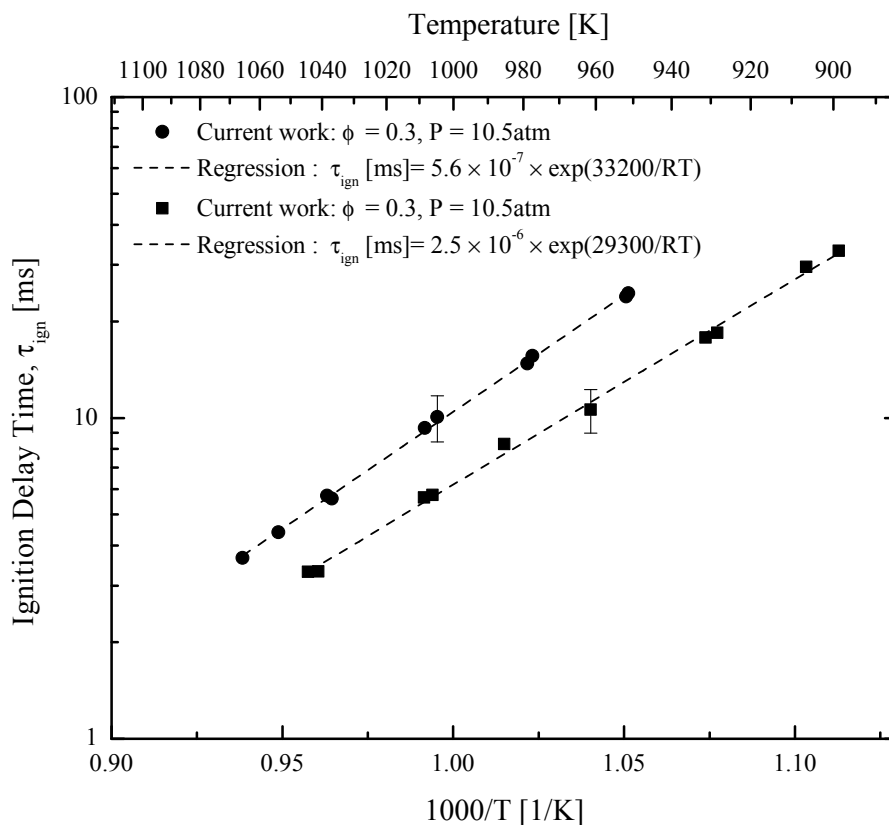
Figure 7.7 Comparison of current ($P_{eff} \cong 10.5$ atm data) ignition delay time studies for the unsaturated ester isomers, methyl crotonate (circles) and methyl trans-3-hexenoate (squares). The lines through the UM RCF data are Eqs. (7.3) and (7.4).

faster than those of methyl crotonate for the temperature, pressure, and equivalence ratio conditions considered. This is in agreement with the increase in reactivity of long chain alkanes when compared to shorter chains, as hydrogen abstraction requires less energy as the chain lengths increase.

The ignition delay time data for methyl trans-3-hexenoate do not demonstrate any NTC behavior over the conditions considered in this study. This is an important observation, as real biodiesel fuels do exhibit NTC behavior under similar operating conditions. Further experimental investigation of larger unsaturated esters, and possible blends with fuels known to demonstrate NTC behavior is necessary to identify

surrogates for real biodiesel ignition studies. Larger esters are very challenging to study in the UM RCF, and will require modification of the facility.
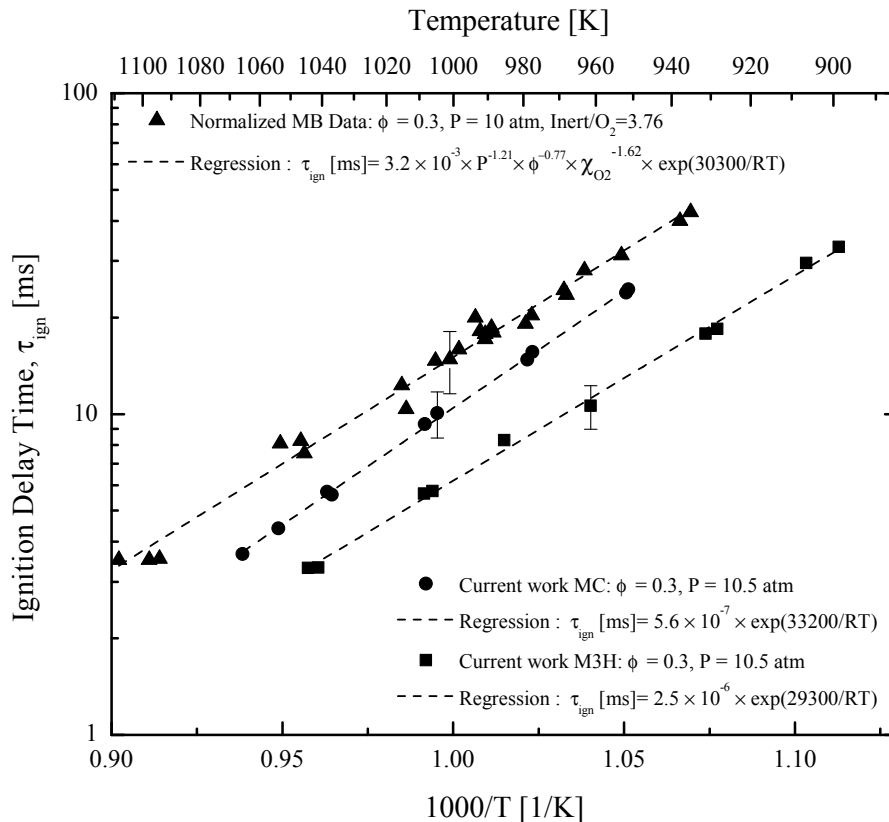
Figure 7.8 Comparison of current ($P_{eff} \cong 10.5$ atm data) ignition delay time studies for the unsaturated ester isomers, methyl crotonate (circles) and methyl trans-3-hexenoate (squares) and the previous methyl butanoate data. The lines through the UM RCF data are Eqs. (7.3), (7.4), and (4.3).

Figure 7.8 compares the reactivity of the two unsaturated esters with methyl butanoate on an Arrhenius plot. This figure shows that methyl crotonate exhibits ignition delay times that are approximately 30% faster than those of the saturated ester. The increased reactivity of the unsaturated isomer is not surprising because of the presence of the double bond, and is analagous to the increased reactivity of alkenes relative to alkanes. Also, methyl crotonate is a primary intermediate in the

combustion of methyl butanoate. However, the quantitative difference in ignition delay times has not been previously demonstrated. In fact, Sarathy *et al.* (20) had concluded that these two C_5 esters has similar reactivity based on speciation results of ester studies in an opposed flow diffusion flame and a jet stirred reactor.

The difference in the reactivity of the different esters considered in Fig. 7.8 suggests potential for blending biodiesel fuels with specific reactivity. As the figure shows, there is a notable difference in the ignition delay time results over the range of conditions studied. Since real biodiesel plant feedstocks result in different types of esters, some saturated, some unsaturated and of different chain lengths, opportunity exists to blend different esters into fuels optimized for targeted levels of reactivity.

Chapter 8

Ignition Behavior of Reference Biofuel Blends: Methyl trans-3-Hexenoate and n-Heptane

8.1 Introduction

In addition to fundamental studies of single reference compounds, experimental investigation of the ignition properties of blended compounds can provide new insights into synergies in fuel chemistry. Studies of fuel blends also have practical significance as biodiesel is currently being blended with petroleum diesel in ratios from 0% to 100%, 20% biodiesel becoming common. The compound most structurally suited to represent biodiesel that has been studied in the UM RCF is methyl trans-3-hexenoate because of its relatively large size and level of unsaturation. A commonly accepted single compound surrogate for ignition studies of petroleum diesel fuel is n-heptane. The blended fuels used for the ignition studies presented here are comprised of these two fuels; methyl trans-3-hexenoate and n-heptane.

For this study fuel blends between 0% and 100% n-heptane in methyl trans-3-hexenoate have been studied. The targeted experimental conditions for all of the blends are P_{eff}=10.5 atm, T_{eff}=925 K, ϕ=0.30, inert/O_2=3.76. All blends are determined on a mole basis. The overall equivalence ratio was held constant despite including

the effects of the different stoichiometric ratios for the different fuel compounds. This was done to quantify the changes in reactivity for various fuel blending ratios. These are the first experimental ignition studies of blends of methyl trans-3-hexenoate and n-heptane of which we are aware. These data are vital to understanding the ignition behavior of oxygenated hydrocarbon/hydrocarbon fuel blends, and the development of chemical kinetic models of blended fuels.

8.2   Typical Methyl trans-3-Hexenoate and n-Heptane Blend Ignition: Pressure and Imaging Results

The mixtures and conditions for study were selected to facilitate comparison with previous UM RCF ignition studies of single component fuels, including methyl butanoate, butyl methanoate, ethyl propanoate, methyl crotonate, methyl trans-3-hexenoate. As with previous studies it is also important that the conditions be relevant to low temperature engine combustion strategies.

Figure 8.1 presents typical pressure time-histories for two different methyl trans-3-hexenoate/n-heptane blend ratios. One with a fuel blend of 20% n-heptane and 80% methyl trans-3-hexenoate, and another with a fuel blend of 80% n-heptane and 20% methyl trans-3-hexenoate. The initial rise pressure is due to the compression of the test gas mixture ahead of the sabot. At the end of compression the pressure reaches its first maximum and this time is set as t=0 ms, as with previous UM RCF studies. The pressure then slowly decreases as there is some cooling to the test manifold walls. This is followed by a sharp rise in pressure, and the maximum in the pressure derivative is marked as the time of ignition.

As with previous autoignition studies in the UM RCF, high speed imaging was acquired for each ignition experiment, and can be used to quantitatively evaluate the homogeneity of ignition. Only homogeneous, volumetric ignition was observed for the
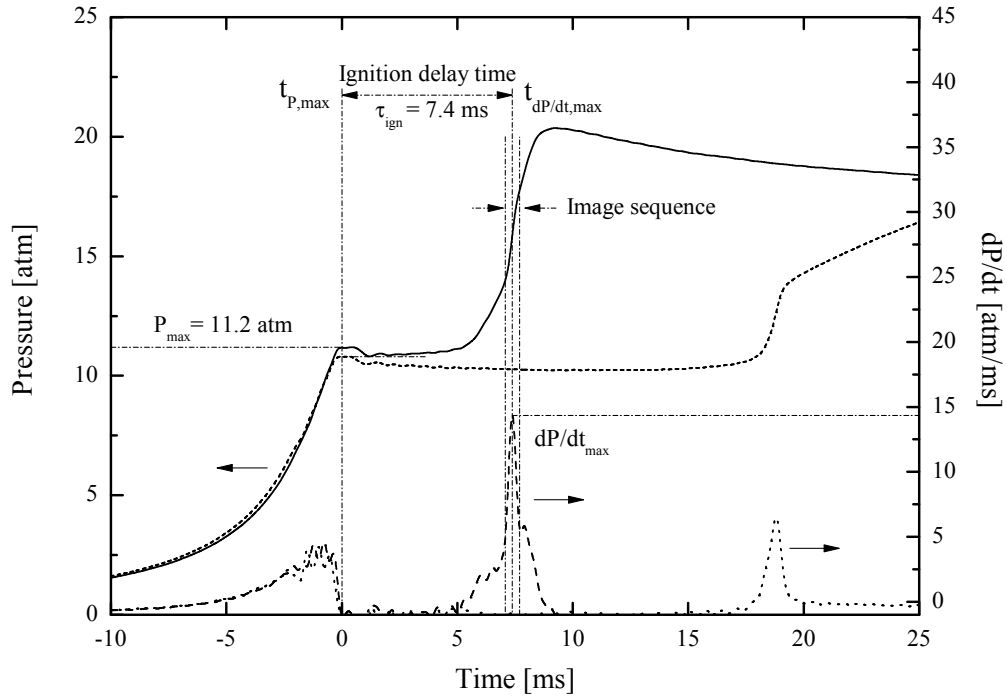
Figure 8.1 Typical pressure and pressure derivative time-histories for two methyl trans-3-hexenoate and n-heptane ignition experiments, targeted experimental conditions of: P_{eff}=10.5 atm, T_{eff}=925 K, ϕ=0.30, Inert/O_2=3.76. The short dashed line pressure time history and dotted pressure derivative time history are associated with a fuel blend comprised of 20% n-heptane and 80% methyl trans-3-hexenoate.The solid line pressure time history and dashed pressure derivative time history are associated with a fuel blend comprised of 80% n-heptane and 20% methyl trans-3-hexenoate. The high speed imaging sequence from the 80% n-heptane experiment is found in Fig. 8.2.

conditions studied. The imaging sequence corresponding to the pressure time-history for the mixture of 80% n-heptane and 20% methyl trans-3-hexenoate of Fig. 8.1 is shown in Fig. 8.2. It is evident from the images that the mixture ignites very uniformly, with little spatially resolved structure. Ignition is seen visually as a increase in blue emission, with the peak in blue emission associated with the time of the maximum of the pressure derivative. All off the fuel blend ratios from 0% n-heptane to 100% n-heptane demonstrated similar ignition behavior.
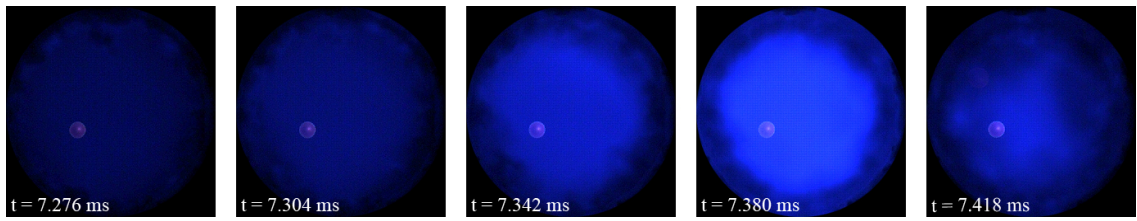
Figure 8.2 Imaging sequence corresponding to the 80% n-heptane and 20% methyl trans-3-hexenoate ignition data and time interval of Fig. 8.1. Targeted conditions of P_{eff}=10.5 atm, T_{eff}=925 K, ϕ=0.30, Inert/O_2=3.76, τ_{ign}=7.4 ms, 26,000 fps (color adjusted for clarity). The time interval spanned for these frames is shown in Fig. 8.1.

8.3 Summary of Methyl trans-3-Hexenoate and n-Heptane Blend Ignition Data

A summary of the methyl trans-3-hexenoate/n-heptane blend ignition data, including the ignition delay time, mixture conditions, and test conditions is found in Table 8.1. In the table, the equivalence ratio (ϕ) is defined as the actual carbon to oxygen ratio in the test mixture divided by the stoichiometric carbon to oxygen ratio. The inert gas to O_2 molar ratio is also provided in Table 8.1, as an indication of the dilution of the mixture. The inert gases used included nitrogen, and argon. The mixture components are provided on a mole fraction basis (e.g. χ_{O_2} is the mole fraction of oxygen in the mixture on a percent basis).

Some of the experiments noted in Table 8.1 are not correctly defined using the previous definitions of effective conditions, and these will be discussed later. The effective test conditions included in Table 8.1 were all defined using the same definition as earlier studies. All of the experiments are included for reference. The effective pressure is the time-integrated average pressure from the maximum pressure (P_{max}) at the end of compression to the point of maximum rate of pressure rise (dP/dt_{max}), or

$$P_{eff} = \frac{1}{(t_{dP/dt_{max}} - t_{P_{max}})} \int_{t_{P_{max}}}^{t_{dP/dt_{max}}} P \cdot dt \,. \tag{8.1}$$

The effective temperature for each experiment was determined, as in previous UM RCF studies (25; 26; 27; 28; 29), using the effective pressure and by numerical integration of the isentropic relation

$$\int_{T_o}^{T_{eff}} \frac{\gamma}{\gamma - 1} \, d\ln(T) = \ln\left(\frac{P_{eff}}{P_o}\right) \,, \tag{8.2}$$

where P_o is the initial charge pressure, T_o is the initial temperature (typically 298 K), and γ is the temperature-dependent ratio of the specific heats of the unreacted test

123

gas mixture, which is determined using the NASA thermodynamic data base (33). The temperature dependent specific heat data of methyl trans-3-hexenoate was taken from Dayma *et al.* (36), which is part of their mechanism for the saturated C_7 ester, methyl hexanoate.

Table 8.1 Summary of experimental conditions and results for methyl trans-3-hexenoate/n-heptane ignition. The targeted mixture condition is $\phi=0.3$, and Inert/O_2=3.76. The actual mixture composition is provided on a mole basis.

| ϕ | % C_7H_{16} | Inert /O_2 | Test gas composition | | | | | P_{eff} [atm] | T_{eff} [K] | τ_{ign} [ms] |
			χ_{m3h} [%]	χ_{c7h16} [%]	χ_{O_2} [%]	χ_{N_2} [%]	χ_{CO_2} [%]			
0.3	0	3.76	0.69	-	20.87	75.44	2.99	10.4	928	18.4
0.3	0	3.76	0.69	-	20.87	75.44	2.99	10.5	931	17.8
0.3	20	3.76	0.49	0.13	20.92	75.24	3.22	10.4	929	18.8
0.3	40	3.76	0.38	0.23	20.89	75.21	3.29	10.5	932	18.1
0.3	40	3.76	0.38	0.23	20.89	75.21	3.29	10.6	933	17.4
0.3	60	3.76	0.25	0.37	20.88	75.12	3.39	11.0^a	941^a	16.8
0.3	60	3.76	0.25	0.37	20.88	75.12	3.39	10.7^a	935^a	14.7
0.3	80	3.76	0.11	0.47	20.87	75.08	3.46	11.1^a	942^a	8.3
0.3	80	3.76	0.13	0.47	20.87	75.07	3.46	11.5^a	949^a	7.4
0.3	100	3.76	-	0.57	20.90	75.01	3.53	11.8^a	956^a	3.1
0.3	100	3.76	-	0.57	20.90	75.01	3.53	11.8^a	956^a	2.8
0.3	100	3.76	-	0.57	20.90	75.13	3.53	11.8^a	954^a	2.8
0.3	100	3.76	-	0.57	20.90	75.00	3.53	12.3^a	968^a	1.9

^{a}Reaction during compression renders these effective conditions invalid. They are included only for reference.

8.4 Discussion of Methyl trans-3-Hexenoate and n-Heptane Igntion

The reactivity of the different blends of methyl trans-3-hexenoate and n-heptane are compared as ignition delay time vs. blend ratio as shown in Fig. 8.3. Figure 8.3 includes each of the experiments of Table 8.1. The figure shows that the reactivity of the blends is fairly constant for fuel blending ratios from 0% to 40% n-heptane.

With blending ratios above 40% n-heptane the reactivity of the fuel mixture increases dramatically. However, the data presented in Fig. 8.3 were not held at the targeted effective conditions of P_{eff}=10.5 atm, T_{eff}=925 K, ϕ=0.30, inert/O_2=3.76. The actual end of compression conditions varied from the targeted conditions for certain mixture compositions. Specifically, for each experiment using a blend with over 40% n-heptane, reaction during compression was detected.

Ignition Delay times of n-Heptane / Methyl trans-3-Hexenoate Blends
Targeted Conditions: CR=27, ϕ = 0.3, P = 10.5 atm, T = 925 K, Inert/O_2 = 3.76
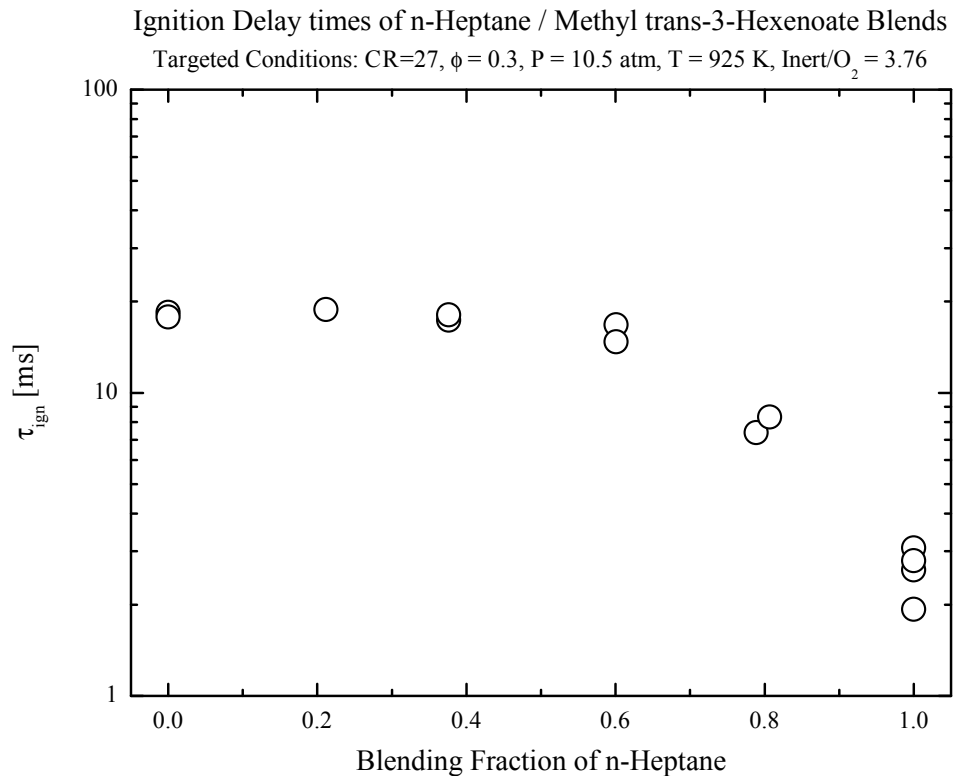
Figure 8.3 Comparison of ignition delay time results for methyl trans-3-hexenoate and n-heptane ignition experiments where volumetric ignition is observed, targeted experimental conditions of: P_{eff}=10.5 atm, T_{eff}=925 K, ϕ=0.30, Inert/O_2=3.76. Fuel bend composition was varied from 100% methyl trans-3-hexenoate to 100% n-heptane.

Reaction during compression is not unexpected as n-heptane is known to exhibit NTC behavior at state conditions near those investigated here. The first indication that reaction was occurring during compression was the relatively large variability in

end of compression pressures of P=10.5 atm and T=925 K. The end of compression pressures were consistently higher than the targeted pressure. Knowing that P_{max} at the end of compression generally has a standard deviation of less than 0.24%, several experiments were conducted to investigate experimental repeatability. Experiments with high n-heptane fractions consistently exhibited higher variability in the end of compression conditions, even with similar initial pressure trajectories. The high variability is attributed to the reaction during compression.

For systems that display reaction during compression, the traditional UM RCF definitions for effective pressure and temeterature are not appropriate. New definitions for the experimental conditions are necessary for UM RCF studies of fuels that exhibit significant NTC behavior. However, the results of Fig. 8.3 still demonstrate the increased reactivity of blends with high fractions of n-heptane. The NTC behavior, where reaction occurring during the compression process, leads to higher pressures and temperatures at the end of compression. The higher pressures and temperatures accelerate reaction, leading to dramatically shorter ignition delay times than those blends that do not exhibit reaction during compression. The low temperature heat release that leads to the increased pressure and temperature can be expected to occur in temperature combustion systems that operate at similar state conditions.

Blends with high fractions of methyl trans-3-hexenoate do not demonstrate reaction during compression. The unsaturated methyl trans-3-hexenoate ester kinetics appear to suppress the NTC behavior of the n-heptane as a non-linear rate, not just as a function of the blending fraction.

To more rigorously quantify the effects of reaction during compression on ignition behavior of fuels that exhibit NTC behavior, new definitions of the experimental conditions are necessary. This is beyond the scope of this work, as a new telemetry system would be needed to accurately define the location of the sabot (free piston) during the compression process. A telemetry system would allow redefinition of the

entire compression and ignition process as a function of volume using a geometric compression ratio (similar to crank angle degrees in engine studies), instead of as a function of time as is currently done in UM RCF studies.

Chapter 9

Conclusions and Recommendations for Future Work

The detailed conclusions for each of the experimental investigations conducted as part of this study are included in the corresponding chapters. This chapter summarizes the most important outcomes and presents recommendations for future work, including improvements to the University of Michigan Rapid Compression Facility.

9.1 Conclusions

These are the first experimental data to systematically consider the effects of structure on the reactivity of ester compounds at high-pressure and intermediate-temperature conditions. The data provide quantitative understanding (e.g. activation energies) of the structural effects on ester reactivity which are directly relevant to low temperature combustion technologies. Esters such as butyl methanoate and ethyl propanoate which have molecular structures capable of forming intermediate ring compounds during decomposition were more reactive than esters which do not form ring intermediates. Unsaturated esters ignited noticeably faster than fully saturated esters of similar size. Increasing the size of the ester also led to large increases in reactivity which was attributed to decreased energy required for H-abstraction from the parent fuel.

The significance of ester molecular structure is not only important for identifying and quantifying ignition properties. Researchers have suggested that the formation of an intermediate ring structure can lead to the formation of aromatics and soot through the formation of highly reactive alkenes, such as propene and the subsequent formation of propargyl radicals. The RCF speciation data from this study provide quantitative targets for improving the reaction mechanism pathways representing the formation of propene and other hydrocarbon species.

Negative temperature coefficient (NTC) behavior was observed for n-heptane, but not for any of the ester species at the conditions considered in this UM RCF study. Additionally, blends of methyl trans-3-hexenoate suppressed the NTC effects from the n-heptane. Because biodiesel fuels exhibit NTC behavior, the five reference ester considered here would not accurately represent the NTC chemical characteristics of biodiesels.

Two ignition regimes were identified for the saturated ester methyl butanoate. The behavior was clearly evident via high-speed imaging and is similar to behavior observed in previous UM RCF studies of iso-octane and syngas. Certain fuel lean conditions ($\phi \leq 0.4$) were found where homogeneous ignition always occurred for methyl butanoate. Less fuel lean conditions ($\phi \geq 0.6$) exhibited the presence of ignition kernels prior to volumetric ignition.

9.2 Recommended Future Studies

The University of Michigan Rapid Compression Facility (UM RCF) is a unique, well behaved and well characterized experimental apparatus capable of utilizing a broad assortment of diagnostics to quantify the auto-ignition phenomena of single and multicomponent fuels at state conditions relevant to practical combustion systems. By design, the UM RCF does not have a constrained volumetric compression ratio.

This makes quantification of ignition data from compounds exhibiting NTC behavior difficult. Many real fuels and larger reference compounds exhibit NTC behavior, where the NTC chemistry has high uncertainties. This motivates the development and implementation of new UM RCF diagnostics to rigorously investigate the ignition properties of these fuels.

Further studies of oxygenated compound auto-ignition are important to the continued understanding of the ignition of biofuels. Compounds that closely approximate real fuels such as biodiesel are of greatest interest; however, these compounds are experimentally and numerically difficult to investigate because of their large size and low volatility. Modifications which allow the investigation of heavier fuels in the UM RCF open new research possibilities and introduce new challenges.

The results of this study facilitate the development of fuels blended to specific targets of reactivity, to work in concert with specific combustion strategies. The results also provide the necessary background to develop rules for reaction which should be validated beyond the species considered in this work.

Appendices

Appendix A

Experimental Approach

A.1 UM RCF Line of Sight OH Absorption

The development of a line of sight laser diagnostic capable of quantifying OH radical concentrations, and a detailed description of its final form is presented in Donovan (23) and He (24). This diagnostic is a valuable tool for use in the UM RCF, however was not used in the work presented here.

The OH radical is very important in controlling the auto-ignition kinetics of fuel mixtures at the conditions studied in the UM RCF, due to its large role in in hydrogen peroxide formation:

$$\text{OH} + \text{OH} \ (+\text{M}) \rightleftharpoons \text{H}_2\text{O}_2 \ (+\text{M}). \tag{A.1}$$
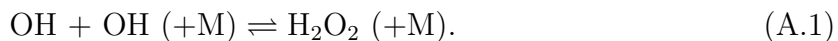
Quantitative measurements of this reaction, and others involving the OH radical, as well as other key radical species is valuable to understanding fuel oxidation at these conditions, and to developing chemical kinetic mechanisms to model the reacting systems.

The challenges of investigating such a short lived radical in a highly unsteady environment can be met by using a very fast laser diagnostic, such as the fixed-frequency *uv* laser absorption diagnostic developed. This tool is used to provide *in situ* mole fraction time-histories of OH during the ignition process. This information, when used in conjunction with rate of production analysis of appropriate chemical kinetic mechanisms can provide valuable insight and understanding of the reactions and species controlling radical formation, and other auto-ignition characteristics. An example of the type of data recorded is shown in Fig. A.1 for a lean iso-octane experiment, where the OH concentration during the compression and ignition process is shown in the lower frame as fractional absorption. The fractional absorption can be converted to a quantitative mole fraction through Beer's Law in conjunction with the development of the appropriate line shape function, assuming the test conditions along the path length of the laser can be considered uniform. For all cases of volumetric ignition, the OH concentration increased very rapidly during ignition, and was quickly consumed immediately following. Following ignition, it is important to note that the OH concentration falls to a steady state plateau level, that slowly decreases as the temperature in the test section decreases. This gives an indication of the long test times available in the UM RCF.

The data acquired using this diagnostic, such as the maximum value of OH, and the plateau value, in addition to its temporal history are valuable to the understanding the kinetics driving the ignition event. These data also provides valuable targets for the development and refinement of chemical mechanisms.
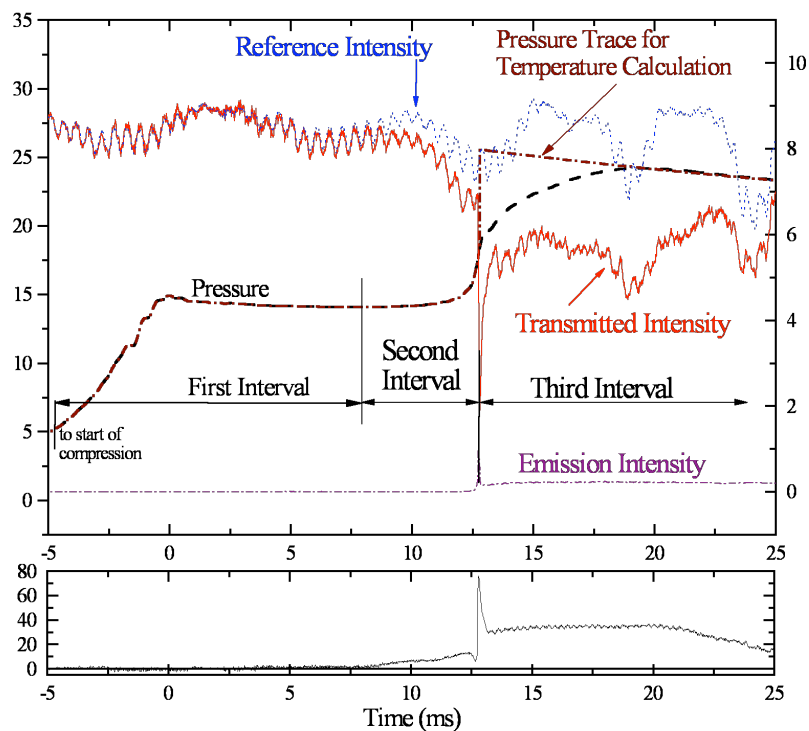
Figure A.1 Typical experimental results for pressure, transmitted, reference, and spontaneous emission time-histories for lean iso-octane ignition, experimental conditions of $P_{eff} = 14.27$ atm, $T_{eff} = 971$ K, $\phi = 0.35$, and $\chi_{O_2} = 16.6\%$. The fractional absorption shown in the lower panel was determined used the difference between the reference and the transmitted intensities. From He (24).

A.2   Camera Response Curves

Phantom v7.0

Spectral Response Curve
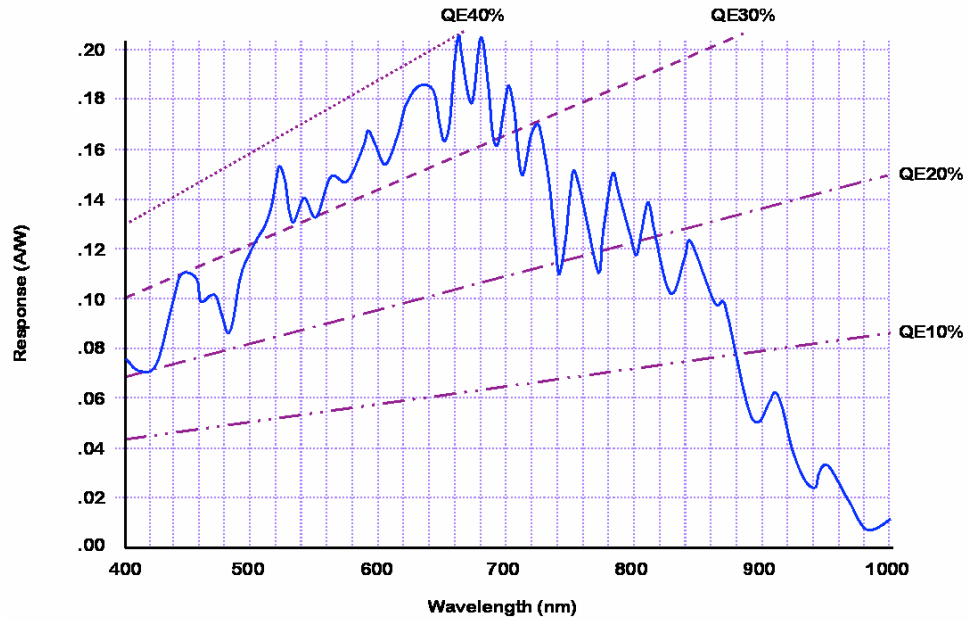
Color Response Curve
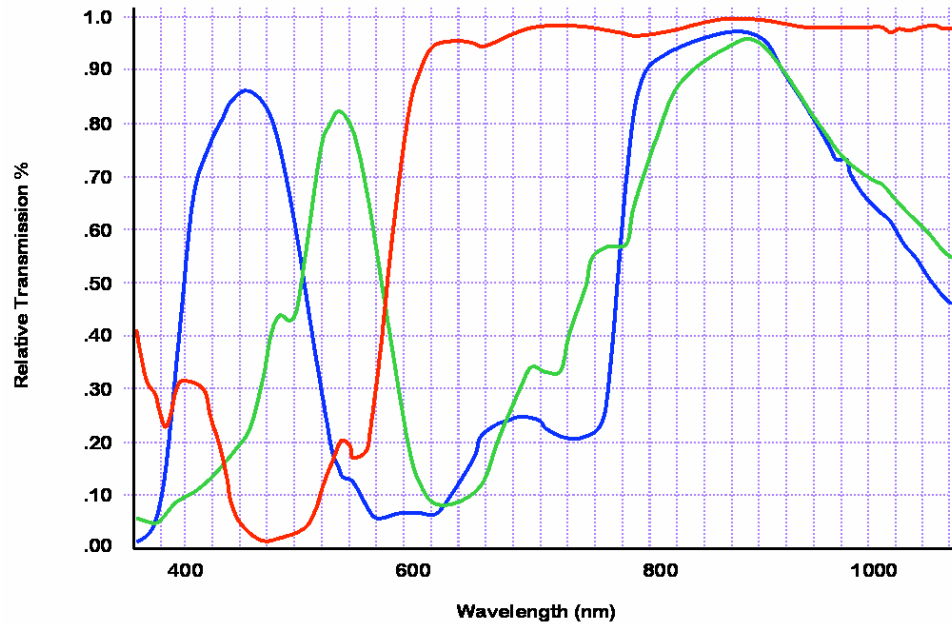
Figure A.2   Spectral response curve, and color response curves for the Phantom v7.1 high-speed digital camera.

A.3   Nose Cone Damage

Prior to each experiment, a nose cone must be chosen for use. The nosecone lifespan is affected by many things, including how hard the sabot hit, whether or not the sabot bounced back into the nosecone, if it has already been used many times, etc. A photograph of a new nosecone is shown in the Figure below, as well as photographs highlighting some of the features that render a nosecone dead.

(a) Good nosecone

(b) Nosecone with ridge on annulus from partial seating (left), and nosecone after it has been hit too hard(right)

(c) Nosecone with damage on fillet from misaligned seating

(d) Nosecone with damage on sabot fitment to sabot from sabot bouncing
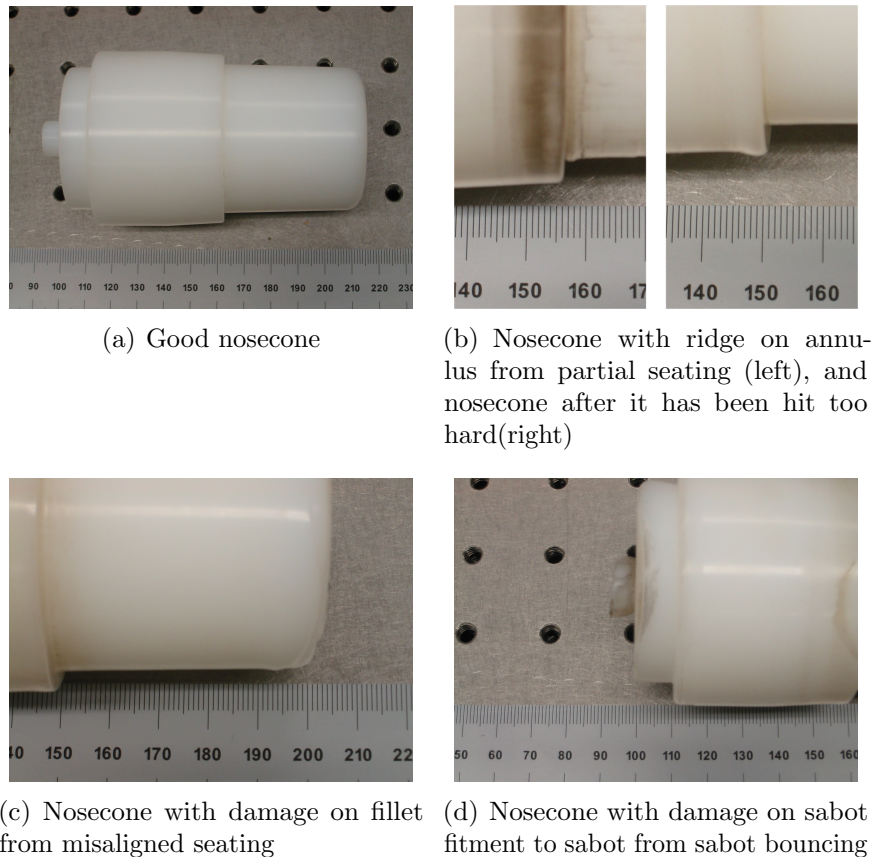
Figure A.3   The top left frame shows a new nosecone. Note the smooth fillet, and slightly conical shape near the front of the nosecone that allows for a smooth interference fit with the extension section. The top right frame shows the ridges that develop when the nosecone is only partially seated during an experiment. If the ridges appear to have a larger diameter than the annulus immediately on both sides of the ridge, the nosecone must not be used. This frame also shows a nosecone that has been seated to hard, and the step is deformed outward. The lower left frame shows the dents that can form at the front of the nosecone if it did not seat concentrically during an experiment. Again, if these are large, the nosecone must not be used. The lower right frame shows the damage that can occur if the sabot rebounds into the back of the nosecone after it is initially seated. In this case the nosecone will no longer fit onto the sabot during assembly.

A.4   Mylar Sheet

The plastic sheet used the separate the driven section from the globe valve is .002"
thick Mylar®. The plastic sheet is cut and scored carefully using a rotary cutter.
It is then cleaned and placed between the flanges of the driven section and globe
valve. The large o-ring, and the flange on the driven section should be cleaned and
greased prior to installation of the plastic sheet. This is done to ensure a good seal,
and adequately locate the sheet.
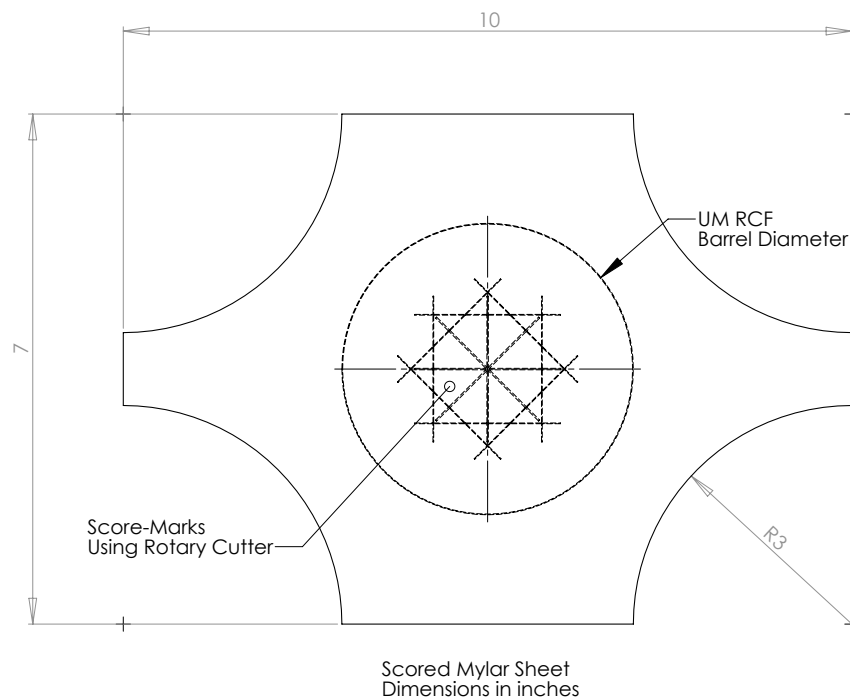
Figure A.4   Dimensioned drawing of the plastic sheet, highlighting the score marks and
their proximity to the barrel of the driven section.

A.5   Compression Ratios

Table A.1   Summary of UM RCF test manifold configurations, and the resulting approximate compression ratio.

Nosecone	Long ext. sec.	Short ext. sec.	S.S. thermo. sec.	Test sec.	S.V. imaging sec.	C.R.
Short		•		•		29
Short		•	•	•		26
Short		•		•	•	23

Many other discrete steps of compression ratios are available through different combinations of test manifold components, however the common ones used are listed here. Another option to increase the compression ratio is to use the long nosecone design.

A.6 Experiment Record Sheet

Date		Fuel-					Notes
Target Temp		Target Press					
ϕ		Inert/O2					
N2 fraction							
Target CR							
Actual CR							
TC Section							
Extension Section							
Ambient Temp							
Driver Pressure							
Initial Pressure	|	Sampling Info					
Target Press		Trigger Delay					
Charge Pressure		Pulse Width					
Estimated Tign		Old Amp Sens.					
Actual Tign		Old Amp Scale					
Target Mixture	initial-	fuel-	O2-	N2-	Ar-	CO2-	
Target Mixture	initial-	fuel-	O2-	N2-	Ar-	CO2-	
Actual Mixture	initial-	fuel-	O2-	N2-	Ar-	CO2-	

Figure A.5 The information regarding the each experiment is recorded on this single sheet for the purpose of experiment design, taking short notes, and recording additional parameters not recorded by any of the digital data acquisition programs.

A.7   Triggering Circuit
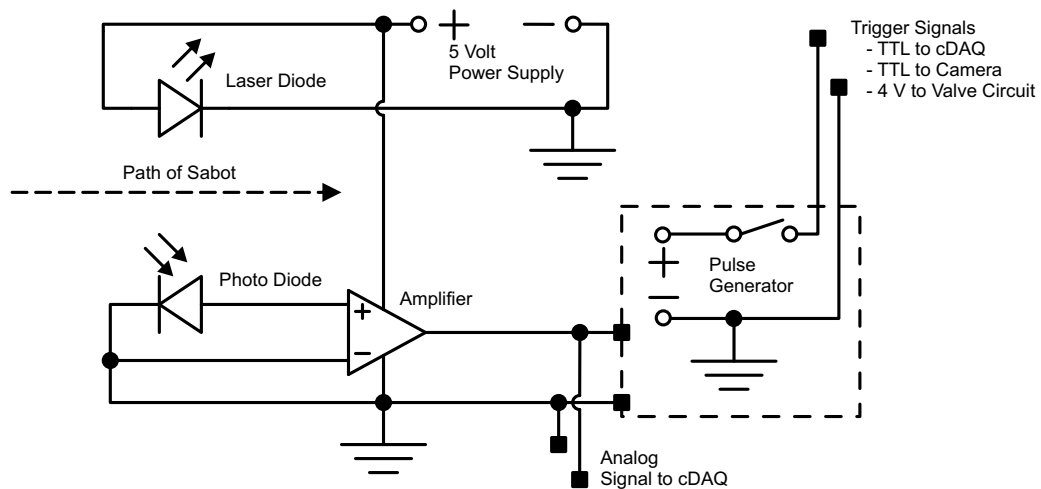
Figure A.6   Schematic of the circuit used to trigger and synchronize the data acquisition system, the high-speed camera, and the high-speed gas sampling system.

A.8 Gas Sampling System Design

(a) Old style sampling valve attachment

(b) New style sampling valve attachment
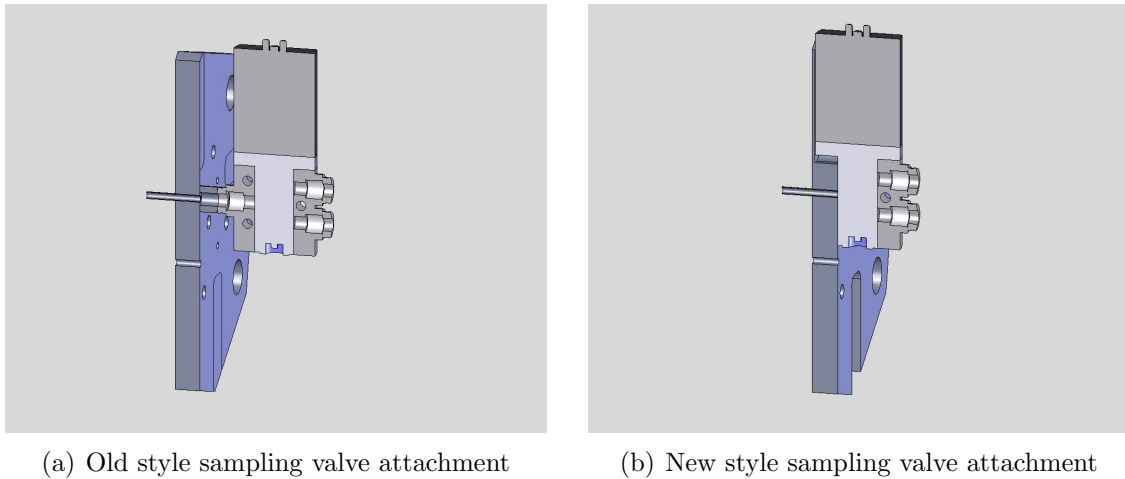
Figure A.7 Cross sectioned isometric view of the gas sampling end wall designs. Note the much smaller dead volume in the new design, between the end of the sampling tube to body of the poppet valve.

original spring
— L = 0.25"
— rate = ~65 lb/in

valve

solenoid

armature

new spring
— century spring part # II-96
— L = 0.25"
— rate = 125 lb/in
preloaded
— 3 x 0.01825" washers
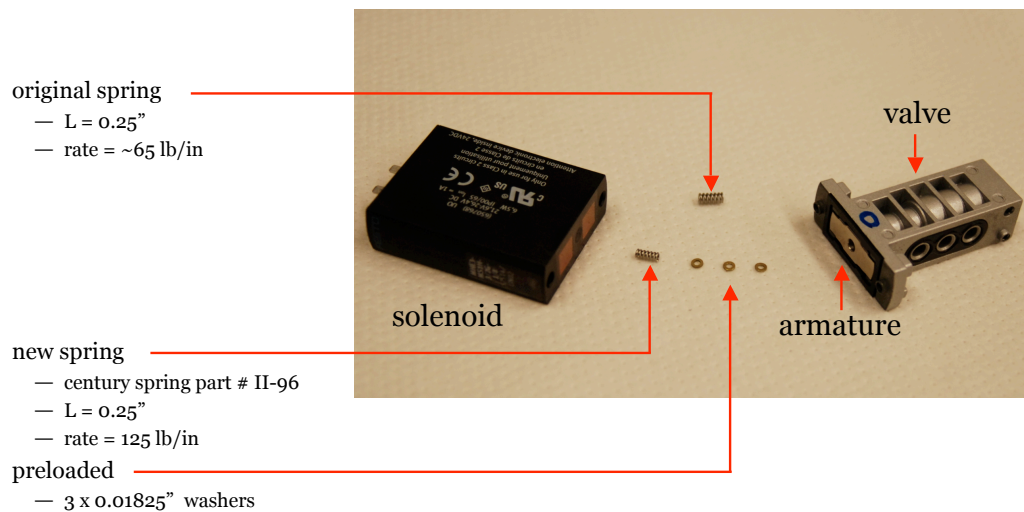
Figure A.8 Exploded view of a dissembled sampling valve (Festo MHE3). The original return spring has been replaced with a much stronger spring. The spring has additionally been preloaded using brass washers.
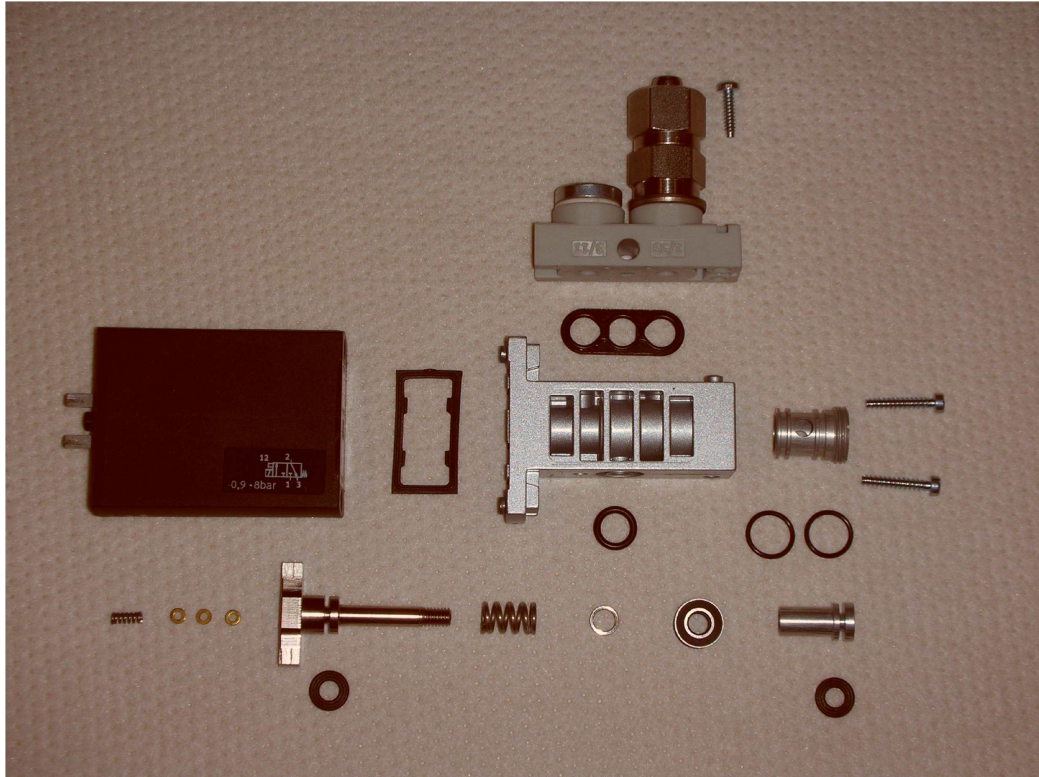
Figure A.9 Exploded view of a dissembled sampling valve (Festo MHE3). This view highlights the internal components of the poppet valve assembly. When leaking, these valves can be rebuilt by entirely disassembling them, cleaning, and generously regreasing the seals. The armature position is then slowly tightened into position, while the coil is fired. The armature is in the proper location when you first hear an audible "CLICK".
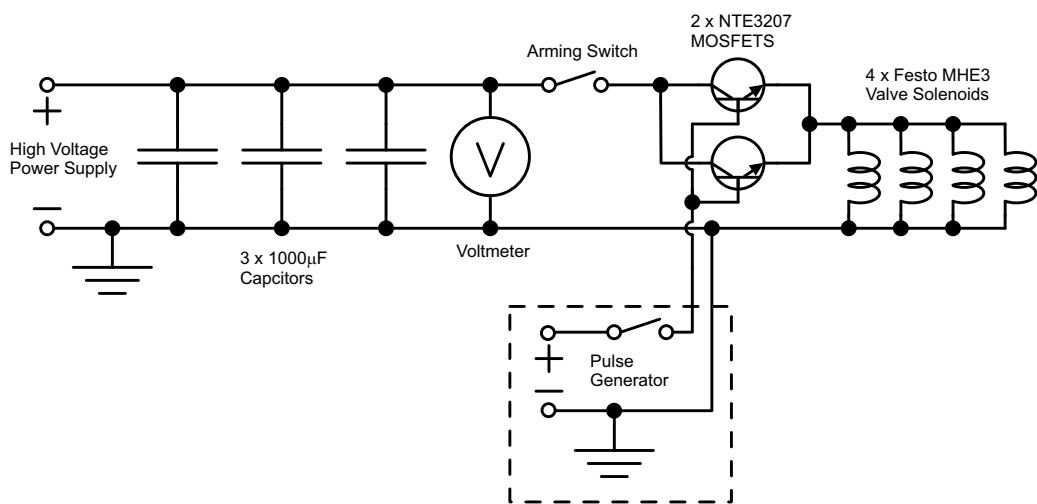
Figure A.10 Schematic of the custom power supply used to drive the modified high-speed valves.

A.9 Gas Chromatography

A.9.1 Column Parameters

Table A.2 Summary of the GC equipment and the maximum column temperatures.

Oven	Column	Col. Dimensions	T_{max}	$T_{16hrs.}$
GC1-	Varian CP Molsieve 5A FS	25m x 0.53mm i.d.	350°C	350°C
P.E. Autosystem GC	Varian Porobond Q FS	25m x 0.53mm i.d.	320°C	250°C
GC2-	Varian CP PLOT LowOx FS	10m x 0.53mm i.d.	350°C	300°C
P.E. Autosystem GC				
GC3-	Varian CP Al_2O_3/Na_2SO_4 FS	50m x 0.53mm i.d.	200°C	200°C
P.E. Autosystem GC				
GC4-	Restek RTX-1 FS (A)	60m x 0.32mm i.d.	320°C	150°C
P.E. Clarus 500GC	Restek Shin-Carbon ST (B)	5m x 0.75mm i.d.	330°C	150°C

A.9.2 Column Preparation

Table A.3 Summary of the GC preparation programs. Both sets of preparation programs are run with the 10-port valves in the sampling position. The detector heaters are turned on for the conditioning program and for the standby programs with the same range and attenuation values that are used for analysis. Note that the GC's return to the start of program temperature when the cycle is completed. Also note that the standby programs start and end at the start of program temperatures used for analysis.

Oven	Conditioning (Method 3, 18hr)	Standby (Method 4, 8hr)
GC1	30°C (18 min) → 5°C/min → 320°C (30min) → -5°C/min → 250°C (16hr)	30°C (2min) → 5°C/min → 250°C (2.5hr) → -5°C/min → 30°C (4hr)
GC2	40°C (18 min) → 5°C/min → 350°C (30min) → -5°C/min → 300°C (16hr)	80°C (24 min) → 5°C/min → 300°C (2hr) → -5°C/min → 40°C (4hr)
GC3	40°C (28 min) → 5°C/min → 200°C (17hr)	40°C (26 min) → 5°C/min → 200°C (2.5hr) → -5°C/min → 40°C (4hr)
GC4	40°C (30 min) → 5°C/min → 320°C (3hr) → -5°C/min → 150°C (13hr)	40°C (16 min) → 5°C/min → 150°C (3hr) → -5°C/min → 40°C (4hr)

A.9.3   Analysis Programs

Table A.4   Summary of the GC analysis programs. All programs contain 54 minutes of analysis, followed by 6 minutes of increasing temperature to purge the column. GC's with TCD's have isothermal analysis programs. Valves are all started in the sampling position (ON). The flowrates for the FID flames are 45 ml/min H_2 and 450 ml/min air.

Detector (Method 5)	Temperature Program, 1hr	Events	Carrier Gas/ Setting	Detector/ Temp.	Range/ Atten.
GC1	30°C (55 min) → 10°C/min → 100°C	0.01 GSV1 OFF 1.83 GSV1 ON	Helium 26.0 cm/sec	TCD 150°C	3 4
GC2	80°C (10 min) → 10°C/min → 150°C (33 min) → 10°C/min → 310°C	0.03 GSV1 OFF	Helium 34.0 cm/sec	FID 150°C	1 1
GC3	40°C (10 min) → 10°C/min → 140°C (34 min) → 10°C/min → 200°C	0.03 GSV1 OFF	Helium 36.0 cm/sec	FID 150°C	1 1
GC4A	40°C (54 min) → 10°C/min → 100°C	0.01 GSV3 ON 0.10 GSV1 ON	Helium 20.0 cm/sec	FID 150°C	1 1
GC4B	40°C (54 min) → 10°C/min → 100°C	0.01 GSV3 ON 0.10 GSV1 ON	Argon 15.0 ml/min	TCD 200°C	+40 mA 1

A.10 Labview Data Acquisition Code
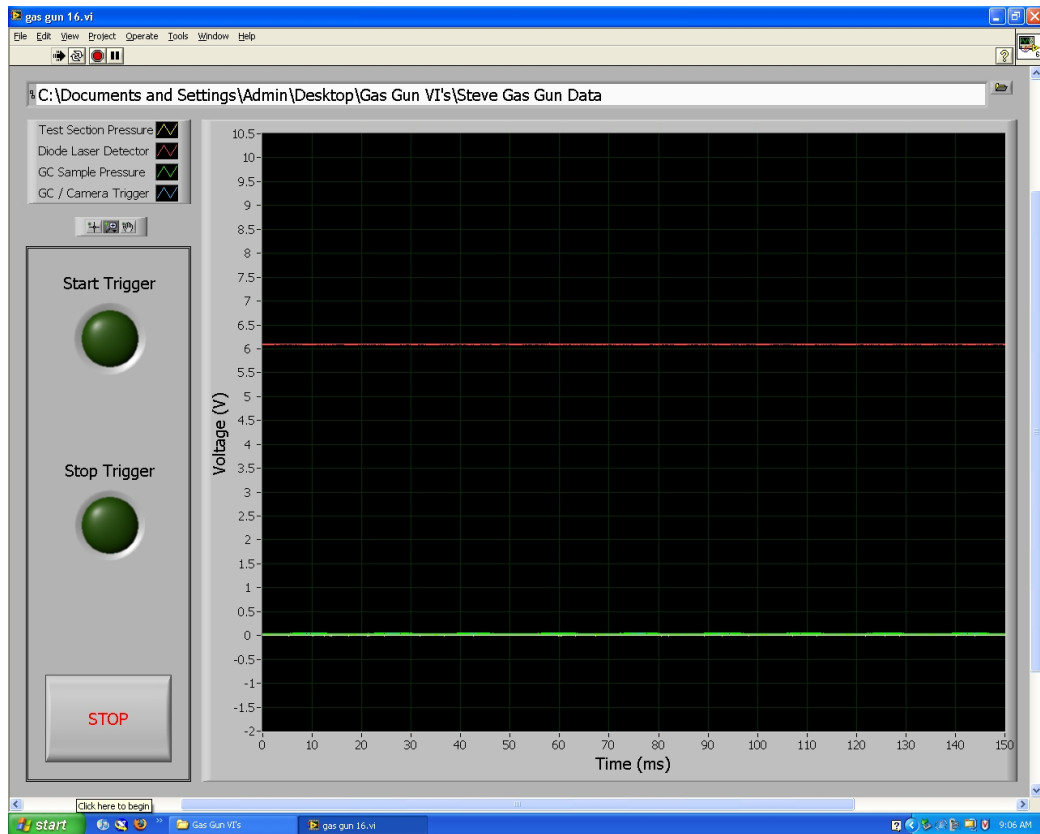
Figure A.11 Screenshot of the Labview Front Panel used for data acquisition.
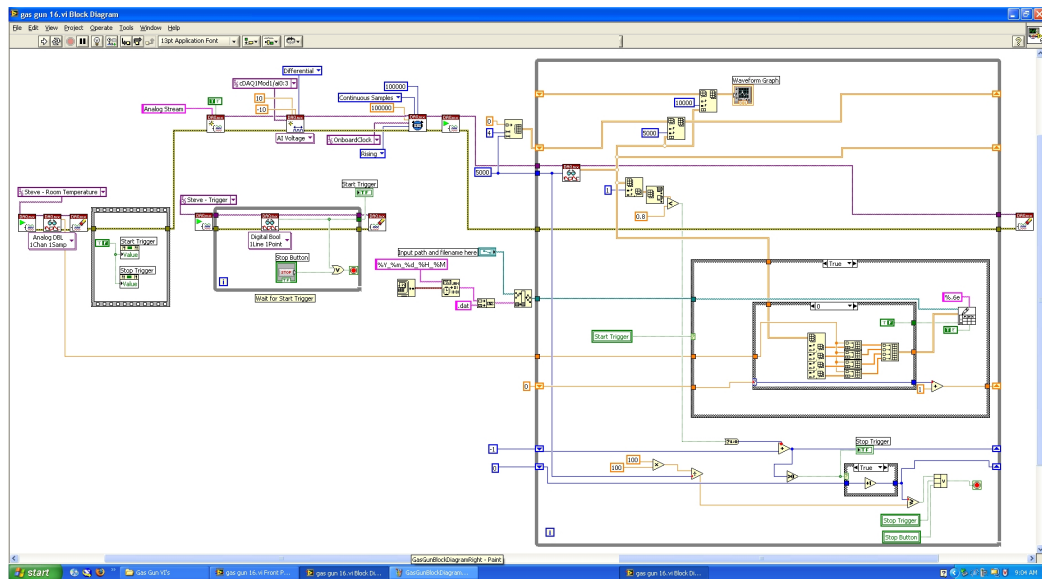
Figure A.12 Screenshot of the Labview Block Diagram used for data acquisition.

A.11 Globe Valve Settings

A.11.1 Servo Controller Settings

The settings for the Shore Western SC-3000C hydraulic servo controller are as follows: the controller must be set to the Stroke function, with the X1 multiplier, meter function 6, with the integrator OFF.

Table A.5 The following are the potentiometer values.

Parameter	Value
STROKE	10.00
LOAD	0.90
STRAIN	0.00
EXCITATION	0.00
RATE	0.00
LOOP	0.30
SETPOINT	2.70
SPAN	9.45

A.11.2 Pulse Generator Settings

HP 8112A Pulse Generator

The pulse generator must be turned on and set to the Trigger mode using the shallowest sloped step.

Table A.6 The following are the pulse parameter values.

Parameter	Value
PER	500 ms
DEL	65.0 ns
WID	100 ms
LEE	10.0 ms
TRE	10.0 ms
HIL	+8.00 V
LOL	-8.00 V

A.12 Pressure Transducer Amplifier Settings

Kistler 5010B Dual Mode Amplifier

The Transducer Sensitivity must be set to 1.39 to output units of psi, which is used in the Matlab readfiles. The Scale is most often set to 50, and this number must be reflected in the Matlab readfiles as well. To prevent the amplifier from going "Overvoltage", the scale is changed to 100 for high pressure runs, and reduced to 30 to increase the resolution for low pressure runs. These changes must also be reflected in the readfiles.

The amplifier is also set to the Charge Mode, and the Time Constant is set to Long. The amplifier must be set to operate immediately prior to the experiment to output the pressure data. This is done to prevent any thermal drift that may occur prior to running the experiment.

A.13 Driver Pressure Guidelines

The driver pressure is varied in order to have the nosecone seat smoothly into the extension section. The driver pressure is changed to accommodate many other parameters. These include the initial charge pressure, the compression ratio, the condition of the nosecone, the condition of the u-rings, and the specific experimental diagnostics being used–remember the line of sight laser diagnostics are very sensitive to mechanical noise.

The driver pressure is increased when the charge pressure is higher, the compression ratio is higher, the u-rings are newer, and the nosecone is newer. The specific pressure is very dependent on the immediate history of the configuration, and must be adjusted after every experiment. A good starting driver pressure is generally between 12-16 psi for experiments with 100 torr charge pressures, and compression ratios between 26 and 29. The pressure will have to be adjusted after observing how hard the the nosecone seats, and what sort of condition it is in after being pressed out.

Appendix B

Results Analysis MATLAB Codes
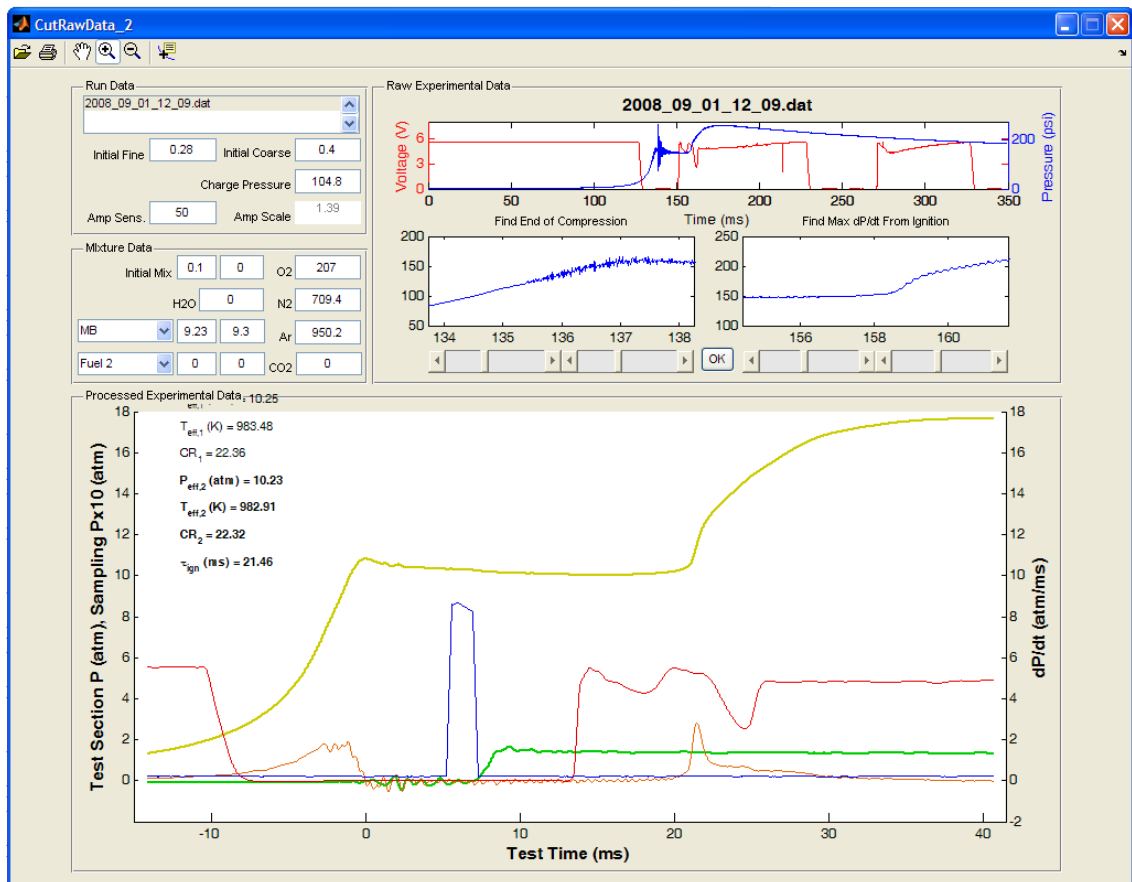
Figure B.1 Screenshot of the MATLAB experiment analysis graphical user interface.
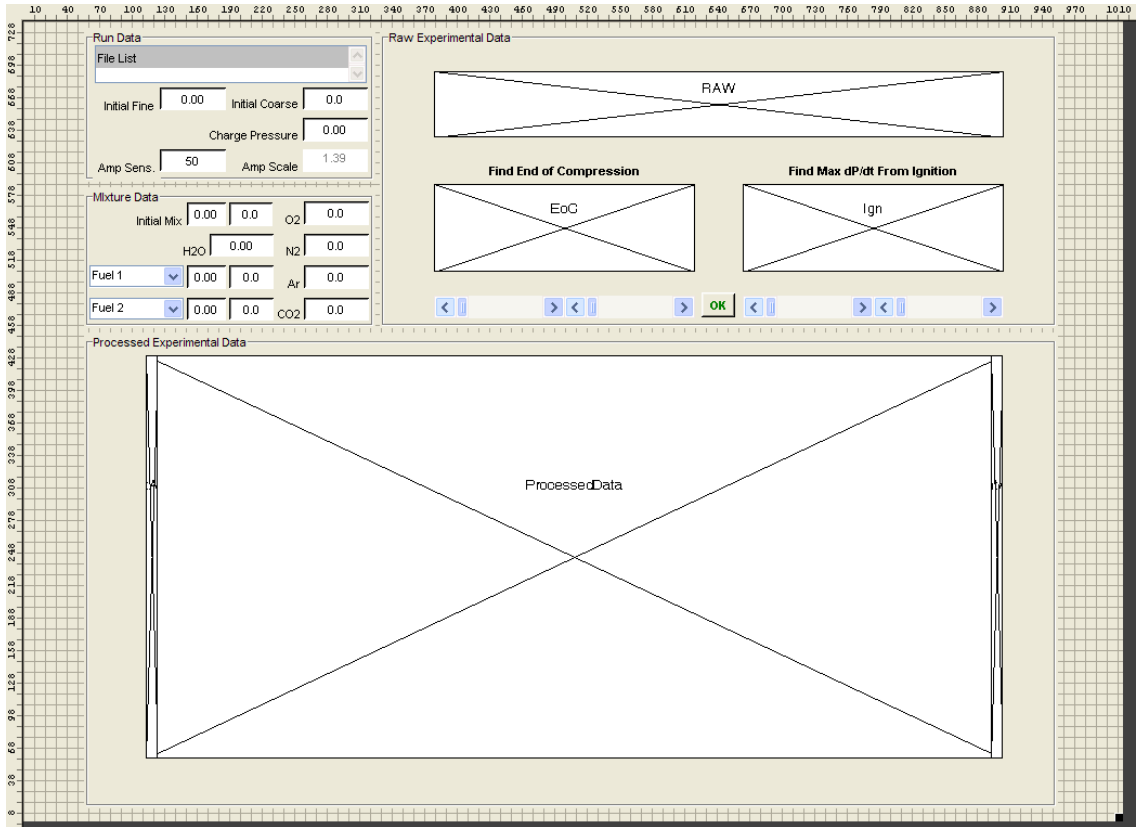
Figure B.2 Screenshot of the MATLAB figure layout for the graphical user interface.

B.1   Experiment Design Code

The following code is used to design an experiment.

```
clear all
global Molar_H2 Molar_O2 Molar_Ar Molar_N2...
       Molar_CO2 Molar_H2O Molar_CO Molar_mb

%INPUT DATA%
CR=30        %compression ratio
total=950;     %initial pressure (torr)

%EQUATION FOR MOLAR COEFFICIENTS%
Phi=.4;
I_O2=3.76;
mb_=1;
O2_=6.5/Phi;

H2_=0;
CO_=0;
H2O_=0;

%INERT RATIO
Inert= (6.5/Phi)*I_O2;
%PICK BALANCE GAS (N2 PLUS AR OR CO2)
N2fraction=.991;
N2_=N2fraction*Inert;
Ar_= (1-N2fraction)*Inert;
CO2_= 0;
% Ar_ = 0;
% CO2_=(1-N2fraction)*Inert;
TotMol=mb_+O2_+N2_+Ar_+CO2_;

%CONVERT FOR CHARGE PRESSURE%
PresPerMole=total/TotMol;
H2_=H2_*PresPerMole;
CO_=CO_*PresPerMole;
H2O_=H2O_*PresPerMole;
O2_=O2_*PresPerMole;
N2_=N2_*PresPerMole;
Ar_=Ar_*PresPerMole;
CO2_=CO2_*PresPerMole;
mb_=mb_*PresPerMole;

%CHANGE TO XINS VARIABLES%
Molar_H2=H2_;
Molar_H2=H2_/total;
Molar_CO=CO_;
Molar_CO=CO_/total;
Molar_H2O=H2O_;
Molar_H2O=H2O_/total;
Molar_O2=O2_
Molar_O2=O2_/total;
Molar_N2=N2_
Molar_N2=N2_/total;
Molar_Ar=Ar_
Molar_Ar=Ar_/total;
Molar_CO2=CO2_
Molar_CO2=CO2_/total;
Molar_mb=mb_
Molar_mb=mb_/total;

%SETUP TO EXPORT FOR VARIABLE SPECIFIC HEATS%
T0=273.15+24;    %initial temperature
P0=total;  %initial pressure (torr)
T=T0;
P=P0;
x=0.001;
for i=1:x:CR-x
    [gamma]=gamma_all(T);
    T=T*((i+x)/i)^(gamma-1);
    P=P*((i+x)/i)^gamma;
end

P=P*0.133322/6.894757;
P_psi=P
P_atm=P_psi*.068046
T;
T_kelvin=T
CR;
```

B.2   Experiment Analysis Code

The following code is used to analyze the raw data following an experiment.

```
%This program is a GUI used to analyze cDAQ data
%Written by Stephen M. Walton February 2008
function varargout = CutRawData_2(varargin);
% CUTRAWDATA_2 M-file for CutRawData_2.fig
%      CUTRAWDATA_2, by itself, creates a new CUTRAWDATA_2 or raises the existing
%      singleton*.
%
%      H = CUTRAWDATA_2 returns the handle to a new CUTRAWDATA_2 or the handle to
%      the existing singleton*.
%
%      CUTRAWDATA_2('CALLBACK',hObject,eventData,handles,...) calls the local
%      function named CALLBACK in CUTRAWDATA_2.M with the given input arguments.
%
%      CUTRAWDATA_2('Property','Value',...) creates a new CUTRAWDATA_2 or raises the
%      existing singleton*.  Starting from the left, property value pairs are
%      applied to the GUI before CutRawData_1_OpeningFunction gets called.  An
%      unrecognized property name or invalid value makes property application
%      stop.  All inputs are passed to CutRawData_2_OpeningFcn via varargin.
%
%      *See GUI Options on GUIDE's Tools menu.  Choose "GUI allows only one
%      instance to run (singleton)".
%
% See also: GUIDE, GUIDATA, GUIHANDLES
% Edit the above text to modify the response to help CutRawData_2
% Last Modified by GUIDE v2.5 04-Feb-2008 18:20:03
% Begin initialization code - DO NOT EDIT
clc;
gui_Singleton = 1;
gui_State = struct('gui_Name',       mfilename, ...
                   'gui_Singleton',  gui_Singleton, ...
                   'gui_OpeningFcn', @CutRawData_2_OpeningFcn, ...
                   'gui_OutputFcn',  @CutRawData_2_OutputFcn, ...
                   'gui_LayoutFcn',  [] , ...
                   'gui_Callback',   []);
if nargin && ischar(varargin{1})
    gui_State.gui_Callback = str2func(varargin{1});
end

if nargout
    [varargout{1:nargout}] = gui_mainfcn(gui_State, varargin{:});
else
    gui_mainfcn(gui_State, varargin{:});
end
% End initialization code - DO NOT EDIT


% --- Executes just before CutRawData_2 is made visible.
function CutRawData_2_OpeningFcn(hObject, eventdata, handles, varargin)
% This function has no output args, see OutputFcn.
% hObject    handle to figure
% eventdata  reserved - to be defined in a future version of MATLAB
% handles    structure with handles and user data (see GUIDATA)
% varargin   command line arguments to CutRawData_2 (see VARARGIN)
% Declare and create all the UI objects in this GUI here so that they can
% be used in any functions

guidata(hObject, handles);
load_listbox(pwd,handles);

if 2 == exist('fileselected.mat')
load('fileselected.mat');
set(handles.FileList,'Value',index_selected);
end

if 2 == exist('inputfilename.mat')
load('inputfilename');
end

if 2 == exist('TestInfo.mat')
load('TestInfo');
%%%%%%% Reading off amplifier, scale should read 1.39 to output psi
%%%%%%% from calibration card from pressure transducer
%set(handles.AmpScale,'String',num2str(AmpScale));
set(handles.AmpSensitivity,'String',num2str(AmpSensitivity));
set(handles.InitialFineExp,'String',num2str(InitialFineExp));
set(handles.InitialCoarseExp,'String',num2str(InitialCoarseExp));
set(handles.ChargePressure,'String',num2str(ChargePressure));
AMP = AmpSensitivity;
CHARGE_PRESSURE = ChargePressure;  %torr
end

if 2 == exist('MixtureInfo.mat')
load('MixtureInfo');
set(handles.InitialMix,'String',num2str(InitialMix));
set(handles.InitialMixC,'String',num2str(InitialMixC));
```

```matlab
set(handles.H2O,'String',num2str(H2O));
set(handles.CO2,'String',num2str(CO2));
set(handles.Ar,'String',num2str(Ar));
set(handles.N2,'String',num2str(N2));
set(handles.O2,'String',num2str(O2));
set(handles.Fuel1F,'String',num2str(Fuel1F));
set(handles.Fuel1C,'String',num2str(Fuel1C));
set(handles.Fuel2F,'String',num2str(Fuel2F));
set(handles.Fuel2C,'String',num2str(Fuel2C));
set(handles.Fuel1menu,'Val',Fuel1menu);
set(handles.Fuel2menu,'Val',Fuel2menu);
end

%%%%%%%%%%%%%%  Plot raw data in psi if info is present, otherwise plot in
%%%%%%%%%%%%%%  voltage, or not at all
if (2 == exist('inputfilename.mat'))&& (2 == exist('TestInfo.mat'))...
        && (2 == exist('MixtureInfo.mat'))&& (2 == exist('fileselected.mat'))
%%%%%% Define the column variables %%%%%%%%%%%%%%%%%%%%%%%%%%%%%%%%%%%%%%%
cDAQ = dlmread(inputfilename);
Room_Temperature=cDAQ(1,1); %Degrees Celsius
cDAQ = cDAQ(2:size(cDAQ),:); %Cut off Room Temperature Row
[l w]=size(cDAQ); %Find size of array
length_data=l/100; % used to plot search spans
Test_Section_Pressure=cDAQ(:,1); %Voltage From Amplifier
Camera_Trigger=cDAQ(:,2); % Voltage
Gas_Sampling_Pressure=cDAQ(:,3); %Voltage From Amplifier
Gas_Sampling_Trigger=cDAQ(:,4); %Voltage
Test_Time=(0:0.01:(l-1)*0.01)'; %converts row spacing to milliseconds
%%%%%%%%%%%%%%%%%%%%%%%%%%%%%%%%%%%%%%%%%%%%%%%%%%%%%%%%%%%%%%%%%%%%%%%%%%%%
CHARGE_PRESSURE = ChargePressure;
total           = CHARGE_PRESSURE;  %charge pressure  (torr)
Temp            = Room_Temperature; %initial temperature (Celsius)
%%%%%%%%%%%%%%%%%%%%%%%%%%%%%%%%%%%%%%%%%%%%%%%%%%%%%%%%%%%%%%%%%%%%%%%%%%%%
%%%%  CALCULATE ITITIAL PRESSURE in psi, AKA CHARGE PRESSURE     %%%%%%%%%%
Initial_Pressure = CHARGE_PRESSURE * 0.133322/6.894757;   %45torr=2.1077psi
%%%%%%%%%   ADJUST FOR AMPLIFIER VALUE       %%%%%%%%%%%%%%%%%%%%%%%%%%%
Test_Section_Pressure = Test_Section_Pressure*AmpSensitivity;
P_offset = mean(Test_Section_Pressure(1:1000)); %calculate pressure offset
Test_Section_Pressure = Test_Section_Pressure-P_offset+Initial_Pressure;
axes(handles.RAW);
[AX,plot1,plot2] = plotyy(Test_Time,Camera_Trigger,...
                            Test_Time,Test_Section_Pressure,'plot');
title ({inputfilename},'FontSize',12,'FontWeight','bold','Interpreter','none');
xlabel('Time (ms)');
set(plot1,'Color','r');
set(get(AX(1),'Ylabel'),'String','Voltage (V)','Color','r');
set(AX(1),'YLim',[0 8]);
set(AX(1),'YTick',[0:3:8],'Ycolor','r');
set(plot2,'Color','b');
set(get(AX(2),'Ylabel'),'String','Pressure (psi)','Color','b');
set(AX(2),'YLim',[0 max(Test_Section_Pressure*1.05)]);
set(AX(2),'YTick',[0:200:max(Test_Section_Pressure*1.25)],'Ycolor','b');
save('plotrawdata', 'Test_Time', 'Camera_Trigger', 'Test_Section_Pressure'...
    ,'Gas_Sampling_Trigger','Gas_Sampling_Pressure','inputfilename','length_data');
h = zoom;
setAxesZoomMotion(h,AX,'horizontal');
p = pan;
setAllowAxesPan(p,AX,false);
elseif (2 == exist('inputfilename.mat'))&& (2 == exist('fileselected.mat'))
cDAQ = dlmread(inputfilename);
Room_Temperature=cDAQ(1,1); %Degrees Celsius
cDAQ = cDAQ(2:size(cDAQ),:); %Cut off Room Temperature Row
[l w]=size(cDAQ); %Find size of array
length_data=l/100; % used to plot search spans
Test_Section_Pressure=cDAQ(:,1); %Voltage From Amplifier
Camera_Trigger=cDAQ(:,2); % Voltage
Gas_Sampling_Pressure=cDAQ(:,3); %Voltage From Amplifier
Gas_Sampling_Trigger=cDAQ(:,4); %Voltage
Test_Time=(0:0.01:(l-1)*0.01)'; %converts row spacing to milliseconds
[AX,plot1,plot2] = plotyy(Test_Time,Camera_Trigger,...
                            Test_Time,Test_Section_Pressure,'plot');
title ({inputfilename},'FontSize',12,'FontWeight','bold','Interpreter','none');
xlabel('Time (ms)');
set(plot1,'Color','r');
set(get(AX(1),'Ylabel'),'String','Voltage (V)','Color','r');
set(AX(1),'YLim',[0 8]);
set(AX(1),'YTick',[0:3:8],'Ycolor','r');
set(plot2,'Color','b');
set(get(AX(2),'Ylabel'),'String','Voltage (V)','Color','b');
set(AX(2),'YLim',[0 max(Test_Section_Pressure*1.05)]);
set(AX(2),'YTick',[0:5:max(Test_Section_Pressure*1.25)],'Ycolor','b');
save('plotrawdata', 'Test_Time', 'Camera_Trigger', 'Test_Section_Pressure'...
    ,'Gas_Sampling_Trigger','Gas_Sampling_Pressure','inputfilename','length_data');
h = zoom;
setAxesZoomMotion(h,AX,'horizontal');
p = pan;
setAllowAxesPan(p,AX,false);
else
end

axes(handles.ProcessedData);
ax1 = gca;
```

```
xlabel('Test Time (ms)','FontSize',12,'FontWeight','bold');
set(ax1,'Xlim',[-15 35]);
axes(handles.LeftAxis);
ax0 = gca;
set(ax0,'XColor','k','YColor','k');
set(ax0,'ylim',[-2 20]);
set(ax0,'YTick',(-100:2:-100));
set(get(ax0,'YLabel'),'String','Pressure (atm)','FontSize',12,'FontWeight','bold','Color','k');
axes(handles.RightAxis);
ax3 = gca;
set(ax3,'YAxisLocation','right','Color','w','XColor','k','YColor','k');
set(ax3,'ylim',[-2 20]);
set(ax3,'YTick',(-100:2:-100),'YColor','k');
set(get(ax3,'YLabel'),'String','dP/dt (atm/ms)','FontSize',12,'FontWeight','bold','Color','k');


%%%%%%%%% Plot the search spans if they are available %%%%%%%%%%%%%%%%%%%
%%%%%%%%%%%%%%%%%%%%%%%%%%%%%%%%%%%%%%%%%%%%%%%%%%%%%%%%%%%%%%%%%%%%%%%%%%
if (2 == exist('inputfilename.mat'))&& (2 == exist('fileselected.mat'))

set(handles.EoC_min,'Max',length_data,'Min',1);
set(handles.EoC_max,'Max',length_data,'Min',1);
set(handles.EoC_min,'Value',length_data/2);
set(handles.EoC_max,'Value',length_data/2);
if (2 == exist('eocsearch.mat')) &&  (2 == exist('plotrawdata.mat'))...
      && (2 == exist('inputfilename.mat'))&& (2 == exist('fileselected.mat'))
    ploteocsearch(hObject, eventdata, handles)
end

set(handles.Ign_min,'Max',length_data,'Min',1);
set(handles.Ign_max,'Max',length_data,'Min',1);
set(handles.Ign_min,'Value',length_data/2);
set(handles.Ign_max,'Value',length_data/2);
if (2 == exist('ignsearch.mat')) &&  (2 == exist('plotrawdata.mat'))...
      && (2 == exist('inputfilename.mat'))&& (2 == exist('fileselected.mat'))
    plotignsearch(hObject, eventdata, handles)
end
end
% Choose default command line output for CutRawData_2
handles.output = hObject;

% Update handles structure
guidata(hObject, handles);

if (2 == exist('plotprocesseddata.mat')) && (2 == exist('eocsearch.mat')) && (2 == exist('ignsearch.mat'))...
      && (2 == exist('inputfilename.mat'))&& (2 == exist('TestInfo.mat'))&& (2 == exist('MixtureInfo.mat'))...
      && (2 == exist('fileselected.mat'))

    load('fileselected');
    set(handles.FileList,'Value',index_selected);
    Save_Callback(hObject, eventdata, handles);
end

%h = zoom;
%setAllowAxesZoom(h,handles.RAW,false);
%zoom(handles.EoC,'Enable','off');
% hZ = zoom(handles.RAW);
% hM = hZ.ModeHandle;
% set(hM,'Blocking',false);
h = zoom;
setAxesZoomMotion(h,handles.EoC,'horizontal');
setAxesZoomMotion(h,handles.Ign,'horizontal');
set(h,'ActionPostCallback',{@zoomcallback,handles,hObject,eventdata});
set(h,'Enable','on');
p = pan;
setAllowAxesPan(p,handles.EoC,false);
setAllowAxesPan(p,handles.Ign,false);

 % UIWAIT makes CutRawData_2 wait for user response (see UIRESUME)
 % uiwait(handles.figure1);

% --- Outputs from this function are returned to the command line.
function varargout = CutRawData_2_OutputFcn(hObject, eventdata, handles)
% varargout  cell array for returning output args (see VARARGOUT);
% hObject    handle to figure
% eventdata  reserved - to be defined in a future version of MATLAB
% handles    structure with handles and user data (see GUIDATA)

% Get default command line output from handles structure
varargout{1} = handles.output;

function load_listbox(dir_path,handles)
cd (dir_path)
dir_struct = dir(fullfile(dir_path,'*.dat'));
[sorted_names,sorted_index] = sortrows({dir_struct.name}');
handles.file_names = sorted_names;
handles.is_dir = [dir_struct.isdir];
handles.sorted_index = sorted_index;
set(handles.FileList,'String',handles.file_names,'max',2,...
'min',0,'Value',[])
%set(handles.CurDir_txt,'String',pwd)
```

```
% --- Executes on selection change in FileList.
function FileList_Callback(hObject, eventdata, handles)
index_selected = get(handles.FileList,'Value');
save('fileselected','index_selected')
file_list = get(handles.FileList,'String');% Item selected in list box
inputfilename = file_list{index_selected};% name of file selected in list box
cDAQ = dlmread(inputfilename);
Room_Temperature=cDAQ(1,1); %Degrees Celsius
cDAQ = cDAQ(2:size(cDAQ),:); %Cut off Room Temperature Row
[l w]=size(cDAQ); %Find size of array
length_data=l/100; %used to plot search spans
Test_Section_Pressure=cDAQ(:,1); %Voltage From Amplifier
Camera_Trigger=cDAQ(:,2); % Voltage
Gas_Sampling_Pressure=cDAQ(:,3); %Voltage From Amplifier
Gas_Sampling_Trigger=cDAQ(:,4); %Voltage
Test_Time=(0:0.01:(l-1)*0.01)'; %converts row spacing to milliseconds
save('inputfilename', 'inputfilename','l');
axes(handles.RAW);
[AX,plot1,plot2] = plotyy(Test_Time,Camera_Trigger,...
                          Test_Time,Test_Section_Pressure,'plot');
title ({inputfilename},'FontSize',12,'FontWeight','bold','Interpreter','none');
xlabel('Time (ms)');
set(plot1,'Color','r');
set(get(AX(1),'Ylabel'),'String','Voltage (V)','Color','r');
set(AX(1),'YLim',[0 8]);
set(AX(1),'YTick',[0:3:8],'Ycolor','r');
set(plot2,'Color','b');
set(get(AX(2),'Ylabel'),'String','Voltage (V)','Color','b');
set(AX(2),'YLim',[0 max(Test_Section_Pressure*1.05)]);
set(AX(2),'YTick',[0:5:max(Test_Section_Pressure*1.25)],'Ycolor','b');
save('plotrawdata', 'Test_Time', 'Camera_Trigger', 'Test_Section_Pressure'...
    ,'Gas_Sampling_Trigger','Gas_Sampling_Pressure','inputfilename','length_data');

h = zoom;
setAxesZoomMotion(h,AX,'horizontal');
p = pan;
setAllowAxesPan(p,AX,false);

set(handles.EoC_min,'Max',length_data,'Min',1);
set(handles.EoC_max,'Max',length_data,'Min',1);
set(handles.EoC_min,'Value',length_data/2);
set(handles.EoC_max,'Value',length_data/2);
if 2 ==exist('eocsearch.mat')
    ploteocsearch(hObject, eventdata, handles)
end
set(handles.Ign_min,'Max',length_data,'Min',1);
set(handles.Ign_max,'Max',length_data,'Min',1);
set(handles.Ign_min,'Value',length_data/2);
set(handles.Ign_max,'Value',length_data/2);
if 2 ==exist('ignsearch.mat')
    plotignsearch(hObject, eventdata, handles)
end

load_listbox(pwd,handles)

function zoomcallback(obj,evd,handles,hObject,eventdata)
newLim = get(evd.Axes,'XLim');
 if ((evd.Axes) == (handles.EoC))
    set(handles.EoC_min,'Value',newLim(1));
    set(handles.EoC_max,'Value',newLim(2));
    eoc_min = newLim(1);
    eoc_max = newLim(2);
    save('eocsearch', 'eoc_min', 'eoc_max');
    ploteocsearch(hObject, eventdata, handles)
 end

  if ((evd.Axes) == (handles.Ign))
    set(handles.Ign_min,'Value',newLim(1));
    set(handles.Ign_max,'Value',newLim(2));
    Ign_min = newLim(1);
    Ign_max = newLim(2);
    save('ignsearch', 'Ign_min', 'Ign_max');
    plotignsearch(hObject, eventdata, handles)
  end

function ploteocsearch(hObject, eventdata, handles)
load('plotrawdata.mat')
load('eocsearch.mat');
 if (eoc_min < (length_data)) && (eoc_max < (length_data))
     set(handles.EoC_min,'Value',eoc_min);
     set(handles.EoC_max,'Value',eoc_max);
 else
     eoc_min = length_data/2-20;
     eoc_max = eoc_min +20;
     set(handles.EoC_min,'Value',eoc_min);
     set(handles.EoC_max,'Value',eoc_max);
 end
axes(handles.EoC);
plot(Test_Time,Test_Section_Pressure,'b');
xlim([eoc_min eoc_max]);
```

```
set(handles.EoC_min,'Max',length_data,'Min',1);
set(handles.EoC_max,'Max',length_data,'Min',1);

h = zoom;
setAxesZoomMotion(h,handles.EoC,'horizontal');
p = pan;
setAllowAxesPan(p,handles.EoC,false);

function plotignsearch(hObject, eventdata, handles)
load('plotrawdata.mat')
load('ignsearch.mat')
 if (Ign_min < (length_data)) && (Ign_max < (length_data))
     set(handles.Ign_min,'Value',Ign_min);
     set(handles.Ign_max,'Value',Ign_max);
 else
     Ign_min = length_data/2;
     Ign_max = Ign_min+20;
     set(handles.Ign_min,'Value',Ign_min);
     set(handles.Ign_max,'Value',Ign_max);
 end
axes(handles.Ign);
plot(Test_Time,Test_Section_Pressure,'b');
xlim([Ign_min Ign_max]);


set(handles.Ign_min,'Max',length_data,'Min',1);
set(handles.Ign_max,'Max',length_data,'Min',1);

h = zoom;
setAxesZoomMotion(h,handles.Ign,'horizontal');
p = pan;
setAllowAxesPan(p,handles.Ign,false);


% --- Executes during object creation, after setting all properties.
function FileList_CreateFcn(hObject, eventdata, handles)
% hObject    handle to FileList (see GCBO)
% eventdata  reserved - to be defined in a future version of MATLAB
% handles    empty - handles not created until after all CreateFcns called

% Hint: listbox controls usually have a white background on Windows.
%       See ISPC and COMPUTER.
if ispc && isequal(get(hObject,'BackgroundColor'), get(0,'defaultUicontrolBackgroundColor'))
    set(hObject,'BackgroundColor','white');
end


% --- Executes on slider movement.
function EoC_min_Callback(hObject, eventdata, handles)
% hObject    handle to EoC_min (see GCBO)
% eventdata  reserved - to be defined in a future version of MATLAB
% handles    structure with handles and user data (see GUIDATA)

% Hints: get(hObject,'Value') returns position of slider
%        get(hObject,'Min') and get(hObject,'Max') to determine range of
%        slider

eoc_min = get(handles.EoC_min,'Value');
eoc_max = get(handles.EoC_max,'Value');

if (eoc_min < eoc_max)
load('plotrawdata');
axes(handles.EoC);
plot(Test_Time,Test_Section_Pressure,'b');
xLim([eoc_min eoc_max]);
%ylabel('Pressure (psi)','Color','b');
save('eocsearch', 'eoc_min', 'eoc_max');
else
eoc_min = eoc_max-1;
set(handles.EoC_min,'Value',eoc_min);
load('plotrawdata');
axes(handles.EoC);
plot(Test_Time,Test_Section_Pressure,'b');
xLim([eoc_min eoc_max]);
%ylabel('Pressure (psi)','Color','b');
save('eocsearch', 'eoc_min', 'eoc_max');
end
h = zoom;
setAxesZoomMotion(h,handles.EoC,'horizontal');
p = pan;
setAllowAxesPan(p,handles.EoC,false);

% --- Executes during object creation, after setting all properties.
function EoC_min_CreateFcn(hObject, eventdata, handles)
% hObject    handle to EoC_min (see GCBO)
% eventdata  reserved - to be defined in a future version of MATLAB
% handles    empty - handles not created until after all CreateFcns called

% Hint: slider controls usually have a light gray background.
if isequal(get(hObject,'BackgroundColor'), get(0,'defaultUicontrolBackgroundColor'))
    set(hObject,'BackgroundColor',[.9 .9 .9]);
end
```

```matlab
% --- Executes on slider movement.
function EoC_max_Callback(hObject, eventdata, handles)
% hObject    handle to EoC_max (see GCBO)
% eventdata  reserved - to be defined in a future version of MATLAB
% handles    structure with handles and user data (see GUIDATA)

% Hints: get(hObject,'Value') returns position of slider
%        get(hObject,'Min') and get(hObject,'Max') to determine range of slider

eoc_min = get(handles.EoC_min,'Value');
eoc_max = get(handles.EoC_max,'Value');

if (eoc_min < eoc_max)
load('plotrawdata');
axes(handles.EoC);
plot(Test_Time,Test_Section_Pressure,'b');
xLim([eoc_min eoc_max]);
%ylabel('Pressure (psi)','Color','b');
save('eocsearch', 'eoc_min', 'eoc_max');
else
eoc_max = eoc_min+1;
set(handles.EoC_max,'Value',eoc_max);
load('plotrawdata');
axes(handles.EoC);
plot(Test_Time,Test_Section_Pressure,'b');
xLim([eoc_min eoc_max]);
%ylabel('Pressure (psi)','Color','b');
save('eocsearch', 'eoc_min', 'eoc_max');
end
h = zoom;
setAxesZoomMotion(h,handles.EoC,'horizontal');
p = pan;
setAllowAxesPan(p,handles.EoC,false);

% --- Executes during object creation, after setting all properties.
function EoC_max_CreateFcn(hObject, eventdata, handles)
% hObject    handle to EoC_max (see GCBO)
% eventdata  reserved - to be defined in a future version of MATLAB
% handles    empty - handles not created until after all CreateFcns called

% Hint: slider controls usually have a light gray background.
if isequal(get(hObject,'BackgroundColor'), get(0,'defaultUicontrolBackgroundColor'))
    set(hObject,'BackgroundColor',[.9 .9 .9]);
end


% --- Executes on slider movement.
function Ign_min_Callback(hObject, eventdata, handles)
% hObject    handle to Ign_min (see GCBO)
% eventdata  reserved - to be defined in a future version of MATLAB
% handles    structure with handles and user data (see GUIDATA)

% Hints: get(hObject,'Value') returns position of slider
%        get(hObject,'Min') and get(hObject,'Max') to determine range of slider

Ign_min = get(handles.Ign_min,'Value');
Ign_max = get(handles.Ign_max,'Value');

if (Ign_min < Ign_max)
load('plotrawdata');
axes(handles.Ign);
set(gca,'YAxisLocation','right');
plot(Test_Time,Test_Section_Pressure,'b');
xLim([Ign_min Ign_max]);
%ylabel('Pressure (psi)','Color','b');
save('ignsearch', 'Ign_min', 'Ign_max');
else
Ign_min = Ign_max-1;
set(handles.Ign_min,'Value',Ign_min);
load('plotrawdata');
axes(handles.Ign);
set(gca,'YAxisLocation','right');
plot(Test_Time,Test_Section_Pressure,'b');
xLim([Ign_min Ign_max]);
%ylabel('Pressure (psi)','Color','b');
save('ignsearch', 'Ign_min', 'Ign_max');
end
h = zoom;
setAxesZoomMotion(h,handles.Ign,'horizontal');
p = pan;
setAllowAxesPan(p,handles.Ign,false);

% --- Executes during object creation, after setting all properties.
function Ign_min_CreateFcn(hObject, eventdata, handles)
% hObject    handle to Ign_min (see GCBO)
% eventdata  reserved - to be defined in a future version of MATLAB
% handles    empty - handles not created until after all CreateFcns called

% Hint: slider controls usually have a light gray background.
if isequal(get(hObject,'BackgroundColor'), get(0,'defaultUicontrolBackgroundColor'))
```

```
        set(hObject,'BackgroundColor',[.9 .9 .9]);
end


% --- Executes on slider movement.
function Ign_max_Callback(hObject, eventdata, handles)
% hObject    handle to Ign_max (see GCBO)
% eventdata  reserved - to be defined in a future version of MATLAB
% handles    structure with handles and user data (see GUIDATA)

% Hints: get(hObject,'Value') returns position of slider
%        get(hObject,'Min') and get(hObject,'Max') to determine range of slider

Ign_min = get(handles.Ign_min,'Value');
Ign_max = get(handles.Ign_max,'Value');

if (Ign_min < Ign_max)
load('plotrawdata');
axes(handles.Ign);
set(gca,'YAxisLocation','right');
plot(Test_Time,Test_Section_Pressure,'b');
xLim([Ign_min Ign_max]);
%ylabel('Pressure (psi)','Color','b');
save('ignsearch', 'Ign_min', 'Ign_max');
else
Ign_max = Ign_min+1;
set(handles.Ign_max,'Value',Ign_max);
load('plotrawdata');
axes(handles.Ign);
set(gca,'YAxisLocation','right');
plot(Test_Time,Test_Section_Pressure,'b');
xLim([Ign_min Ign_max]);
%ylabel('Pressure (psi)','Color','b');
save('ignsearch', 'Ign_min', 'Ign_max');
end
h = zoom;
setAxesZoomMotion(h,handles.Ign,'horizontal');
p = pan;
setAllowAxesPan(p,handles.Ign,false);

% --- Executes during object creation, after setting all properties.
function Ign_max_CreateFcn(hObject, eventdata, handles)
% hObject    handle to Ign_max (see GCBO)
% eventdata  reserved - to be defined in a future version of MATLAB
% handles    empty - handles not created until after all CreateFcns called

% Hint: slider controls usually have a light gray background.
if isequal(get(hObject,'BackgroundColor'), get(0,'defaultUicontrolBackgroundColor'))
    set(hObject,'BackgroundColor',[.9 .9 .9]);
end


% --- Executes on button press in Save.
function Save_Callback(hObject, eventdata, handles)
% hObject    handle to Save (see GCBO)
% eventdata  reserved - to be defined in a future version of MATLAB
% handles    structure with handles and user data (see GUIDATA)
% Close the GUI and any plot window that is open
load('plotrawdata');
load('eocsearch.mat');
load('ignsearch.mat');
ploteocsearch(hObject, eventdata, handles)
plotignsearch(hObject, eventdata, handles)

if ishandle(handles.Ign) && ishandle(handles.EoC),
load('TestInfo');
load('MixtureInfo');
iC8H18  =   0;
nC7H16  =   0;
C2H4    =   0;
C2H2    =   0;
CH4     =   0;
CH3OH   =   0;
mb      =   0;
nbmeth  =   0;
ep      =   0;
mcrot   =   0;
m3hex   =   0;
H2      =   0;
CO      =   0;

if Ar~=0
Ar      =   Ar-N2;
elseif CO2~=0
CO2     =   CO2-N2;
end

N2      =   N2-O2+(.79*InitialMix);

if H2O~=0
H2O     =   H2O-InitialMix;
```

160

```
end
O2_save = O2;
%%%%%%%  This assumes all fuel is measured using 100 torr transducer
%%%%%%%%%%%%%%%%%%%%%%%%%%%%%%%%%%%%%%%%%%%%%%%%%%%%%%%%%%%%%%%%%%%%%%%%%%%%%
if Fuel1F~=0 && Fuel1C~=0 && (Fuel2F == 0 | Fuel2C == 0 | Fuel2menu == 1 | Fuel2menu == 2)...
        && ((Fuel1menu ~= 1 && Fuel1menu ~= 2))
O2      =   O2-Fuel1C+(.21*InitialMix);
Fuel1   =   Fuel1F-InitialMix;
Fuel2   =   0;
elseif Fuel2F~=0 && Fuel2C~=0 && (Fuel1F == 0 | Fuel1menu == 1 | Fuel1menu == 2)...
        && ((Fuel2menu ~= 1 && Fuel2menu ~= 2))
O2      =   O2-Fuel2C+(.21*InitialMix);
Fuel2   =   Fuel2F-InitialMix;
Fuel1   =   0;
elseif (Fuel2F~=0 && Fuel1F~=0) && (Fuel1menu ~= Fuel2menu) &&...
        (Fuel1menu ~= 1 && Fuel1menu ~= 2 && Fuel2menu ~= 1 && Fuel2menu ~= 2)
O2      =   O2-Fuel2C+(.21*InitialMix);
Fuel2   =   Fuel2F-Fuel1F;
Fuel1   =   Fuel1F-InitialMix;
%elseif Fuel1F==0 && Fuel2F == 0 && Fuel2C==0
%O2      =    O2-Fuel1C+(.21*InitialMix);
elseif (Fuel1F==0 && Fuel2F == 0 && Fuel1C==0 && Fuel2C==0) | ...
        ((Fuel1menu == 1 | Fuel1menu == 2) && (Fuel2menu == 1 | Fuel2menu == 2))
O2      =   O2-InitialMixC+(.21*InitialMix);
Fuel1   =   0;
Fuel2   =   0;
elseif (Fuel1menu == Fuel2menu) && (Fuel1menu ~= 1 | Fuel1menu ~= 2)...
            && ((Fuel1menu ~= 1 && Fuel1menu ~= 2))
O2      =   O2-Fuel1C+(.21*InitialMix);
Fuel1   =   Fuel1F-InitialMix;
Fuel2   =   0;
Fuel2F  =   0;
Fuel2C  =   0;
set(handles.Fuel2F,'String',num2str(Fuel2F));
set(handles.Fuel2C,'String',num2str(Fuel2C));
set(handles.Fuel1menu,'Val',Fuel1menu);
set(handles.Fuel2menu,'Val',1);
MixtureInfoSave(hObject, eventdata, handles)
'You can only use each fuel once.'
end


if 1 == Fuel1menu % Fuel 1
    Fuel1 = 0;
elseif 2 == Fuel1menu % none
    Fuel1 = 0;
elseif 3 == Fuel1menu % H2
    H2 = Fuel1;
elseif 4 == Fuel1menu % CO
    CO = Fuel1;
elseif 5 == Fuel1menu % CH4
    CH4 = Fuel1;
elseif 6 == Fuel1menu % C2H2
    C2H2 = Fuel1;
elseif 7 == Fuel1menu % C2H4
    C4H4 = Fuel1;
elseif 8 == Fuel1menu % CH3OH
    CH3OH = Fuel1;
elseif 9 == Fuel1menu % iso-octane
    iC8H18 = Fuel1;
elseif 10 == Fuel1menu % n=heptane
    nC7H16 = Fuel1;
elseif 11 == Fuel1menu % MB
    mb = Fuel1;
elseif 12 == Fuel1menu % BM
    nbmeth = Fuel1;
elseif 13 == Fuel1menu % EP
    ep = Fuel1;
elseif 14 == Fuel1menu % Methyl Crotonate
    mcrot = Fuel1;
elseif 15 == Fuel1menu % Methyl Hexenoate
    m3hex = Fuel1
end

if 1 == Fuel2menu % Fuel 2
    Fuel2 = 0;
elseif 2 == Fuel2menu % none
    Fuel2 = 0;
elseif 3 == Fuel2menu % H2
    H2 = Fuel2;
elseif 4 == Fuel2menu % CO
    CO = Fuel2;
elseif 5 == Fuel2menu % CH4
    CH4 = Fuel2;
elseif 6 == Fuel2menu % C2H2
    C2H2 = Fuel2;
elseif 7 == Fuel2menu % C2H4
    C4H4 = Fuel2;
elseif 8 == Fuel2menu % CH3OH
    CH3OH = Fuel2;
elseif 9 == Fuel2menu % iso-octane
```

```
    iC8H18 = Fuel2;
elseif 10 == Fuel2menu % n=heptane
    nC7H16 = Fuel2
elseif 11 == Fuel2menu % MB
    mb = Fuel2;
elseif 12 == Fuel2menu % BM
    nbmeth = Fuel2;
elseif 13 == Fuel2menu % EP
    ep = Fuel2;
elseif 14 == Fuel2menu % Methyl Crotonate
    mcrot = Fuel2;
elseif 15 == Fuel2menu % Methyl Hexenoate
    m3hex = Fuel2;
end

%%%%% Define the column variables %%%%%%%%%%%%%%%%%%%%%%%%%%%%%%%%%%%%%
cDAQ = dlmread(inputfilename);
Room_Temperature=cDAQ(1,1); %Degrees Celsius
cDAQ = cDAQ(2:size(cDAQ),:); %Cut off Room Temperature Row
[l w]=size(cDAQ); %Find size of array
Test_Section_Pressure=cDAQ(:,1); %Voltage From Amplifier
Camera_Trigger=cDAQ(:,2); % Voltage
Gas_Sampling_Pressure=cDAQ(:,3); %Voltage From Amplifier
Gas_Sampling_Trigger=cDAQ(:,4); %Voltage
Test_Time=(0:0.01:(l-1)*0.01)'; %converts row spacing to milliseconds
%%%%%%%%%%%%%%%%%%%%%%%%%%%%%%%%%%%%%%%%%%%%%%%%%%%%%%%%%%%%%%%%%%%%%%%
CHARGE_PRESSURE=  ChargePressure;
total          =  CHARGE_PRESSURE;  %charge pressure  (torr)
Temp           =  Room_Temperature; %initial temperature (Celsius)
%%%%%%%%%%%%%%%%%%%%%%%%%%%%%%%%%%%%%%%%%%%%%%%%%%%%%%%%%%%%%%%%%%%%%%%
%%%%  CALCULATE ITITIAL PRESSURE in psi, AKA CHARGE PRESSURE     %%%%%%%%%%
Initial_Pressure = CHARGE_PRESSURE * 0.133322/6.894757;   %45torr=2.1077psi
%%%%%%%%%%   ADJUST FOR AMPLIFIER VALUE      %%%%%%%%%%%%%%%%%%%%%%%%%%
Test_Section_Pressure = Test_Section_Pressure*AmpSensitivity;
P_offset = mean(Test_Section_Pressure(1:1000)); %calculate pressure offset
Test_Section_Pressure = Test_Section_Pressure-P_offset+Initial_Pressure;
cut_offset = round(eoc_min*100)-5001;
if (cut_offset < 1)
    cut_offset =  5000;
end
if (length(Test_Section_Pressure)-(cut_offset+19999)) < 0
    cut_offset =  length(Test_Section_Pressure) - 19999;
end

Y = Test_Section_Pressure(cut_offset:cut_offset+19999);
Camera_Trigger = Camera_Trigger(cut_offset:cut_offset+19999);
YY = Gas_Sampling_Pressure(cut_offset:cut_offset+19999);
Gas_Sampling_Trigger = Gas_Sampling_Trigger(cut_offset:cut_offset+19999);
Test_Time = Test_Time(cut_offset:cut_offset+19999);
%%%%%   NOW FILTER NOISY DATA    %%%%%%%%%%%%%%%%%%%%%%%%%%%%%%%%%%%%%%
YHz = fft(Y,length(Y));
YHz(500:10000)=0;
YHz(10001:19500)=0;
Test_Section_Pressure_fft2=real(ifft(YHz));
Test_Section_Pressure_fft = smooth(Test_Section_Pressure_fft2,35,'moving');
YHz_2 = fft(YY,length(YY));
YHz_2(500:10000)=0;
YHz_2(10001:19500)=0;
Gas_Sampling_Pressure_fft2=real(ifft(YHz_2));
Gas_Sampling_Pressure_fft = smooth(Gas_Sampling_Pressure_fft2,35,'moving');
Camera_Trigger = smooth(Camera_Trigger,35,'moving');
Gas_Sampling_Trigger = smooth(Gas_Sampling_Trigger,35,'moving');
%%%%%      set x axis search index and find max P after compression %%%%%
index = round((eoc_max*100-cut_offset)); %set x axis search index and find max P after compression
p=Test_Section_Pressure_fft(1000:index);
[a,b]=max(p);
b=b+1000;
Test_Time=(Test_Time-Test_Time(1,1))-b/100;

%%%%%%      calculate effective pressure 1,    %%%%%%%%%%%%%%%%%%%%%%%%%
[p_min_val,p_min_index]=min(Test_Section_Pressure_fft(b:round((Ign_max*100-cut_offset)))); %find minimum pressure after compression
p_min_index=b+p_min_index-1;
P_eff_1_atm=mean(Y(b:p_min_index))*.068046;
[p_max_val,p_max_index]=max(Test_Section_Pressure_fft(p_min_index:19999)); %find max pressure after combustion
p_max_index=p_min_index+p_max_index;
%%%%%      Make the dP/dt matrix   %%%%%%%%%%%%%%%%%%%%%%%%%%%%%%%%%%%%
Test_Section_Pressure_fft_1 = Test_Section_Pressure_fft';
Test_Section_Pressure_fft_2 = [0,Test_Section_Pressure_fft_1(1:(length(Test_Section_Pressure_fft)-1))];
dPdt = (Test_Section_Pressure_fft_1 - Test_Section_Pressure_fft_2) * .068046 * 100;  % dP/dt in atm/millisec
%%%%%      Calulate effective pressure 2    %%%%%%%%%%%%%%%%%%%%%%%%%%%
offset   = round((Ign_min*100)-cut_offset);  %use this if the search is not long enough
offset_2 = round((Ign_max*100)-cut_offset);
%[dPdt_max_val,dPdt_max_index] = max(dPdt(b+offset:b+4000));  NON GUI
[dPdt_max_val,dPdt_max_index] = max(dPdt(offset:offset_2));
%dPdt_max_index = b + dPdt_max_index + offset - 1;   NON GUI
dPdt_max_index = dPdt_max_index + offset - 1;
P_eff_2_atm = mean(Y(b:dPdt_max_index))*.068046;
%%%%%      Calculate the ignition delay Test_Time    %%%%%%%%%%%%%%%%%%%%
t_ign_actual_ms = (dPdt_max_index - b) / 100;
x_index=Test_Time(p_max_index:3000);
%%%%%      Find max pressure after combustion     %%%%%%%%%%%%%%%%%%%%%%%%
[c,d]=max(Test_Section_Pressure_fft(1:19900));
```

162

```
Max_Pressure_atm = c * .068046;
%%%%%%   Find Temperature after compression      %%%%%%%%%%%%%%%%%%%%%%%%%%
initial_coarse=InitialCoarseExp;
initial_fine=InitialFineExp;

all=iC8H18+CO2+CO+Ar+H2O+O2+N2+C2H2+H2+nC7H16+CH4+C2H4+CH3OH+mb+nbmeth+ep+mcrot+m3hex;
scale=1;
T0=273.15+Temp;
Molar_N2        =  (N2      /all*(total-initial_coarse)+initial_fine*0.79)/total*scale;
Molar_O2        =  (O2      /all*(total-initial_coarse)+initial_fine*0.21)/total*scale;
Molar_isooctane =  iC8H18   /all*(total-initial_coarse)/total*scale;
Molar_CO2       =  CO2      /all*(total-initial_coarse)/total*scale;
Molar_Ar        =  Ar       /all*(total-initial_coarse)/total*scale;
Molar_H2O       =  H2O      /all*(total-initial_coarse)/total*scale;
Molar_CO        =  CO       /all*(total-initial_coarse)/total*scale;
Molar_C2H2      =  C2H2     /all*(total-initial_coarse)/total*scale;
Molar_H2        =  H2       /all*(total-initial_coarse)/total*scale;
Molar_nheptane  =  nC7H16   /all*(total-initial_coarse)/total*scale;
Molar_CH4       =  CH4      /all*(total-initial_coarse)/total*scale;
Molar_C2H4      =  C2H4     /all*(total-initial_coarse)/total*scale;
Molar_CH3OH     =  CH3OH    /all*(total-initial_coarse)/total*scale;
Molar_mb        =  mb       /all*(total-initial_coarse)/total*scale;
Molar_nbmeth    =  nbmeth   /all*(total-initial_coarse)/total*scale;
Molar_ep        =  ep       /all*(total-initial_coarse)/total*scale;
Molar_mcrot     =  mcrot    /all*(total-initial_coarse)/total*scale;
Molar_m3hex     =  m3hex    /all*(total-initial_coarse)/total*scale;

P0=total*0.133322/6.894757;            %initial pressure (torr)

%%%%%%%%%%%% Solving for T_eff_1 using P_eff_1 %%%%%%%%%%%%%%%%%%%%%%%%%%%%%
%%%%%%%%%%%%%%%%%%%%%%%%%%%%%%%%%%%%%%%%%%%%%%%%%%%%%%%%%%%%%%%%%%%%%%%%%%%%
P_eff_1=P_eff_1_atm/.068046;
P_old=P0;
P_new=P0;
x=0.001;
i=1;
T=T0;
while (P_old<P_eff_1)&&(P_new<P_eff_1)
    P_old=P_new;
    [gamma]=gamma_all_9(T, Molar_isooctane, Molar_Ar, Molar_N2,...
                    Molar_O2, Molar_CO2, Molar_H2O, Molar_CO,...
                    Molar_C2H2, Molar_H2, Molar_nheptane,...
                    Molar_CH4, Molar_C2H4, Molar_CH3OH, Molar_mb,...
                    Molar_nbmeth, Molar_ep, Molar_mcrot, Molar_m3hex);
    T=T*((i+x)/i)^(gamma-1);
    P_new=P_old*((i+x)/i)^gamma;
    i=i+x;
end
i=i-x;
CR1=i+x;
T_eff_1=T;

%%%%%%%%%%%% Solving for T_eff_2 using P_eff_2 %%%%%%%%%%%%%%%%%%%%%%%%%%%%%
%%%%%%%%%%%%%%%%%%%%%%%%%%%%%%%%%%%%%%%%%%%%%%%%%%%%%%%%%%%%%%%%%%%%%%%%%%%%
P_eff_2=P_eff_2_atm/.068046;
P_old=P0;
P_new=P0;
x=0.001;
i=1;
T=T0;
while (P_old<P_eff_2)&&(P_new<P_eff_2)
    P_old=P_new;
    [gamma]=gamma_all_9(T, Molar_isooctane, Molar_Ar, Molar_N2,...
                    Molar_O2, Molar_CO2, Molar_H2O, Molar_CO,...
                    Molar_C2H2, Molar_H2, Molar_nheptane,...
                    Molar_CH4, Molar_C2H4, Molar_CH3OH, Molar_mb,...
                    Molar_nbmeth, Molar_ep, Molar_mcrot, Molar_m3hex);
    T=T*((i+x)/i)^(gamma-1);
    P_new=P_old*((i+x)/i)^gamma;
    i=i+x;
end
i=i-x;
CR2=i+x;
T_eff_2=T;

%%%%%        PLOT Final Processed and Cut DATA      %%%%%%%%%%%%%%%%%%%%%%%%
%%%%%%%%%%%%%%%%%%%%%%%%%%%%%%%%%%%%%%%%%%%%%%%%%%%%%%%%%%%%%%%%%%%%%%%%%%%%
Test_Time_1 = Test_Time;
Test_Section_Pressure_fft_atm = Test_Section_Pressure_fft*.068046;
%Gas_Sampling_Pressure_fft_atm_old = ((Gas_Sampling_Pressure_fft*137.73)-0.605)* (0.001315789*10);
Gas_Sampling_Pressure_fft_bar = Gas_Sampling_Pressure_fft/2;  % 0-10 V output gives 0-5 bar
Gas_Sampling_Pressure_fft_atm = Gas_Sampling_Pressure_fft_bar*0.986923267 ; %convert bar to atm
save('plotprocesseddata', 'Test_Time', 'Test_Section_Pressure_fft_atm','Gas_Sampling_Pressure_fft_atm', ...
    'dPdt', 'Camera_Trigger', 'Gas_Sampling_Trigger','d','b','inputfilename');
load('plotprocesseddata', 'Test_Time', 'Test_Section_Pressure_fft_atm', 'Gas_Sampling_Pressure_fft_atm', ...
    'dPdt', 'Camera_Trigger', 'Gas_Sampling_Trigger','d','b','inputfilename')
axes(handles.ProcessedData);
cla;
hl1 = line(Test_Time,real(Test_Section_Pressure_fft_atm),'Color',[.8 .8 0],'LineWidth',2);
hl2 = line(Test_Time,real(Gas_Sampling_Pressure_fft_atm*10),'Color',[0 .8 0],'LineWidth',2);
ax1 = gca;
set(ax1,'XColor','k','YColor','k');
```

```matlab
set(ax1,'xlim',[-15 (t_ign_actual_ms+20)]);
xlabel('Test Time (ms)','FontSize',12,'FontWeight','bold');
 text(-12,.70*(Max_Pressure_atm*1.5),['P_e_f_f_,_1 (atm) = ',num2str(roundn(P_eff_1_atm))],'fontsize',8);
 text(-12,.65*(Max_Pressure_atm*1.5),['T_e_f_f_,_1 (K) = ',num2str(roundn(T_eff_1))],'fontsize',8);
 text(-12,.60*(Max_Pressure_atm*1.5),['CR_1 = ',num2str(roundn(CR1))],'fontsize',8);
 text(-12,.55*(Max_Pressure_atm*1.5),['P_e_f_f_,_2 (atm) = ',num2str(roundn(P_eff_2_atm))],'fontsize',8,'fontweight','bold');
 text(-12,.50*(Max_Pressure_atm*1.5),['T_e_f_f_,_2 (K) = ',num2str(roundn(T_eff_2))],'fontsize',8,'fontweight','bold');
 text(-12,.45*(Max_Pressure_atm*1.5),['CR_2 = ',num2str(roundn(CR2))],'fontsize',8,'fontweight','bold');
 text(-12,.40*(Max_Pressure_atm*1.5),['\tau_i_g_n (ms) = ',num2str(roundn(t_ign_actual_ms))],'fontsize',8,'fontweight','bold');


inputfilename_length = length(inputfilename);
inputfilename_cut = inputfilename(1:(inputfilename_length-4));
outputfilename = ['Data_Out_',inputfilename_cut];
save(outputfilename,'P_eff_1_atm','T_eff_1','CR1','P_eff_2_atm','T_eff_2','CR2','t_ign_actual_ms',...
                    'Molar_isooctane', 'Molar_Ar', 'Molar_N2',...
                    'Molar_O2', 'Molar_CO2', 'Molar_H2O', 'Molar_CO',...
                    'Molar_C2H2', 'Molar_H2', 'Molar_nheptane',...
                    'Molar_CH4', 'Molar_C2H4', 'Molar_CH3OH', 'Molar_mb',...
                    'Molar_nbmeth', 'Molar_ep', 'Molar_mcrot', 'Molar_m3hex');


 ax2 = gca;
set(ax2,'XAxisLocation','bottom','xlim',[-15 (t_ign_actual_ms+20)]);
linkaxes([ax1 ax2]);
hl10 = line(Test_Time,dPdt,'Color','k','Parent',ax2,'Color',[.9 .4 0],'LineWidth',1);
hl11 = line(Test_Time,Camera_Trigger*1,'Color','k','Parent',ax2,'Color',[.9 0 0],'LineWidth',1);
hl12 = line(Test_Time,Gas_Sampling_Trigger*10,'Color','k','Parent',ax2,'Color',[0 0 .9],'LineWidth',1);
axes(handles.LeftAxis);
ax0 = gca;
set(ax0,'XColor','k','YColor','k');
set(ax0,'ylim',[-2 (Max_Pressure_atm*1.5)]);
set(ax0,'YTick',(0:2:100));
set(get(ax0,'YLabel'),'String','Test Section P (atm), Sampling Px10 (atm)','FontSize',12,'FontWeight','bold','Color','k');
axL(1)=handles.ProcessedData;
axL(2)=handles.LeftAxis;
linkaxes([axL],'y');
axes(handles.RightAxis);
ax3 = gca;
set(ax3,'YAxisLocation','right','Color','w','XColor','k','YColor','k');
%set(ax3,'ylim',[-2 (max(dPdt(1000:19000))*3)]);
set(ax3,'ylim',[-2 (Max_Pressure_atm*1.5)]);
set(ax3,'YTick',(-100:2:100),'YColor','k');
set(get(ax3,'YLabel'),'String','dP/dt (atm/ms)','FontSize',12,'FontWeight','bold','Color','k');
axR(1)=handles.ProcessedData;
axR(2)=handles.RightAxis;
axR(3)=handles.LeftAxis;
linkaxes([axR],'y');
orient landscape % for auto landscape printing
end




%%%%%%%%%%%  This function calculates gamma for the mixture and is returned
%%%%%%%%%%%  for calculation of the mixture temperature
function [gamma]=gamma_all_9(T, Molar_isooctane, Molar_Ar, Molar_N2,...
                    Molar_O2, Molar_CO2, Molar_H2O, Molar_CO,...
                    Molar_C2H2, Molar_H2, Molar_nheptane,...
                    Molar_CH4, Molar_C2H4, Molar_CH3OH, Molar_mb,...
                    Molar_nbmeth, Molar_ep, Molar_mcrot, Molar_m3hex);
%%%%%%%%%%%% This is the Thermo Data from the JANNAF tables %%%%%%%%%%%%%%%
%%%%%%%%%%%%%%%%%%%%%%%%%%%%%%%%%%%%%%%%%%%%%%%%%%%%%%%%%%%%%%%%%%%%%%%%%%%%
if(T>1000)
    isooctane = 1.59899273E+1  +5.53184790E-2  *T  -1.95267072E-5  *T^2 +3.11779172E-9   *T^3  -1.85312577E-13  *T^4;
    N2        = 2.95257626     +1.39690057E-3  *T  -4.92631691E-7  *T^2 +7.86010367E-11  *T^3  -4.60755321E-15  *T^4;
    O2        = 3.66096083     +6.56365523E-4  *T  -1.41149485E-7  *T^2 +2.05797658E-11  *T^3  -1.29913248E-15  *T^4;
    CO2       = 4.63659493     +2.74131991E-3  *T  -9.95828531E-7  *T^2 +1.60373011E-10  *T^3  -9.16103468E-15  *T^4;
    H2O       = 2.67703787     +2.97318329E-3  *T  -7.73769690E-7  *T^2 +9.44336689E-11  *T^3  -4.26900959E-15  *T^4;
    CO        = 3.04848583     +1.35172818E-3  *T  -4.85794075E-7  *T^2 +7.88536486E-11  *T^3  -4.69807489E-15  *T^4;
    CH4       = 1.63552643     +1.00842795e-2  *T  -3.36916254e-6  *T^2 +5.34958667e-10  *T^3  -3.15518833e-14  *T^4;
    C2H4      = 3.99182761E+00  +1.04833910E-02 *T  -3.71721385E-06 *T^2 +5.94628514E-10  *T^3  -3.53630526E-14  *T^4;
    nheptane  = 2.22148969e+01  +3.47675750e-02 *T  -1.18407129e-05 *T^2 +1.83298478e-09  *T^3  -1.06130266e-13  *T^4;
    CH3OH     = 0.04029061e+02  +0.09376593e-01 *T  -0.03050254e-04 *T^2 +0.04358793e-08  *T^3  -0.02224723e-12  *T^4;
    mb        = 1.90094725e+01  +2.36503722e-02 *T  -8.22978452e-06 *T^2 +1.29246265e-09  *T^3  -7.55862836e-14  *T^4;
    nbmeth    = 1.95422034e+01  +2.33601261e-02 *T  -8.16729241e-06 *T^2 +1.28676535e-09  *T^3  -7.54230804e-14  *T^4;
    ep        = 1.85206452E+01  +2.42136696E-02 *T  -8.36114469E-06 *T^2 +1.30627199E-09  *T^3  -7.61151064E-14  *T^4;
    mcrot     = 1.80897111e+01  +1.98686931e-02 *T  -6.95006986e-06 *T^2 +1.09534848e-09  *T^3  -6.42176494e-14  *T^4;
    m3hex     = 0.41019386e+0   +0.72655748E-02 *T  +0.91848387E-05 *T^2 -0.24325599E-08  *T^3  +0.20354227E-12  *T^4;
else
    isooctane = 8.15737338E-1  +7.32643959E-2  *T  +1.78300688E-5  *T^2 -6.93589620E-8   *T^3  +3.21629382E-11  *T^4;
    N2        = 3.53100528     -1.23660987E-4  *T  -5.02999437E-7  *T^2 +2.43530612E-09  *T^3  -1.40881235E-12  *T^4;
    O2        = 3.78245636     -2.99673415E-3  *T  +9.84730200E-6  *T^2 -9.68129508E-09  *T^3  +3.24372836E-12  *T^4;
    CO2       = 2.35677352     +8.98459677E-3  *T  -7.12356269E-6  *T^2 +2.45919022E-09  *T^3  -1.43699548E-13  *T^4;
    H2O       = 4.19864056     -2.03643410E-3  *T  +6.52040211E-6  *T^2 -5.48797062E-09  *T^3  +1.77197817E-12  *T^4;
    CO        = 3.57953347     -6.10353680E-4  *T  +1.01681433E-6  *T^2 +9.07005884E-10  *T^3  -9.04424499E-13  *T^4;
    CH4       = 5.14987613     -1.36709788e-2  *T  +4.91800599e-5  *T^2 -4.84743026e-8   *T^3  +1.66693956e-11  *T^4;
    C2H4      = 3.95920148E+00  -7.57052247E-03 *T  +5.70990292E-05 *T^2 -6.91588753E-08  *T^3  +2.69884373E-11  *T^4;
    nheptane  = -1.26836187e+00  +8.54355820e-02 *T  -5.25346786e-05 *T^2 +1.62945721e-08  *T^3  -2.02394925e-12  *T^4;
    CH3OH     = 0.02660115e+02  +0.07341508e-01 *T  -0.07170051e-04 *T^2 -0.08793194e-07  *T^3  -0.02390570e-10  *T^4;
    mb        = 3.16208825e+00  +5.52915358e-02 *T  -3.11610102e-05 *T^2 +8.42394129e-09  *T^3  -8.72222021e-13  *T^4;
    nbmeth    = 1.44556474e+00  +6.07605168e-02 *T  -3.65779067e-05 *T^2 +1.07102077e-08  *T^3  -1.22703399e-12  *T^4;
    ep        = 1.65296696E+00  +6.20471776E-02 *T  -4.15063299E-05 *T^2 +1.49723063E-08  *T^3  -2.32098805E-12  *T^4;
    mcrot     = 2.12280888e+00  +5.41231045e-02 *T  -3.47438144e-05 *T^2 +1.13620695e-08  *T^3  -1.54117689e-12  *T^4;
    m3hex     = 0.72920524E-01  +0.63392982E-01 *T  -0.22414801E-04 *T^2 -0.75199867E-10  *T^3  +0.28531133E-13  *T^4;
```

```
    end

Ar=2.5;
%%%%%%%%%%%%%%%%%%%%%%%%%%%%%%%%%%%%%%%%%%%%%%%%%%%%%%%%%%%%%%%%%%%%%%%%%%%
%Universal gas constant
R=8.31451;  %J/(mol-K)
%%%%%%%%% Remember when adding species to add them here as well %%%%%%%%%%%
%%%%%%%%% as in the function call and the thermo data          %%%%%%%%%%%
Cp=(   isooctane  *  Molar_isooctane         +...
       N2         *  Molar_N2                +...
       O2         *  Molar_O2                +...
       Ar         *  Molar_Ar                +...
       CO2        *  Molar_CO2               +...
       H2O        *  Molar_H2O               +...
       CO         *  Molar_CO                +...
       nheptane   *  Molar_nheptane          +...
       CH4        *  Molar_CH4               +...
       C2H4       *  Molar_C2H4              +...
       CH3OH      *  Molar_CH3OH             +...
       mb         *  Molar_mb                +...
       nbmeth     *  Molar_nbmeth            +...
       ep         *  Molar_ep                +...
       mcrot      *  Molar_mcrot             +...
       m3hex       *  Molar_m3hex              +...
    0)*R;
%%%%%%%%%%%%%%%%%%%%%%%%%%%%%%%%%%%%%%%%%%%%%%%%%%%%%%%%%%%%%%%%%%%%%%%%%%%
Cv=Cp-R;
gamma=Cp/Cv;


function MixtureInfoSave(hObject, eventdata, handles)
% hObject    handle to H2O (see GCBO)
% eventdata  reserved - to be defined in a future version of MATLAB
% handles    structure with handles and user data (see GUIDATA)
%guidata(hObject, handles);
InitialMix=get(handles.InitialMix,'String');
InitialMix=str2num(InitialMix);
InitialMixC=get(handles.InitialMixC,'String');
InitialMixC=str2num(InitialMixC);
H2O=get(handles.H2O,'String');
H2O=str2num(H2O);
Fuel1menu=get(handles.Fuel1menu,'Value');
Fuel1F=get(handles.Fuel1F,'String');
Fuel1F=str2num(Fuel1F);
Fuel1C=get(handles.Fuel1C,'String');
Fuel1C=str2num(Fuel1C);
Fuel2menu=get(handles.Fuel2menu,'Value');
Fuel2F=get(handles.Fuel2F,'String');
Fuel2F=str2num(Fuel2F);
Fuel2C=get(handles.Fuel2C,'String');
Fuel2C=str2num(Fuel2C);
O2=get(handles.O2,'String');
O2=str2num(O2);
N2=get(handles.N2,'String');
N2=str2num(N2);
Ar=get(handles.Ar,'String');
Ar=str2num(Ar);
CO2=get(handles.CO2,'String');
CO2=str2num(CO2);

if exist('MixtureInfo.mat')
    save('MixtureInfo','-append','InitialMix','InitialMixC','H2O','Fuel1menu','Fuel1F',...
        'Fuel1C','Fuel2menu','Fuel2F','Fuel2C','O2','N2','Ar','CO2');
else
    save('MixtureInfo','InitialMix','InitialMixC','H2O','Fuel1menu','Fuel1F',...
        'Fuel1C','Fuel2menu','Fuel2F','Fuel2C','O2','N2','Ar','CO2');
end


function InitialMix_Callback(hObject, eventdata, handles)
% hObject    handle to InitialMix (see GCBO)
% eventdata  reserved - to be defined in a future version of MATLAB
% handles    structure with handles and user data (see GUIDATA)
MixtureInfoSave(hObject, eventdata, handles)

% Hints: get(hObject,'String') returns contents of InitialMix as text
%        str2double(get(hObject,'String')) returns contents of InitialMix as a double


% --- Executes during object creation, after setting all properties.
function InitialMix_CreateFcn(hObject, eventdata, handles)
% hObject    handle to InitialMix (see GCBO)
% eventdata  reserved - to be defined in a future version of MATLAB
% handles    empty - handles not created until after all CreateFcns called

% Hint: edit controls usually have a white background on Windows.
%       See ISPC and COMPUTER.
if ispc && isequal(get(hObject,'BackgroundColor'), get(0,'defaultUicontrolBackgroundColor'))
    set(hObject,'BackgroundColor','white');
end
```

```matlab
function InitialMixC_Callback(hObject, eventdata, handles)
MixtureInfoSave(hObject, eventdata, handles)


function InitialMixC_CreateFcn(hObject, eventdata, handles)
if ispc && isequal(get(hObject,'BackgroundColor'), get(0,'defaultUicontrolBackgroundColor'))
    set(hObject,'BackgroundColor','white');
end


function H2O_Callback(hObject, eventdata, handles)
MixtureInfoSave(hObject, eventdata, handles)


function H2O_CreateFcn(hObject, eventdata, handles)
if ispc && isequal(get(hObject,'BackgroundColor'), get(0,'defaultUicontrolBackgroundColor'))
    set(hObject,'BackgroundColor','white');
end


function Fuel1F_Callback(hObject, eventdata, handles)
MixtureInfoSave(hObject, eventdata, handles)


function Fuel1F_CreateFcn(hObject, eventdata, handles)
if ispc && isequal(get(hObject,'BackgroundColor'), get(0,'defaultUicontrolBackgroundColor'))
    set(hObject,'BackgroundColor','white');
end


function Fuel1C_Callback(hObject, eventdata, handles)
MixtureInfoSave(hObject, eventdata, handles)


function Fuel1C_CreateFcn(hObject, eventdata, handles)
if ispc && isequal(get(hObject,'BackgroundColor'), get(0,'defaultUicontrolBackgroundColor'))
    set(hObject,'BackgroundColor','white');
end


function Fuel1menu_Callback(hObject, eventdata, handles)
MixtureInfoSave(hObject, eventdata, handles)


function Fuel1menu_CreateFcn(hObject, eventdata, handles)
if ispc && isequal(get(hObject,'BackgroundColor'), get(0,'defaultUicontrolBackgroundColor'))
    set(hObject,'BackgroundColor','white');
end


function Fuel2menu_Callback(hObject, eventdata, handles)
MixtureInfoSave(hObject, eventdata, handles)


function Fuel2menu_CreateFcn(hObject, eventdata, handles)

if ispc && isequal(get(hObject,'BackgroundColor'), get(0,'defaultUicontrolBackgroundColor'))
    set(hObject,'BackgroundColor','white');
end


function Fuel2F_Callback(hObject, eventdata, handles)
MixtureInfoSave(hObject, eventdata, handles)


function Fuel2F_CreateFcn(hObject, eventdata, handles)
if ispc && isequal(get(hObject,'BackgroundColor'), get(0,'defaultUicontrolBackgroundColor'))
    set(hObject,'BackgroundColor','white');
end


function Fuel2C_Callback(hObject, eventdata, handles)
MixtureInfoSave(hObject, eventdata, handles)


function Fuel2C_CreateFcn(hObject, eventdata, handles)
if ispc && isequal(get(hObject,'BackgroundColor'), get(0,'defaultUicontrolBackgroundColor'))
    set(hObject,'BackgroundColor','white');
end


function O2_Callback(hObject, eventdata, handles)
MixtureInfoSave(hObject, eventdata, handles)


function O2_CreateFcn(hObject, eventdata, handles)
if ispc && isequal(get(hObject,'BackgroundColor'), get(0,'defaultUicontrolBackgroundColor'))
    set(hObject,'BackgroundColor','white');
end


function N2_Callback(hObject, eventdata, handles)
MixtureInfoSave(hObject, eventdata, handles)


function N2_CreateFcn(hObject, eventdata, handles)
if ispc && isequal(get(hObject,'BackgroundColor'), get(0,'defaultUicontrolBackgroundColor'))
    set(hObject,'BackgroundColor','white');
end


function Ar_Callback(hObject, eventdata, handles)
MixtureInfoSave(hObject, eventdata, handles)


function Ar_CreateFcn(hObject, eventdata, handles)
if ispc && isequal(get(hObject,'BackgroundColor'), get(0,'defaultUicontrolBackgroundColor'))
    set(hObject,'BackgroundColor','white');
end


function CO2_Callback(hObject, eventdata, handles)
MixtureInfoSave(hObject, eventdata, handles)
```

```
function CO2_CreateFcn(hObject, eventdata, handles)
if ispc && isequal(get(hObject,'BackgroundColor'), get(0,'defaultUicontrolBackgroundColor'))
    set(hObject,'BackgroundColor','white');
end


function TestInfoSave(hObject, eventdata, handles)
InitialFineExp=get(handles.InitialFineExp,'String');
InitialFineExp=str2num(InitialFineExp);
InitialCoarseExp=get(handles.InitialCoarseExp,'String');
InitialCoarseExp=str2num(InitialCoarseExp);
ChargePressure=get(handles.ChargePressure,'String');
ChargePressure=str2num(ChargePressure);
AmpSensitivity=get(handles.AmpSensitivity,'String');
AmpSensitivity=str2num(AmpSensitivity);
AmpScale=get(handles.AmpScale,'String');
AmpScale=str2num(AmpScale);
if exist('TestInfo.mat')
    save('TestInfo','-append','InitialFineExp','InitialCoarseExp','ChargePressure',...
        'AmpSensitivity','AmpScale');
else
    save('TestInfo','InitialFineExp','InitialCoarseExp','ChargePressure',...
        'AmpSensitivity','AmpScale');
end


function InitialFineExp_Callback(hObject, eventdata, handles)
TestInfoSave(hObject, eventdata, handles)

function InitialFineExp_CreateFcn(hObject, eventdata, handles)
if ispc && isequal(get(hObject,'BackgroundColor'), get(0,'defaultUicontrolBackgroundColor'))
    set(hObject,'BackgroundColor','white');
end

function InitialCoarseExp_Callback(hObject, eventdata, handles)
TestInfoSave(hObject, eventdata, handles)

function InitialCoarseExp_CreateFcn(hObject, eventdata, handles)
if ispc && isequal(get(hObject,'BackgroundColor'), get(0,'defaultUicontrolBackgroundColor'))
    set(hObject,'BackgroundColor','white');
end

function ChargePressure_Callback(hObject, eventdata, handles)
TestInfoSave(hObject, eventdata, handles)

function ChargePressure_CreateFcn(hObject, eventdata, handles)
if ispc && isequal(get(hObject,'BackgroundColor'), get(0,'defaultUicontrolBackgroundColor'))
    set(hObject,'BackgroundColor','white');
end

function AmpSensitivity_Callback(hObject, eventdata, handles)
TestInfoSave(hObject, eventdata, handles)

function AmpSensitivity_CreateFcn(hObject, eventdata, handles)
if ispc && isequal(get(hObject,'BackgroundColor'), get(0,'defaultUicontrolBackgroundColor'))
    set(hObject,'BackgroundColor','white');
end

function AmpScale_Callback(hObject, eventdata, handles)
TestInfoSave(hObject, eventdata, handles)

function AmpScale_CreateFcn(hObject, eventdata, handles)
if ispc && isequal(get(hObject,'BackgroundColor'), get(0,'defaultUicontrolBackgroundColor'))
    set(hObject,'BackgroundColor','white');
end
```

B.3 Intermediate Species Filtering Code

The following code is used to filter the CHEMKIN data by maximum concentration.

```
clear all
clc;

% Read in Chemkin Output File (*.csv)
%[Chemkin_Data Chemkin_Variables] = xlsread('export.csv');
[Chemkin_Data Chemkin_Variables] = xlsread('export_MB_975_10_04_376_ALL.csv');
[Chemkin_Data_Length Chemkin_Data_Width] = size(Chemkin_Data);

%For Good *.pdf Figures
Conditions = ('MB, \phi=0.4, T=975 K, P=10 atm, I/O_2=3.76');
Fontscale = 1;
% set(gcf, 'PaperUnits', 'inches');
% set(gcf, 'PaperSize', [11/Fontscale 8.5/Fontscale]);
% set(gcf, 'PaperPosition', [-.5/Fontscale 0 12/Fontscale 8.5/Fontscale]);
% print -r720 -dpdf figure(1)

% For All Plot Analysis Columns (8) to (Chemkin_Data_Width-4)
% Sort Species Rows by Max Concentrations
for n = 8:(Chemkin_Data_Width-7)
    a(n-7,1) = max(Chemkin_Data(:,n));
    a(n-7,2) = n;
end
b = sortrows(a,[-1]);
for n = 8:(Chemkin_Data_Width-7)
    Chemkin_Data_New(:,n-7) = Chemkin_Data(:,b(n-7,2));
    Chemkin_Variables_New(n-7) = Chemkin_Variables(b(n-7,2));
end


%%%%%%%%%%%%%%%%%%%%%%%%%%%%%%%%%%%%%%%%%%%%%%%%%%%%%%%%%%%%%%%%%%%%%%%%%%%
%%%% Set Major Species Filters %%%%%%%%%%%%%%%%%%%%%%%%%%%%%%%%%%%%%%%%%%%%
Species_Max_Filter_1_ppm = 1e6;
Species_Min_Filter_1_ppm = 2000;
%%%%%%%%%%%%%%%%%%%%%%%%%%%%%%%%%%%%%%%%%%%%%%%%%%%%%%%%%%%%%%%%%%%%%%%%%%%
%%%%%%%%%%%%%%%%%%%%%%%%%%%%%%%%%%%%%%%%%%%%%%%%%%%%%%%%%%%%%%%%%%%%%%%%%%%
Species_Max_Filter_1 =  Species_Max_Filter_1_ppm/1e6;
Species_Min_Filter_1 =  Species_Min_Filter_1_ppm/1e6;
% Filter Major Species
Species_Max_Count_1 =  1;
for n = 1:length(b)
    if b(n,1) >= Species_Max_Filter_1
       Species_Max_Count_1 = n+1;
    end
    if b(n,1) >= Species_Min_Filter_1
       Species_Min_Count_1 = n;
    end
end
% Plot Major Filtered Species
figure(1)
semilogy(Chemkin_Data(:,1)*1000,Chemkin_Data_New(:,Species_Max_Count_1:Species_Min_Count_1),'LineWidth',1)
colormap(jet)
xlim([0 1000*max(Chemkin_Data(:,1))]);
ylim([1e-6 Species_Max_Filter_1]);%  b(length(b),1)*1.1]);
title (['Species Concentration Time-History for ',Conditions,' (Filtered Above ',num2str(Species_Min_Filter_1_ppm),...
    ' ppm Maximum Concentration)']);xlabel('Time [ms]');
ylabel('Mole Fraction');
legend(Chemkin_Variables_New(Species_Max_Count_1:Species_Min_Count_1),'Location','nw');
hold off

% Export Species Time-Histories as *.csv for Plotting in Origin
[ll ww] = size(Chemkin_Data_New);
Origin_Out_All_Plot_1 = zeros(ll+1,(Species_Min_Count_1-Species_Max_Count_1)+1);
Origin_Out_All_Plot_1(2:ll+1,1) = Chemkin_Data(:,1)*1000;
Origin_Out_All_Plot_1(2:ll+1,2:(Species_Min_Count_1-Species_Max_Count_1)+2) = ...
    Chemkin_Data_New(:,Species_Max_Count_1:Species_Min_Count_1);
csvwrite('Origin_Out_All_Plot_1.csv',Origin_Out_All_Plot_1);

%For Good *.pdf Figures
set(gcf, 'PaperUnits', 'inches');
set(gcf, 'PaperSize', [11/Fontscale 8.5/Fontscale]);
set(gcf, 'PaperPosition', [-.5/Fontscale 0 12/Fontscale 8.5/Fontscale]);
print -r720 -dpdf figure(1)

%%%%%%%%%%%%%%%%%%%%%%%%%%%%%%%%%%%%%%%%%%%%%%%%%%%%%%%%%%%%%%%%%%%%%%%%%%%
%%%% Set Species Filters %%%%%%%%%%%%%%%%%%%%%%%%%%%%%%%%%%%%%%%%%%%%%%%%%%
Species_Max_Filter_2_ppm = 2000;
Species_Min_Filter_2_ppm = 1000;
%%%%%%%%%%%%%%%%%%%%%%%%%%%%%%%%%%%%%%%%%%%%%%%%%%%%%%%%%%%%%%%%%%%%%%%%%%%
%%%%%%%%%%%%%%%%%%%%%%%%%%%%%%%%%%%%%%%%%%%%%%%%%%%%%%%%%%%%%%%%%%%%%%%%%%%
Species_Max_Filter_2 =  Species_Max_Filter_2_ppm/1e6;
Species_Min_Filter_2 =  Species_Min_Filter_2_ppm/1e6;
% Filter Species
Species_Max_Count_2 =  1;
for n = 1:length(b)
    if b(n,1) >= Species_Max_Filter_2
```

```
            Species_Max_Count_2 = n+1;
        end
        if b(n,1) >= Species_Min_Filter_2
            Species_Min_Count_2 = n;
        end
    end
end
% Plot Filtered Species
figure(2)
semilogy(Chemkin_Data(:,1)*1000,Chemkin_Data_New(:,Species_Max_Count_2:Species_Min_Count_2),'LineWidth',1)
colormap(jet)
xlim([0 1000*max(Chemkin_Data(:,1))]);
ylim([1e-6 Species_Max_Filter_2]);%  b(length(b),1)*1.1]);
title (['Species Concentration Time-History for ',Conditions,' (Filtered Between ',num2str(Species_Min_Filter_2_ppm),...
    ' ppm and ',num2str(Species_Max_Filter_2_ppm),' ppm Maximum Concentration)']);xlabel('Time [ms]');
ylabel('Mole Fraction');
legend(Chemkin_Variables_New(Species_Max_Count_2:Species_Min_Count_2),'Location','nw');
hold off

% Export Species Time-Histories as *.csv for Plotting in Origin
[ll ww] = size(Chemkin_Data_New);
Origin_Out_All_Plot_2 = zeros(ll+1,(Species_Min_Count_2-Species_Max_Count_2)+1);
Origin_Out_All_Plot_2(2:ll+1,1) = Chemkin_Data(:,1)*1000;
Origin_Out_All_Plot_2(2:ll+1,2:(Species_Min_Count_2-Species_Max_Count_2)+2) = ...
    Chemkin_Data_New(:,Species_Max_Count_2:Species_Min_Count_2);
csvwrite('Origin_Out_All_Plot_2.csv',Origin_Out_All_Plot_2);

%For Good *.pdf Figures
set(gcf, 'PaperUnits', 'inches');
set(gcf, 'PaperSize', [11/Fontscale 8.5/Fontscale]);
set(gcf, 'PaperPosition', [-.5/Fontscale 0 12/Fontscale 8.5/Fontscale]);
print -r720 -dpdf figure(2)

%%%%%%%%%%%%%%%%%%%%%%%%%%%%%%%%%%%%%%%%%%%%%%%%%%%%%%%%%%%%%%%%%%%%%%%%%%%
%%%% Set Major Species Filters %%%%%%%%%%%%%%%%%%%%%%%%%%%%%%%%%%%%%%%%%%%%%
Species_Max_Filter_3_ppm = 1000;
Species_Min_Filter_3_ppm = 100;
%%%%%%%%%%%%%%%%%%%%%%%%%%%%%%%%%%%%%%%%%%%%%%%%%%%%%%%%%%%%%%%%%%%%%%%%%%%%
%%%%%%%%%%%%%%%%%%%%%%%%%%%%%%%%%%%%%%%%%%%%%%%%%%%%%%%%%%%%%%%%%%%%%%%%%%%%
Species_Max_Filter_3 =  Species_Max_Filter_3_ppm/1e6;
Species_Min_Filter_3 =  Species_Min_Filter_3_ppm/1e6;
% Filter Species
Species_Max_Count_3 =  1;
for n = 1:length(b)
    if b(n,1) >= Species_Max_Filter_3
        Species_Max_Count_3 = n+1;
    end
    if b(n,1) >= Species_Min_Filter_3
        Species_Min_Count_3 = n;
    end
end
% Plot Filtered Species
figure(3)
semilogy(Chemkin_Data(:,1)*1000,Chemkin_Data_New(:,Species_Max_Count_3:Species_Min_Count_3),'LineWidth',1)
colormap(jet)
xlim([0 1000*max(Chemkin_Data(:,1))]);
ylim([1e-6 Species_Max_Filter_3]);%  b(length(b),1)*1.1]);
title (['Species Concentration Time-History for ',Conditions,' (Filtered Between ',num2str(Species_Min_Filter_3_ppm),...
    ' ppm and ',num2str(Species_Max_Filter_3_ppm),' ppm Maximum Concentration)']);xlabel('Time [ms]');
ylabel('Mole Fraction');
legend(Chemkin_Variables_New(Species_Max_Count_3:Species_Min_Count_3),'Location','nw');
hold off

% Export Species Time-Histories as *.csv for Plotting in Origin
[ll ww] = size(Chemkin_Data_New);
Origin_Out_All_Plot_3 = zeros(ll+1,(Species_Min_Count_3-Species_Max_Count_3)+1);
Origin_Out_All_Plot_3(2:ll+1,1) = Chemkin_Data(:,1)*1000;
Origin_Out_All_Plot_3(2:ll+1,2:(Species_Min_Count_3-Species_Max_Count_3)+2) = ...
    Chemkin_Data_New(:,Species_Max_Count_3:Species_Min_Count_3);
csvwrite('Origin_Out_All_Plot_3.csv',Origin_Out_All_Plot_3);

%For Good *.pdf Figures
set(gcf, 'PaperUnits', 'inches');
set(gcf, 'PaperSize', [11/Fontscale 8.5/Fontscale]);
set(gcf, 'PaperPosition', [-.5/Fontscale 0 12/Fontscale 8.5/Fontscale]);
print -r720 -dpdf figure(3)

%%%%%%%%%%%%%%%%%%%%%%%%%%%%%%%%%%%%%%%%%%%%%%%%%%%%%%%%%%%%%%%%%%%%%%%%%%%%
%%%% Set Major Species Filters %%%%%%%%%%%%%%%%%%%%%%%%%%%%%%%%%%%%%%%%%%%%%
Species_Max_Filter_4_ppm = 100;
Species_Min_Filter_4_ppm = 10;
%%%%%%%%%%%%%%%%%%%%%%%%%%%%%%%%%%%%%%%%%%%%%%%%%%%%%%%%%%%%%%%%%%%%%%%%%%%%
%%%%%%%%%%%%%%%%%%%%%%%%%%%%%%%%%%%%%%%%%%%%%%%%%%%%%%%%%%%%%%%%%%%%%%%%%%%%
Species_Max_Filter_4 =  Species_Max_Filter_4_ppm/1e6;
Species_Min_Filter_4 =  Species_Min_Filter_4_ppm/1e6;
% Filter Species
Species_Max_Count_4 =  1;
for n = 1:length(b)
    if b(n,1) >= Species_Max_Filter_4
        Species_Max_Count_4 = n+1;
    end
    if b(n,1) >= Species_Min_Filter_4
        Species_Min_Count_4 = n;
```

```
    end
end
% Plot Filtered Species
figure(4)
semilogy(Chemkin_Data(:,1)*1000,Chemkin_Data_New(:,Species_Max_Count_4:Species_Min_Count_4),'LineWidth',1)
colormap(jet)
xlim([0 1000*max(Chemkin_Data(:,1))]);
ylim([1e-6 Species_Max_Filter_4]);%  b(length(b),1)*1.1]);
title (['Species Concentration Time-History for ',Conditions,' (Filtered Between ',num2str(Species_Min_Filter_4_ppm),...
    ' ppm and ',num2str(Species_Max_Filter_4_ppm),' ppm Maximum Concentration)']);xlabel('Time [ms]');
ylabel('Mole Fraction');
legend(Chemkin_Variables_New(Species_Max_Count_4:Species_Min_Count_4),'Location','nw');
hold off

% Export Species Time-Histories as *.csv for Plotting in Origin
[ll ww] = size(Chemkin_Data_New);
Origin_Out_All_Plot_4 = zeros(ll+1,(Species_Min_Count_4-Species_Max_Count_4)+1);
Origin_Out_All_Plot_4(2:ll+1,1) = Chemkin_Data(:,1)*1000;
Origin_Out_All_Plot_4(2:ll+1,2:(Species_Min_Count_4-Species_Max_Count_4)+2) = ...
    Chemkin_Data_New(:,Species_Max_Count_4:Species_Min_Count_4);
csvwrite('Origin_Out_All_Plot_4.csv',Origin_Out_All_Plot_4);

%For Good *.pdf Figures
set(gcf, 'PaperUnits', 'inches');
set(gcf, 'PaperSize', [11/Fontscale 8.5/Fontscale]);
set(gcf, 'PaperPosition', [-.5/Fontscale 0 12/Fontscale 8.5/Fontscale]);
print -r720 -dpdf figure(4)

%%%%%%%%%%%%%%%%%%%%%%%%%%%%%%%%%%%%%%%%%%%%%%%%%%%%%%%%%%%%%%%%%%%%%%%
%%%% Set Major Species Filters %%%%%%%%%%%%%%%%%%%%%%%%%%%%%%%%%%%%%%%%
Species_Max_Filter_5_ppm = 10;
Species_Min_Filter_5_ppm = 1;
%%%%%%%%%%%%%%%%%%%%%%%%%%%%%%%%%%%%%%%%%%%%%%%%%%%%%%%%%%%%%%%%%%%%%%%
%%%%%%%%%%%%%%%%%%%%%%%%%%%%%%%%%%%%%%%%%%%%%%%%%%%%%%%%%%%%%%%%%%%%%%%
Species_Max_Filter_5 =  Species_Max_Filter_5_ppm/1e6;
Species_Min_Filter_5 =  Species_Min_Filter_5_ppm/1e6;
% Filter Species
Species_Max_Count_5 =  1;
for n = 1:length(b)
    if b(n,1) >= Species_Max_Filter_5
       Species_Max_Count_5 = n+1;
    end
    if b(n,1) >= Species_Min_Filter_5
       Species_Min_Count_5 = n;
    end
end
% Plot Filtered Species
figure(5)
semilogy(Chemkin_Data(:,1)*1000,Chemkin_Data_New(:,Species_Max_Count_5:Species_Min_Count_5),'LineWidth',1)
colormap(jet)
xlim([0 1000*max(Chemkin_Data(:,1))]);
ylim([1e-6 Species_Max_Filter_5]);%  b(length(b),1)*1.1]);
title (['Species Concentration Time-History for ',Conditions,' (Filtered Between ',num2str(Species_Min_Filter_5_ppm),...
    ' ppm and ',num2str(Species_Max_Filter_5_ppm),' ppm Maximum Concentration)']);
xlabel('Time [ms]');
ylabel('Mole Fraction');
legend(Chemkin_Variables_New(Species_Max_Count_5:Species_Min_Count_5),'Location','nw');
hold off

% Export Species Time-Histories as *.csv for Plotting in Origin
[ll ww] = size(Chemkin_Data_New);
Origin_Out_All_Plot_5 = zeros(ll+1,(Species_Min_Count_5-Species_Max_Count_5)+1);
Origin_Out_All_Plot_5(2:ll+1,1) = Chemkin_Data(:,1)*1000;
Origin_Out_All_Plot_5(2:ll+1,2:(Species_Min_Count_5-Species_Max_Count_5)+2) = ...
    Chemkin_Data_New(:,Species_Max_Count_5:Species_Min_Count_5);
csvwrite('Origin_Out_All_Plot_5.csv',Origin_Out_All_Plot_5);

%For Good *.pdf Figures
set(gcf, 'PaperUnits', 'inches');
set(gcf, 'PaperSize', [11/Fontscale 8.5/Fontscale]);
set(gcf, 'PaperPosition', [-.5/Fontscale 0 12/Fontscale 8.5/Fontscale]);
print -r720 -dpdf figure(5)

%%%%%%%%%%%%%%%%%%%%%%%%%%%%%%%%%%%%%%%%%%%%%%%%%%%%%%%%%%%%%%%%%%%%%%%%
%%%% Set Major Species Filters %%%%%%%%%%%%%%%%%%%%%%%%%%%%%%%%%%%%%%%%%
Species_Max_Filter_6_ppm = 1;
Species_Min_Filter_6_ppm = 1e-3;
%%%%%%%%%%%%%%%%%%%%%%%%%%%%%%%%%%%%%%%%%%%%%%%%%%%%%%%%%%%%%%%%%%%%%%%%
%%%%%%%%%%%%%%%%%%%%%%%%%%%%%%%%%%%%%%%%%%%%%%%%%%%%%%%%%%%%%%%%%%%%%%%%
Species_Max_Filter_6 =  Species_Max_Filter_6_ppm/1e6;
Species_Min_Filter_6 =  Species_Min_Filter_6_ppm/1e6;
% Filter Species
Species_Max_Count_6 =  1;
for n = 1:length(b)
    if b(n,1) >= Species_Max_Filter_6
       Species_Max_Count_6 = n+1;
    end
    if b(n,1) >= Species_Min_Filter_6
       Species_Min_Count_6 = n;
    end
end
% Plot Filtered Species
```

```
figure(6)
semilogy(Chemkin_Data(:,1)*1000,Chemkin_Data_New(:,Species_Max_Count_6:Species_Min_Count_6),'LineWidth',1)
colormap(jet)
xlim([0 1000*max(Chemkin_Data(:,1))]);
ylim([1e-9 Species_Max_Filter_6]);%  b(length(b),1)*1.1]);
title (['Species Concentration Time-History for ',Conditions,' (Filtered Between ',num2str(Species_Min_Filter_6_ppm),...
    ' ppm and ',num2str(Species_Max_Filter_6_ppm),' ppm Maximum Concentration)']);
xlabel('Time [ms]');
ylabel('Mole Fraction');
legend(Chemkin_Variables_New(Species_Max_Count_6:Species_Min_Count_6),'Location','nw');
hold off

% Export Species Time-Histories as *.csv for Plotting in Origin
[ll ww] = size(Chemkin_Data_New);
Origin_Out_All_Plot_6 = zeros(ll+1,(Species_Min_Count_6-Species_Max_Count_6)+1);
Origin_Out_All_Plot_6(2:ll+1,1) = Chemkin_Data(:,1)*1000;
Origin_Out_All_Plot_6(2:ll+1,2:(Species_Min_Count_6-Species_Max_Count_6)+2) = ...
    Chemkin_Data_New(:,Species_Max_Count_6:Species_Min_Count_6);
csvwrite('Origin_Out_All_Plot_6.csv',Origin_Out_All_Plot_6);

%For Good *.pdf Figures
set(gcf, 'PaperUnits', 'inches');
set(gcf, 'PaperSize', [11/Fontscale 8.5/Fontscale]);
set(gcf, 'PaperPosition', [-.5/Fontscale 0 12/Fontscale 8.5/Fontscale]);
print -r720 -dpdf figure(6)
```
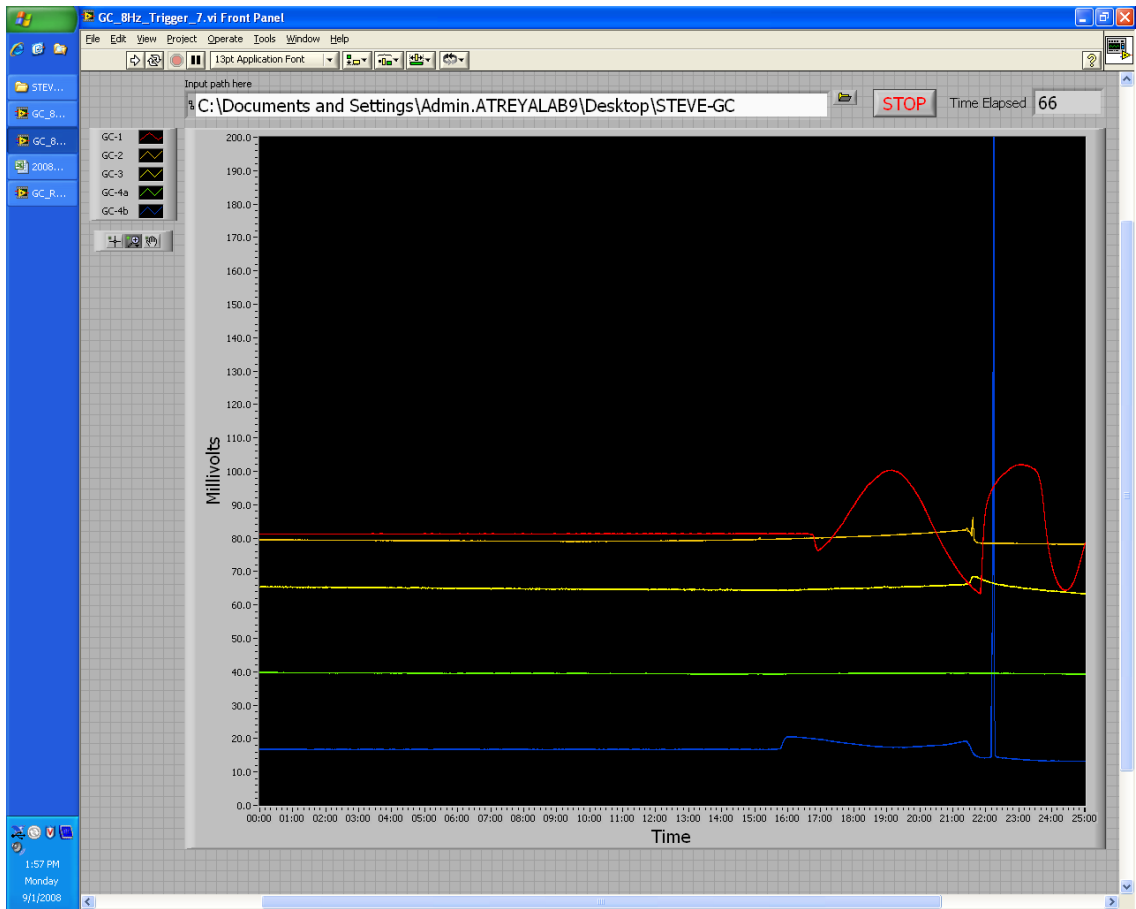
Figure B.3 Screenshot of the LABVIEW chromatogram acquisition graphical user interface.
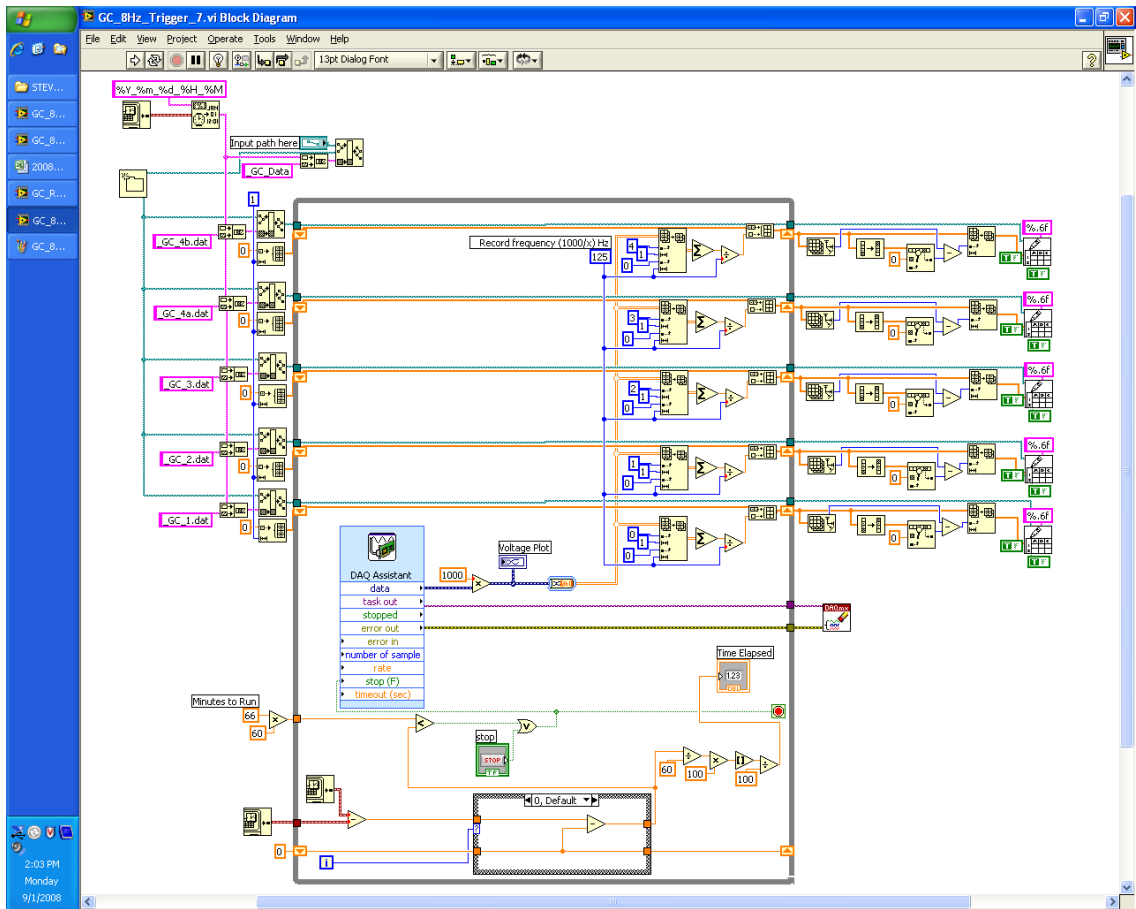
Figure B.4 Screenshot of the block diagram defining the LABVIEW chromatogram acquisition program.

Appendix C

Demonstration of distinct ignition regimes using high-speed digital imaging of iso-octane mixtures

An experimental investigation of iso-octane ignition phenomena

S.M. Walton [*], X. He, B.T. Zigler, M.S. Wooldridge, A. Atreya

Department of Mechanical Engineering, University of Michigan, 2350 Hayward St., Ann Arbor, MI 48109-2125, USA

Abstract

High-speed digital imaging has been used in rapid compression facility (RCF) studies to investigate ignition phenomena of iso-octane/air mixtures. Sequential images were captured for each experiment. The results indicate the existence of two ignition regimes. In one domain, ignition is rapid, typically less than 76 μs, and ignition occurs simultaneously throughout the test volume. In the other domain, reaction fronts form and propagate within the test volume prior to volumetric ignition. The data span equivalence ratios from $\phi = 0.20$ to 1.98, with inert/O_2 gas ratios from 1.38 to 5.89, pressures from 8.7 to 16.6 atm, and temperatures from 903 to 1020 K. The transition between the two regimes is discussed in the context of the mixture composition and experimental conditions. The analysis shows that the fuel mole fraction is a key parameter dictating the boundary between the modes of ignition. Below a critical mole fraction limit, volumetric ignition is observed; above the critical limit, reaction fronts are consistently present prior to volumetric ignition. The ignition delay times for both ignition regimes are well reproduced using a homogeneous simulation with detailed reaction chemistry, when the state conditions are modified to account for the presence of the reaction fronts. The results are discussed in terms of proposed reaction chemistry, ignition theory, and previous studies of iso-octane ignition.
© 2006 The Combustion Institute. Published by Elsevier Inc. All rights reserved.

Keywords: Ignition; Ignition delay time; Iso-octane; Reaction front; Rapid compression facility

1. Introduction

Intermediate-temperature, premixed, lean fuel conditions are of considerable importance in many advanced combustion approaches that focus on simultaneously reducing pollutant emissions and increasing combustion efficiencies, such as homogeneous charge compression ignition (HCCI) engines [1] and integrated gasification combined cycle (IGCC) power plants [2]. The reaction kinetics often plays a significant role in the combustion characteristics that control performance of the devices based on lean premixed technologies. As a consequence, there have been significant efforts to investigate the chemical kinetics of fuel/air mixtures under conditions relevant to these recent combustion applications (e.g., [3–9]). The high-temperature, high-pressure conditions created by shock tubes and rapid compression facilities (RCF) make these apparatus ideal for isolating the reaction chemistry and quantifying the ignition behavior of the fuel/air mixtures over a broad parametric space, including equivalence ratio and dilution. Ignition data are also useful as one means to validate and

---

[*] Corresponding author. Fax: +1 734 647 3170.
E-mail address: smwalton@umich.edu (S.M. Walton).

refine detailed, skeletal, and reduced chemical reaction mechanisms.

Several RCF and shock tube ignition studies of hydrocarbon fuels [5–7,10–16] have observed the presence of complex preignition behavior, often spatially resolved, under intermediate-temperature and high-pressure conditions. For example, during recent RCF ignition studies of iso-octane mixtures [3,4], the presence of reaction fronts prior to volumetric ignition was observed under certain conditions through simultaneous imaging and pressure data, while volumetric ignition with no spatially resolved features occurred under other conditions. Studies of engines operating in the HCCI mode have also indicated the presence of reaction fronts under conditions below the lean flammability limit, where flames are not considered self-sustaining [17–20]. Additional analytical and numerical studies have proposed the existence of multiple ignition regimes that may be present prior to volumetric ignition [21–24]. The presence of reaction fronts at lean conditions can have critical effects on ignition timing and pollutant emissions [17,18] and on safety considerations.

Zeldovich [21] first proposed criteria delineating regimes of deflagration, spontaneous propagation, and normal detonation. Gu et al. [22] built on that theory and proposed five regimes of ignition or propagation modes in computational ignition studies when hot spots were introduced into otherwise homogeneous mixtures of hydrogen/air and hydrogen/carbon monoxide/air. Gu et al. [22] suggested the regimes are delineated by the local temperature gradient, the critical temperature gradient, and the acoustic velocity of the test gas mixture. Similarly, Sankaran et al. [23] identified two ignition regimes (spontaneous explosion and flame-like deflagration) in their computational study of ignition of hydrogen/air mixtures in turbulent scalar fields of temperature gradients. Unfortunately, there are few experimental data available for quantitative evaluation of the ignition theories proposed by these and other groups.

Based on the need to understand the effects of reaction fronts on ignition properties, the objective of the current work was to identify and quantify the characteristics and modes of ignition of lean, intermediate-temperature iso-octane/air mixtures and to provide a quantitative understanding of the chemical and physical mechanisms that are important in differentiating the ignition regimes observed. The technical approach used was to measure the ignition delay times for iso-octane mixtures over a broad experimental domain using a rapid compression facility and simultaneously use high-speed digital imaging to capture the ignition phenomena. The results are discussed in terms of proposed reaction chemistry, ignition theory, and previous studies of iso-octane ignition.

2. Experimental approach

2.1. The rapid compression facility

All experiments were conducted in the well-controlled and well-characterized environment of the University of Michigan Rapid Compression Facility (UM RCF). The ignition behavior of iso-octane mixtures was investigated in terms of several parameters, including equivalence ratio (ϕ), inert gas to oxygen ratio (dilution), temperature, and pressure. High-speed digital imaging and pressure and emission time-histories were used to characterize the ignition experiments. A detailed description of the UM RCF, the operating procedure, and the results of benchmark experimental studies characterizing performance can be found in Donovan et al. [25], He et al. [3,4], and Donovan [26].

Briefly, the UM RCF consists of five major components: the driver section, the driven section, the test manifold, the sabot (free piston), and the hydraulic control valve assembly. The driver section (154 mm i.d.) contains pressurized air and is separated from the driven section (2.74 m long, 101.2 mm i.d.) by a fast-acting hydraulic globe valve assembly and a scored sheet of plastic (0.05 mm, Mylar). The driven section is a long stainless steel tube with a honed and chromed interior surface that is connected to the test manifold. The sabot has a replaceable nosecone that is made of ultra-high-molecular-weight polyethylene. The body of the sabot is solid (Delrin) and contains a copper counterweight to balance the nosecone. U-ring seals (virgin Teflon with stainless steel radial springs) eliminate gas blow-by past the sabot.

A schematic of the test manifold and imaging system is shown in Fig. 1. The four main components of the test manifold are the convergent section, the extension section, the instrumented test section, and a transparent end wall. The stainless steel convergent section bridges the 101.2-mm bore of the driven section to the 50.8-mm bore of the remainder of the test manifold components. The total length of the extension section is variable by design (through combinations of subcomponents) to yield different compression ratios. The test section has a length of 50.6 mm and is equipped with two optical ports for laser access, a pressure transducer port, and two additional instrumentation ports. For the current study, the test section was instrumented with a piezoelectric transducer (Kistler 6041AX4) and a charge amplifier (Kistler 5010B) for pressure measurements. The end wall seals the test manifold and allows optical access to the test volume.

Two end walls, quartz or polycarbonate, were used to provide optical access to the test manifold. The quartz end wall (with a diameter of 78 mm and

(a) Isometric cross-section view

(b) Cross-section view
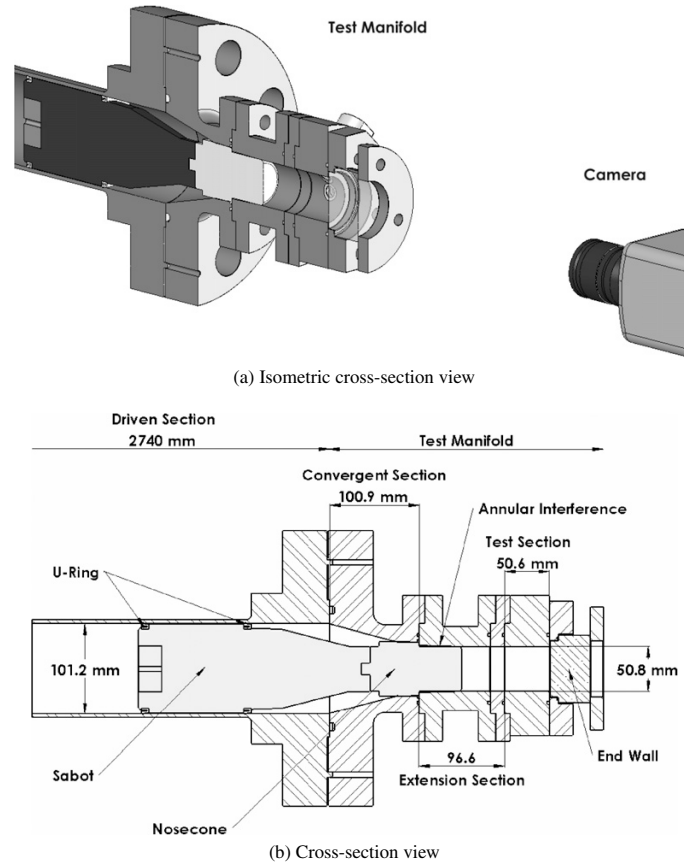
Fig. 1. Experimental schematic of the test section of the UM RCF, demonstrating the camera perspective for high-speed imaging. The sabot nosecone is shown in the final seated position.

a thickness of 45.25 mm) has a double-layer anti-reflective coating on both faces. The coatings are optimized for transmission of visible wavelengths and the window has excellent reflection- and glare-reduction properties. The polycarbonate (Lexan) end walls are polished (140 × 140 mm square with a thickness of 12.5 mm) and have no coatings. Peak transmission for the polycarbonate end walls occurs at visible wavelengths. When the polycarbonate windows were used, the windows were replaced regularly (every 5–10 experiments) to maintain high image quality.

The test gas mixtures were made in a dedicated mixing tank, and the mixture composition was determined by measurement of the relative partial pressures of the gas-phase reactants. The specific heats of the mixtures were controlled through the balance of argon, carbon dioxide, and nitrogen as inert gas diluents. The specific heat of the mixture, the experimen-

tal compression ratios, and the initial charge pressures were varied to achieve the targeted temperatures and pressures.

Prior to each experiment, the sabot is placed at the upstream end of the driven section, downstream of the hydraulic valve assembly and the scored plastic sheet. The RCF is evacuated. Then the driven section and test manifold are charged with the test gas mixture, and the driver section is charged with high-pressure air. The hydraulic valve is opened, breaking the plastic sheet and launching the sabot down the length of the driven section. The test gas mixture is compressed ahead of the sabot. The sabot comes to rest in the test manifold when the nosecone seals (via an annular interference fit) with the extension section. The core region of the test gases is sealed in the test manifold, while the cooler gases near the walls are sealed in the shoulder region of the convergent section.

2.2. High-speed imaging details

The large size of the quartz and polycarbonate end walls allows the entire test volume to be imaged using a high-speed color digital video camera (Vision Research, Phantom V7.1, 800×600 pixel SR-CMOS 48-bit color array, capable of 160 kHz at reduced spatial resolution). The camera array records RGB signals using spectral filters. The red channel uses a high-pass filter with approximately 95% transmission above 615 nm. The green channel uses a bandpass filter with approximately 82% peak transmission at 530 nm. The blue channel uses a bandpass filter with approximately 86% peak transmission at 460 nm. A fast 50-mm lens (f/0.95 Navitar TV Lens) and c-mount extension tube were used with the camera to optimize the capture of available light emission. No additional spectral filtering was used.

The camera sensor array was calibrated for each frame rate and spatial resolution setting using the following procedure. The camera was first aligned with the test manifold approximately 40 cm from the end wall, and the camera was focused on a plane inside the test section, 2 cm from the end wall. To maximize the capture of the emission from the test section and limit the depth of field, the wide aperture lens was used in the fully open position. The camera frame rate and spatial resolution were set at this time. The camera sensor was then calibrated using a black reference (where the camera lens was covered) and the zero signal level of each pixel in the CMOS array was assigned.

For this study, the high-speed digital camera was used to acquire continuous full-frame color video sequences of visible emission from the ignition experiments at speeds from 10,000 to 60,000 frames per second (fps). The frame rate has an inverse relation to the total spatial resolution, and at 26,000 fps (the typical frame rate used), the spatial resolution was maintained at the maximum allowable setting of 256×256 pixels. These settings resulted in each frame corresponding to approximately 38 µs, and each pixel in the CMOS array imaging focused light from a volume with a height × width × depth of approximately 198 µm × 198 µm × 2 mm.

The camera was triggered by a circuit designed to output a pulse to the trigger input of the camera. The signal to the triggering circuit was supplied by a photodetector (Hamamatsu S1787-12) located on the driven section of the RCF. Emission from a laser diode (TIM-201-3, 3 mW, 650 nm) was directed onto the active element of the photodetector so that the laser emission was orthogonal to the path of the sabot. When the sabot passed the laser diode, the change in signal from the photodetector triggered the camera. Using this arrangement, images were acquired throughout the compression and ignition processes.

3. Results

Typical pressure and pressure derivative data for RCF iso-octane ignition experiments are shown in Figs. 2 and 3. At the end of compression, the pressure reaches the first maximum. This time is set as $t = 0$ s and is labeled P_{max} in the figures. The pressure then decreases slightly due to cooling losses to the test
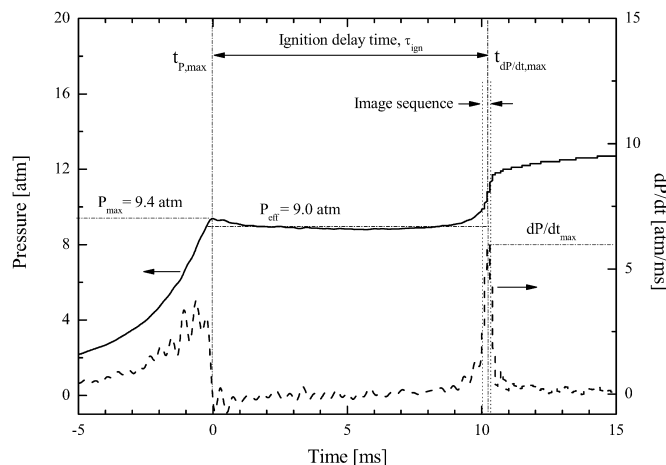
Fig. 2. Typical pressure (—) and pressure derivative (- - -) time-histories for iso-octane ignition experiments where no indications of reaction fronts are observed prior to volumetric ignition. Experimental conditions are $\phi = 0.30$ and inert/$O_2 = 5.00$. The effective temperature based on the effective pressure, $P_{eff} = 9.0$ atm, is $T_{eff} = 1020$ K.
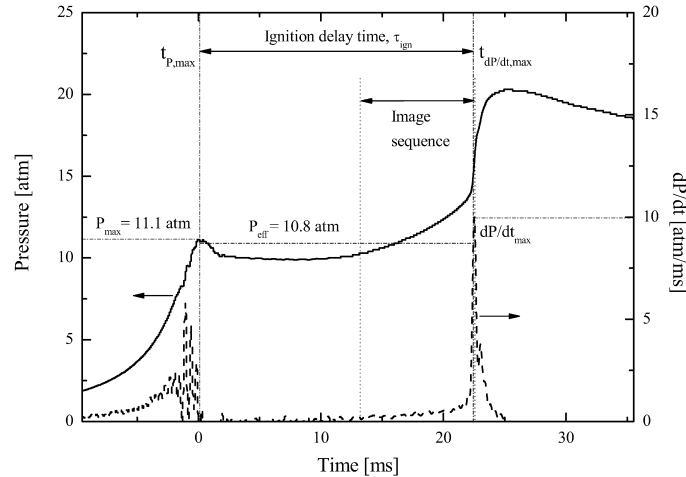
Fig. 3. Typical pressure (—) and pressure derivative (- - -) time-histories for iso-octane ignition experiments where reaction front propagation prior to volumetric ignition is observed. Experimental conditions are $\phi = 0.20$ and inert/$O_2 = 1.38$. The effective temperature based on the effective pressure, $P_{eff} = 10.8$ atm, is $T_{eff} = 917$ K.
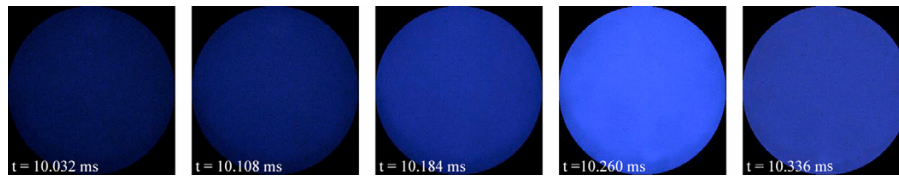
Fig. 4. Imaging sequence corresponding to the data of Fig. 2 and conditions of volumetric ignition where $\phi = 0.30$, $T_{eff} = 1020$ K, $P_{eff} = 9.0$ atm, inert/$O_2 = 5.00$, $\tau_{ign} = 10.3$ ms, 26,000 fps (color adjusted for clarity). Note that not all frames in the imaging sequence are presented. The time interval spanned by these frames is shown in Fig. 2.

volume walls. After a delay period, the mixture auto-ignites, resulting in a rapid increase in pressure for both examples shown. However, the results demonstrate the presence of two different ignition regimes. Conditions exist where only volumetric ignition occurred (Fig. 2), and also where reaction fronts preceded volumetric ignition (Fig. 3). In both data sets, the initial pressure rise is due to compression of the test gas mixture ahead of the sabot.

Fig. 4 presents a selection of the frames from the imaging sequence corresponding to the volumetric ignition data of Fig. 2. As seen in Fig. 4, blue emission occurred uniformly throughout the test volume with increasing intensity until maximum emission levels were observed at $t = 10.260$ ms. No structures or spatial nonuniformities were observed in the emission images for this condition, and ignition occurred simultaneously throughout the test volume. The peak in the emission intensity occurred at the same time as the peak in the pressure derivative. For all conditions where only volumetric ignition was observed, ignition exhibited the same general features as seen in Fig. 4,

i.e., intense homogeneous blue emission that typically spanned less than two frames (76 μs).

Frames from the imaging sequence corresponding to the pressure data of Fig. 3 are shown in Fig. 5. The images show the presence of discrete regions of reaction in the test volume. The reaction fronts are observed early in the image sequence ($t = 6.098$ ms) and they propagate throughout the test volume until volumetric ignition is recorded at $t = 22.534$ ms. Note the small bright spots in the images are from particles occasionally present in the test section. As the particles pass in and out of the focal plane, halos appear in the images.

Figs. 6 and 7 provide additional examples of still frame image sequences acquired from other experiments where reaction fronts were present. The general features are the same. When reaction fronts were observed, more than one reaction front was typically present. Reaction fronts did not consistently initiate in the same location of the test volume; in some cases the fronts started in the center or top of the test volume, as compared to the data of Fig. 5. When volumetric
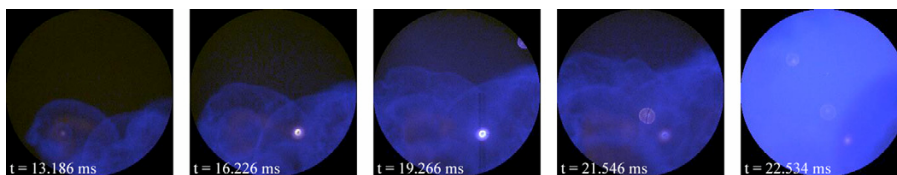
Fig. 5. Imaging sequence corresponding to the data of Fig. 3, where reaction fronts are present prior to volumetric ignition and $\phi = 0.20$, $T_{eff} = 917$ K, $P_{eff} = 10.8$ atm, inert/$O_2 = 1.38$, $\tau_{ign} = 22.5$ ms, 26,000 fps (color adjusted for clarity). Note that not all frames in the imaging sequence are presented. The time interval spanned by these frames is shown in Fig. 3.
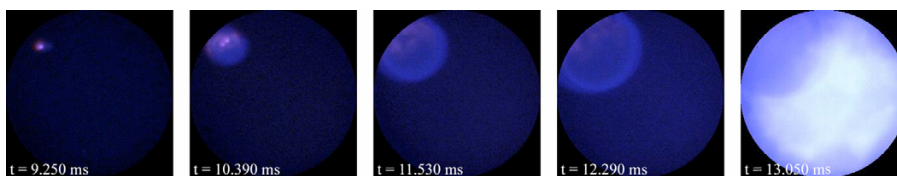
Fig. 6. Imaging sequence of reaction fronts prior to volumetric ignition for conditions of $\phi = 0.57$, $T_{eff} = 988$ K, $P_{eff} = 8.7$ atm, inert/$O_2 = 4.99$, $\tau_{ign} = 13.1$ ms, 26,000 fps (color adjusted for clarity). Note that not all frames in the imaging sequence are presented.
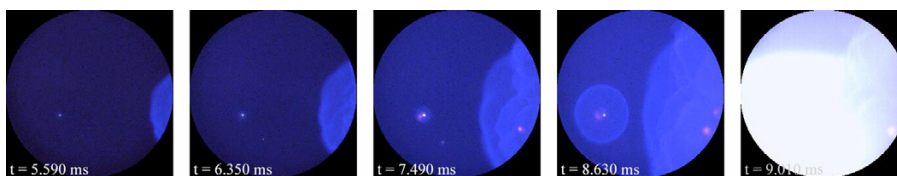
Fig. 7. Imaging sequence of reaction fronts prior to volumetric ignition for conditions of $\phi = 0.77$, $T_{eff} = 999$ K, $P_{eff} = 9.1$ atm, inert/$O_2 = 5.00$, $\tau_{ign} = 9.0$ ms, 26,000 fps (color adjusted for clarity). Note that not all frames in the imaging sequence are presented.
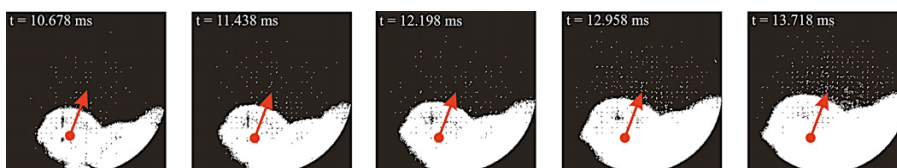
Fig. 8. Example of the image analysis used to determine the reaction front propagation rates. The images are presented in binary form to enhance clarity. The vector indicates the direction used to determine the speed and is set orthogonal to the surface of the propagating reaction front. The images are from the data set shown (in part) in Fig. 5, where $\phi = 0.20$, $T_{eff} = 917$ K, $P_{eff} = 10.8$ atm, inert/$O_2 = 1.38$, $\tau_{ign} = 22.5$ ms, 26,000 fps.

ignition occurs, the region of the test section where the reactants were previously consumed by the reaction fronts exhibits lower emission intensity (e.g., the half-moon-shaped areas in Figs. 5 and 6) as a result of the lower remaining unburned reactant fraction. In some experiments the reaction fronts appear to originate from the hot particles (e.g., Fig. 7).

For each experiment where reaction fronts were observed, the rate of propagation of the reaction fronts, U [m/s], was determined from the image se-

quences, as shown schematically in Fig. 8. Note that in order to make the presence and propagation of the reaction fronts clearer, Fig. 8 presents data from the same imaging file as that of Fig. 5, where a threshold filter has been applied to create binary images. The propagation rates were determined by tracking features on the reaction surface through time. The result is an estimate for the propagation rate in the direction normal to the surface of the reaction front. The image analysis indicated that the highest propagation rates

of the reaction fronts were associated with propagation into the unconstrained environment toward the center of the test volume (as opposed to propagation into gases bounded by the test chamber walls). Only the maximum velocities are reported here.

The effect of the propagation of the discrete zones of reaction is apparent in the pressure time history. The pressure data show a slow increase at times consistent with the formation and propagation of the reaction fronts, prior to the rapid increase in pressure associated with volumetric ignition (see Fig. 3). The expansion of the reaction fronts serves to further compress the unignited test gas mixture and consequently the pressure and temperature in the test section gradually increase prior to volumetric ignition. On the contrary, the pressure data corresponding to (only) volumetric ignition (Fig. 2) show little pressure rise during the delay period prior to the ignition.

The effective pressure (P_{eff}) for each experiment was defined as the time-integrated average pressure from the maximum pressure (P_{max}) due to compression to the point of maximum rate of pressure rise (dP/dt_{max}), or

$$P_{eff} = \frac{1}{(t_{dP/dt_{max}} - t_{P_{max}})} \int_{t_{P_{max}}}^{t_{dP/dt_{max}}} P \, dt. \tag{1}$$

The effective temperature for each experiment was determined as in previous UM RCF studies [3] using the effective pressure and by numerical integration of the isentropic relation

$$\int_{T_0}^{T_{eff}} \frac{\gamma}{\gamma - 1} \, d\ln T = \ln\left(\frac{P_{eff}}{P_0}\right), \tag{2}$$

where P_0 is the charge pressure, T_0 is the initial temperature (typically 298 K), and γ is the temperature-dependent ratio of the specific heats of the unreacted test gas mixture, which is determined using the NASA thermodynamic data base [27].

For each experiment, the ignition delay time (τ_{ign}) was determined using the pressure time history. A different definition for τ_{ign} has been used in this work than in to previous UM-RCF studies [3,4]. In this work the ignition delay time was defined as the time between P_{max} and dP/dt_{max}. This definition for τ_{ign} is illustrated in Figs. 2 and 3. When compared with the previous data for τ_{ign} [3,4], this definition for τ_{ign} yields an average difference of less than 2%.

A summary of the iso-octane ignition data, including the measured ignition delay time and maximum propagation rate for each experiment, is presented in Table 1. In the table, the equivalence ratio ϕ is defined as the actual iso-octane to oxygen ratio divided by the stoichiometric iso-octane to oxygen ratio. The

inert gas to O_2 molar ratio is also provided in Table 1 as an indication of the dilution of the mixture. The inert gases studied include nitrogen, argon, and carbon dioxide. The mixture components are each provided on a mole fraction basis (e.g., χ_{fuel} is the mole fraction of iso-octane in the mixture on a percentage basis). The range of conditions and mixture compositions spanned $\phi = 0.2$–1.98, inert gas/O_2 ratios of 1.38–5.89, pressures of $P_{eff} = 8.7$–16.6 atm, and temperatures of $T_{eff} = 903$–1020 K. The imaging and pressure data for each experiment were designated as one of the two categories of ignition described above: volumetric ignition or reaction front propagation/volumetric ignition. The volumetric ignition data are identified by a "V" designation in the table.

Regression analysis can be used to identify trends in the τ_{ign} data and to isolate the effects of each parameter of interest, e.g., temperature. Regression analysis was conducted on the complete τ_{ign} data set of Table 1. Multiple forms to the expression were considered yielding similar qualities of fit. For consistency, the same form as was used previously [3] is used here, with a best-fit R^2 value of 0.92:

$$\tau_{ign} = 2.8 \times 10^{-3} P^{-1.25} \phi^{-0.79} \chi_{O_2}^{-1.14}$$
$$\times \exp(27{,}300/R_{[cal/mol/K]}T). \tag{3}$$

In Eq. (3), τ_{ign} is the ignition delay time [ms], P is the pressure [atm], ϕ is the equivalence ratio, χ_{O_2} is the oxygen mole percentage, R is the universal gas constant, and T is the temperature [K]. Although the fit parameters differ from those determined by He et al. [3], the new correlation yields only slight changes in the predicted values for τ_{ign}, as seen in Figs. 9–12.

Summaries of the effects of temperature, pressure, equivalence ratio, and oxygen mole fraction on τ_{ign} are presented in Figs. 9–12, respectively, where the data have been normalized as necessary using Eq. (3). Equation (3) is provided for reference in each of the figures as the solid line. The recommended uncertainty in the ignition delay time measurements (presented as the error bars in Fig. 9) is ±13% and is based on the standard deviation of τ_{ign} relative to the correlation provided in Eq. (3).

Trends in the rate of propagation of the reaction fronts, U, as a function of the state conditions and the mixture properties were also investigated. The analysis indicated no strong direct correlation with temperature, pressure, equivalence ratio, or oxygen mole fraction, and even extremely fuel lean mixtures were capable of sustaining a reaction front. However, there was a strong dependence of U on fuel mole fraction (χ_{fuel}), as seen in Fig. 13, where U increases nearly linearly with increasing χ_{fuel}. When compared with conditions where only volumetric ig-

Table 1
Summary of experimental conditions and results

ϕ	Inert/O_2	Test gas composition				P_{eff}[a] [atm]	T_{eff} [K]	U [m/s]	a[b] [m/s]	Ignition delay time [ms]		
		$\chi_{i\text{-}C_8H_{18}}$ [%]	χ_{O_2} [%]	χ_{N_2} [%]	χ_{Ar} [%]					τ_{ign}	τ_{reg}[c]	τ_{pred}[d]
0.20	1.38	0.7	41.8	57.5	0.0	10.8	917	1.1	578	22.5	23.2	26.2
0.30	1.39	1.0	41.4	51.2	6.4	12.1	936	3.3	576	8.3	10.9	11.7
0.30	3.65	0.5	21.4	75.2	2.8	10.8	947	0.5	596	23.9	22.5	20.3
0.30	4.00	0.5	19.9	70.8	8.8	10.7	958	0.5	597	21.6	21.0	17.8
0.40	3.01	0.8	24.8	62.7	11.7	10.9	945	2.7	585	17.3	15.5	13.9
0.40	3.76	0.7	20.9	71.2	7.3	11.0	951	1.9	593	17.9	17.0	15.0
0.40	2.28	1.0	30.2	51.0	17.8	11.8	964	3.6	582	14.2	8.4	7.4
0.40	3.01	0.8	24.8	62.7	11.7	11.8	971	3.0	592	9.9	9.5	8.1
0.50	3.76	0.8	20.8	66.1	12.3	10.3	944	2.7	586	20.8	17.3	14.8
0.50	2.50	1.1	28.2	48.3	22.4	11.2	947	4.7	572	10.1	10.5	9.4
0.50	3.76	0.8	20.8	66.1	12.3	11.0	955	2.8	589	14.5	13.4	11.5
0.50	2.50	1.1	28.2	48.3	22.4	12.1	969	7.5	579	5.1	6.9	5.9
0.51	5.01	0.7	16.5	69.0	13.8	11.3	970	0.9	596	13.9	13.3	11.0
0.51	5.01	0.7	16.5	69.0	13.8	11.7	979	2.3	599	12.4	11.2	9.2
0.57	4.99	0.8	16.6	64.9	17.8	8.7	988	3.6	597	13.1	13.0	8.8
0.58	5.03	0.8	16.5	65.1	17.7	12.0	989	2.7	598	9.1	8.5	7.0
0.60	4.95	0.8	16.7	71.9	10.6	11.1	945	4.3	589	18.5	17.2	15.1
0.60	4.95	0.8	16.7	71.9	10.6	11.4	952	3.9	591	16.1	15.0	13.0
0.77	5.00	1.0	16.5	56.8	25.7	9.1	999	4.4	592	9.0	8.4	6.7
0.80	3.76	1.3	20.7	50.8	27.2	11.4	961	3.9	574	8.3	8.2	6.8
0.80	4.94	1.1	16.7	63.7	18.6	11.9	961	5.4	585	10.4	9.9	8.4
0.80	3.76	1.3	20.7	50.9	27.1	11.6	962	5.8	574	6.0	7.9	6.5
0.80	3.76	1.3	20.7	50.8	27.2	12.8	983	7.8	580	4.7	5.1	4.3
0.99	4.92	1.3	16.7	55.5	26.5	12.3	970	6.6	579	6.5	7.0	6.1
1.98	3.75	3.2	20.4	19.1	57.3	16.6	903	3.3	515	6.2	6.3	4.4
1.98	3.75	3.2	20.4	19.1	57.3	13.5	918	6.5	519	6.4	6.4	4.4
0.20	3.78	0.3	20.9	78.8	0.0	10.3	940	V	598	37.8	37.7	35.4
0.20	3.78	0.3	20.9	78.8	0.0	9.7	928	V	595	50.8	49.1	47.4
0.25	5.00	0.3	16.6	79.2	3.9	15.4	987	V	612	13.4	12.4	11.4
0.25	5.00	0.3	16.6	79.2	3.9	14.0	965	V	605	21.2	19.2	18.3
0.30	3.76	0.5	20.9	76.3	2.3	10.9	945	V	596	24.0	23.6	21.4
0.30	3.76	0.5	20.9	76.3	2.3	10.5	937	V	594	29.8	28.0	25.8
0.30	5.00	0.4	16.6	77.2	5.8	9.0	1020	V	619	10.3	13.4	8.1
0.32	4.99	0.4	16.6	77.1	5.8	9.2	981	V	608	19.1	21.1	15.9
0.35	5.89	0.4	14.5	80.0	0.0[e]	11.1	932	V	589	27.6	37.9	34.7
0.35	5.89	0.4	14.5	80.0	0.0[e]	11.0	930	V	589	29.4	39.6	36.6
0.40	4.29	0.6	18.9	75.4	5.4	11.3	955	V	598	19.1	17.3	15.0
0.40	4.29	0.6	18.9	75.4	5.4	11.0	949	V	596	21.0	19.6	17.3
0.40	5.01	0.5	16.6	72.9	10.0	11.3	972	V	601	14.5	15.6	12.9
0.40	5.01	0.5	16.6	72.9	10.0	9.3	927	V	588	43.6	39.5	34.7
0.50	5.00	0.7	16.6	76.4	6.4	10.8	946	V	594	25.0	20.4	17.9
0.50	5.00	0.7	16.6	76.4	6.4	10.1	931	V	589	33.0	28.0	24.7

Note. The mixture composition is provided on a mole basis. The equivalence ratio is based on iso-octane to O_2 molar ratios.
Experiments where only volumetric ignition was observed are denoted V.

[a] P_{eff} determined using Eq. (1).

[b] Speed of sound based on T_{eff} and the unreacted mixture composition.

[c] Predicted value for ignition delay time using Eq. (3).

[d] Predicted value for ignition delay time using the single-zone model and the reaction mechanism of Curran et al. [28].

[e] Balance CO_2.

nition was observed, the data of Fig. 13 imply the existence of a critical fuel mole fraction limit, $\chi_{fuel,crit}$, above which reaction fronts are self-sustaining, and below which only volumetric ignition is observed. Using a linear fit to the U data and extrapolating to $U = 0$ m/s, yields a value for $\chi_{fuel,crit}$ of 0.4.
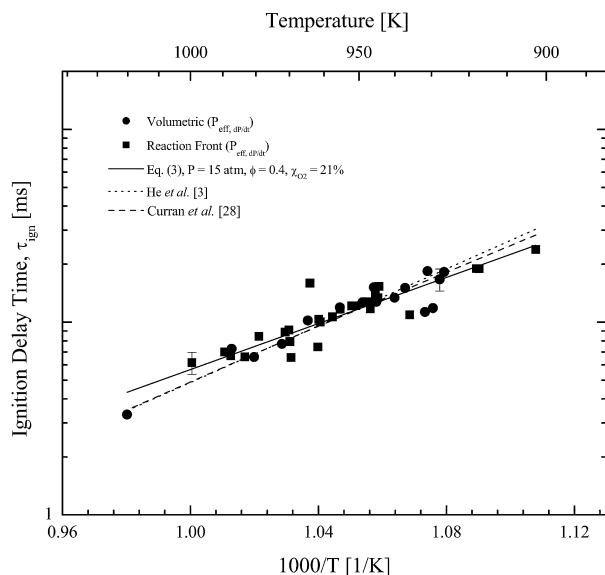
Fig. 9. Summary of reaction front and volumetric ignition data for iso-octane ignition delay time as a function of inverse temperature. The experimental data have been normalized to $P = 15$ atm, $\phi = 0.4$, and $\chi_{O_2} = 21\%$ using Eq. (3). Equation (3), the correlation developed by He et al. [3], and the results of model predictions for τ_{ign} based on the reaction mechanism of Curran et al. [28] are provided for comparison. The error bars represent the uncertainty in the measurements based on the standard deviation in the data.

4. Discussion

4.1. Reaction kinetics

The experimental data for τ_{ign} were compared with predictions using a single-zone model and the detailed chemical reaction mechanism developed for iso-octane by Curran et al. [28]. For the modeling, the Aurora/Chemkin 4.0.1 suite of programs [29] was used, assuming a homogeneous, adiabatic, constant-volume system. The compression process and the initial heat losses to the test volume walls were not simulated, as previous modeling studies [3] have shown that little reaction occurs during compression for the iso-octane mixtures and conditions studied in this work, and ignition delay times were typically within 5% of the values determined when these effects were considered. Consequently, the effective state conditions (P_{eff} and T_{eff}) and the composition of the unreacted mixture were used in the calculations as the initial conditions, assuming no heat losses.

The effects of changing the diluent composition in the test gas mixture were also explored using the model. Simulations were conducted under conditions of $P = 15$ atm, $T = 980$ K, $\phi = 0.4$, and $\chi_{O_2} = 21\%$. The balance of diluent in the mixture was then set at the limits explored experimentally. A gas composition of 100% N_2 resulted in $\tau_{ign} = 6.92$ ms; 6% CO_2, bal-

ance N_2 resulted in $\tau_{ign} = 6.93$ ms; 75% Ar, balance N_2 resulted in $\tau_{ign} = 6.18$ ms. These results indicate that the chemical kinetic effects of changing the composition of the inert gas in the mixture are small for the nominal conditions used in the experiments. The effects of the inert gas composition and concentration on the thermophysical properties of the mixture are discussed further below.

A summary of the model predictions for ignition delay time are provided in Table 1 as τ_{pred}. The trends based on the mechanism of Curran et al. are also provided for comparison in Figs. 9–12. As seen in Table 1 and Figs. 9–12, the predictions for τ_{ign} are in excellent agreement with the experimental data (within an average of 11% for the volumetric ignition data, and within an average of 15% for the reaction front data). The ability to accurately reproduce τ_{ign} in the UM RCF using P_{eff} and T_{eff} for the conditions where reaction fronts were observed using a homogeneous model is an important finding, which supports the hypothesis that the primary effects of the reaction fronts on the unignited reactants is volumetric by means of an increase in pressure. Transport effects, which are localized and are not captured by the single-zone model used, do not appear to significantly influence τ_{ign}.

Negative-temperature coefficient (NTC) chemistry has been proposed to lead to faster ignition
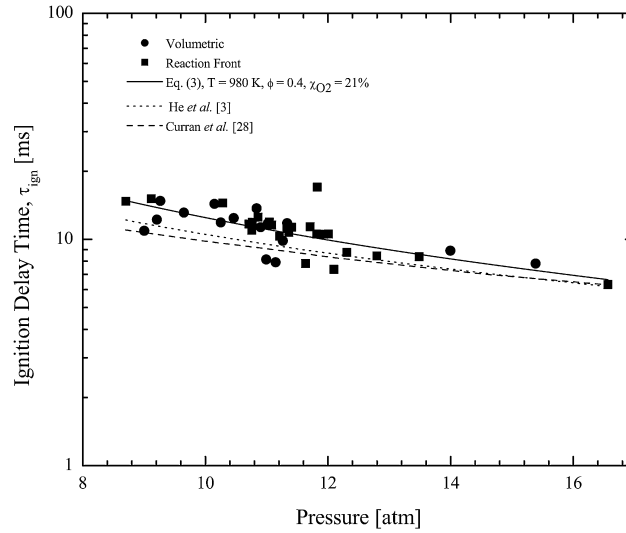
Fig. 10. Summary of reaction front and homogeneous ignition data for iso-octane ignition delay time as a function of pressure. The experimental data have been normalized to $T = 980$ K, $\phi = 0.4$, and $\chi_{O_2} = 21\%$ using Eq. (3). Equation (3), the correlation developed by He et al. [3], and the results of model predictions for τ_{ign} based on the reaction mechanism of Curran et al. [28] are provided for comparison.
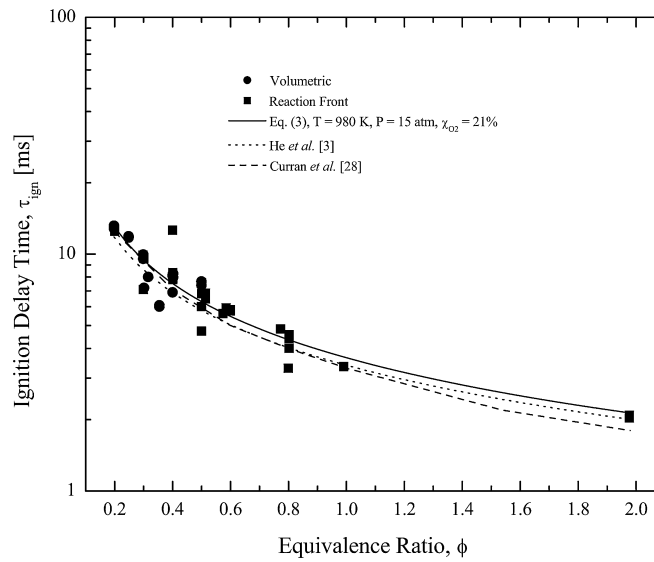
Fig. 11. Summary of reaction front and homogeneous ignition data for iso-octane ignition delay time as a function of equivalence ratio. The experimental data have been normalized to $T = 980$ K, $P = 15$ atm, and $\chi_{O_2} = 21\%$ using Eq. (3). Equation (3), the correlation developed by He et al. [3], and the results of model predictions for τ_{ign} based on the reaction mechanism of Curran et al. [28] are provided for comparison.

of cooler regions of test gas mixtures in some low-temperature ignition studies of iso-octane [11]. However, the formation of the reaction fronts observed

in this work is not attributed to NTC chemistry. Iso-octane does not exhibit NTC behavior at the pressures and temperatures considered here [4]. Additionally,
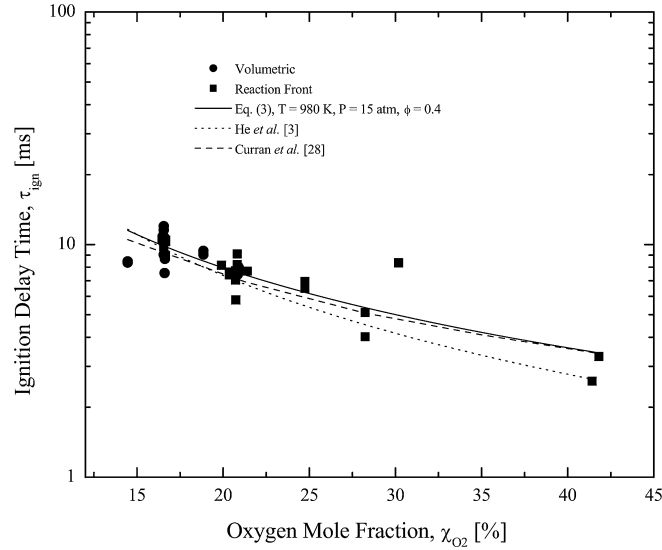
Fig. 12. Summary of reaction front and homogeneous ignition data for iso-octane ignition delay time as a function of oxygen mole fraction. The experimental data have been normalized to $T = 980$ K, $P = 15$ atm, and $\phi = 0.4$ using Eq. (3). Equation (3), the correlation developed by He et al. [3], and the results of model predictions for τ_{ign} based on the reaction mechanism of Curran et al. [28] are provided for comparison.

modeling studies using the iso-octane reaction mechanism of Curran et al. [28] indicate that ignition is not accelerated at the lower temperatures expected in the near-wall region of the test section.

4.2. Ignition theory

Several studies of ignition theory propose the existence of regimes where reaction fronts can form prior to volumetric ignition [21–24]. The classification of ignition regimes between the limits of thermal explosion and detonation in the presence of nonuniform initial conditions, such as temperature gradients, was first proposed by Zeldovich [21]. He describes the regimes based on the relative values of the laminar flame speed (u_l), the rate of spontaneous propagation of the reaction fronts (u_{sp}), the speed of sound (a), and the rate of normal detonation (u_J).

The maximum propagation rate for each experiment where reaction fronts were present is provided in Table 1. Calculated reaction front velocities ranged from 0.5 to 7.8 m/s and were far below the speed of sound for the mixtures, which is also provided in Table 1 (a, based on the unreacted gas composition at T_{eff} and P_{eff}). The propagation rates are generally faster than laminar flame speeds for iso-octane. For example, Bradley et al. [30] experimentally measured burning velocities for iso-octane for a range of conditions. They found burning velocities decreasing from

approximately 0.5 m/s at $P = 1$ atm to approximately 0.27 m/s at $P = 10$ atm for $T = 450$ K and $\phi = 0.8$. Johnston and Farrell [31] measured similar values at comparable temperatures and pressures with a maximum laminar burning velocity of 0.5 m/s at $\phi = 1.1$ for $T = 450$ K and 3 atm.

Based on the values provided in Table 1, the results of the current work are in the regime of spontaneous propagation or the third category described by Zeldovich, where $u_l < U \ll a < u_J$. Zeldovich stated that in this regime, the propagation of reaction fronts is slow, so that "the pressure has sufficient time to equalize," and the speed of the reaction fronts "is determined by initial conditions," which is consistent with the observations made here. Zeldovich proposed that in the regime of spontaneous propagation, the reaction fronts propagate at a rate of

$$u_{sp} = \left(\frac{\partial \tau_{ign}}{\partial x} \right)^{-1}, \tag{4}$$

where the gradient of the ignition delay time is related to the local temperature gradient by

$$u_{sp} = \left[\left(\frac{\partial \tau_{ign}}{\partial T} \right) \left(\frac{\partial T}{\partial x} \right) \right]^{-1}. \tag{5}$$

The rates measured for U can be compared with estimates for u_{sp} to determine if there is a relationship between the observed speeds and the theory proposed by
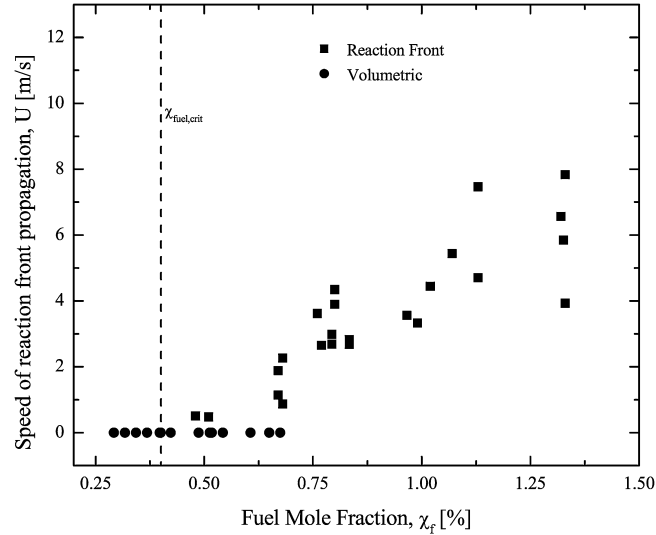
Fig. 13. Experimental results for reaction front propagation rates for lean iso-octane mixtures as a function of fuel mole fraction in the test gas mixture. The critical limit based on linear extrapolation of the experimental data for reaction fronts is presented as the dashed line.

Zeldovich. Characterization studies of the UM RCF conducted earlier [25] indicate that the variability in the temperature field in the core region ($\sim$40 mm in diameter) is typically less than 10 K after compression of inert gas mixtures to nominal temperatures between 920 and 970 K. However, it is known that reacting mixtures can create changes in the RCF temperature field that differ from inert gas conditions [12]. Thus, a reasonable estimate for the temperature gradient in the core region of the test section prior to the formation of the reaction fronts is $\partial T/\partial x \cong 3$ K/mm. Values for $\partial \tau_{ign}/\partial T$ are found using the conditions listed in Table 1 and the relation

$$\left| \left(\frac{\partial \tau_{ign}}{\partial T} \right) \right| = \tau_{ign} \frac{27,300}{R_{[cal/mol/K]} T^2}, \tag{6}$$

which is based on the correlation provided in Eq. (3). The calculations for $\partial \tau_{ign}/\partial T$ and u_{sp} are provided in Table 2. A comparison of u_{sp} and U indicates good agreement between the predicted rates of spontaneous propagation based on the temperature gradients induced by compression and the front velocities observed experimentally, as seen in Fig. 14. Alternatively, the speed of the measured reaction fronts can be compared to $\partial \tau_{ign}/\partial T$ as shown in Fig. 15. In semi-log co-ordinates, there appears to be a linear relationship between U and $\partial \tau_{ign}/\partial T$, as was observed by Chen et al. [24] for plots of instantaneous displacement speed, s_d, versus $|\nabla T|$.

The extent of the thermal inhomogeneities in the UM RCF is primarily determined by the motion of

the fluid off the nosecone of the sabot and the mixing of the cooler fluid near the wall. Consequently, the temperature gradients that exist initially in each experiment are expected to be of the same magnitude when the sabot velocity profiles are similar, as they were in this study. But the reaction fronts are observed only at certain conditions that appear to correlate well with fuel mole fraction. The role of fuel mole fraction suggests a dependence on the reactant thermophysical properties. Specifically, the rate at which the temperature gradients dissipate is determined by the thermal diffusivity $\alpha = k/\rho C_p$ of the test gas mixture. The larger the thermal diffusivity, the faster the thermal gradients are dissipated. Table 2 provides a summary of the thermal diffusivities of the test gas mixtures based on the state conditions and mixtures provided in Table 1. Comparing the mixture thermal diffusivities and reaction front velocities shown in Table 2, it is seen that experiments with high thermal conductivity demonstrate volumetric ignition, while experiments with low thermal conductivity exhibit reaction fronts. This highlights the tendency for mixtures with great ability to dissipate thermal gradients into a resulting homogeneous temperature field, which then will exhibit volumetric ignition.

In an effort to determine a priori if spontaneous propagation of reaction fronts will occur, Gu et al. [22] proposed the dimensionless temperature gradient,

$$\xi = a(\partial T/\partial x)(\partial \tau_{ign}/\partial T) = a/u_{sp}, \tag{7}$$

Table 2

Summary of thermophysical properties of mixtures and conditions studied in this work and estimates for rates of spontaneous propagation, u_{sp}, based on Eq. (5) and an assumed temperature gradient of 3 K/mm

ϕ	Test gas composition				P [atm]	T [K]	U [m/s]	$\partial\tau_{ing}/\partial T$ [ms/K]	u_{sp} [m/s]	$\alpha \times 10^5$ [m²/s]
	$\chi_{i-C_8H_{18}}$ [%]	χ_{O_2} [%]	χ_{N_2} [%]	χ_{Ar} [%]						
0.20	0.7	41.8	57.5	0.0	10.8	917	1.1	0.37	0.91	1.28
0.30	0.5	21.4	75.2	2.8	10.8	947	0.5	0.37	0.91	1.37
0.30	1.0	41.4	51.2	6.4	12.1	936	3.3	0.13	2.57	1.14
0.30	0.5	19.9	70.8	8.8	10.7	958	0.5	0.32	1.03	1.40
0.40	1.0	30.2	51.0	17.8	11.8	964	3.6	0.21	1.59	1.22
0.40	0.8	24.8	62.7	11.7	10.9	945	2.7	0.27	1.25	1.31
0.40	0.8	24.8	62.7	11.7	11.8	971	3.0	0.14	2.31	1.26
0.40	0.7	20.9	71.2	7.3	11.0	951	1.9	0.27	1.22	1.32
0.50	1.1	28.2	48.3	22.4	11.2	947	4.7	0.15	2.15	1.22
0.50	1.1	28.2	48.3	22.4	12.1	969	7.5	0.08	4.44	1.18
0.50	0.8	20.8	66.1	12.3	10.3	944	2.7	0.32	1.04	1.37
0.50	0.8	20.8	66.1	12.3	11.0	955	2.8	0.22	1.53	1.30
0.51	0.7	16.5	69.0	13.8	11.3	970	0.9	0.20	1.64	1.32
0.51	0.7	16.5	69.0	13.8	11.7	979	2.3	0.18	1.87	1.30
0.57	0.8	16.6	64.9	17.8	8.7	988	3.6	0.18	1.81	1.75
0.58	0.8	16.5	65.1	17.7	12.0	989	2.7	0.13	2.62	1.27
0.60	0.8	16.7	71.9	10.6	11.1	945	4.3	0.28	1.17	1.28
0.60	0.8	16.7	71.9	10.6	11.4	952	3.9	0.24	1.36	1.26
0.77	1.0	16.5	56.8	25.7	9.1	999	4.4	0.12	2.69	1.65
0.80	1.3	20.7	50.9	27.1	11.6	962	5.8	0.09	3.73	1.18
0.80	1.1	16.7	63.7	18.6	11.9	961	5.4	0.15	2.16	1.18
0.80	1.3	20.7	50.8	27.2	11.4	961	3.9	0.12	2.69	1.20
0.80	1.3	20.7	50.8	27.2	12.8	983	7.8	0.07	4.96	1.11
0.99	1.3	16.7	55.5	26.5	12.3	970	6.6	0.09	3.53	1.13
1.98	3.2	20.4	19.1	57.3	16.6	903	3.3	0.10	3.19	0.60
1.98	3.2	20.4	19.1	57.3	13.5	918	6.5	0.10	3.21	0.75
0.20	0.3	20.9	78.8	0.0	9.7	928	V	0.81	0.41	1.50
0.20	0.3	20.9	78.8	0.0	10.3	940	V	0.59	0.57	1.45
0.25	0.3	16.6	79.2	3.9	14.0	965	V	0.31	1.07	1.10
0.25	0.3	16.6	79.2	3.9	15.4	987	V	0.19	1.76	1.04
0.30	0.5	20.9	76.3	2.3	10.5	937	V	0.47	0.71	1.38
0.30	0.5	20.9	76.3	2.3	10.9	945	V	0.37	0.90	1.35
0.30	0.4	16.6	77.2	5.8	9.0	1020	V	0.14	2.46	1.87
0.32	0.4	16.6	77.1	5.8	9.2	981	V	0.27	1.22	1.71
0.35	0.4	14.5	80.0	0.0[a]	11.0	930	V	0.47	0.71	1.27
0.35	0.4	14.5	80.0	0.0[a]	11.1	932	V	0.44	0.76	1.26
0.40	0.5	16.6	72.9	10.0	9.3	927	V	0.70	0.48	1.52
0.40	0.5	16.6	72.9	10.0	11.3	972	V	0.21	1.59	1.36
0.40	0.6	18.9	75.4	5.4	11.0	949	V	0.32	1.04	1.32
0.40	0.6	18.9	75.4	5.4	11.3	955	V	0.29	1.16	1.30
0.50	0.7	16.6	76.4	6.4	10.1	931	V	0.52	0.64	1.38
0.50	0.7	16.6	76.4	6.4	10.8	946	V	0.38	0.87	1.33

[a] Balance CO_2.

as a means of quantifying the boundaries between ignition regimes. Here, we compare the dimensionless ratio of the speed of sound to the measured maximum rate of propagation (a/U). Fig. 16 presents the results as a function of χ_{fuel} for the experiments where reaction fronts were observed. The results indicate a clear trend delineating the ignition regimes. At low values of χ_{fuel}, the ratio exponen-

tially approaches a limit consistent with the value $\chi_{fuel,crit} = 0.4$.

4.3. Comparison with previous experimental studies

It is well known that localized regions of higher reactivity can occur in RCF, engines, and shock tubes due to heat transfer effects, fluid motion, particles,
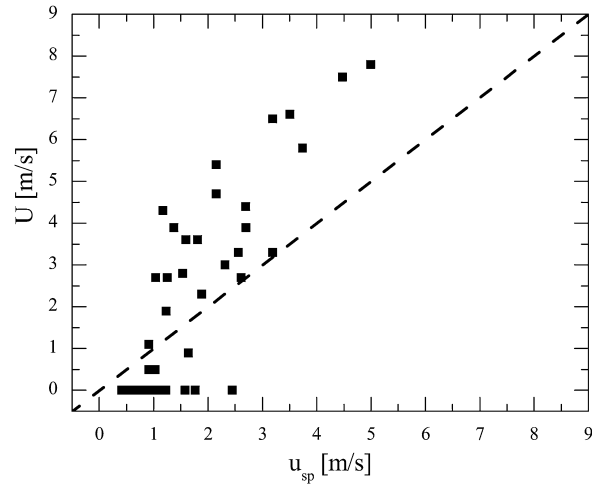
Fig. 14. Comparison of measured maximum rates of propagation, U, with estimates based on ignition theory for propagation rates of spontaneous ignition, u_{sp}, assuming a temperature gradient of 3 K/mm. The dashed line, $x = y$, is provided for reference.
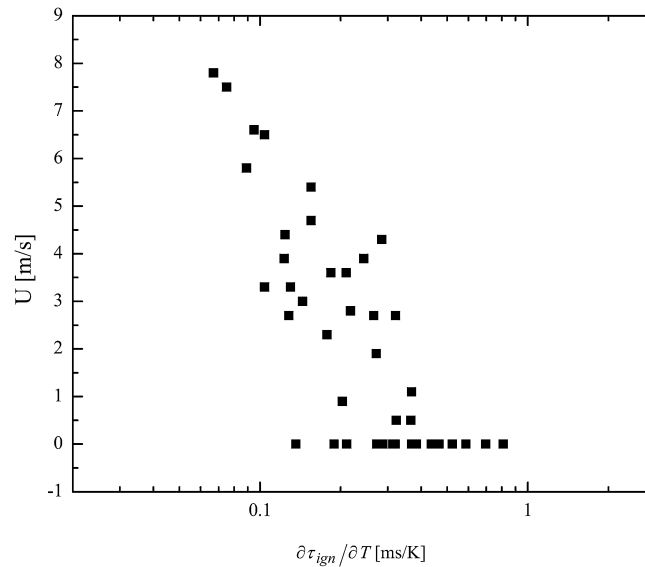
Fig. 15. Maximum rate of propagation as a function of $\partial \tau_{ign}/\partial T$.

and preignition reactions [7,10,12,13,15,22,32–34]. The regions of higher reactivity can be due to gradients in temperature and/or composition. Several studies have documented the temporal variations in the temperature fields developed in RCF experiments and the effects on ignition studies [11–14,35,36]. Although RCF devices generally have unique geometries, and therefore unique flow fields, some trends can be broadly applied. Thermal inhomogeneities are

created by the roll-up of the cooler gases in the thermal boundary layer along the wall of the cylinder (or driven section) during the travel of the piston. Vortex roll-up is generally suppressed through the use of creviced piston designs or other gas-trapping methods [25,35,36], leading to an adiabatic core region of the test gases that is considered homogeneous in composition and temperature. In some cases, cooler gases have been observed to "push" off the face of the pis-

188
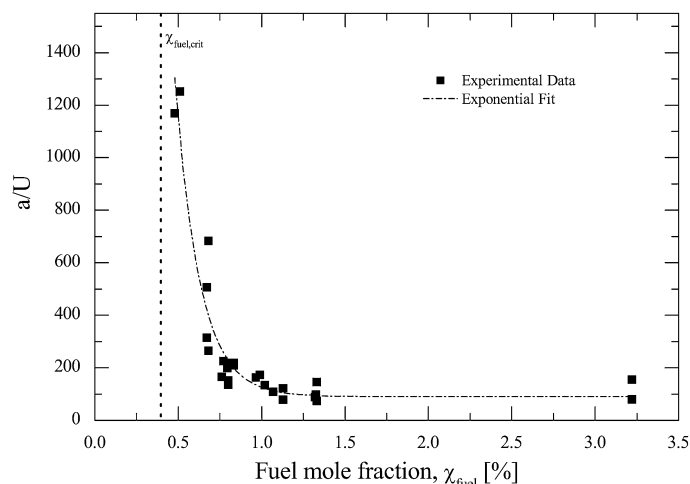
Fig. 16. Speed of sound normalized by the measured maximum rate of reaction front propagation as a function of fuel mole fraction. The critical fuel mole fraction limit based on the experimental data for U is presented as the dashed line.

ton, and after a period of time, to penetrate into the core region of the test gases [11,14]. Thus, conditions can arise in an RCF where hotter gases are located in a toroidal region near the walls of the test chamber with cooler gases located in the center of the test section. For fuels which exhibit NTC behavior, reaction can accelerate in the cooler regions as was observed in the numerical simulations by Griffiths et al. [11]. Such behavior was suggested to suppress the effects of thermal gradients in the RCF study of iso-octane ignition by Desgroux et al. [12] when the studies were conducted under conditions where NTC chemistry is important. The sensitivity of the ignition phenomena to thermal inhomogeneities depends on the type of fuel considered, the mixture composition, and the state conditions. Several studies of iso-octane ignition have observed preignition behavior consistent with that observed in the current work.

Vermeer et al. [32] studied ignition of highly dilute (70% argon) stoichiometric iso-octane/air mixtures in shock tube experiments. The authors monitored ignition in the test volume using pressure transducers and high-speed Schlieren photography and identified two distinct ignition regimes: mild and strong. The transition from mild ignition to strong ignition occurred for temperatures above 1400 K. For the cases of strong ignition, highly uniform images of volumetric ignition were obtained. For the cases of mild ignition, many distinct reaction centers were formed throughout the test volume. For the shock tube study, a fixed mixture composition with $\chi_{\text{i-}C_8H_{18}} = 2.2\%$ was used, which is higher than the critical limit determined in the current work. However, the shock tube study was conducted at higher temperatures (1250–1740 K)

and lower pressures (1.71–4.8 atm) than the current work. When the thermal diffusivities of the mixtures used by Vermeer et al. are considered, the trends are in good agreement with this study, where increasing thermal diffusivity led to homogeneous ignition behavior. Specifically, for the imaging example of mild ignition provided in [32] $\alpha = 9.5 \times 10^{-5}$ m^2/s ($T = 1280$ K, $P = 1.96$ atm) and for the imaging example of strong ignition $\alpha = 15.4 \times 10^{-5}$ m^2/s ($T = 1560$ K, $P = 1.71$ atm).

Fieweger et al. [7] conducted a shock tube study of iso-octane ignition where they also used Schlieren imaging and pressure measurements to characterize the ignition regimes. In their study, Fieweger et al. [7] used fixed mixture compositions of stoichiometric amounts of iso-octane and air where $\chi_{\text{i-}C_8H_{18}} = 1.65\%$. The authors confirmed that several distinct areas of reaction often appeared prior to volumetric ignition for many conditions, with homogeneous ignition occurring at the highest temperatures considered. The authors describe the regions of discrete reaction as deflagrations and refer to the time period prior to volumetric ignition as the inhomogeneous deflagrative phase of the process. A general summary of the conditions and corresponding observations made by Fieweger et al. [7] is provided in Table 3. Note that the pressures and temperatures considered in this shock tube study ($P \cong 13$ atm, $T = 970$–1330 K) are comparable to the current work. In agreement with trends observed in the current work, strong (homogeneous) ignition is exhibited by mixtures with higher thermal conductivity, while mild ignition (with apparent reaction fronts) is observed for mixtures with lower thermal conductivity.

Table 3
Summary of conditions and general observations made in the shock tube study of iso-octane ignition by Fieweger et al. [7]

P [atm]	T [K]	Test gas composition			$\alpha \times 10^5$ [m^2/s]	Observations
		$\chi_{i\text{-}C_8H_{18}}$ [%]	χ_{O_2} [%]	χ_{N_2} [%]		
39.5	770	1.65	20.7	77.7	0.24	mild ignition + deflagration + secondary explosion
12.5	973	1.65	20.7	77.7	1.09	mild ignition + deflagration
13.3	1028	1.65	20.7	77.7	1.12	deflagration + secondary explosion
13.2	1029	1.65	20.7	77.7	1.13	deflagration + secondary explosion
13.4	1105	1.65	20.7	77.7	1.25	mild ignition + secondary explosion
13.4	1328	1.65	20.7	77.7	1.68	strong ignition

As a final comparison with previous studies, it is interesting to consider the results of the current work in the context of the observations made by Kaiser et al. [17] in their study of a research engine operated in HCCI mode using gasoline fuel. Kaiser et al. observed a dramatic change in the engine-out emissions as the air-to-fuel ratio increased above 70–75 (corresponding to a decrease in fuel mole fraction below approximately 0.3%). Specifically, the carbon monoxide emissions increased dramatically, while the carbon dioxide emissions simultaneously decreased dramatically at high air-to-fuel ratios. The authors proposed that the shift in emissions was an indication of a change in the form of combustion from a high-temperature flame process (predominant at low air-to-fuel ratios) to a low-temperature autoignition mechanism (predominant at high air-to-fuel ratios). The results of the current work demonstrate the significance of the local heat dissipation rates and thermal gradients under these low-temperature, low-fuel-mole-fraction conditions. The shift in emissions observed by Kaiser et al. [17] may be directly related to the decrease in the thermal diffusivity of the fuel/air mixtures, thus affecting the presence of reaction fronts at low load conditions.

5. Conclusions

The current work has demonstrated the existence of two distinct ignition regimes for iso-octane at high pressures and intermediate temperatures. The regimes are consistent with ignition theory and the results serve as the first experimental data to capture and quantify the characteristics of the modes of ignition. For the range of conditions studied, the regimes are delineated by a critical fuel mole fraction. The reaction fronts propagate at a rate proportional to a characteristic temperature gradient and their presence

appears to be a function of the thermal diffusivity of the test gas mixture. The results for ignition delay time indicate that the primary effect of the reaction fronts is to increase the pressure in the test chamber and thereby accelerate volumetric ignition. A homogeneous model and the reaction mechanism for iso-octane by Curran et al. [28] yield predictions for τ_{ign} that are in excellent agreement with the experimental data. As many advanced combustion methods utilize lean, low-temperature premixed strategies under conditions similar to those studied in the current work, the data provide both valuable insight into anticipated ignition performance and quantitative data critical to validating and refining ignition theory.

Acknowledgment

References

[1] K. Epping, S. Aceves, R. Bechtold, J. Dec, SAE Paper 2002-02-1923 (2002).

[2] J. Neathery, D. Gray, D. Challman, F. Derbyshire, Fuel 78 (7) (1999) 815–823.

[3] X. He, M.T. Donovan, B.T. Zigler, T.R. Palmer, S.M. Walton, M.S. Wooldridge, A. Atreya, Combust. Flame 142 (2005) 266–275.

[4] X. He, B.T. Zigler, S.M. Walton, M.S. Wooldridge, A. Atreya, Combust. Flame 145 (2006) 552–570.

[5] S.M. Walton, X. He, B.T. Zigler, M.S. Wooldridge, An experimental investigation of the ignition properties of hydrogen and carbon monoxide mixtures for syngas turbine applications, Proc. Combust. Inst. (2006) doi:10.1016/j.proci.2006.08.059.

[6] D.F. Davidson, B.M. Gauthier, R.K. Hanson, Proc. Combust. Inst. 30 (2005) 1175–1182.

[7] K. Fieweger, R. Blumenthal, G. Adomeit, Combust. Flame 109 (4) (1997) 599–619.

[8] R. Minetti, M. Carlier, M. Ribaucour, E. Therssen, L.R. Sochet, Proc. Combust. Inst. 26 (1996) 747–753.

[9] S. Tanaka, F. Ayala, J.C. Keck, J.B. Heywood, Combust. Flame 132 (2) (2003) 219–239.

[10] J.E. Elsworth, W.W. Haskell, I.A. Read, Combust. Flame 13 (4) (1969) 437–438.

[11] J.F. Griffiths, D.J. Rose, M. Schreiber, J. Meyer, K.F. Knoche, Combust. Flame 91 (1992) 209–212.

[12] P. Desgroux, R. Minetti, L.R. Sochet, Combust. Sci. Technol. 113–114 (1996) 193–203.

[13] J.F. Griffiths, J.P. McNamara, C.G.W. Sheppard, D.A. Turton, B.J. Whitaker, Fuel 81 (2002) 2219–2225.

[14] J. Clarkson, J.F. Griffiths, J.P. McNamara, B.J. Whitaker, Combust. Flame 125 (2001) 1162–1175.

[15] E. Murase, K. Hanada, T. Miyaura, J. Ikeda, Combust. Sci. Technol. 177 (2005) 1699–1723.

[16] J.F. Griffiths, W. Nimmo, Combust. Flame 60 (1985) 215–218.

[17] E.W. Kaiser, J. Yang, T. Culp, N. Xu, M.M. Maricq, Int. J. Eng. Res. 3 (2002) 185–195.

[18] E.W. Kaiser, M.M. Maricq, N. Xu, J. Yang, SAE Paper 2005-01-3749, 2005.

[19] Y. Ishibashi, M. Asai, K. Nishida, SAE Paper 972077, 1997 (also JSAE Paper 9734106).

[20] A. Hultqvist, M. Christensen, B. Johansson, M. Richter, J. Nygren, J. Hult, M. Aldjn, SAE Paper 2002-01-0424, 2002.

[21] Ya.B. Zeldovich, Combust. Flame 39 (1980) 211–214.

[22] X.J. Gu, D.R. Emerson, D. Bradley, Combust. Flame 133 (2003) 63–74.

[23] R. Sankaran, H.G. Im, E.R. Hawkes, J.H. Chen, Proc. Combust. Inst. 30 (2004) 875–882.

[24] J.H. Chen, E.R. Hawkes, R. Sankaran, S.D. Mason, H.G. Im, Combust. Flame 145 (2006) 128–144.

[25] M.T. Donovan, X. He, B.T. Zigler, T.R. Palmer, M.S. Wooldridge, A. Atreya, Combust. Flame 137 (2004) 351–365.

[26] M.T. Donovan, Ph.D. dissertation, Department of Mechanical Engineering, University of Michigan, 2003.

[27] B.J. McBride, S. Gordon, M.A. Reno, NASA Thermodynamic Data Base, NASA Technical Memorandum 4513, October 1993.

[28] H.J. Curran, P. Gaffuri, W.J. Pitz, C.K. Westbrook, Combust. Flame 129 (3) (2002) 253–280.

[29] R.J. Kee, F.M. Rupley, J.A. Miller, M.E. Coltrin, J.F. Grcar, E. Meeks, H.K. Moffat, A.E. Lutz, G. Dixon-Lewis, M.D. Smooke, J. Warnatz, G.H. Evans, R.S. Larson, R.E. Mitchell, L.R. Petzold, W.C. Reynolds, M. Caracotsios, W.E. Stewart, P. Glarborg, C. Wang, O. Adigun, W.G. Houf, C.P. Chou, S.F. Miller, P. Ho, D.J. Young, CHEMKIN Release 4.0.1, Reaction Design, Inc., San Diego, CA, 2004.

[30] D. Bradley, R.A. Hicks, M. Lawes, C.G.W. Sheppard, R. Woolley, Combust. Flame 115 (1–2) (1998) 126–144.

[31] R.J. Johnston, J.T. Farrell, Proc. Combust. Inst. 30 (2005) 217–224.

[32] D.J. Vermeer, J.W. Meyer, A.K. Oppenheim, Combust. Flame 18 (3) (1972) 327–336.

[33] J.F. Griffiths, S.K. Scott, Prog. Energy Combust. Sci. 13 (1987) 161–197.

[34] K. Chen, G.A. Karim, H.C. Watson, J. Eng. Gas Turb. Power 125 (2003) 458–465.

[35] D. Lee, S. Hochgreb, Combust. Flame 114 (1998) 531–545.

[36] J. Würmel, J.M. Simmie, Combust. Flame 141 (2005) 417–430.

Appendix D

An experimental investigation of the ignition properties of hydrogen and carbon monoxide mixtures for syngas turbine applications

S.M. Walton, X. He, B.T. Zigler, and M.S. Wooldridge, An experimental investigation of the ignition properties of hydrogen and carbon monoxide mixtures for syngas turbine applications, *31st Proceedings of the Combustion Institute*, 3147-3154, 2007.

An experimental investigation of the ignition properties of hydrogen and carbon monoxide mixtures for syngas turbine applications

S.M. Walton *, X. He, B.T. Zigler, M.S. Wooldridge

Department of Mechanical Engineering, University of Michigan, 2350 Hayward St., Ann Arbor, MI 48109-2125, USA

Abstract

Ignition studies of simulated syngas mixtures of hydrogen (H_2), carbon monoxide (CO), oxygen (O_2), nitrogen (N_2), and carbon dioxide (CO_2) were performed using a rapid compression facility. Experiments were conducted using pressure time-histories and high-speed imaging to measure ignition delay times (τ_{ign}), over a broad range of conditions relevant to current and proposed gas-turbine technologies, and which included fuel compositions consistent with typical gasification facilities. Specifically, the τ_{ign} data spanned pressures from $P = 7.1$ to 26.4 atm, temperatures from $T = 855$ to 1051 K, equivalence ratios from $\phi = 0.1$ to 1.0, oxygen mole fractions from $\chi_{O_2} = 15\%$ to 20% and H_2:CO ratios from H_2:CO $= 0.25$ to 4.0 (mole basis). Regression analysis yielded the following best-fit to the composite data set:

$$\tau_{ign} = 3.7 \times 10^{-6} P^{-0.5} \phi^{-0.4} \chi_{O_2}^{-5.4} \exp(12,500/R_{[cal/mol/K]}T)$$

In this expression, τ_{ign} is the ignition delay time [ms], P is pressure [atm], T is temperature [K], ϕ is the equivalence ratio (based on the H_2 and CO to O_2 molar ratio), and χ_{O_2} is the oxygen mole fraction. The uncertainty in the measured values for τ_{ign} is estimated as less than 30%. The experimental data are in good agreement with model predictions based on a recently proposed detailed reaction mechanism for H_2 and CO.
© 2006 The Combustion Institute. Published by Elsevier Inc. All rights reserved.

Keywords: Carbon monoxide; Hydrogen; Syngas; Ignition; Rapid compression facility

1. Introduction

Syngas offers considerable opportunity for clean use of coal in power generation applications with potential for near zero pollutant emissions, including greenhouse gases such as carbon dioxide (CO_2). In particular, the integrated gasification combined cycle (IGCC) can improve thermal efficiencies, dramatically lower environmental impact compared to traditional coal-fired power plants [1], and deliver electricity or hydrogen for fuel at competitive costs [2,3]. However, improvements in coal gasification power plant efficiencies to competitive levels (greater than 40%) are essential to make IGCC processes attractive alternatives to natural-gas fired, combined cycle power plants. Specifically, the US Department of Energy's

* Corresponding author. Fax: +1 734 647 3170.
E-mail address: smwalton@umich.edu (S.M. Walton).

Fossil Energy Turbines Program has set a target of 60% plant efficiencies for coal-fueled power systems by 2020 [4]. A primary area for IGCC development with high potential for improving plant efficiencies is in the syngas turbine design [5].

The successful operation of gas turbines using syngas (including hydrogen fuel concentrations >90%) has been demonstrated at numerous facilities in the United States and abroad [6–8]; although there are difficulties. The syngas mixtures can vary widely in the relative hydrogen (H_2) and carbon monoxide (CO) concentrations [7], complicating turbine operation and design. The high-temperatures associated with the hydrogen kinetics can lead to high nitrogen oxide (NO_x) emissions, and existing dry low-NO_x gas-turbine technologies are not amenable to the high mass flow rates and fuel concentrations (from 15% to 40%) required for syngas mixtures [6,8]. As a result, the current approach is to fire syngas with high levels of dilution (typically using nitrogen (N_2) or steam) [9]. Lean premixed turbine operation can overcome the concerns of low efficiency and high emissions, and design of new syngas turbines focuses on such premixed approaches. For premixed operation, flashback and pre-ignition are safety and turbine performance concerns.

There are some key experimental investigations of H_2 and CO mixtures [10–13, and references therein] and more recent studies on developing revised H_2 and CO reaction mechanisms [14–16]. However, the reaction kinetics of syngas mixtures remains largely unexplored at conditions relevant to gas turbine applications, with few data at elevated pressures and temperatures and using non-dilute fuel/air mixtures. Experimental studies which can provide an improved understanding of the reaction kinetics and other fundamental combustion characteristics of syngas mixtures are vital to advancing syngas turbine design, and the future of IGCC applications. Specifically, the objective of the current work is to create the first experimental database of combustion kinetic benchmarks at conditions and compositions relevant to syngas combustors, to develop a quantitative understanding of the ignition behavior of simulated syngas mixtures as a function of key state and compositional conditions, and to quantify the performance of an updated H_2/CO chemical reaction mechanism at accurately reproducing the experimental benchmarks.

2. Experimental

In order to meet the stated objectives and isolate the chemical kinetics relevant to syngas combustor operation, ignition experiments were conducted using the University of Michigan (UM) rapid compression facility (RCF). The UM-RCF is an innovative and unique experimental apparatus that can be used to create uniform high-temperature ($T = 500$–3000 K) and high-pressure ($P = 0.5$–60 atm) conditions [17] that are directly applicable to many combustion devices, including gas turbines. In ignition studies, the ignition delay time (τ_{ign}) is an important chemical kinetic characteristic of the combustion mixture. In RCF experiments, τ_{ign} is controlled by the chemistry of the reactant mixture and the temperature and pressure conditions of the experiment. Experimental data for τ_{ign} are invaluable as an indication of the magnitude of the reaction kinetics and as targets for benchmarking detailed, skeletal, and reduced reaction mechanisms [14,16,18].

A detailed description of the UM-RCF, the operating procedure, and the results of studies characterizing the performance can be found in [17–20]. Briefly, the UM-RCF consists of five major components: the driver section, the driven section, the test manifold, the sabot (i.e. the free piston), and the hydraulic control valve assembly. For each experiment, the driven section is evacuated with a diffusion pump; the driver section is filled with high-pressure air and the sabot is located at the upstream end of the driven section. The driver and driven sections are separated by the hydraulic control valve assembly and a scored sheet of polyester film (0.05 mm thick, Mylar®). After filling the driven section with the prepared test gas mixture, a globe valve is opened (using the hydraulic control valve assembly), permitting the high-pressure driver gas to break the polyester film, enter the driven section, and rapidly accelerate the sabot. The test gas mixture in the driven section is compressed in front of the sabot and sealed within the test manifold when the sabot nose cone seats by an annular fit with the test manifold walls. The compression process can be considered isentropic, and uniform high-temperature and high-pressure conditions are created in the test section as a result of the compression process.

The test manifold is equipped with two optical ports, a pressure transducer port, and two additional instrumentation ports. The end wall seals the test manifold and allows optical access to the test volume. For the current study, the test section was instrumented with a piezoelectric transducer (Kistler 6041AX4) and charge amplifier (Kistler 5010B) for pressure measurements, and a polycarbonate end wall was used to provide optical access to the test manifold.

Digital imaging, using a high-speed color digital video camera (Vision Research, Phantom V7.1, maximum acquisition of 160,000 frames per second (fps), maximum resolution of 800×600 pixels, SR-CMOS 48 bit color array), and pressure time-histories were used to characterize the ignition for each experiment. A fast 50 mm lens (f/0.95 Navitar TV Lens) and c-mount extension tubes were used with the camera.

The high-speed digital camera was used to acquire full-frame video sequences of the ignition experiments at speeds of 26,000 fps, with the spatial resolution maintained at the maximum allowable setting of 256×256 pixels. These settings result in each frame corresponding to 38 μs, and each pixel in the CMOS array imaging focused light from a volume with a height $\times$ width $\times$ depth of approximately 198 μm $\times$ 198 μm $\times$ 2 mm. All test gas mixtures were made using a dedicated mixing tank, and the mixture composition was determined by measurement of the relative partial pressures of the reactants.

3. Results

Mixtures and conditions for study were selected based on existing and expected syngas turbine operation. Specifically, syngas compositions including H_2:CO ratios from 0.25 to 4.0, stoichi-

Fig. 1. Typical experimental results for pressure and pressure derivative time-histories for experimental conditions of $T_{eff} = 1004$ K, $P_{eff} = 11.3$ atm, $\phi = 0.4$, inert: O_2 ratio = 3.76, syngas fuel = 20% H_2, 80% CO.

ometric and lean conditions, elevated pressures, and dilution with N_2 are of interest for modern gas-turbine design. In the current study, the ignition behavior of simulated syngas mixtures of H_2 and CO was investigated in terms of equivalence ratio, H_2:CO ratio, temperature, pressure, and oxygen concentration. Pure H_2 experiments were conducted for comparison with previous RCF ignition studies [21], as well as pure CO experiments.

Figure 1 presents the pressure and pressure derivative time-histories for a typical H_2 and CO ignition experiment, and Fig. 2 presents the corresponding imaging sequence. The pressure data indicate a smooth compression process, where the end of compression is indicated by the first peak in the pressure profile. After the test gases are sealed in the test section, a period of time exists where the pressure remains relatively constant, followed by a rapid increase in pressure which indicates ignition of the test gas mixture (set as $t = 0$ s in Figs. 1 and 2). Examination of the pressure data near the time of ignition indicates an initial slow increase in pressure followed by a more rapid increase. The change in the rate of pressure rise is associated with the presence of reaction fronts prior to volumetric ignition, which is supported by the imaging data shown in Fig. 2.

Visible emission is observed in the imaging data as early as 14 ms prior to volumetric ignition, corresponding to the start of the gradual increase in pressure in the test volume after the end of compression. As seen in Fig. 2, the emission expands throughout a portion of the test volume, and an increase in pressure is observed in this same time frame (see Fig. 1). Note that Fig. 2 presents a subset of the total imaging data which were acquired throughout compression and ignition. At time $t = 0$ ms, a rapid increase in the emission intensity is observed throughout the test volume. The peak in the volumetric emission intensity corresponds with the peak rate of increase in pressure. Consequently, this is designated as the time of ignition,
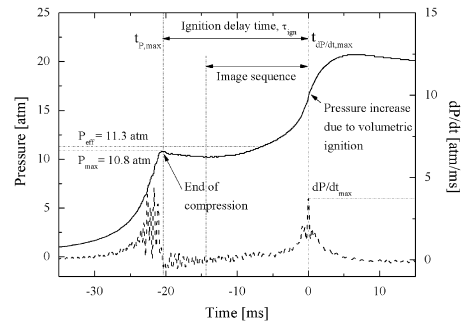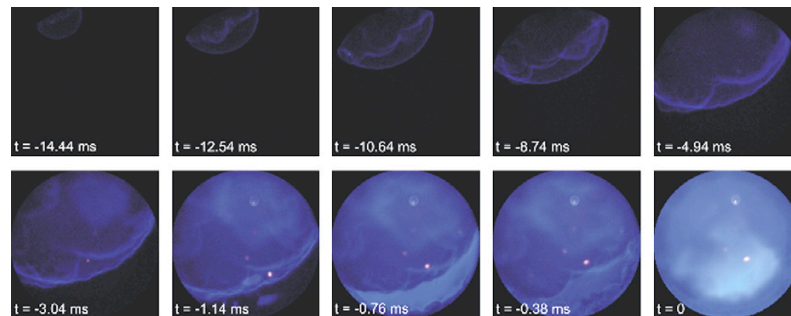

Fig. 2. Imaging sequence corresponding to the conditions and results of Fig. 1. The color in each image has been enhanced (each to the same level) for clarity.

and τ_{ign} is determined from each experiment as the time between P_{max} at the end of compression and the maximum value of dP/dt (see Fig. 1).

The presence of localized reaction fronts and propagation throughout the test chamber has been observed in previous ignition studies of hydrocarbon and hydrogen fuels using shock tube and rapid compression facilities [22–26]. In studies of the *iso*-octane/air system using the UM-RCF [25,26], volumetric ignition with no reaction front propagation occurred for fuel mole fractions below a critical limit and reaction fronts were consistently observed above the limit. Similarly, volumetric ignition with no reaction front propagation was observed in the current study for a limited number of experiments at very lean conditions. The increased pressure associated with the reaction fronts serves to further compress the unignited gases in the test chamber. Consequently, the pressure and temperature at the time of volumetric ignition are higher than the conditions at the end of compression. In the *iso*-octane studies, the use of time-integrated average pressures were found to yield excellent agreement with ignition data where no reaction fronts were observed [25,26]. The same approach is used here (see Fig. 1), where the effective pressure (P_{eff}) for each experiment is defined as the time-integrated average pressure between the time of maximum pressure due to compression (P_{max}) and the time of maximum rate of pressure rise (dP/dt_{max}).

The effective temperature for each experiment is determined as in previous RCF studies [18] using the P_{eff} and by numerical integration of the isentropic relation

$$\int_{T_o}^{T_{eff}} \frac{\gamma}{\gamma - 1} d\ln T = \ln\left(\frac{P_{eff}}{P_o}\right) \tag{1}$$

where P_o is the charge pressure, T_o is the initial temperature (typically 298 K), and γ is the temperature dependent ratio of the specific heats of the unreacted test gas mixture, which is determined using the NASA Thermodynamic Database [27]. The effects of the determination of P_{eff} and T_{eff} on the measured τ_{ign} data are considered in the uncertainty analysis, described below.

Table 1 presents a summary of the mixtures and conditions for the RCF experiments and the resulting ignition data. The complete data set, including mixtures which did not ignite, span $P_{eff} = 7.1–26.4$ atm, $T_{eff} = 752–1051$ K, $\phi = 0.1–2.0$, H_2:CO = 0.25–4.0 (mole basis) and $\chi_{O_2} = 1.2–20.2\%$ (mole basis). The equivalence ratio is based on the molar ratio of the H_2 and CO to O_2. Note fuel mixtures of 100% H_2 and 100% CO were included in the experimental matrix. As expected, the 100% CO mixture did not ignite within the test times available in the UM-RCF. Due to the high sensitivity of CO to moisture and other impurities, the pure CO exper-

iments serve as an indication that the experimental approach is not affected by uncontrolled impurities. Other experiments which did not ignite indicate the boundaries of conditions that were feasible to study using the UM-RCF. For example, the $T = 752$ K experiment set a lower limit on the temperature conditions.

Figure 3 provides a summary of how the current range of pressures and temperatures compare with previous studies of CO and H_2 ignition. Figure 4 presents a summary of experimental results for the product of τ_{ign} and oxygen concentration as a function of inverse temperature. For comparison, the results of the RCF study of H_2/O_2 ignition delay times by Lee and Hochgreb [21] are included in the figures. The results of the two RCF studies overlap in state conditions examined and agree well on the order of magnitude of the ignition times measured. A more quantitative comparison is complicated by the fact that the study by Lee and Hochgreb considered stoichiometric conditions, used argon as the diluent, and used more dilute O_2 concentrations ($\chi_{O_2} = 12.5\%$, mole basis) than studied in the current work.

As seen in Figs. 3 and 4, when mixtures of H_2 and CO are considered, we are unaware of existing data at conditions comparable to those studied here. The shock tube studies of Gardiner et al. [10] and Dean et al. [11] focused on dilute, high-temperature, near-atmospheric conditions. The work by Fotache et al. [12] used a counterflow diffusion flame apparatus to study ignition of H_2/CO opposed heated air flow.

Regression analysis of the Table 1 data was conducted in order to quantify the effects of the state and mixture conditions on the H_2 and CO ignition properties. Several forms of regression were considered, including the absolute and relative fuel concentrations (as apposed to mole fraction) of H_2 and CO, the concentration of O_2, and incorporating fuel and oxygen effects via only the equivalence ratio. Ultimately, pressure (P [atm]), temperature (T [K]), equivalence ratio (ϕ), and oxygen mole fraction (χ_{O_2}) were required to determine an expression with the highest correlation coefficient for the complete data set presented in Table 1 (excluding mixtures which did not ignite). The form of the expression is similar to that determined in previous ignition studies [18].

$$\begin{aligned} \tau_{ign} = 3.7 &\times 10^{-6} P^{-0.5} \phi^{-0.4} \chi_{O_2}^{-5.4} \\ &\times \exp(12,500/\bar{R}_{[cal/mol/K]} T) \end{aligned} \tag{2}$$

In Eq. (2), $\bar{R}_{[cal/mol/K]}$ is the universal gas constant. Figures 5–7 present a summary of the effects of T, P, and ϕ on τ_{ign}, respectively, where the data have been normalized as necessary using the functional dependence provided in Eq. (2) to isolate each parameter of interest.

Table 1
Summary of experimental conditions and results for ignition delay time

ϕ	Test gas composition[a]				P_{eff} (atm)	T_{eff} (K)	Ignition delay time (ms)		
	H_2 (%)	CO (%)	O_2 (%)	N_2 (%)			τ_{ign}	τ_{reg}	τ_{pred}
0.10	2.4	1.6	20.2	63.9	10.5	916	NI[b]	—	215.0
0.15	3.6	2.4	19.8	74.3	7.1	1011	15.8	11.2	9.9
0.15	3.6	2.4	19.8	74.3	7.6	1028	10.1	9.8	6.2
0.15	3.6	2.4	19.8	74.3	14.9	1033	9.6	6.9	6.2
0.15	3.6	2.4	19.8	74.3	15.9	1051	5.4	6.1	4.0
0.15	3.6	2.4	19.8	74.3	8.1	1046	4.9	8.5	3.8
0.20	4.7	3.1	19.4	60.8	11.1	929	19.2	15.5	81.4
0.30	6.7	4.5	18.6	43.4	19.5	855	23.9	22.0	398.0
0.30	6.7	4.5	18.7	57.9	12.0	944	9.1	13.8	38.6
0.30	6.7	4.5	18.7	57.9	13.0	963	10.5	11.6	22.8
0.40	2.9	11.5	18.0	60.0	11.6	1009	14.0	9.8	4.8
0.40	2.9	11.5	18.0	60.0	11.3	1004	20.5	10.2	5.5
0.40	2.9	11.5	18.0	60.0	11.3	1005	13.1	10.1	5.3
0.40	11.5	2.9	18.0	62.9	17.2	1009	4.7	8.1	6.1
0.40	11.5	2.9	18.0	62.9	10.7	994	7.7	11.1	9.7
0.40	2.9	11.5	18.0	63.5	17.6	1017	9.9	7.6	3.7
0.40	2.9	11.5	18.0	63.5	11.4	1009	11.1	9.9	4.6
0.40	2.4	9.4	14.7	65.2	26.4	1009	22.3	19.7	5.6
0.40	7.2	7.2	18.0	63.2	23.5	1015	7.2	6.7	3.9
0.40	7.2	7.2	18.0	63.2	17.8	1017	6.9	7.6	3.9
0.40	7.2	7.2	18.0	63.2	11.0	999	7.7	10.6	6.4
0.40	5.8	8.6	18.0	55.5	12.5	886	NI[b]	—	144.0
0.70	13.6	9.1	16.2	44.1	15.5	923	15.8	20.7	33.8
1.00	24.0	16.0	20.0	17.6	14.1	881	8.9	8.2	64.8
0.50	10.4	6.9	17.4	10.8	16.5	752	NI[b]	—	NI[b]
0.10	4.0	0.0	20.2	75.8	10.2	1035	8.4	8.8	9.8
0.10	4.0	0.0	20.2	75.8	14.9	1030	8.5	7.6	10.6
0.15	5.9	0.0	19.8	74.3	14.7	1033	5.5	6.9	7.8
2.01	4.7	0.0	1.2	48.5	4.49	938	NI[b]	—	212.0
0.40	0.0	14.3	17.9	41.2	18.6	849	NI[b]	—	NI[b]

The mixture composition is provided on a mole basis. Predictions for τ_{pred} were determined using the revised mechanism of Davis et al. [15]. τ_{reg} was determined using Eq. (2).
[a] Balance CO_2.
[b] No ignition within 1 s.

Error analysis was conducted to quantify the uncertainty in the τ_{ign} data. The primary sources of uncertainty in τ_{ign} are due to the presence of reaction fronts prior to volumetric ignition, uncertainties in the pressure measurement (which are primarily due to the definition of P_{eff}
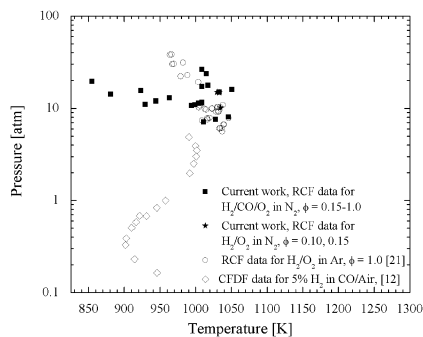

Fig. 3. Previous and current range of conditions of experimental H_2 and CO ignition studies. The CFDF data of [12] are results of a counterflow diffusion flame study.
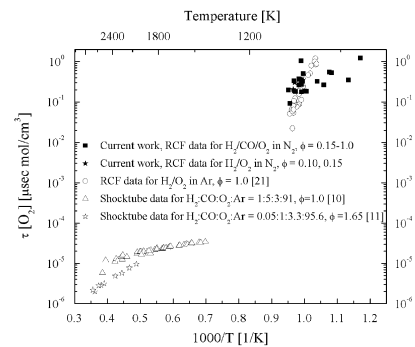

Fig. 4. Summary of previous and current experimental data for ignition of H_2 and CO presented as the product ignition delay time and oxygen concentration.
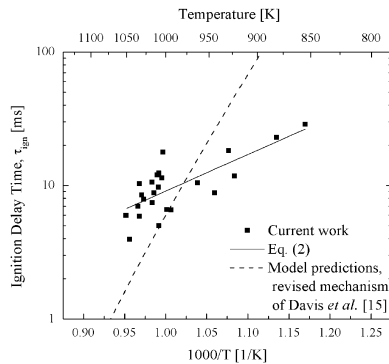
Fig. 5. Comparison of experimentally measured H_2 and CO ignition delay time data with model predictions as a function of inverse temperature. The experimental data have been normalized to $P = 15$ atm, $\phi = 0.4$, $\chi_{O_2} = 18\%$ using Eq. (2).
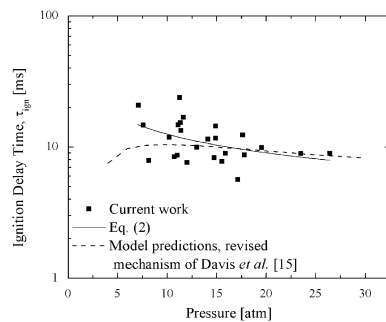

Fig. 6. Comparison of experimentally measured H_2 and CO ignition delay time data with model predictions as a function of pressure. The experimental data have been normalized to $T = 980$ K, $\phi = 0.4$, $\chi_{O_2} = 18\%$ using Eq. (2).
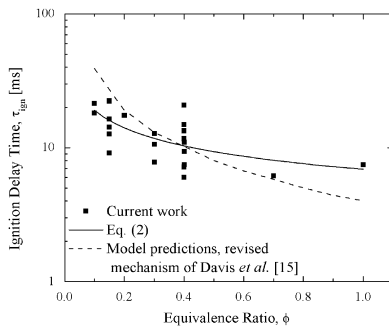
Fig. 7. Comparison of experimentally measured H_2 and CO ignition delay time data with model predictions as a function of equivalence ratio. The experimental data have been normalized to $T = 980$ K, $P = 15$ atm, $\chi_{O_2} = 18\%$ using Eq. (2).

and the accuracy of the pressure transducer and charge amplifier), corresponding uncertainties in the calculated T_{eff}, and uncertainties in the mixture composition (which yields an uncertainty of 0.4% in the determination of ϕ and 0.2% in χ_{O_2}). Combining the uncertainties as independent sources of error using a square-root-of-the-sum-of-the-squares approach yields an estimated uncertainty in the measured ignition delay time of ±28%.

4. Discussion

The experimental data for τ_{ign} were compared with predictions based on the mechanism developed by Wang and co-workers [15,28]. The mechanism was primarily that of Davis et al. [15], which was based on the work by Mueller et al. [14]. Davis et al. revised the mechanism of [14] with updated thermodynamic data and reaction chemistry and optimized the mechanism performance to reproduce experimentally measured H_2 and CO combustion data obtained over a range of conditions. The mechanism was subsequently revised per Wang [28] to include an increase in the rate coefficient for the $CO + HO_2 = CO_2 + OH$ reaction to $k = 1.35 \times 10^{-3} T^{5.0} \exp(-14,950_{[cal/mol]}/\bar{R}_{[cal/mol/K]}/T_{[K]})$.

The revised mechanism of Davis et al. [15] was used with the CHEMKIN 4.0.1 suite of programs [29] to predict ignition delay time using an adiabatic, constant-volume model. The modeling predictions, τ_{pred}, are provided in Table 1 and Figs. 5–8. The model results agree well with the experimental data for most of the range of conditions studied, with particularly good prediction of the quantitative trends of pressure and ϕ. The model predicts higher activation energy than that observed in

Fig. 8. OH sensitivity analysis based on the revised reaction mechanism by Davis et al. [15], for conditions of $T = 1009$ K, $P = 11.6$ atm, $\phi = 0.4$, H_2:CO = 0.25.

the current work ($E_{a,model} = 49.5$ kcal/mol versus $E_{a,experimental} = 12.5$ kcal/mol). The difference in the modeling an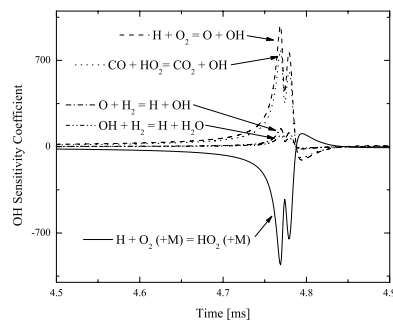d experimental results may be attributable to the large uncertainty in the $CO + HO_2 = CO_2 + OH$ reaction, which is discussed further below.

Sensitivity analysis using the revised mechanism by Davis et al. [15] was conducted in the current work to identify the reactions with the largest effects on τ_{ign} for the H_2 and CO mixtures studied. Results for temperature, H, OH, and O were similar and sensitivity data for OH are presented in Fig. 8 for representative experimental conditions. The OH is most sensitive to the chain-branching $H + O_2 = O + OH$ reaction, the $H + O_2$ recombination reaction to form HO_2, and the $CO + HO_2 = CO_2 + OH$ reaction. H_2O_2 decomposition appears to play a less significant role in this system compared to the sensitivity data for 100% H_2 ignition presented by Lee and Hochgreb [21] and the sensitivity data for lean *iso*-octane ignition presented by He et al. [20]. This shift from the importance of H_2O_2 to HO_2 is consistent with the reduced H concentrations available in the lean H_2 and CO mixtures studied here. The relatively high uncertainty (a factor of 2 [15]) and the large role of the $CO + HO_2 = CO_2 + OH$ reaction, may be the primary source of the discrepancies between the model predictions and the experimental data.

5. Conclusions

A significant handicap to syngas turbine design is the severe lack of data on syngas combustion properties such as flammability limits, flame speeds, and ignition characteristics (excluding 100% H_2 studies) at conditions relevant to syngas combustor operation. The results of the current work are the first experimental ignition data of which we are aware for H_2 and CO fuel mixtures at elevated temperatures and pressures greater than 5 atm. The data provide quantitative understanding of the effects of combustion conditions and reactant compositions on the ignition properties of H_2 and CO mixtures over a broad range of conditions with direct relevance to syngas-fired combustors and provide experimental data critical for validation of H_2 and CO reaction mechanisms. The regression results for τ_{ign} isolate the trends of ignition delay time as a function of pressure, temperature, equivalence ratio, and dilution. The relation for τ_{ign} also provides a means to estimate ignition properties and is in a simplified form that facilitates integration into computationally intense combustor design codes, where detailed chemical kinetic models can be costly.

References

[1] J. Neathery, D. Gray, D. Challman, F. Derbyshire, *Fuel* 78 (7) (1999) 815–823.
[2] P. Chiesa, S. Consonni, T. Kreutz, R. Williams, *Int. J. Hydrogen Energy* 30 (7) (2005) 747–767.
[3] T. Kreutz, R. Williams, S. Consonni, P. Chiesa, *Int. J. Hydrogen Energy* 30 (7) (2005) 769–784.
[4] http://www.netl.doe.gov/coal/turbines/.
[5] P. Chiesa, E. Macchi, *Trans. ASME. J. Eng. Gas Turb. Power* 126 (4) (2004) 770–785.
[6] G. Parkinson, *Turbmach. Int.* 45 (2004) 6.
[7] D.M. Todd, R.A. Battista, Demonstrated Applicability of Hydrogen Fuel for Gas Turbines, in: Proceedings of Gasification for the Future, Noordwijk, Nederland, 2000.
[8] N. Shilling, R.M. Jones, The Response of Gas Turbines to a CO_2 Constrained Environment, Gasification Technology Conference Report, GE Power Systems, 2003.
[9] P. Chiesa, G. Lozza, L. Mazzocchi, *Trans. ASME. J. Eng. Gas Turb. Power* 127 (1) (2005) 73–80.
[10] W.C. Gardiner Jr., M. McFarland, K. Morinaga, T. Takeyama, B.F. Walker, *J. Phys. Chem.* 75 (1971) 1504–1509.
[11] A.M. Dean, D.L. Steiner, E.E. Wang, *Combust. Flame* 32 (1978) 73–83.
[12] C.G. Fotache, Y. Tan, C.J. Sung, C.K. Law, *Combust. Flame* 120 (2000) 417–426.
[13] I. Wierzba, V. Kilchyk, *Int. J. Hydrogen Energy* 26 (2001) 639–643.
[14] M.A. Mueller, R.A. Yetter, F.L. Dryer, *Int. J. Chem. Kinet.* 31 (1999) 705–724.
[15] S.G. Davis, A.V. Joshi, H. Wang, F. Egolfopoulos, *Proc. Combust. Inst.* 30 (2005) 1283–1292.
[16] I.Gy. Zsély, J. Zádor, T. Turányi, *Proc. Combust. Inst.* 30 (2005) 1273–1281.
[17] M.T. Donovan, X. He, B.T. Zigler, T.R. Palmer, M.S. Wooldridge, A. Atreya, *Combust. Flame* 137 (2004) 351–365.
[18] X. He, M.T. Donovan, B.T. Zigler, T.R. Palmer, S.M. Walton, M.S. Wooldridge, A. Atreya, *Combust. Flame* 142 (2005) 266–275.
[19] M.T. Donovan, Ph.D. Dissertation, Department of Mechanical Engineering, University of Michigan, 2003.
[20] X. He, B.T. Zigler, S.M. Walton, M.S. Wooldridge, A. Atreya, *Combust. Flame* 145 (2006) 552–570.
[21] D. Lee, S. Hochgreb, *Int. J. Chem. Kinet.* 30 (1998) 385–406.
[22] J.E. Elsworth, W.W. Haskell, I.A. Read, *Combust. Flame* 13 (4) (1969) 437–438.
[23] D.J. Vermeer, J.W. Meyer, A.K. Oppenheim, *Combust. Flame* 18 (3) (1972) 327–336.
[24] K. Fieweger, R. Blumenthal, G. Adomeit, *Combust. Flame* 109 (4) (1997) 599–619.

[25] S.M. Walton, X. He, B.T. Zigler, M.S. Woold-ridge, A. Atreya, in: Proc. Fourth Joint Meeting of the US Sections of The Combust. Inst. (2005).

[26] S.M. Walton, X. He, B.T. Zigler, M.S. Wooldridge, A. Atreya, *Combust. Flame*, in press.

[27] B.J. McBride, S. Gordon, M.A. Reno, NASA Thermodynamic Data Base, *NASA Technical Memorandum 4513*, 1993.

[28] H. Wang, private communication (2005).

[29] *Chemkin Collection*, Release 4.0.1, Reaction Design, Inc., San Diego, CA.

Comments

Simone Hochgreb, Cambridge University, UK. Given that the auto-ignition of these mixtures is not homogeneous, is it justified to model the system as a zero dimensional homogeneous constant volume case?

Reply. We have found that by defining a time-averaged pressure, P_{eff} (and thus T_{eff}), to account for the slow increase in pressure associated with the formation and propagation of the reaction fronts, we achieve good agreement with a single-zone model when either homogeneous or reaction front cases are observed. In other words, the primary effects of the reaction fronts on the unignited reactants are volumetric by means of an increase in pressure. Transport effects, which are localized and are not captured by the single-zone model, do not appear to significantly influence τ_{ign}. For a more detailed discussion see work by Walton et al. [1].

Reference

[1] S.M. Walton, X. He, B.T. Zigler, M.S. Wooldridge, A. Atreya, Demonstration of distinct ignition regimes using high-speed digital imaging of *iso*-octane mixtures, *Combust. Flame*, in press (2006).

●

Jerry Seitzman, Georgia Institute of Technology, USA. You present an ignition time correlation for the complete H_2/CO composition range. Could you comment on any systematic variations in τ_{ign} at the edges of the composition range, e.g., $H_2/CO = 0.1$ or 10? For example, could the pressure dependence be similar but perhaps the ϕ or T coefficients might change?

Reply. Within the uncertainty of the data, we did not observe any systematic variations in τ_{ign} as a function of the CO/H_2 concentration.

Bibliography

[1] R. L. McCormick, M. S. Graboski, T. L. Alleman, A. M. Herring, and K. S. Tyson. Impact of biodiesel source material and chemical structure on emissions of criteria pollutants from a heavy-duty engine. *Environmental Science and Technology*, 35(9):1742–1747, 2001. Compilation and indexing terms, Copyright 2006 Elsevier Inc. All rights reserved.

[2] Wang Ying, Zhou Longbao, and Wang Hewu. Diesel emission improvements by the use of oxygenated dme/diesel blend fuels. *Atmospheric Environment*, 40(13):2313–2320, 2006. Compilation and indexing terms, Copyright 2006 Elsevier Inc. All rights reserved.

[3] Gong Yanfeng, Liu Shenghua, Guo Hejun, Hu Tiegang, and Z. Longbao. A new diesel oxygenate additive and its effects on engine combustion and emissions. *Applied Thermal Engineering*, 27(1):202–7, 01 2007. M1: Copyright 2006, The Institution of Engineering and Technology.

[4] E. W. Kaiser, T. J. Wallington, M. D. Hurley, J. Platz, H. J. Curran, W. J. Pitz, and C. K. Westbrook. Experimental and modeling study of premixed atmospheric-pressure dimethyl ether-air flames. *Journal of Physical Chemistry A*, 104(35):8194–8206, 2000.

[5] P. A. Glaude, W. J. Pitz, and M. J. Thomson. Chemical kinetic modeling of dimethyl carbonate in an opposed-flow diffusion flame. *Proceedings of the Combustion Institute 30*, pages 1095–1102, 2004.

[6] Y. F Lue, Y. Y Yeh, and C. H Wu. The emission characteristics of a small d.i. diesel engine using biodiesel blended fuels. *Journal of Environmental Science and Health - Part A Toxic/Hazardous Substances and Environmental Engineering*, 36(5):845–859, 2001. Compilation and indexing terms, Copyright 2006 Elsevier Inc. All rights reserved.

[7] D. Y. C. Leung, Y. Luo, and T. L. Chan. Optimization of exhaust emissions of a diesel engine fuelled with biodiesel. *Energy and Fuels*, 20(3):1015–1023, 2006. Compilation and indexing terms, Copyright 2006 Elsevier Inc. All rights reserved.

[8] Mustafa Canakci, Ahmet Erdil, and Erol Arcaklioglu. Performance and exhaust emissions of a biodiesel engine. *Applied Energy*, 83(6):594–605, 2006. Compilation and indexing terms, Copyright 2006 Elsevier Inc. All rights reserved.

[9] Gerhard Knothe, Christopher A. Sharp, and Thomas W. Ryan III. Exhaust emissions of biodiesel, petrodiesel, neat methyl esters, and alkanes in a new technology engine. *Energy and Fuels*, 20(1):403–408, 2006. Compilation and indexing terms, Copyright 2006 Elsevier Inc. All rights reserved.

[10] C. K. Westbrook, W. J. Pitz, and H. J. Curran. Chemical kinetic modeling study of the effects of oxygenated hydrocarbons on soot emissions from diesel engines. *Journal of Physical Chemistry A*, 110(21):6912–6922, 2006.

[11] C. J. Mueller and G. C. Martin. Effects of oxygenated compounds on combustion and soot evolution in a di diesel engine: broadband natural luminosity imaging. *SAE Paper Number 2002-01-1631*, 2002.

[12] M. A. Gonzales D., W. Piel, T. Asmus, W. Clark, J. Garbak, E. Liney, M. Natarajan, D. W. Naegli, D. Yost, E. A. Frame, and J. P. Wallace III. Oxygenates screening for advanced petroleum-based diesel fuels: part 2. the effect of oxygenate blending compounds on exhaust emissions. *SAE Paper Number 2001-01-3632*, 2001.

[13] N. Miyamoto, H. Ogawa, N. M. Nurun, K. Obata, and T. Arima. Smokeless, low nox, high thermal efficiency, and low noise diesel combustion with oxygenated agents as main fuel. *SAE Paper Number 980506*, 1998.

[14] Massimo Cardone, Maria Vittoria Prati, Vittorio Rocco, Maurizia Seggiani, Adolfo Senatore, and Sandra Vitolo. Brassica carinata as an alternative oil crop for the production of biodiesel in italy: Engine performance and regulated and unregulated exhaust emissions. *Environmental Science and Technology*, 36(21):4656–4662, 2002. Compilation and indexing terms, Copyright 2006 Elsevier Inc. All rights reserved.

[15] Xiaoyan Shi, Xiaobing Pang, Yujing Mu, Hong He, Shijin Shuai, Jianxin Wang, Hu Chen, and Rulong Li. Emission reduction potential of using ethanol-biodiesel-diesel fuel blend on a heavy-duty diesel engine. *Atmospheric Environment*, 40(14):2567–2574, 2006. Compilation and indexing terms, Copyright 2006 Elsevier Inc. All rights reserved.

[16] E. M. Fisher, W. J. Pitz, H. J. Curran, and C. K. Westbrook. Detailed chemical kinetic mechanisms for combustion of oxygenated fuels. In *28th International Symposium on Combustion*, volume 28, pages 1579–1586, Edinburgh, United Kingdom, Jul 30-Aug 4 2000 2000. Sibley School of Mech./Aerosp. Eng., Cornell University, Ithaca, NY 14853, United States, Combustion Institute. Compilation and indexing terms, Copyright 2006 Elsevier Inc. All rights reserved; T3: Symposium (International) on Combustion.

[17] B. I. Parsons and C. Hinshelwood. The oxidation of hydrocarbons and their derivatives .2. structural effects in the ester series. *Journal of the Chemical Society*, (JUN):1799–1803, 1956. PT: J; NR: 6; TC: 7; J9: J CHEM SOC; PG: 5; GA: WK651.

[18] D. E. Hoare, Li Ting-Man, and A. D. Walsh. Cool flames and molecular structure. *Proceedings of the Combustion Institute*, 11:879–887, 1967.

[19] S. Gal, M. J. Thomson, S. M. Sarathy, S. A. Syed, P. Dagaut, P. Divart, A. J. Marchese, and F. L. Dryer. A wide-ranging kinetic modeling study of methyl butanoate combustion. *Proceedings of the Combustion Institute*, 31(1):305–311, 2007/1.

[20] S. M. Sarathy, S. Gal, S. A. Syed, M. J. Thomson, and P. Dagaut. A comparison of saturated and unsaturated c4 fatty acid methyl esters in an opposed flow diffusion flame and a jet stirred reactor. *Proceedings of the Combustion Institute*, 31(1):1015–1022, 2007/1.

[21] W. K. Metcalfe, S. Dooley, H. J. Curran, J. M. Simmie, A. M. El-Nahas, and M. V. Navarro. Experimental and modeling study of c5h10o2 ethyl and methyl esters. *Journal of Physical Chemistry A*, 111(19):4001–4014, 2007.

[22] W. R. Schwartz, C. S. McEnally, and L. D. Pfefferle. Decomposition and hydrocarbon growth processes for esters in non-premixed flames. *Journal of Physical Chemistry A*, 110(21):6643–6648, 2006.

[23] M. T. Donovan. Experimental study of the role of oh in sio2 particle nucleation in sih4 combustion using uv absorption spectroscopy. *Ph.D. Thesis, University of Michigan*, 2003.

[24] X. He. An investigation of iso-octane auto-ignition using a rapid compression facility. *Ph.D. Thesis, University of Michigan*, 2005.

[25] M. T. Donovan, X. He, B. T. Zigler, T. R. Palmer, M. S. Wooldridge, and A. Atreya. Demonstration of a free-piston rapid compression facility for the study of high temperature combustion phenomena. *Combustion and Flame*, 137(3):351–365, 2004. Compilation and indexing terms, Copyright 2005 Elsevier Engineering Information, Inc.

[26] X. He, M. T. Donovan, B. T. Zigler, T. R. Palmer, S. M. Walton, M. S. Wooldridge, and A. Atreya. An experimental and modeling study of iso-octane ignition delay times under homogeneous charge compression ignition conditions. *Combustion and Flame*, 142:266–275, 2005. Compilation and indexing terms, Copyright 2006 Elsevier Inc. All rights reserved; 3.

[27] X. He, B. T. Zigler, S. M. Walton, M. S. Wooldridge, and A. Atreya. A rapid compression facility study of oh time histories during iso-octane ignition. *Combustion and Flame*, 145:552–570, 2006. Compilation and indexing terms, Copyright 2006 Elsevier Inc. All rights reserved; 3.

[28] S. M. Walton, X. He, B. T. Zigler, M. S. Wooldridge, and A. Atreya. An experimental investigation of iso-octane ignition phenomena. *Combustion and Flame*, 150:246–262, 2007.

[29] S. M. Walton, X. He, B. T. Zigler, and M. S. Wooldridge. An experimental investigation of the ignition properties of hydrogen and carbon monoxide mixtures for syngas turbine applications. *Proceedings of the Combustion Institute*, 31(2):3147–3154, 2007/1.

[30] B. T. Zigler M. S. Wooldridge A.Atreya X. He, S. M. Walton. Experimental investigation of the intermediates of isooctane during ignition. *International Journal of Chemical Kinetics*, 39(9):498–517, 2007.

[31] Henry J. Curran, P. Gaffuri, W. J. Pitz, and C. K. Westbrook. A comprehensive modeling study of iso-octane oxidation. *Combustion and Flame*, 129(3):253–280, 2002. Compilation and indexing terms, Copyright 2005 Elsevier Engineering Information, Inc.

[32] S. M. Walton, C. Perez, and M. S. Wooldridge. An experimental investigation of the auto-ignition properties of two c5 esters: methyl butanoate and butyl methanoate. *ASME-IMECE*, 2007.

[33] B. J. McBride, S. Gordon, and M. A. Reno. Nasa thermodynamic data base. *NASA Technical Memorandum 4513*, 1993.

[34] Chemkin collection. *Reaction Design Inc., San Diego, CA*.

[35] C.. K. Westbrook, W. J. Pitz, P. R. Westmoreland, F. L. Dryer, M. Chaos, P. Osswald, K. Kohse-Hoinghaus, T. A. Cool, J. Wang, B. Yang, H. Hansen, and T. Kasper. 2008.

[36] Guillaume Dayma, Sandro Gal, and Philippe Dagaut. Experimental and kinetic modeling study of the oxidation of methyl hexanoate. *Energy and Fuels*, 22(3):1469–1479, 2008.

[37] Eric L. Petersen, Mouna Lamnaouer, Jaap de Vries, Henry J. Curran, John M. Simmie, M Fikri, C Schulz, and Gilles Bourque. Discrepancies between shock-tube and rapid compression machine ignition at low temperatures and high pressures. 2007.

[38] Charles K. Westbrook, William J. Pitz, Olivier Herbinet, Henry J. Curran, and Emma J. Silke. A detailed chemical kinetic reaction mechanism for n-alkane hydrocarbons from n-octane to n-hexadecane. In preparation for submission.

[39] Methyl acetate oxidation in a jsr: Experimental and detailed kinetic modeling study. *Combustion Science and Technology*, 127(1):275, 1997.

[40] Tareq A. Albahri. Flammability characteristics of pure hydrocarbons. *Chemical Engineering Science*, 58(16):3629–3641, 2003. Compilation and indexing terms, Copyright 2005 Elsevier Engineering Information, Inc.

[41] Manuel Arias-Zugasti. Intra-bubble-combustion. premixed limit, stage i: Dynamics of rapid premixed flame propagation inside a bubble. *Combustion Theory and Modelling*, 7(2):269–300, 2003. Compilation and indexing terms, Copyright 2005 Elsevier Engineering Information, Inc.

[42] K. J. Bosschaart and L. P. H. De Goey. The laminar burning velocity of flames propagating in mixtures of hydrocarbons and air measured with the heat flux method. *Combustion and Flame*, 136(3):261–269, 2004. Compilation and indexing terms, Copyright 2005 Elsevier Engineering Information, Inc.

[43] M. Canakci. Performance and emissions characteristics of biodiesel from soybean oil. *Proceedings of the Institution of Mechanical Engineers, Part D: Journal of Automobile Engineering*, 219(7):915–922, 2005. Compilation and indexing terms, Copyright 2006 Elsevier Inc. All rights reserved.

[44] Jacqueline H. Chen, Evatt R. Hawkes, Ramanan Sankaran, Scott D. Mason, and Hong G. Im. Direct numerical simulation of ignition front propagation in a constant volume with temperature inhomogeneities: I. fundamental analysis and diagnostics. *Combustion and Flame*, 145(1):128–144, 2006. Compilation and indexing terms, Copyright 2006 Elsevier Inc. All rights reserved; -2.

[45] K. Chen, G. A. Karim, and H. C. Watson. Experimental and analytical examination of the development of inhomogeneities and autoignition during rapid compression of hydrogen-oxygen-argon mixtures. *Journal of Engineering for Gas Turbines and Power*, 125:458–465, 2003. Compilation and indexing terms, Copyright 2006 Elsevier Inc. All rights reserved; 2.

[46] J. Clarkson, J. F. Griffiths, J. P. MacNamara, and B. J. Whitaker. Temperature fields during the development of combustion in a rapid compression machine. *Combustion and Flame*, 125:1162–1175, 2001. Compilation and indexing terms, Copyright 2006 Elsevier Inc. All rights reserved; 3.

[47] Sergio Machado Correa and Graciela Arbilla. Aromatic hydrocarbons emissions in diesel and biodiesel exhaust. *Atmospheric Environment*, 40(35):6821–6826, 2006. Compilation and indexing terms, Copyright 2006 Elsevier Inc. All rights reserved.

[48] A. Cox, J. F. Griffiths, C. Mohamed, H. J. Curran, W. J. Pitz, and C. K. Westbrook. Extents of alkane combustion during rapid compression leading to single- and two-stage ignition. In *Proceedings of the 1996 26th International Symposium on Combustion. Part 2 (of 2), Jul 28-Aug 2 1996*, volume 2 of *Symposium (International) on Combustion*, pages 2685–2692, Napoli, Italy, 1996. The University, Leeds, Engl, Combustion Inst, Pittsburg, PA, USA. Compilation and indexing terms, Copyright 2005 Elsevier Engineering Information, Inc.

[49] Philippe Dagaut, Nicolas Smoucovit, and Michel Cathonnet. Methyl acetate oxidation in a jsr: Experimental and detailed kinetic modeling study. *Combustion Science and Technology*, 127(1):275, 1997.

[50] D. F. Davidson, B. M. Gauthier, R. K. Hanson, Volker Sick, and John Kiefer. Shock tube ignition measurements of iso-octane/air and toluene/air at high pressures. *Proceedings of the Combustion Institute*, 30(1):1175–1182, 2005. Compilation and indexing terms, Copyright 2005 Elsevier Engineering Information, Inc.

[51] Guillaume Dayma, Sandro Gal, and Philippe Dagaut. Experimental and kinetic modeling study of the oxidation of methyl hexanoate. *Energy Fuels*, 22(3):1469–1479, 2008.

[52] Tarek Echekki and Jacqueline H. Chen. High-temperature combustion in autoigniting non-homogeneous hydrogen/air mixtures. In *Twenty-Ninth International Symposium on Combustion Hokkaido University Sapporo Japan, Jul 21-25 2002*, volume 29 of *Proceedings of the Combustion Institute*, pages 2061–2068, Sapporo, Japan, 2002. Department of Mechanical Engineering, North Carolina State University, Campus Box 7910, Raleigh, NC 27695-7910, United States, Combustion Institute. Compilation and indexing terms, Copyright 2005 Elsevier Engineering Information, Inc.

[53] K. Fieweger, R. Blumenthal, and G. Adomeit. Self-ignition of s.i. engine model fuels: a shock tube investigation at high pressure. *Combustion and Flame*, 109:599–619, 1997. Compilation and indexing terms, Copyright 2006 Elsevier Inc. All rights reserved; 4.

[54] Paolo Gaffuri, Tiziano Faravelli, Eliseo Ranzi, Nicholas P. Cernansky, David Miller, Andrea d'Anna, and Anna Ciajolo. Comprehensive kinetic model for the low-temperature oxidation of hydrocarbons. *AICHE Journal*, 43(5):1278–1286, 1997. Compilation and indexing terms, Copyright 2005 Elsevier Engineering Information, Inc.

[55] L. Gasnot, V. Decottignies, and J. F. Pauwels. Kinetics modelling of ethyl acetate oxidation in flame conditions. *Fuel,*, 84(5):505–518, 3 2005.

[56] B. M. Gauthier, D. F. Davidson, and R. K. Hanson. Shock tube determination of ignition delay times in full-blend and surrogate fuel mixtures. *Combustion and Flame*, 139(4):300–311, 2004. Compilation and indexing terms, Copyright 2005 Elsevier Engineering Information, Inc.

[57] Pierre A. Glaude, William J. Pitz, and Murray J. Thomson. Chemical kinetic modeling of dimethyl carbonate in an opposed-flow diffusion flame. *Proceedings of the Combustion Institute,*, 30(1):1111–1118, 1 2005.

[58] Michael S. Graboski and Robert L. McCormick. Combustion of fat and vegetable oil derived fuels in diesel engines. *Progress in Energy and Combustion Science*, 24(2):125–164, 1998. Compilation and indexing terms, Copyright 2006 Elsevier Inc. All rights reserved.

[59] P. Gray, J. F. Griffiths, S. M. Hasko, and P. G. Lignola. Novel, multiple-stage ignitions in the spontaneous combustion of acetaldehyde. 43(2):175–186, 1981. Compilation and indexing terms, Copyright 2005 Elsevier Engineering Information, Inc.

[60] J. F. Griffiths, P. A. Halford-Maw, and D. J. Rose. Fundamental features of hydrocarbon autoignition in a rapid compression machine. *Combustion and Flame*, 95(3):291–306, 1993. Compilation and indexing terms, Copyright 2005 Elsevier Engineering Information, Inc.

[61] J. F. Griffiths and S. M. Hasko. Two-stage ignitions during rapid compression: Spontaneous combustion in lean fuel-air mixtures. 393(1805):371–395, 1984. Compilation and indexing terms, Copyright 2005 Elsevier Engineering Information, Inc.

[62] J. F. Griffiths, K. J. Hughes, R. Porter, John Simmie, and P. Gokulakrishnan. The role and rate of hydrogen peroxide decomposition during hydrocarbon two-stage autoignition. *Proceedings of the Combustion Institute*, 30(1):1083–1091, 2005. Compilation and indexing terms, Copyright 2005 Elsevier Engineering Information, Inc.

[63] J. F. Griffiths, J. P. MacNamara, C. G. W. Sheppard, D. A. Turton, and B. J. Whitaker. The relationship of knock during controlled autoignition to temperature inhomogeneities and fuel reactivity. *Fuel*, 81(17):2219–2225, 2002. Compilation and indexing terms, Copyright 2005 Elsevier Engineering Information, Inc.

[64] J. F. Griffiths and W. Nimmo. Spontaneous ignition and engine knock under rapid compression. *Combustion and Flame*, 60:215–218, 1985. Compilation and indexing terms, Copyright 2006 Elsevier Inc. All rights reserved; 2.

[65] J. F. Griffiths, D. J. Rose, M. Schreiber, J. Meyer, and K. F. Knoche. Novel features of end-gas autoignition revealed by computational fluid dynamics. *Combustion and Flame*, 91:209–212, 1992. Compilation and indexing terms, Copyright 2006 Elsevier Inc. All rights reserved; 2.

[66] J. F. Griffiths and S. K. Scott. Thermokinetic interactions: Fundamentals of spontaneous ignition and cool flames. *Progress in Energy and Combustion Science*, 13(3):161–197, 1987. Compilation and indexing terms, Copyright 2005 Elsevier Engineering Information, Inc.

[67] J. F. Griffiths and B. J. Whitaker. Thermokinetic interactions leading to knock during homogeneous charge compression ignition. *Combustion and Flame*, 131(4):386–399, 2002. Compilation and indexing terms, Copyright 2005 Elsevier Engineering Information, Inc.

[68] X. J. Gu, D. R. Emerson, and D. Bradley. Modes of reaction front propagation from hot spots. *Combustion and Flame*, 133(1-2):63–74, 2003. Compilation and indexing terms, Copyright 2005 Elsevier Engineering Information, Inc.

[69] Shahrokh Hajireza, Fabian Mauss, and Bengt Sunden. Hot-spot autoignition in spark ignition engines. In *28th International Symposium on Combustion, Jul 30-Aug 4 2000*, volume 28 of *Symposium (International) on Combustion*, pages 1169–1175, Edinburgh, United Kingdom, 2000. Division of Heat Transfer, Lund Institute of Technology, 221 00 Lund, Sweden, Combustion Institute. Compilation and indexing terms, Copyright 2005 Elsevier Engineering Information, Inc.

[70] Y. Huang, C. J. Sung, and J. A. Eng. Dilution limits of n-butane/air mixtures under conditions relevant to hcci combustion. *Combustion and Flame*, 136(4):457–466, 2004. Compilation and indexing terms, Copyright 2005 Elsevier Engineering Information, Inc.

[71] R. J. Johnston, J. T. Farrell, David Smith, and Philippe Dagaut. Laminar burning velocities and markstein lengths of aromatics at elevated temperature and pressure. In *30th International Symposium on Combustion*, volume 30 I, pages 217–224, Chicago, IL, United States, Jul 25-30 2004 2005. Corporate Strategic Research Laboratories, ExxonMobil Research und Engineering Co., Annandale, NJ 08801, United States, Elsevier Ltd, Oxford, OX5 1GB, United Kingdom. Compilation and indexing terms, Copyright 2006 Elsevier Inc. All rights reserved; T3: Proceedings of the Combustion Institute.

[72] Yiguang Ju and C. W. Choi. An analysis of sub-limit flame dynamics using opposite propagating flames in mesoscale channels. *Combustion and Flame*, 133(4):483–493, 2003. Compilation and indexing terms, Copyright 2005 Elsevier Engineering Information, Inc.

[73] Heejung Jung, David B. Kittelson, and Michael R. Zachariah. Characteristics of sme biodiesel-fueled diesel particle emissions and the kinetics of oxidation. *Environmental Science and Technology*, 40(16):4949–4956, 2006. Compilation and indexing terms, Copyright 2006 Elsevier Inc. All rights reserved.

[74] E. W. Kaiser, T. J. Wallington, M. D. Hurley, J. Platz, H. J. Curran, W. J. Pitz, and C. K. Westbrook. Experimental and modeling study of premixed atmospheric-pressure dimethyl ether - air flames. *Journal of Physical Chemistry A*, 104(35):8194–8206, 2000. Compilation and indexing terms, Copyright 2005 Elsevier Engineering Information, Inc.

[75] Mouna Lamnaouer, Eric L. Petersen, Robert C. Ryder, and Andreja Brankovic. Reduced combustion time model for methane in gas turbine flow fields. In *45th AIAA Aerospace Sciences Meeting 2007*, volume 7, pages 4673–4696, Reno, NV, United States, Jan 8-11 2007 2007. University of Central Florida, Orlando, FL 32816, American Institute of Aeronautics and Astronautics Inc., Reston, VA 20191-4344, United States. Compilation and indexing terms, Copyright 2007 Elsevier Inc. All rights reserved; T3: Collection of Technical Papers - 45th AIAA Aerospace Sciences Meeting.

[76] C. K. Law and O. C. Kwon. Effects of hydrocarbon substitution on atmospheric hydrogen-air flame propagation. *International Journal of Hydrogen Energy*, 29(8):867–879, 2004. Compilation and indexing terms, Copyright 2005 Elsevier Engineering Information, Inc.

[77] D. Lee and S. Hochgreb. Suppression of corner vortex in a rapid compression machine. In *Proceedings of the 1997 Fall Technical Meeting on Chemical and Physical Processes in Combustion*, page 357, Hartford, CT, USA, Oct 27-29 1997

1997. Massachusetts Inst of Technology, Cambridge, MA, USA. Compilation and indexing terms, Copyright 2006 Elsevier Inc. All rights reserved; T3: Chemical and Physical Processes in Combustion, Fall Technical Meeting, The Eastern States Section.

[78] Daeyup Lee and Simone Hochgreb. Rapid compression machines: Heat transfer and suppression of corner vortex. *Combustion and Flame*, 114(3-4):531–545, 1998. Compilation and indexing terms, Copyright 2005 Elsevier Engineering Information, Inc.

[79] Daeyup Lee and Simone Hochgreb. Rapid compression machines: Heat transfer and suppression of corner vortex. *Combustion and Flame*, 114(3):531–545, 1998. Compilation and indexing terms, Copyright 2006 Elsevier Inc. All rights reserved; -4.

[80] Daeyup Lee and Simone Hochgreb. Hydrogen autoignition at pressures above the second explosion limit (0.6-4.0 mpa). *International Journal of Chemical Kinetics*, 30:385–406, 1998. Compilation and indexing terms, Copyright 2006 Elsevier Inc. All rights reserved; 6.

[81] J. Lee, S. H. Won, S. H. Jin, S. H. Chung, O. Fujita, and K. Ito. Propagation speed of tribrachial (triple) flame of propane in laminar jets under normal and micro gravity conditions. *Combustion and Flame*, 134(4):411–420, 2003. Compilation and indexing terms, Copyright 2005 Elsevier Engineering Information, Inc.

[82] B. Lewis and G. Von Elbe. Physics of flames and explosions of gases. *Journal of Applied Physics*, 10(6):344–359, 1939. Compilation and indexing terms, Copyright 2005 Elsevier Engineering Information, Inc.

[83] Hung-Pin Li. An investigation of the ignition manner effects on combustion synthesis. *Materials Chemistry and Physics*, 80(3):758–767, 2003. Compilation and indexing terms, Copyright 2005 Elsevier Engineering Information, Inc.

[84] Bonnie J. McBride, Sanford Gordon, and Martin A. Reno. Coefficients for calculating thermodynamic and transport properties of individual species. Technical report, 1993. Compilation and indexing terms, Copyright 2006 Elsevier Inc. All rights reserved; 3.

[85] Charles S. McEnally and Lisa D. Pfefferle. Experimental study of fuel decomposition and hydrocarbon growth processes for practical fuel components in nonpremixed flames: Mtbe and related alkyl ethers. *International Journal of Chemical Kinetics*, 36(6):345–358, 2004.

[86] Charles S. McEnally and Lisa D. Pfefferle. Fuel decomposition and hydrocarbon growth processes for oxygenated hydrocarbons: butyl alcohols. *Proceedings of the Combustion Institute,*, 30(1):1363–1370, 1 2005.

[87] Simona Silvia Merola, Bianca Maria Vaglieco, and Ezio Mancaruso. Multiwavelength ultraviolet absorption spectroscopy of no and oh radical concentration applied to a high-swirl diesel-like system. *Experimental Thermal and Fluid Science*, 28(4):355–367, 2004. Compilation and indexing terms, Copyright 2005 Elsevier Engineering Information, Inc.

[88] W. K. Metcalfe, S. Dooley, H. J. Curran, J. M. Simmie, A. M. El-Nahas, and M. V. Navarro. Experimental and modeling study of c5h10o2 ethyl and methyl esters. *Journal of Physical Chemistry A*, 2007.

[89] R. Minetti, M. Carlier, M. Ribaucour, E. Therssen, and L. R. Sochet. Comparison of oxidation and autoignition of the two primary reference fuels by rapid compression. In *Proceedings of the 1996 26th International Symposium on Combustion. Part 1 (of 2), Jul 28-Aug 2 1996*, volume 1 of *Symposium (International) on Combustion*, pages 747–753, Napoli, Italy, 1996. Universite des Sciences et Technologies de Lille, Villeneuve d'Ascq, Fr, Combustion Inst, Pittsburg, PA, USA. Compilation and indexing terms, Copyright 2005 Elsevier Engineering Information, Inc.

[90] R. Minetti, M. Carlier, M. Ribaucour, E. Therssen, and L. R. Sochet. Rapid compression machine investigation of oxidation and auto-ignition of n-heptane: measurements and modeling. *Combustion and Flame*, 102(3):298, 1995. Compilation and indexing terms, Copyright 2005 Elsevier Engineering Information, Inc.

[91] R. Minetti, M. Ribaucour, M. Carlier, C. Fittschen, and L. R. Sochet. Experimental and modeling study of oxidation and autoignition of butane at high pressure. *Combustion and Flame*, 96(3):201–211, 1994. Compilation and indexing terms, Copyright 2005 Elsevier Engineering Information, Inc.

[92] E. Murase and K. Hanada. Ignition timing control of homogeneous charge compression ignition engines by pulsed flame jets. *Combustion Science and Technology*, 174(5-6):129–140, 2002. Compilation and indexing terms, Copyright 2005 Elsevier Engineering Information, Inc.

[93] E. Murase, K. Hanada, T. Miyaura, and J. Ikeda. Photographic observation and emission spectral analysis of hcci combustion. *Combustion Science and Technology*, 177:1699–1723, 2005. Compilation and indexing terms, Copyright 2006 Elsevier Inc. All rights reserved; 9.

[94] J. Neathery, D. Gray, D. Challman, and F. Derbyshire. Pioneer plant concept: Co-production of electricity and added-value products from coal. *Fuel*, 78:815–823, 1999. Compilation and indexing terms, Copyright 2006 Elsevier Inc. All rights reserved; 7.

[95] M. A. Oehlschlaeger, D. F. Davidson, and R. K. Hanson. High-temperature thermal decomposition of benzyl radicals. *Journal of Physical Chemistry A*, 110(21):6649–6653, 2006.

[96] J. P. Orme, H. J. Curran, and J. M. Simmie. Experimental and modeling study of methyl cyclohexane pyrolysis and oxidation. *Journal of Physical Chemistry A*, 110(1):114–131, 2006.

[97] P. Osswald, U. Struckmeier, T. Kasper, K. Kohse-Hoinghaus, J. Wang, T. A. Cool, N. Hansen, and P. R. Westmoreland. Isomer-specific fuel destruction pathways in rich flames of methyl acetate and ethyl formate and consequences for the combustion chemistry of esters. *Journal of Physical Chemistry A*, 111(19):4093–4101, 2007.

[98] Pyongwan Park and James C. Keck. Rapid compression machine measurements of ignition delays for primary reference fuels. *SAE (Society of Automotive Engineers) Transactions*, 99(Sect 4):11–23, 1990. Compilation and indexing terms, Copyright 2005 Elsevier Engineering Information, Inc.

[99] A. A. Pekalski, J. F. Zevenbergen, H. J. Pasman, S. M. Lemkowitz, A. E. Dahoe, and B. Scarlett. The relation of cool flames and auto-ignition phenomena to process safety at elevated pressure and temperature. *Journal of hazardous materials*, 93(1):93–105, 2002. Compilation and indexing terms, Copyright 2005 Elsevier Engineering Information, Inc.

[100] Eric L. Petersen, Danielle M. Kalitan, Stefanie Simmons, Gilles Bourque, Henry J. Curran, and John M. Simmie. Methane/propane oxidation at high pressures: Experimental and detailed chemical kinetic modeling. In *31st International Symposium on Combustion*, volume 31 I, pages 447–454, Heidelberg, Germany, Aug 5-11 2006 2007. Mechanical, Materials and Aerospace Engineering, University of Central Florida, Orlando, FL 32816-2450, United States, Elsevier Ltd, Oxford, OX5 1GB, United Kingdom. Compilation and indexing terms, Copyright 2007 Elsevier Inc. All rights reserved; T3: Proceedings of the Combustion Institute.

[101] Thomas W. III Ryan and Samuel S. Lestz. Laminar burning velocity of isooctane, n-heptane, methanol, methane, and propane at elevated temperature and pressures in the presence of a diluent. (800103):14, 1980. Compilation and indexing terms, Copyright 2005 Elsevier Engineering Information, Inc.

[102] Khizer Saeed and C. R. Stone. Measurements of the laminar burning velocity for mixtures of methanol and air from a constant-volume vessel using a multizone model. *Combustion and Flame*, 139(1-2):152–166, 2004. Compilation and indexing terms, Copyright 2005 Elsevier Engineering Information, Inc.

[103] R. Sankaran, H. G. Im, E. R. Hawkes, and J. H. Chen. The effects of non-uniform temperature distribution on the ignition of a lean homogeneous hydrogen-air mixture. *Proceedings of the Combustion Institute*, 30:875–82, 2004. M1: Copyright 2005, IEE.

[104] M. Schreiber, A. Sudat Sakak, A. Lingens, and J. F. Griffiths. Reduced thermokinetic model for the autoignition of fuels with variable octane-ratings. In

Proceedings of the 25th Symposium (International) on Combustion, Jul 31-Aug 5 1994, Symposium (International) on Combustion, page 933, Irvine, CA, USA, 1994. Combustion Inst, Pittsburg, PA, USA. Compilation and indexing terms, Copyright 2005 Elsevier Engineering Information, Inc.

[105] S. H. Starner, R. W. Bilger, J. H. Frank, D. F. Marran, and M. B. Long. Mixture fraction imaging in a lifted methane jet flame. *Combustion and Flame*, 107(3):307–313, 1996. Compilation and indexing terms, Copyright 2005 Elsevier Engineering Information, Inc.

[106] Akifumi Takahashi, Youkichi Urano, Kazuaki Tokuhashi, and Shigeo Kondo. Effect of vessel size and shape on experimental flammability limits of gases. *Journal of hazardous materials*, 105(1-3):27–37, 2003. Compilation and indexing terms, Copyright 2005 Elsevier Engineering Information, Inc.

[107] Shigeyuki Tanaka, Ferran Ayala, and James C. Keck. A reduced chemical kinetic model for hcci combustion of primary reference fuels in a rapid compression machine. *Combustion and Flame*, 133(4):467–481, 2003. Compilation and indexing terms, Copyright 2005 Elsevier Engineering Information, Inc.

[108] Shigeyuki Tanaka, Ferran Ayala, James C. Keck, and John B. Heywood. Two-stage ignition in hcci combustion and hcci control by fuels and additives. *Combustion and Flame*, 132(1-2):219–239, 2003. Compilation and indexing terms, Copyright 2005 Elsevier Engineering Information, Inc.

[109] D. J. Vermeer, J. W. Meyer, and A. K. Oppenheim. Auto-ignition of hydrocarbons behind reflected shock waves. *Combustion and Flame*, 18:327–336, 1972. Compilation and indexing terms, Copyright 2006 Elsevier Inc. All rights reserved; 3.

[110] C. K. Westbrook, H. J. Curran, W. J. Pitz, J. F. Griffiths, C. Mohamed, and S. K. Wo. Effects of pressure, temperature, and concentration on the reactivity of alkanes: Experiments and modeling in a rapid compression machine. *Symposium (International) on Combustion*, 1:371–378, 1998. Compilation and indexing terms, Copyright 2005 Elsevier Engineering Information, Inc.

[111] J. Wurmel and J. M. Simmie. Cfd studies of a twin-piston rapid compression machine. *Combustion and Flame*, 141:417–430, 2005. Compilation and indexing terms, Copyright 2006 Elsevier Inc. All rights reserved; 4.

[112] J. R Yang and S. C Wong. On the suppression of negative temperature coefficient (ntc) in autoignition of n-heptane droplets. *Combustion and Flame*, 132(3):475–491, 2003. Compilation and indexing terms, Copyright 2005 Elsevier Engineering Information, Inc.

[113] Y. Zeldovich. Flame propagation in a substance reacting at initial temperature. *Combustion and Flame*, 39:219–224, 1980. Compilation and indexing terms, Copyright 2006 Elsevier Inc. All rights reserved; 3.

[114] X. L. Zheng, T. F. Lu, C. K. Law, C. K. Westbrook, and H. J. Curran. Experimental and computational study of nonpremixed ignition of dimethyl ether in counterflow. *Proceedings of the Combustion Institute,*, 30(1):1101–1109, 1 2005.